m-Terphenyl Transition Metal Complexes: Catalysis and Small Molecule Activation

Helen R. Sharpe, MSci (Hons)

Thesis submitted to the University of Nottingham for the degree of Doctor of Philosophy

May 2017

Declaration

The work described in this thesis was carried out at the University of Nottingham between October 2013 and May 2017, under the supervision of Dr Deborah L. Kays. All of the work is my own unless stated to the contrary, and has not previously been submitted for any degrees at this or any other university.

Helen R. Sharpe

Abstract

Herein, the synthesis, reactivity and catalytic activity of low-coordinate transition metal complexes bearing the *m*-terphenyl ligands is reported. Synthesis of the low-coordinate complexes are achieved *via* metathesis reactions between the aryl lithium dimer [2,6-$Ar_2C_6H_3Li]_2$ and the transition metal dihalide (MX_2) in a mixture of toluene and THF. The steric demands of the ligand were altered through variation of the flanking aryl (Ar) by substitution of methyl groups in either the 2,6-positions (2,6-Xyl), 2,4,6-positions (Mes) or 2,4,5-positions (Tmp).

Two-coordinate group 12 complexes (**7**-**9**) exhibit conformational isomerism in solution due to rotation of the flanking aryl substituent. The analogous open shell transition metal complexes are three-coordinate where the coordination sphere features two *m*-terphenyl ligands with coordination of a THF molecule to the metal centre (**15** and **16**).

Coordination of acetonitrile to the two-coordinate complexes **10** and **11** afforded the four-coordinate complexes **17** and **18** highlighting the steric demands of the 2,6-$Mes_2C_6H_3^-$ ligand are not great enough to prevent access of small molecules to the metal centre.

Two- and three-coordinate complexes of manganese and iron (**10**, **11**, **15**, and **16**) were found to be efficient precatalysts for the cyclotrimerisation of primary aliphatic isocyanates. Secondary, tertiary aliphatic and aryl isocyanates were not effective in this reaction where it is proposed that a metal-amidate species forms deactivating the catalytically active species towards cyclotrimerisation. Kinetic measurements between the reaction of **10** with EtNCO revealed the rate to be 1st order with respect to both substrates.

Iron complexes **11** and **16** were efficient precatalysts for the hydrophosphination of isocyanates producing mono- (**21**) and/or diinsertion (**22**) products where the latter is a new family of derivatised phosphines. The product obtained is a result of the steric demands of the isocyanate where bulky isocyanates yield the mono-insertion product exclusively and the less bulky aryl isocyanates produce a mixture. The selectivity of the reaction can be controlled with minor modifications to the reaction conditions. Initial coordination chemistry of the diinsertion product **22a** was investigated towards [Ru(*p*-cym)$Cl_2]_2$.

Manganese complexes **10**, **13** and **15** were efficient precatalysts in the dehydrocoupling of $Me_2NH{\cdot}BH_3$ affording the cyclic dimer $[Me_2N–BH_2]_2$ under mild conditions. Small changes in the sterics of the ligand drastically alter the reaction mechanism (homogeneous *vs.* heterogeneous).

The reactivity of two-coordinate iron complexes **11** and **14** were investigated towards CO under ambient conditions which formed novel squaraines (**29^{Mes}** and **29$^{2,6\text{-}Xyl}$**) and diiron carboxylate complexes (**30$^{2,6\text{-}Xyl}$**) as a result of CO bond scission. Carbon-13 labelling studies verified the origin of the carbons from the central C_4O_2 unit of the squaraine though analysis *via* EPR, NMR and IR spectroscopies, mass spectrometry and DFT calculations.

Acknowledgements

First and foremost, thanks go to my supervisor Dr Debbie Kays, for her constant support, advice and encouragement though out the course of my studies. Also thanks to Prof. Neil Champness for supervision and advice in the final year of my PhD.

Many thanks to Dr Ana Geer, who joined the Kays group in part way through my second year, a particularly difficult time in my PhD: this thesis would not be half of what it is without you. You helped turn around my project, offered constant and unrelenting support and friendship throughout. Your incredible knowledge, never ending ideas and suggestions, dedication, attention to detail and passion for chemistry are truly inspirational and you have made me the researcher that I am today of which I can't thank you enough.

Thanks go to all members of the Kays group, past and present for help, support and friendship, in particular Dr Katherine Shaw, whose friendship, support and kindness have been invaluable during my PhD. Thanks also go to my project students Gareth, Charlotte, Pooja and Piriya. I'd like to thank the Champness and Liddle groups and other friends at the School for help and support.

Thanks also go to Dr Will Lewis help and patience in teaching me crystallography, Dr Huw Williams for all your help with NMR and letting me loose on the 600 MHz NMR for the many reaction monitoring experiments, Dr E. Stephen Davis for EPR and CV measurements, Dr David Robinson and Dr Jon McMaster for DFT calculations on the squaraine compounds, Dr Mick Cooper for mass spec measurements, Miss Beth Adams and Dr Raphael Horvath for help with IR and UV/Vis spectroscopies. Thanks to Dr Michael Fey and Mr Rhys Lodge for TEM, STEM and EDX measurements and Dr Graham Rance for DLS measurements at the Nanoscale and Microscale Research Centre, University of Nottingham, and Mr Stephen Boyer of the London Metropolitan University for elemental analysis. Thanks also go to technical support and stores staff, in particular Mr Mark Guyler for always keeping the lab, Sue for tea and friendly chats and also to Mr Clive Dixon for always fixing my broken glassware as a top priority!

Finally, thanks to friends and family, in particular my mother, step father, sister and my partner, Josh for constant unwavering support throughout my entire PhD studies.

Publications

H. R. Sharpe, A. M. Geer, H. E. L. Williams, T. J. Blundell, W. Lewis, A. J. Blake and D. L. Kays, Cyclotrimerisation of isocyanates catalysed by low-coordinate Mn(II) and Fe(II) *m*-terphenyl complexes. *Chem. Commun.* **2017**, *53*, 937–940.

H. R. Sharpe, A. M. Geer, W. Lewis, A. J. Blake and D. L. Kays, Iron(II) Catalysed Hydrophosphination of Isocyanates, *Angew. Chem. Int. Ed.,* **2017,** *56*, 4845–4848.

H. R. Sharpe, A. M. Geer, T. J. Blundell, F. R. Hastings, W. Lewis, A. J. Blake, G. A. Rance, M. W. Fay, and D. L. Kays, Dehydrocoupling of Dimethylamine-Borane Promoted by Manganese(II) *m*-Terphenyl Complexes, *submitted manuscript.*

H. R. Sharpe, A. M. Geer, T. J. Blundell, E. S. Davis, J. McMaster, D. Robinson, W. Lewis, A. J. Blake and D. L. Kays, Reductive Coupling of Carbon Monoxide by Fe(II) *m*-Terphenyl Complexes, *manuscript in preparation.*

Contents

Declaration……..….ii

Abstract…….....iii

Acknowledgements……...…..iv

Publications……..v

Contents…….…..vi

Abbreviations……..….xiv

Chapter I – Introduction …….....1

1.1 Introduction……....2

1.2 Low-Coordinate Complexes……...3

1.3 *m*-Terphenyl Transition Metal Complexes…….....5

1.4 Catalysis with Low-Coordinate Transition Metal Complexes……19

1.5 Aims……..……...25

1.6 References.……...26

Chapter II – Low-Coordinate Complexes ……31

2.1 Introduction……..32

2.2 Experimental……34

2.2.1 Ligand Synthesis……...34

2.2.1.1 2,6-$Ar_2C_6H_3I$ (Ar = Mes, 2,4,6-$Me_3C_6H_2$, **1**; 2,6-Xyl, 2,6-$Me_2C_6H_3$, **2**; Tmp, 2,4,5-$Me_3C_6H_2$, **3**…….....34

2.2.1.2 [2,6-$Ar_2C_6H_3Li]_2$ (Ar = Mes, 2,4,6-$Me_3C_6H_2$, **4**; 2,6-Xyl, 2,6-$Me_2C_6H_3$, **5**; Tmp, 2,4,5-$Me_3C_6H_2$, **6**…….....36

2.2.2 Two-Coordinate Complexes……..38

2.2.2.1 $(2,6\text{-}Tmp_2C_6H_3)_2Zn$ (**7**)…….....38

2.2.2.2 $(2,6\text{-}Tmp_2C_6H_3)_2Cd$ (**8**)…….....38

2.2.2.3 $(2,6\text{-}Tmp_2C_6H_3)_2Hg$ (**9**)…….....39

2.2.2.4 $(2,6\text{-}Mes_2C_6H_3)_2Mn$ (**10**)……40

2.2.2.5 (2,6-$Mes_2C_6H_3)_2Fe$ (**11**)…….....40

2.2.2.6 (2,6-$Mes_2C_6H_3)_2Co$ (**12**)…….....40

2.2.2.7 (2,6-(2,6-$Xyl)_2C_6H_3)_2Mn$ (**13**)……41

2.2.2.8 (2,6-(2,6-$Xyl)_2C_6H_3)_2Fe$ (**14**)…….....41

2.2.3 Three-Coordinate Complexes……42

2.2.3.1 (2,6-$Tmp_2C_6H_3)_2Mn(THF)$ (**15**)……..…...42

2.2.3.2 (2,6-$Tmp_2C_6H_3)_2Fe(THF)$ (**16**)……...42

2.2.4 Four-Coordinate Complexes…….....43

2.2.4.1 (2,6-$Mes_2C_6H_3)_2Mn(MeCN)_2$ (**17**)…….....43

2.2.4.2 (2,6-$Mes_2C_6H_3)_2Fe(MeCN)_2$ (**18**) ……..43

2.3 Results and Discussion…….....45

2.3.1 Ligand Synthesis……...45

2.3.1.1 *m*-Terphenyl Iodides……...45

2.3.1.2 *m*-Terphenyl Lithium Complexes……..46

2.3.2 Two-Coordinate Complexes……..47

2.3.2.1 Disubstitution of Group 12 Halides……47

2.3.2.1.1 Crystallographic Analysis……...49

2.3.2.2 Disubstitution of Transition Metal Halides……....52

2.3.3 Three-Coordinate Complexes……53

2.3.3.1 Disubstitution of Transition Metal Halides……....53

2.3.3.2 Crystallographic Analysis……..55

2.3.4 Four-Coordinate Complexes…….....59

2.3.4.1 Crystallographic Analysis……..60

2.4 Conclusions……..64

2.5 Future Work…….....66

2.6 References……67

Chapter III – Catalytic Cyclotrimerisation of Isocyanates……...……..……70

3.1 Introduction……..71

3.2 Experimental……73

3.2.1 Initial Assessments……73

3.2.2 Standard Procedure for the Catalytic Cyclotrimerisation of Isocyanates…….……73

3.2.3 Standard Procedure for the Synthesis of Cyclotrimerisation Products **19a-d**……..74

3.2.3.1 1,3,5-Tri(ethyl)-isocyanurate (**19a**).……...75

3.2.3.2 1,3,5-Tri(*n*-propyl)-isocyanurate (**19b**).…….....75

3.2.3.3 1,3,5-Tri(*n*-hexyl)-isocyanurate (**19c**).……...75

3.2.3.4 1,3,5-Tri(benzyl)-isocyanurate (**19d**) ……76

3.2.4 Stoichiometric Reaction of 3,5-Dimethoxyphenyl Isocyanate with **11** to Form Carboxamide, 2,6-$Mes_2C_6H_3C(O)NH$-3,5-$(OMe)_2C_6H_3$ (**20**)……..76

3.2.5 Catalyst Poisoning Tests……...77

3.2.5.1 Mercury Drop Test…….....77

3.2.5.2 Radical Trap Test……...77

3.2.6 General Procedure for Kinetic NMR Experiments……...78

3.2.7 Cyclotrimerisation with Mixed Isocyanates……..78

3.3 Results and Discussion…….....80

3.3.1 Preliminary Testing……...80

3.3.2 Catalytic Cyclotrimerisation of Primary Alkyl Isocyanates……..81

3.3.3 Reactions with Aromatic, Secondary and Tertiary Alkyl Isocyanates… ……84

3.3.4 Reaction of 3,5-Dimethoxyphenyl Isocyanate with **11**….……85

3.3.5 Mechanistic Studies……...88

3.3.5.1 Proposed Mechanism…….90

3.3.5.2 Cyclotrimerisation with Mixed Isocyanates…….....92

3.3.5.3 Kinetic Studies…….....95

3.4 Conclusions……..98

3.5 Future Work……...100

3.6 References……..102

Chapter IV – Hydrophosphination of Isocyanates……105

4.1 Introduction……106

4.2 Experimental……..108

4.2.1 Standard Procedure for the Catalytic Hydrophosphination of Isocyanates……...108

4.2.2 Standard Procedure for *in situ* NMR Reaction Monitoring for the Catalytic Hydrophosphination of Isocyanates……..108

4.2.3 Standard Procedure for the Catalytic Hydrophosphination of Isocyanates in THF……..109

4.2.4 Catalytic Hydrophosphination of Isocyanates with Additives……109

4.2.4.1 *In situ* NMR Reaction Monitoring for the Catalytic Hydrophosphination of Isocyanates with Additives…….....109

4.2.4.2 Catalytic Hydrophosphination of Isocyanates with Weak Base/Acid……110

4.2.5 Hydrophosphination with Isocyanate Mixtures……..110

4.2.6 Scale up of Hydrophosphination Products **21** and **22**……111

4.2.6.1 Synthesis of **21a**, **c**, and **d**……111

4.2.6.2 Synthesis of **21f-h**……112

4.2.6.3 Synthesis of **22a-d**……112

4.2.6.4 Large Scale Synthesis of **22a**……...112

4.2.7 Spectroscopic Data……..113

4.2.7.1 $Ph_2PC(=O)NH(Ph)$ (**21a**)……113

4.2.7.2 $Ph_2PC(=O)NH[3,5\text{-}(OMe)_2C_6H_3]$ (**21c**)……...113

4.2.7.3 $Ph_2PC(=O)NH(4\text{-}BrC_6H_4)$ (**21d**)……..114

4.2.7.4 $PPh_2C(O)NH(Cy)$ (**21f**)……114

4.2.7.5 $PPh_2C(O)NH(^iPr)$ (**21g**)……115

4.2.7.6 $PPh_2C(O)NH(^tBu)$ (**21h**)……..116

4.2.7.7 $PPh_2C(O)N(Ph)C(O)NH(Ph)$ (**22a**)……..116

4.2.7.8 $PPh_2C(O)N(^pTol)C(O)NH(^pTol)$ (**22b**)……117

4.2.7.9 $PPh_2C(O)N(3,5\text{-}(OMe)_2C_6H_3)C(O)NH(3,5\text{-}(OMe)_2C_6H_3)$ (**22c**)……...…..118

4.2.7.10 $PPh_2C(O)N(4\text{-}BrC_6H_4)C(O)NH(4\text{-}BrC_6H_4)$ (**22d**)…….....118

4.2.7.11 $PPh_2C(O)N(^nHx)C(O)NH(^nHx)$ (**22e**)……119

4.2.8 Coordination of Phosphinocarboxamides to Dichloro(*p*-cymene) Ruthenium……120

4.2.8.1 Synthesis of $[Ru(p\text{-cym})\{PPh_2C(O)NH(^iPr)\}Cl_2]$ (**23**)……120

4.2.8.2 Synthesis of $[Ru(p\text{-cym})\{PPh_2C(O)N(^pTol)C(O)NH(^pTol)\}Cl_2]$..… (**24**)……...121

4.3 Results and Discussion……...122

4.3.1 Product Selectivity……..123

4.3.2 Mechanistic Studies…….128

4.3.2.1 Proposed Mechanism……...130

4.3.3 Scale-up of Hydrophosphination Products **21** and **22**…….....132

4.3.3.1 Spectroscopic Analysis…….....133

4.3.3.2 Crystallographic Analysis……135

4.3.4 Coordination of **21g** and **22a** to Dichloro(*p*-cymene) Ruthenium……..139

4.4 Conclusions……145

4.5 Future Work……...147

4.6 References……..148

Chapter V – Dehydrocoupling of Amine-Boranes…….151

5.1 Introduction……152

5.2 Experimental……..154

5.2.1 Catalytic Dehydrocoupling of $NH_3{\cdot}BH_3$…….....154

5.2.2 Catalytic Dehydrocoupling of $NH_3{\cdot}BH_3$, with Hydrogen Acceptor……...154

5.2.3 Standard Procedure for the Catalytic Dehydrocoupling of $Me_2NH{\cdot}BH_3$……..154

5.2.4 *In situ* NMR Reaction Monitoring for the Catalytic Dehydrocoupling of $Me_2HN{\cdot}BH_3$…….....155

5.2.5 Catalyst Poisoning Tests…….....155

5.2.5.1 Mercury Drop Test……...155

5.2.5.2 CS_2……156

5.2.5.3 Radical Trap Test…….....156

5.3 Results and Discussion……...157

5.3.1 Catalytic Dehydrocoupling of $NH_3{\cdot}BH_3$, by Manganese(II) and Iron(II) Precatalysts……...157

5.3.2 Catalytic Dehydrocoupling of $Me_2NH{\cdot}BH_3$ by Manganese(II) Precatalysts……...158

5.3.2.1 Closed Reaction System……...159

5.3.2.2 *In situ* Reaction Monitoring…….....161

5.3.2.3 Catalyst Poisoning Experiments……...165

5.3.3 Particle Size Measurements…….....166

5.3.3.1 Preliminary TEM Measurements…….....166

5.3.3.2 TEM Measurements under Inert Atmosphere……..168

5.3.3.3 DLS Measurements……..170

5.3.4 Proposed Catalytic Cycle……171

5.4 Conclusions……174

5.5 Future Work……...176

5.6 References……..177

Chapter VI – Reductive Coupling of CO by Iron(II) Complexes…….....180

6.1 Introduction……181

6.2 Experimental……..184

6.2.1 Reaction of Iron Diaryls with CO……...184

6.2.1.1 Reaction of **11** with CO……184

6.2.1.2 Reaction of **14** with CO……185

6.2.2 Standard Procedures for Reaction Monitoring……186

6.2.2.1 Reaction Monitoring *via* IR Spectroscopy……...186

6.2.2.2 Reaction Monitoring *via* EPR Spectroscopy……186

6.2.3 ^{13}CO Labelling Studies……186

6.2.3.1 Reaction of **11** with ^{13}CO ……186

6.2.3.2 Reaction Monitoring *via* IR Spectroscopy……...187

6.3 Results and Discussion……...189

6.3.1 Squaraines……...190

6.3.1.1 Spectroscopic Analysis of Squaraines **29^{Mes}** and **29$^{2,6\text{-}Xyl}$**……....192

6.3.1.2 Crystallographic Analysis……200

6.3.2 Diironcarboxylate Complex……203

6.3.2.1 Spectroscopic Analysis of Carboxylate Complex **30$^{2,6\text{-}Xyl}$**..……203

6.3.2.2 Crystallographic Analysis of Carboxylate Complex **30$^{2,6\text{-}Xyl}$** ……..204

6.3.3 *In situ* Reaction Monitoring……206

6.3.3.1 Reaction Monitoring *via* Solution IR Spectroscopy…….....206

6.3.3.2 Reaction Monitoring *via* EPR Spectroscopy ……...209

6.3.4 Carbon-13 Labelling Studies……...212

6.3.4.1 Spectroscopic Analysis of 1,3-(2,6-Mes$_2$C$_6$H$_3$)$_2$^{13}C$_4$O$_2$ (**^{13}C-29^{Mes}**)……..212

6.3.4.2 *In situ* Reaction Monitoring *via* Solution IR with ^{13}CO……...214

6.3.5 Calculations…….....215

6.3.6 Mechanistic Discussion……...218

6.4 Conclusions……222

6.5 Future Work……...225

6.6 References……..227

Chapter VII – Concluding Remarks…….....232

Chapter VIII – General Experimental ……239

8.1 General Experimental Techniques…….240

8.1.1 Manipulation of Air-sensitive Compounds…….240

8.2 Physical Measurements……..240

8.2.1 NMR Spectroscopy…….240

8.2.2 IR Absorption Spectroscopy…….....241

8.2.3 Mass Spectrometry……..241

8.2.4 Elemental Microanalysis…….242

8.2.5 UV/visible Absorption Spectroscopy……..242

8.2.6 Evans Method……..242

8.2.7 X-ray Crystallography…….243

8.2.8 Electron Paramagnetic Resonance Spectroscopy……244

8.2.9 Cyclic Voltammetry……244

8.2.10 Dynamic Light Scattering ……244

8.2.11 Transmission Electron Microscopy ……..245

8.2.12 Scanning Transmission Electron Microscopy…….....245

8.2.13 Energy Dispersive X-ray Spectroscopy …….....245

8.3 Preparation of Solvents and Reagents…….....246

8.4 References……..248

Appendices……...A1

Crystallographic Data……A2

List of Compounds……A9

Abbreviations

2,2,2,-crypt	4,7,13,16,21,24-hexaoxa-1,10-diazabicyclo[8.8.8]hexacosane
2,6-Xyl	2,6-Dimethylphenyl, 2,6-$Me_2C_6H_3^-$
3,5-Xyl	3,5-Dimethylphenyl, 3,5-$Me_2C_6H_3^-$
Å	Angstrom, 10^{-10} m
Ar	Aryl
ATR	Attenuated total reflectance
BAr^F_{24}	$B[3,5\text{-}(CF_3)C_6H_3]_4^-$
BIPY	2,2'-bipyridine
Bn	Benzyl, $C_6H_5CH_2^-$
br	broad
cAAC	Cyclic alkyl(amino) carbene
CHN	Carbon/hydrogen/nitrogen content (elemental analysis)
CIF	Crystallographic information file
Cp	Cyclopentadienyl, $C_5H_5^-$
CV	Cyclic voltammetry
Cy	Cyclohexyl, $C_6H_{11}^-$
DCM	Dichloromethane, CH_2Cl_2
dd	Double doublet (NMR)
DFT	Density functional theory
Dipp	Diisopropylphenyl, 2,6-$^iPr_2C_6H_3^-$
DLS	Dynamic light scattering
DME	1,2-Dimethoxyethane, 1,2-$(MeO)_2C_2H_4$
EDX	Energy-dispersive X-ray
EI	Electron ionisation
EPR	Electron paramagnetic resonance
ESI	Electrospray ionisation
Et	Ethyl, $CH_3CH_2^-$
Fc	Ferrocene
FTIR	Fourier transform infrared spectroscopy
GC	Gas chromatography
h	Hour
HOMO	Highest Occupied Molecular Orbital
i	*ipso*
^{i}Pr	*iso*-Propyl, Me_2CH^-
IPr	1,3-Bis(2,6-diisopropylphenyl)-imidazol-2-yl-idene
IR	Infrared
J	Coupling constant (NMR)
L	Ligand
LC	Liquid chromatography
LUMO	Lowest occupied molecular orbital
m	*meta*
m	Multiplet (NMR)
Me	Methyl, CH_3^-
Mes	Mesityl, 2,4,6-$Me_3C_6H_2^-$
Mes*	Supermesityl, 2,4,6-$^tBu_3C_6H_2^-$
MS	Mass spectrometry

n	Number
Naph	Naphthyl, $C_{10}H_7^-$
NHC	*N*-heterocyclic carbene
^{n}Hx	*n*-Hexyl, $(CH_2)_5CH_3^-$
NMR	Nuclear magnetic resonance
^{n}Pr	*n*-propyl, $MeCH_2CH_2^-$
o	*ortho*
p	*para*
p-cym	*para*-Cymene, 1-Methyl-4-(propan-2-yl)benzene
Ph	Phenyl
ppm	Parts per million
^{p}Tol	*para*-Tolyl,
q	Quartet (NMR)
R	Alkyl; molecular fragment
s	Singlet (NMR); second(s)
STEM	Scanning transmission electron microscopy
t	Triplet (NMR)
^{t}Bu	*tert*-Butyl, $(Me)_3C^-$
TEM	Transmission electron microscopy
THF	Tetrahydrofuran
Tmp	Trimethylphenyl, 2,4,5-$Me_3C_6H_2^-$
Tol	Tolyl, $MeC_6H_4^-$
UV/Vis	Ultraviolet/visible
VT	Variable temperature
XRD	X-Ray diffraction
Xyl	Xylyl, $Me_2C_6H_3^-$
δ	Chemical shift (NMR)
$\Delta\nu_{1/2}$	Half-height peak width
λ	Wavelength
π	Pi (orbital symmetry)
σ	Sigma (orbital symmetry)
$\bar{\nu}$	Wavenumber, $1/\lambda$

Chapter I

Introduction

This chapter aims to give a brief overview of the development of organometallic chemistry in the context of low-coordinate open shell transition metal complexes with the main focus being on the use of the *m*-terphenyl framework. The structure, bonding and subsequent reactivity of these transition metal complexes will be explored and discussed in detail. The final part of this chapter will focus on a few recent examples of low-coordinate open shell transition metal complexes which have been applied as efficient catalysts for organic transformations.

1.1 Introduction

Organometallic chemistry is a substantial research area of chemistry and has attracted significant interest over the past 200 years.[1] Organometallic compounds are characterised by a complex bearing at least one direct metal–carbon bond where the metal can be from the main groups of the periodic table or a transition metal, and the organic moiety may take numerous forms from alkyl (CH_3, C_2H_4) to larger aromatic systems (Cp = $C_5H_5^-$, C_6H_6 *etc.*).[2] The first organometallic compound, synthesised back in 1827, was a water soluble ethylene complex of platinum, $K[PtCl_3C_2H_4]$ obtained through the reaction of a mixture of $PtCl_4$ and $PtCl_2$ in ethanol followed by addition of a KCl solution by Zeise, the discovery of which is widely regarded as the birth of organometallic chemistry.[3] It was not until over 100 years later that its chemical formula was verified by X-ray crystallography.[4] Subsequent developments in this field arose from other initially unrelated discoveries, where some notable examples include $Ni(CO)_4$ by Mond in 1890,[5] Frankland's synthesis of alkyl zinc compounds.[6,7] Nobel prize winning discoveries include Grignard's work on organomagnesium compounds,[8] and the synthesis of bis(η^5-cyclopentadienyl)iron or ferrocene in 1951,[9,10] which was responsible for a new era

of organometallic chemistry in the investigation of 'sandwich complexes' whereby the metal is bonded to two organic ring systems.

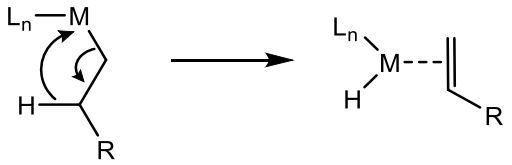
Organometallic complexes have a variety of favourable properties which enables these species to act as catalysts in organic transformations. Examples of these properties include the availability of a wide variety of ligands in which the metal can bind by either π- and σ-bonds; the ability of the ligand to influence the electronics and sterics of the metal centre, and the capability of the metal centre to undergo redox processes and coordination number changes.

These properties have been exploited in industrially and pharmaceutically relevant processes such as olefin polymerisation as pioneered by Ziegler and Natta which saw them win the Nobel prize in 1963,[11] Wilkinson's catalyst, chlorotris(triphenylphosphine)rhodium(I), and derivatives in hydrogenation and hydroformylation of olefins,[12–14] olefin metathesis reactions facilitated by Grubbs or Schrock metal carbene complexes,[15–18] carbon-carbon coupling reactions using transition metal based catalysts as established by Nobel laureates Heck, Negishi and Suzuki amongst others.[19–24]

1.2 Low-Coordinate Complexes

Metal centres with extreme coordinative unsaturation often show unusual coordination geometries and varied reactivity and extensive coordination chemistry.[25,26] The stabilisation of the reactive metal centre with low coordination is largely dominated by the ligand's architecture and electronics, which binds to the metal centre.

It was long thought that homoleptic open shell transition metal alkyl complexes were inherently unstable due to the intrinsically weak M–C bonds when compared to their main group counterparts.[27] This misconception lasted until the 1970s where the understanding of competing side reactions/decomposition route of transition metal alkyls *via* β-hydride elimination (Scheme 1.1).[28] Henceforth, this low energy decomposition pathway was bypassed using ligands which lacked β-hydrogens.



Scheme 1.1 β-hydride elimination.

Early examples where this methodology was employed was by Lappert and Wilkinson where homoleptic transition metal alkyl complexes were obtained using alkyl groups with lacked β-hydrogens.[29–32] However, it was not until 1985 that the first stable homoleptic open shell transition metal complex to feature M−C σ-bonds, $Mn[C(SiMe_3)_3]_2$, was isolated by Eaborn and co-workers. This complex was synthesised *via* the metathesis reaction between $LiC(SiMe_3)_3$ and $MnCl_2$.[33]

The use of sterically demanding ligands offers both kinetic and thermodynamic stabilisation by physically shielding the reactive metal centre therefor preventing interactions between other metal centres inhibiting oligomerisation, and blocking unwanted side reactions. This approach has been utilised effectively in recent years whereby numerous low-coordinate have been successfully isolated through development of sterically demanding ligands. This introduction will focus only on first row, open transition metal complexes with coordination number of four or less.

Early developments saw the use of bulky aryl- and alkoxides which were effective at isolating transition metal complexes with coordination numbers of four through donation of a formal lone pair of electrons into an empty metal *d*-orbital from the Lewis basic donor with a bulky R group (–OR).[34] The use of bulkier silyl amides allowed for the preparation of the monomeric two- or three-coordinate complexes $M\{N(SiMe_3)_2\}_n$ (n = 3, M = Cr, Fe; n = 2; Mn, Co and Ni).[35,36] The related two-coordinate silyl amide complexes of iron, $Fe\{N(SiMe_3)_2\}_2$ and $Fe\{N(SiMePh_2)_2\}_2$, were reported a number of years later.[37-39]

Early reports of the use of aryl based ligands led to the formation of oligomers and polymers, for example, the simplest homoleptic manganese aryl was found to exist as $[MnPh_2]_\infty$ featuring a chain like bonding motif *via* bridging phenyl interactions.[40] Increasing the sterics of the aryl to mesityl (Mes, 2,4,6-$Me_3C_6H_2^-$) afforded the linear trimer $[MnMes_3]$ and the dimers $[MMes_2]_3$ where M = Fe and Co.[41–45] It was not until the more sterically demanding Mes* ligand (2,4,6-$^tBu_3C_6H_2^-$) was employed that the monomeric, two-coordinate homoleptic diaryls $MMes^*_2$ (M = Mn, Fe) were isolated.[44,46] The first cobalt diaryl however, was obtained some years later through use of the bulky *m*-terphenyl framework.[47]

1.3 m-Terphenyl Transition Metal Complexes

The very sterically demanding *m*-terphenyl framework has allowed for the isolation of highly reactive metal centres with low coordination numbers which often exhibit unusual coordination geometries and reactivity.[48] The *m*-terphenyl ligand, usually of the form 2,6-$Ar_2C_6H_3$, features a central aryl ring with substitution of aryl groups in the 2,6 positions, *i.e. meta* to one other. The metal binds to the *ipso* carbon *via* a carbon–metal σ-bond

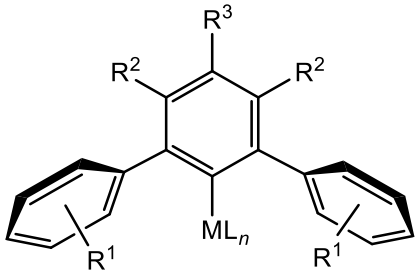
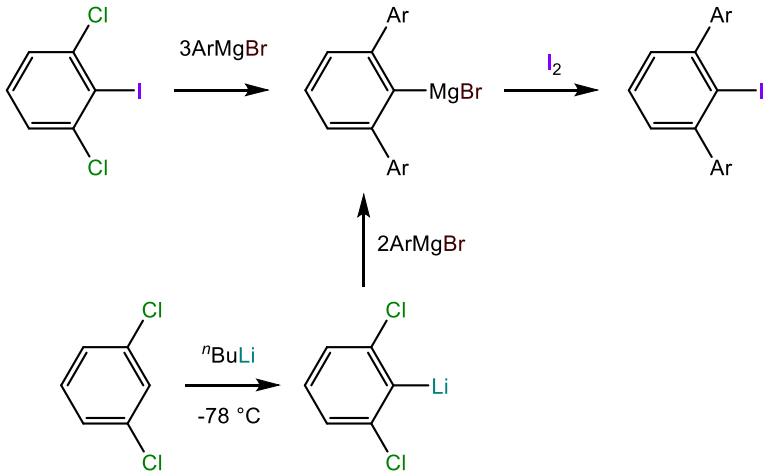


Figure 1.1 General structure of the m-terphenyl.

where the flanking aryls are often orientated orthogonally with respect to the central aryl providing a steric pocket in which the metal resides (Figure 1.1).

The ligand is highly customisable which allows for tailoring of the steric pocket in which the metal is encapsulated. The flanking aryl groups (R^1) can be substituted with sterically demanding groups such as naphthyl (1-Naph, 1-$C_{10}H_7$),[49] diisopropylphenyl (Dipp, 2,6-$^{i}Pr_2C_6H_3$) and triispropylphenyl (Trip, 2,4,6-$^{i}Pr_3C_6H_3$).[50] Power and co-workers have suggested there may be a possible upper limit the sterics that can be opposed by the flanking aryls where attempts to synthesise the *m*-terphenyl with flanking Mes* groups were met without success.[50] The sterics of the ligand can also be increased through substitution on the *meta* position of the central aryl (R^2) with an alkyl therefore reducing the angle between the flanking aryls and the metal centre. This incremented steric bulk has been shown to prevent dimerisation of the chromium(I) species (2,6-$Trip_2$-3,5-$^{i}Pr_2C_6H_2$)Cr(L) where L = THF or PMe_3.[51,52] Substitution in the *para* position on the central aryl (R^3) can also alter the electronic properties of the ligand with substitution of and electron donating or withdrawing groups.[52]

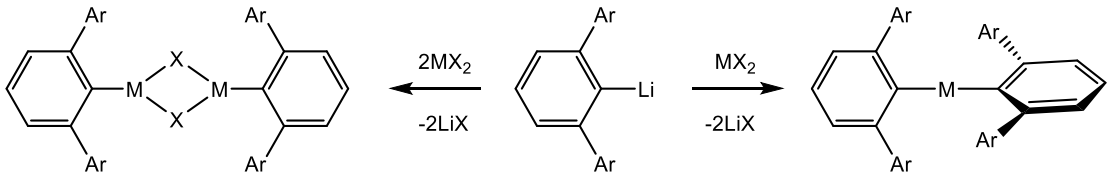
The synthesis of the *m*-terphenyl precursor was first outlined by Hart and co-workers where 1,3-dibromo-2-iodobenzene is treated with three equivalents of a freshly prepared aryl Grignard, ArMgBr, forming the *m*-terphenyl Grignard 2,6-Ar_2-1-$MgBrC_6H_3$ which is subsequently quenched, usually with a halogen, resulting in an air-stable *m*-terphenyl halide (Scheme 1.2, top).[53]



Scheme 1.2 Original (top) and the 'one pot' (bottom) synthetic route to m-terphenyls.

This route has since been superseded by a more convenient one pot route where 1,3-dichlorobenzene undergoes *ortho*-directed lithiation with *n*-butyllithium at low temperatures. The resulting lithium complex is reacted with two equivalents of the freshly prepared aryl Grignard reagent yielding the *m*-terphenyl Grignard which is quenched with a halogen (Scheme 1.2, bottom).[54]

The highly air- and moisture-sensitive *m*-terphenyl lithium aryls $(2,6\text{-}Ar_2C_6H_3Li)_n$ (n = 1, 2), are typically synthesised by the reaction of the *m*-terphenyl iodides with *n*- or *t*-butyllithium (1 or 2 equivalents).[49,50,55,56] These are subsequently reacted with transition metal halides affording the transition metal complexes *via* a salt metathesis reaction where variation of the stoichiometry of ligand to transition metal halide affords either the homolepic (2:1) or heteroleptic (1:1) species (Scheme 1.3). The cobalt dimer $[2,6\text{-}Mes_2C_6H_3Co(THF)(\mu\text{-}Br)]_2$ was synthesised though an alternate route by reaction of the Grignard reagent $[2,6\text{-}Mes_2C_6H_3Mg(THF)(\mu\text{-}Br)]_2$ with $CoCl_2$. The former complex



Scheme 1.3 Heteroleptic (left) and homoleptic (right) complexes.

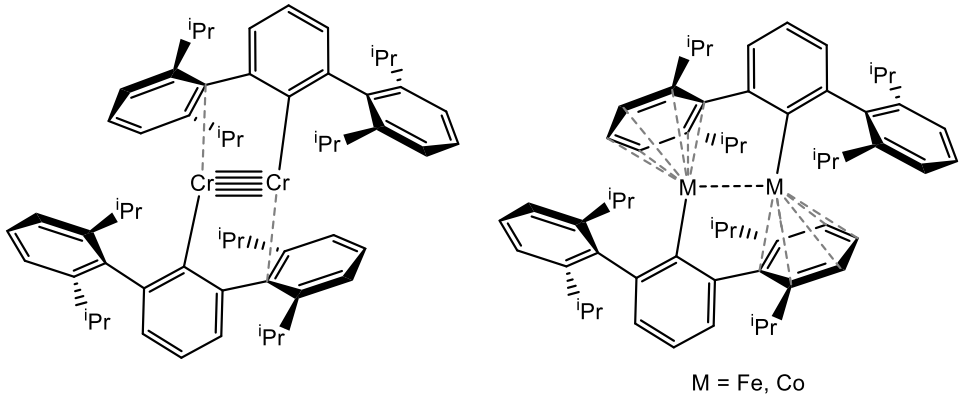
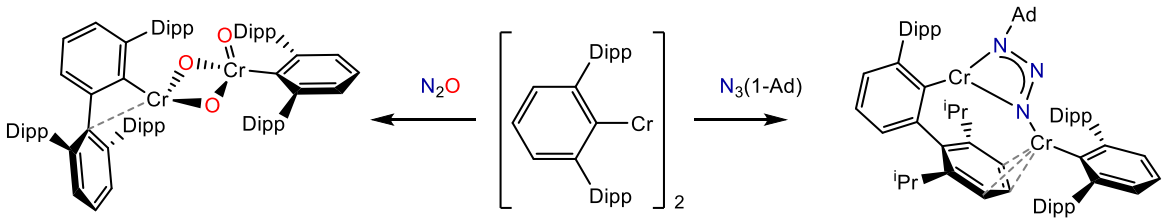


Figure 1.2 Dimeric M(I) species, [Ar'MMAr'], where Ar' = 2,6-Dipp$_2$C$_6$H$_3$; M = Cr (left) which features a fivefold bonding interaction, and M = Fe, Co (right).

represents the first crystallographically verified example of a transition metal complex to bearing an *m*-terphenyl ligand.[57]

The heteroleptic dimeric species [2,6-Dipp$_2$C$_6$H$_3$Cr(μ-Cl)]$_2$ was isolated by Power and co-workers; features two chromium centres in a quasi-four coordinate square-planar geometry through coordination of two bridging chloride ions and a *m*-terphenyl ligand.[58] In contrast, the diethyl either solvated adducts [Li(OEt$_2$)(2,6-Dipp$_2$C$_6$H$_3$)MI$_2$]$_2$ (M = Mn, Fe and Co) which feature a distorted cubane core are afforded when using the same conditions though incomplete elimination of LiI.[58] Chemical reduction using potassium graphite, KC$_8$, in THF of the Cr, Fe and Co homoleptic species yielded the M(I) dimeric species [Ar'MMAr'] where the M–M bonding is vastly different (Figure 1.2).[59,60] The chromium species features a fivefold bonding interaction the two chromium centres with a very short bond distance of 1.8351(4) Å with a weak interaction between the *ipso*-



Scheme 1.4 Products obtained from the reaction with the chromium dimer [(2,6-Dipp$_2$C$_6$H$_3$)Cr]$_2$ with N$_2$O (left) and N$_3$(1-Ad) (right).

carbon of the flanking Dipp group. However, the analogous Fe and Co dimers feature a similar *trans* bent core geometry with a strong η^6-interaction with the flanking Dipp substituent. The M–M bond distances of 2.515(9) Å and 2.8033(5) Å (M = Fe and Co respectively) are much longer than those seen in the Cr species, suggesting the presence of a single (Fe) or weakly bonded (Co) metal centres.[60]

The reactivity of chromium dimer [(2,6-Dipp$_2$C$_6$H$_3$)CrCr(2,6-Dipp$_2$C$_6$H$_3$)] was investigated towards N_2O and the azide N_3(1-Ad) (Ad = 1-adamantanyl) leading to cleavage of the Cr–Cr bond (Scheme 1.4).[57] The reaction with N_2O afforded the compound (2,6-Dipp$_2$C$_6$H$_3$)Cr(μ-O)$_2$Cr(O)(2,6-Dipp$_2$C$_6$H$_3$) where the two metal centres are bridged by two oxo ligands with one of the Cr bound to a terminal oxygen. Both chromium centres have undergone oxidation from Cr(I) to Cr(III)/Cr(V) and possess distorted tetrahedral geometry. The reaction between the chromium dimer and the azide N_3(1-Ad) did not eliminate N_2, alternatively, the azido group inserted into the Cr–Cr quintuple bond. One of the chromium(II) centres is bound to an *m*-terphenyl ligand *via* the *ipso*-carbon, a secondary η^1 interaction with the *ipso* carbon of one of the flanking Dipp groups, and two nitrogen atoms from the azido group. The other Cr(II) is coordinated to the terminal nitrogen of the azide, an *m*-terphenyl and coordination of a Dipp group in an η^3-interaction.[57]

Incorporation of *iso*-propyl butressing groups in the central aryl of the *m*-terphenyl ligand (Figure 1.1, R^2) allowed for the isolation of the monomeric heteroleptic M(I) arene complexes. The reduction of the *in situ* generated halide bridged dimeric species in the presence of KC_8 afforded the Co(I) complex, (2,6-Trip$_2$-3,5-^{i}Pr$_2$-C$_6$H$_3$)Co(η^6-C$_7$H$_8$), in which the Co(I) centre is bound to a toluene solvent molecule *via* an η^6-interaction highlighting that the sterics of the ligand alone can circumvent dimerisation.[61] The

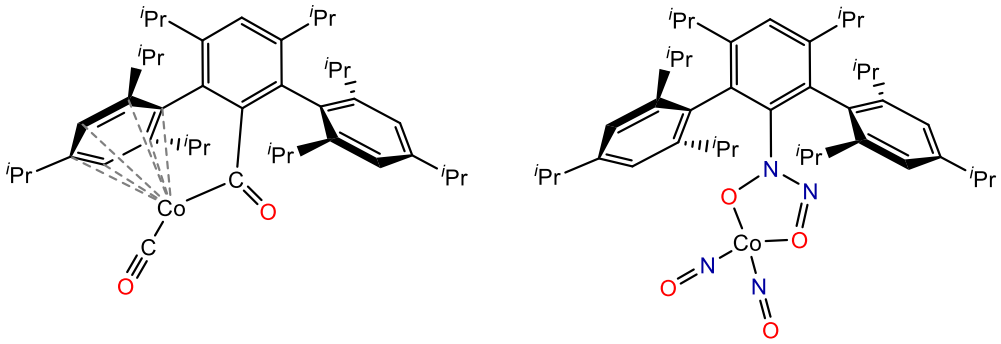


Figure 1.3 Insertion products obtained from the reaction of (2,6-Trip$_2$-3,5-^{i}Pr$_2$-C$_6$H$_3$)Co(η^6-C$_7$H$_8$) with CO (left) and NO (right).

reactivity of this complex towards CO and NO was investigated (Figure 1.3). The reaction with CO resulted in the formation of a carbonyl complex [(2,6-Trip$_2$-3,5-^{i}Pr$_2$C$_6$H$_3$)C(O)Co(CO)] where CO inserted into the C–Co σ-bond with a strong η^6-interaction between the Co and the flanking Dipp aryl.[61] The reaction of the Co(I) arene complex with NO resulted in the formation of four-coordinate cobalt complex [(2,6-Trip$_2$-3,5-^{i}Pr$_2$-C$_6$H$_3$)N(NO)OCo(NO)$_2$] *via* NO insertion into the C–Co σ-bond followed by NO coupling and N–N bond formation which binds to the Co centre in an η^2-O,O interaction.[61] Such double insertion into late-transition metal carbon σ-bonds is rare. Other Co(I) analogues (2,6-Trip$_2$-3,5-^{i}Pr$_2$C$_6$H)Co(η^6-arene) (arene = C$_6$H$_6$, C$_6$H$_5$F) were afforded on reduction of the halide precursor, [2,6-Trip$_2$-3,5-^{i}Pr$_2$C$_6$HCo(μ$_2$-Cl)]$_2$, with KC$_8$ in the presence of other arenes.[62] However, when reduced in C$_6$F$_6$ the Co(II) complex, K[(2,6-Trip$_2$-3,5-^{i}Pr$_2$C$_6$HCo(F)(η^1-C$_6$F$_6$)], was formed as a result of insertion of a 2,6-Trip$_2$-3,5-^{i}Pr$_2$C$_6$HCo moiety in to a C−F bond of C$_6$F$_6$.[62] Manganese(I) and iron(I) arene complexes were also isolated using a similar methodology affording a toluene bridged inverted sandwich complex [(2,6-Trip$_2$-3,5-^{i}Pr$_2$-C$_6$HMn)$_2$(μ$_2$-η^6:η^6-C$_7$H$_8$), Figure 1.4] or a half sandwich complex (2,6-Trip$_2$-3,5-^{i}Pr$_2$C$_6$H)Fe(η^6-C$_6$H$_6$).[63] The reaction of the latter species with the azide N$_3$(1-Ad) resulted in the isolation of an iron(V) bis(imido) complex (2,6-Trip$_2$-3,5-^{i}Pr$_2$-C$_6$H)Fe[N(1-Ad)]$_2$, a rare example of a well characterised iron(V) molecule.[64] Attempts to isolate the analogous chromium complexes (2,6-Trip$_2$-

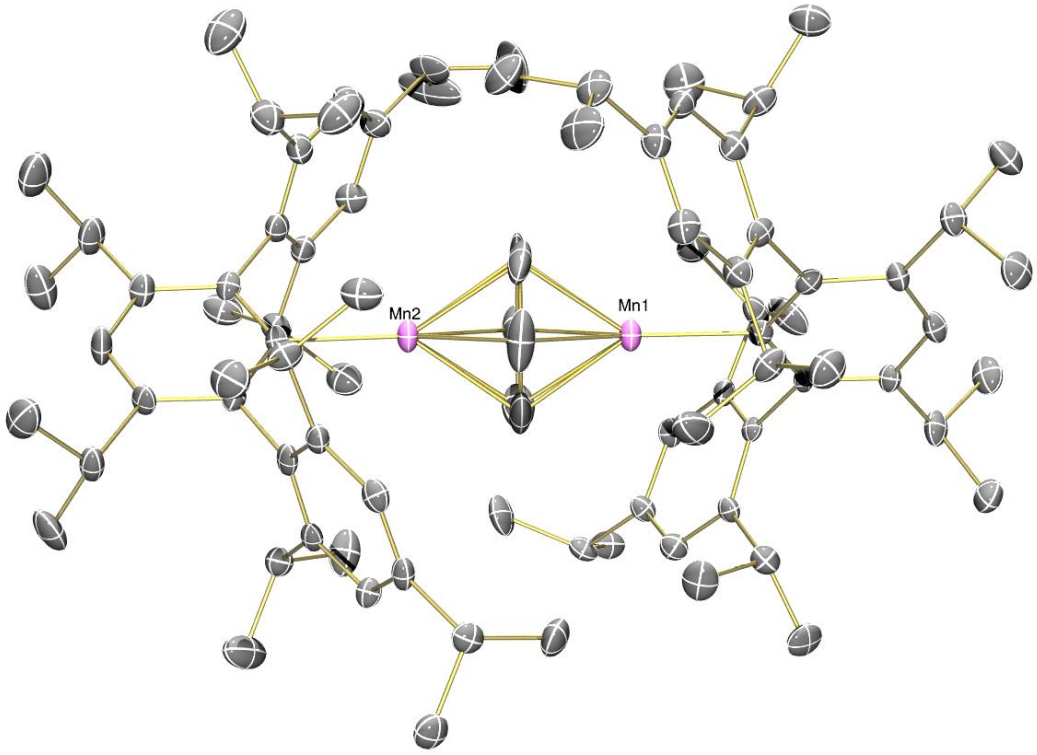


Figure 1.4 Crystal structure of manganese inverted sandwich complex. Hydrogen atoms and solvent of recrystallisation omitted for clarity.

3,5-^{i}Pr$_2$-C$_6$H$_3$)Cr(η^6-arene) led to the formation of intractable brown mixtures. It is thought the unstable arene species is formed but undergoes decomposition due to the low number of valence electrons on the Cr(I) centre whereas the more electron rich counterparts (Mn, Fe, Co) are stable.[63] The related binuclear species sandwich complex 2,6-Trip$_2$-3,5-^{i}Pr$_2$C$_6$HCr(η^3:η^6-CH$_2$Ph)Cr(2,6-Trip$_2$-3,5-^{i}Pr$_2$C$_6$H$_2$) was instead isolated (Figure 1.5).[52] The complex features one metal centre [Cr(II)] bonded to the *m*-terphenyl ligand *via* a carbon σ-bond to the *ipso*-carbon of the central aryl and an interaction from the *ipso*-carbon of a Trip flanking group, with an η^3-interaction with the benzyl moiety. The other chromium centre [Cr(0)] is sandwiched in an η^6:η^6 fashion between the aryl ring of the CH$_2$Ph moiety and the flanking Trip moiety of the 2,6-Trip$_2$-3,5-^{i}Pr$_2$C$_6$H$_2$ ligand. Isolation of the monomeric Cr(I) complex was achieved *via* reduction of the halide precursor with KC$_8$ in the presence of a Lewis base forming the two-coordinate

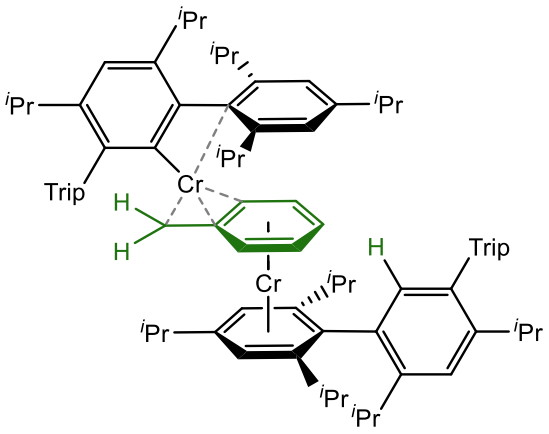


Figure 1.5 Disproportionation product from the reaction of [2,6-Trip$_2$-3,5-^{i}Pr$_2$C$_6$HCr(μ-Cl)] with KC$_8$.

complexes (2,6-Trip$_2$-3,5-^{i}Pr$_2$-C$_6$H$_3$)Cr(L) where L = THF, PMe$_3$.[51] When the analogous reduction reactions between the iron and cobalt species [2,6-Dipp$_2$-3,5-^{i}Pr$_2$C$_6$HM(μ-X)]$_2$ were performed in the presence of the Lewis base, PMe$_3$, different reaction products resulted.[65] The iron(I) complex [(2,6-Dipp$_2$-3,5-^{i}Pr$_2$-C$_6$H)FePMe$_3$], features the iron centre bonded to the *m*-terphenyl ligand *via* the *ipso*-carbon of the central aryl with an η^6-interaction with the flanking Trip moiety, and coordination of a PMe$_3$ ligand.[65] The cobalt(I) allyl complex isolated (Figure 1.6) features the cobalt metal centre coordinated to three carbons which originated from the ^{i}Pr group of the Dipp substituent ($C_3H_4^-$) in an η^3-fashion, where the proton has shifted onto the *ipso*-carbon of the central aryl, with coordination of three PMe$_3$ ligands. The mechanism of the formation of this complex is not understood however is postulated to arise from dehydrogenation of the inert alkyl groups *via* remote C–H activation.[65]

The halide precursors, [2,6-Dipp$_2$-3,5-^{i}Pr$_2$C$_6$HM(μ-Cl)]$_2$, (M = Cr, Mn, Fe) have also been shown to react with K[CpFe(CO)$_2$] (Cp = η^5-C$_5$H$_5$) to form short, unsupported M–Fe bonds in the complexes 2,6-Dipp$_2$-3,5-^{i}Pr$_2$C$_6$HM–FeCp(CO)$_2$. The chromium centre adopts a quasi trigonal planar geometry (C–Cr–Fe = 141.31(6)°) due to the close interaction of the chromium centre with the *ipso*-carbon of the flanking Dipp substituent,

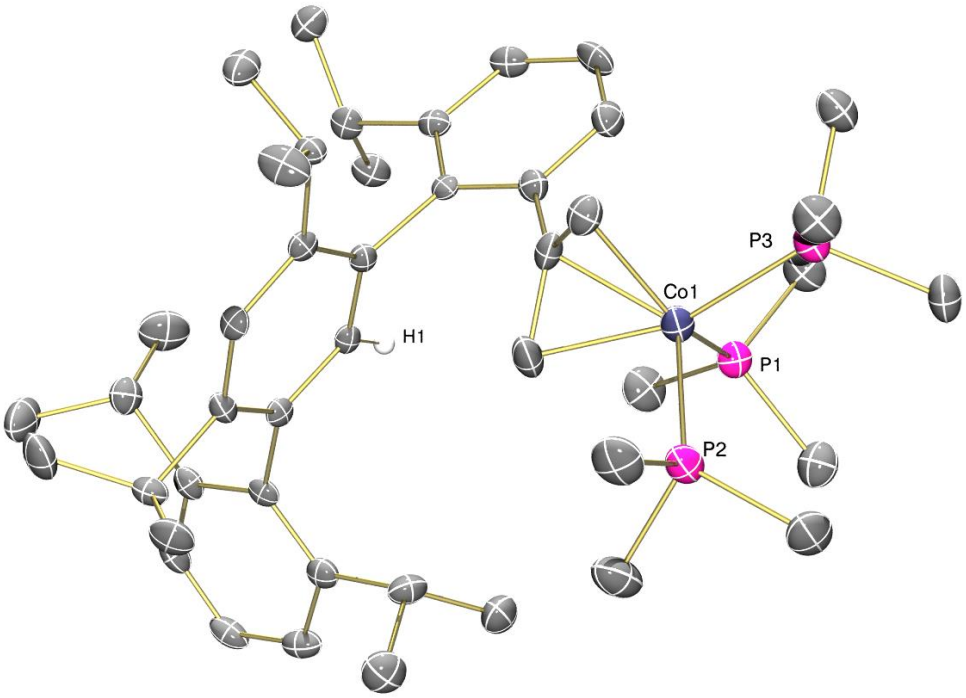


Figure 1.6 Cobalt(I) allyl complex obtained from the reaction of [(2,6-Trip$_2$-3,5-^{i}Pr$_2$-C$_6$H$_3$)Co(μ-Cl)]$_2$ with KC$_8$ and PMe$_3$. Hydrogen atoms (except H1) omitted for clarity.

whereas the analogous iron and manganese complexes adopt a more linear conformation (C–M–Fe: M = Mn, 166.82(6)°; Fe, 163.94(12)°). The M–Fe distances (Mn–Fe, 2.4512(5) Å; Fe–Fe, 2.3931(8) Å) from the X-ray crystal structures were in good agreement DFT calculations which revealed a dative bonding interaction between the two metals.

The reactivity of the aryl manganese halide [Li(THF)(2,6-Dipp$_2$C$_6$H$_3$)MnI$_2$]$_2$ has been explored with a variety of organo lithium substrates revealing a propensity for lithium inclustion into the resulting products.[66] Reactions with LiC≡C^{t}Bu and LiC≡CPh yielded the cubanes as shown in Figure 1.7, which both feature a MnLi$_3$C$_3$ core where the manganese atom, in a distorted tetrahedral geometry, is bound to three C≡CR (R = ^{t}Bu or Ph) units though the β-carbons and to one *m*-terphenyl ligand.[66] This is in stark contrast to the analogous reactions with the iron aryl halide [(2,6- Dipp$_2$C$_6$H$_3$)FeBr]$_2$.[67] The reaction of the iron halide and LiC≡C^{t}Bu yields the iron(II) complex {Li(THF)}$_2$[(2,6-Dipp$_2$C$_6$H$_3$)Fe(C≡C^{t}Bu)$_2$whereas the reaction with LiC≡CPh resulted in the formation of

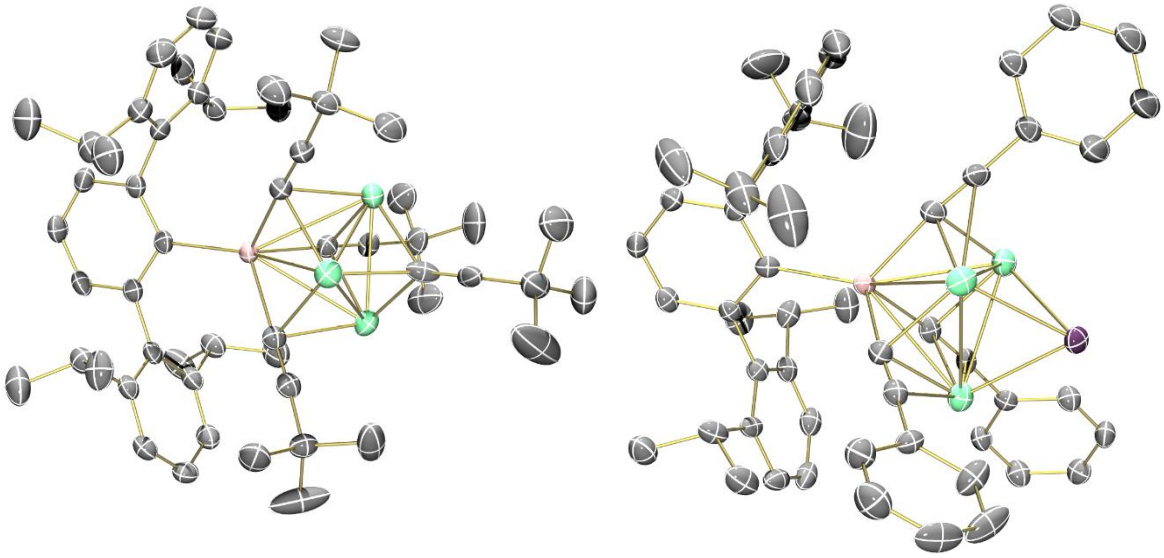


Figure 1.7 Cubane products obtained from the reaction of [Li(THF)(2,6-Dipp$_2$C$_6$H$_3$)MnI$_2$]$_2$ with LiC≡CR where R = ^{t}Bu (left) or Ph.(right). Hydrogen atoms, coordinated solvent molecules to Li$^+$ ions and minor disordered components omitted for clarity. Carbon = grey, manganese = pink, lithium = turquoise, iodine = purple.

the Fe(I) coupled derivative Fe$_2$[(2,6-Dipp$_2$C$_6$H$_3$)C≡C(Ph)–C(Ph)≡C(2,6-Dipp$_2$C$_6$H$_3$)].[67] The reaction between [Li(THF)(2,6-Dipp$_2$C$_6$H$_3$)MnI$_2$]$_2$ and two equivalents of TripMgBr(THF)$_2$ afforded the complex [I-Li(THF)][(2,6-Dipp$_2$C$_6$H$_3$)Mn(Trip)] where the manganese is bonded to an *m*-terphenyl, Trip ligand and an iodide ion. The lithium ion features an η^6-interaction of the Trip ligand with coordination of a THF molecule. When this complex is reacted with another equivalent of the Grignard reagent, the bulky 2,6-Trip$_2$C$_6$H$_3^-$ is displaced rather than the halide yielding [Mn(Trip)(μ-Trip)]$_2$.

The synthesis and reactivity of the homoleptic open shell transition metal *m*-terphenyl diaryl complexes are comparatively underdeveloped than the heteroleptic counterparts. A series of two-coordinate homoleptic diaryls (2,6-Mes$_2$C$_6$H$_3$)$_2$M (M = Mn, Fe, and Co) were synthesised *via* metathesis reactions of the lithium aryl [2,6-Mes$_2$C$_6$H$_3$Li]$_2$ and the transition metal dihalide by Kays in 2007 where the cobalt complex was the first structurally authenticated two-coordinate, homoleptic cobalt(II) complex featuring

σ-bonded aryl ligands.[47] These complexes feature a significant distortion from linearity where the C(*ipso*)–M–C(*ipso*) angles are in the range of 162.8(1)–173.0(1)° and the M–C distances were found to decrease from Mn, Fe, Co which reflects the decrease in ionic radius from Mn^{2+}, Fe^{2+} to Co^{2+}.[47] The analogous series of two-coordinate diaryls (2,6-$Dipp_2C_6H_3)_2M$ (where M = Mn, Fe, Co) were synthesised by reaction of the lithium aryl with the transition metal halide (Fe) or by an alternative route where the aryl transition metal halide is treated with one equivalent of the lithium aryl (Mn and Co).[66,68,69] The increased steric demands of the Dipp *vs.* Mes substituent is reflected in the slightly longer M–C bond lengths observed in (2,6-$Dipp_2C_6H_3)_2M$ (Mn–C = 2.113(2) Å, Fe–C = 2.059(1) Å, Co–C = 2.014(2) Å) *vs*. those in (2,6-$Mes_2C_6H_3)_2M$ (Mn–C = 2.095(3), Fe–C = 2.040(3) and Co–C 2.001(3) Å).[47,66,68,69]

The iron diaryl, (2,6-$Mes_2C_6H_3)_2Fe$, has been used to facilitate the formation of a pentagonal prismatic Zintl ion cage with an encapsulated interstitial iron atom $[Fe@Ge_{10}]^{3-}$. The reaction of a Zintl phase precursor K_4Ge_9 with the diaryl in the presence of 2,2,2-crypt and ethylenediamine (en) yielded the Zintl ion cage which co crystallised with three cationic potassium cryptands as $[[K(2,2,2\text{-crypt})]_3[Fe@Ge_{10}]\cdot 2en$

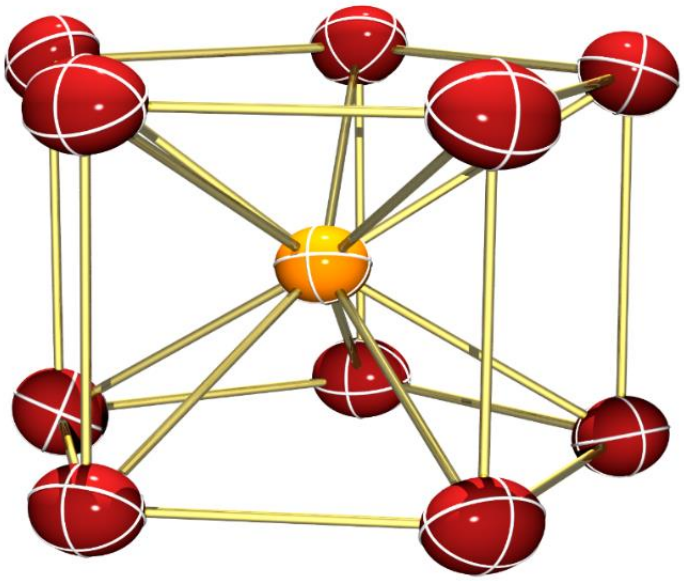


Figure 1.8 Crystal structure of $[Fe@Ge_{10}]^{3-}$ where iron = orange, germanium = red.

(Figure 1.8) and is a remarkable example of a substituent-free group 14 cluster.[70] The Zintl ion cage is formed *via* reductive cleavage of the two Fe–C(*ipso*) bonds by solvated electrons in ethylenediamine solution of K_4Ge_9 followed by proton abstraction of a solvent molecule by the 2,6-$Mes_2C_6H_3^-$ species. The reaction proceeds non-stoichiometrically where the reaction leads to the encapsulated species $[Fe@Ge_{10}]^{3-}$ along with unreacted Ge clusters, $[Ge_9]^{3-}$ and $[Ge_9{-}Ge_9]^{6-}$.

The three-coordinate cobalt diaryl (2,6-$Naph_2C_6H_3)_2Co(OEt_2)$ was synthesised *via* a metathesis reaction between the aryl lithium complex and $CoBr_2$(DME) (where DME = 1,2-dimethoxyethane) in diethyl ether at low temperature. The crystal structure (Figure 1.9) reveals the cobalt centre bound to two *m*-terphenyl ligands with coordination of Et_2O in a distorted trigonal planar geometry. The bent C(*ipso*)–Co–C(*ipso*) geometry (137.49(15)°) together with the flanking Naph moieties orientated in the *syn* conformation, allows for the formation of weak intramolecular CH$\cdots\pi$ interactions. The reactivity of the two- and three-coordinate cobalt diaryls (2,6- $Ar_2C_6H_3)_2Co(OEt_2)_n$ (Ar = Naph, n = 1; Ar = Mes, n = 0) towards CO were found to produce sterically encumbered ketones whose structures varies depending on the flanking aryl substituent.[71]

The two-coordinate iron diaryl, (2,6-$Dipp_2C_6H_3)_2Fe$, isolated by Power and co-workers was found to react with CO at low temperatures affording the η^2-acyl-carbonyl complex (η^2-(2,6-$Dipp_2C_6H_3$)C=O)$_2Fe(CO)_2$ formed as a result of CO insertion into the C(*ipso*)–Fe bond. The reactivity of these diaryl complexes towards CO is explored and discussed in greater detail in Chapter VI. The iron diaryl (2,6-$Dipp_2C_6H_3)_2Fe$ was also found to react with O_2 at low temperatures to produce the monomeric, two-coordinate Fe(II) aryloxide (2,6-$Dipp_2C_6H_3O)_2Fe$ which is resistant to further oxidation upon exposure to excess O_2.[69] This result was surprising due to the fact that other model iron complexes for non-heme oxygen activation generally undergo oxidation to yield an iron(III) species. The

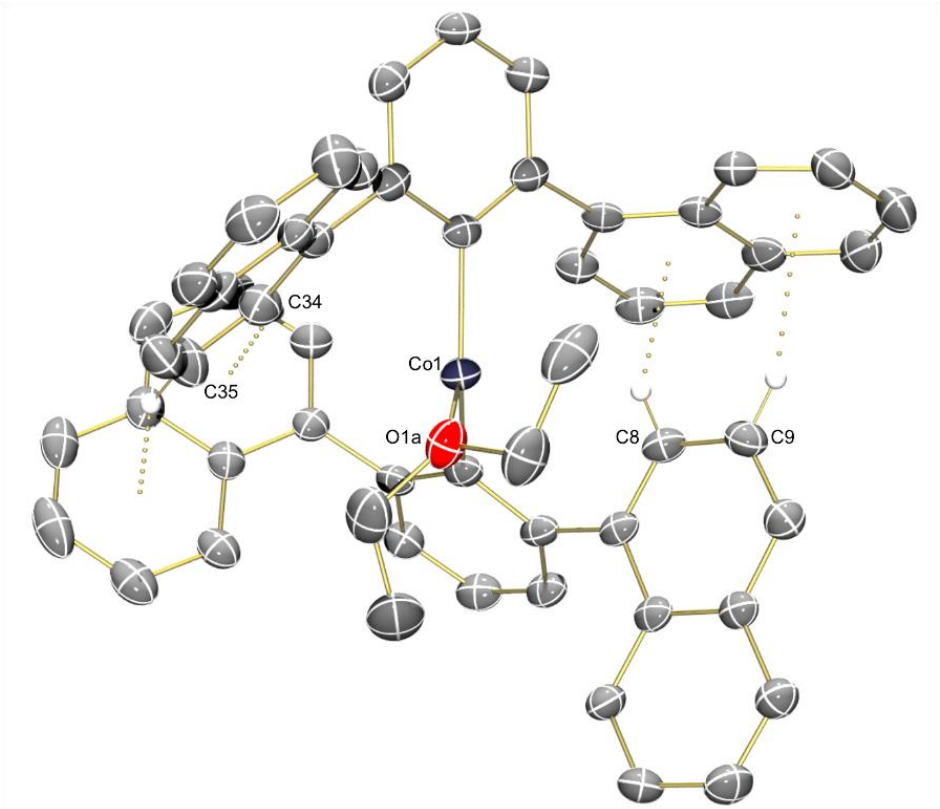
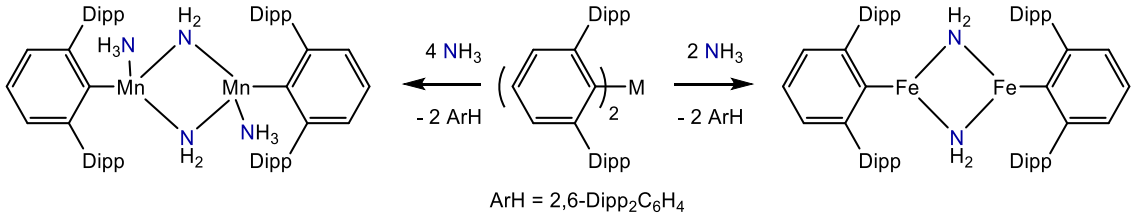


Figure 1.9 Crystal structure of (2,6-Naph$_2$C$_6$H$_3$)$_2$Co(OEt$_2$). Hydrogen atoms (except H8, H9, H34, and H35) and minor disordered components omitted for clarity.

crystal structure of the aryl oxide features a linear crystallographically imposed angle of 180° about the iron centre where a weak secondary interaction is suggested by the short Fe···C distance from the *ipso*-carbon of the flanking Dipp substituent of 2.765(3) Å.

Treatment of the diaryls (2,6-Dipp$_2$C$_6$H$_3$)$_2$M (where M = Mn and Fe) with ammonia lead to the formation of the parent amido species 2,6-Dipp$_2$C$_6$H$_3$M(NH$_3$)$_n$(μ-NH$_2$)]$_2$ (M = Mn, n = 1; M = Fe, n = 0) *via* N–H bond activation (Scheme 1.5). Reactions with the related cobalt diaryl with ammonia did not yield crystalline material. The mechanism for the formation of the amido complexes is currently unknown, but is postulated that NH$_3$ coordinates to the diaryl to form the Lewis base adduct, (2,6-Dipp$_2$C$_6$H$_3$)$_2$M(NH$_3$), then cleavage of the N–H bond and elimination of the arene (2,6-Dipp$_2$C$_6$H$_4$) forms the amido species: (2,6-Dipp$_2$C$_6$H$_3$)$_2$M(NH$_2$). This complex then dimerises though bridging NH$_2^-$



Scheme 1.5 Reactions of (2,6-Dipp$_2$C$_6$H$_3$)$_2$M with ammonia (M = Mn and Fe).

groups forming [(2,6-Dipp$_2$C$_6$H$_3$)M(μ-NH$_2$)]$_2$. For manganese, an additional NH$_3$ molecule coordinates to the metal, completing the coordination sphere.

The examples discussed in this section demonstrate how the *m*-terphenyl framework has allowed for the isolation of highly unsaturated, first row open shell transition metal complexes in unusual coordination geometries and bonding modes which are not readily available in when using other less bulky ligand systems. The resulting complexes have demonstrated unusual reactivity where these complexes have activated small molecules producing structurally diverse reaction products.

1.4 Catalysis with Low-Coordinate Transition Metal Systems

There is a growing need to replace homogeneous catalysts which feature highly expensive transition metal centres with earth-abundant transition metal based systems which are environmentally benign, less toxic and much less expensive.[72] For example, there has been increased interest in iron, the second most abundant element in the Earth's crust, cobalt, nickel and manganese based systems where excellent reviews have detailed how systems based on these transition metals have been shown to activate unreactive chemical bonds (*e.g.* C–H, C–O, and C–C).[73–77] The interest in low-coordinate transition metal complexes as stoichiometric and catalyst precursors have been shown to lead to unusual reactivity and gives rise to unique reaction mechanisms.[25,26] This section aims to introduce some recent examples of low-coordinate (two or three), first row transition metal complexes which have been found to be efficient catalysts for organic transformations.

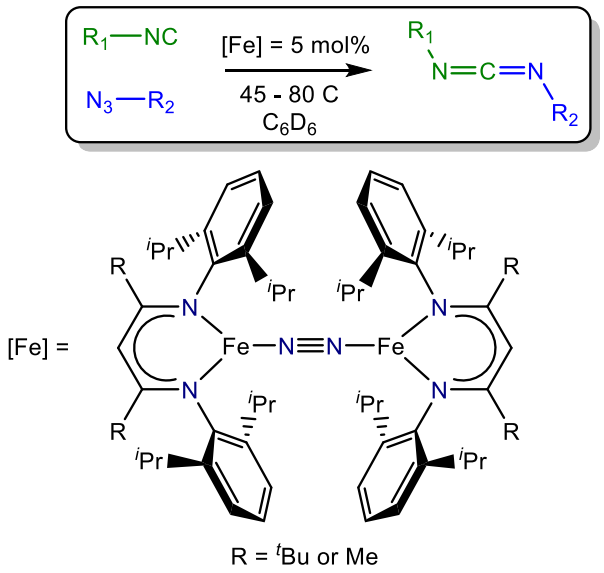
Two-coordinate bis(amido) complexes of iron and nickel have been shown to be efficient precatalysts in hydrosilylation reactions. The iron complex $Fe[N(SiMe_3)_2]_2$ was found to be highly active in the hydrosilylation of carbonyl compounds (using Ph_2SiH_2) under low catalyst loadings (0.01 mol%) and mild conditions as demonstrated by Tilley and co-workers.[78] The reaction was effective for a variety of functional groups however the reaction was not effective for more bulky silanes (Ph_3SiH, Et_3SiH and $(Trip)PhSiH_2$).[78] Preliminary investigations found the two-coordinate nickel complex $Ni[N(SiMe_3)(Dipp)]_2$ was active in the reaction of 1-octene with Ph_2SiH, resulting in the formation of the addition product (*n*-octyl)diphenyl silane.[79] This nickel(II) species has also shown to be effective in C–C cross coupling reactions of Grignard reagents with alkyl and aryl halides at ambient temperatures.[80]

The first heteroleptic two-coordinate Fe(I) complex, (NHC)FeN[(SiMe$_3$)(Dipp)] (NHC = *N*-heterocyclic carbene) reported by Tilley *et al.* was shown active in trimerization of simple terminal and internal alkynes.[81] Bulky or election withdrawing substituents were not effective for this reaction and under low catalyst loading (5 and 2 mol%) a certain degree of catalyst decomposition was observed in the postcatalytic mixture.[81]

Cobalt(II) amide complexes, Co[N(SiMe$_3$)$_2$]$_2$, and the three coordinate NHC adducts, (NHC)Co[N(SiMe$_3$)$_2$]$_2$, were found to be effective precatalysts for the hydrosilylation of alkenes with tertiary silanes without the need of an external activator.[82] The activation mode of the for the precatalysts were investigated though stoichiometric reaction of the cobalt complex, [(IPr)Co(N(SiMe$_3$)$_2$)$_2$], (IPr = 1,3-bis(2,6-diisopropylphenyl)imidazol-2-ylidene) with the alkene and silane. The complex was unreactive with respect to the alkene (1-octene) however, reaction with HSi(OEt)$_3$ lead to the formation of the two-coordinate cobalt(I) complex [(IPr)Co(N(SiMe$_3$)$_2$)] which, when reacted with a further equivalent of the silane, produced the cobalt(I) hydride complex [(IPr)Co(η^6-C$_6$H$_6$)H]. The silylamide Si(OEt)$_3$(N(SiMe$_3$)$_2$ and H_2 were also detected in the reaction mixture suggesting formation of the Co(I) complex possibly results from Co−H bond cleavage reaction of a cobalt(II) hydride intermediate (IPr)Co(H)(N(SiMe$_3$)$_2$) which is formed from the σ-bond metathesis reaction of the precatalyst with HSi(OEt)$_3$.

The highly tuneable β-diketiminate framework has been used to great effect in stabilising low-coordinate first row transition metal complexes which have applications as catalysts in the synthesis of small molecules.[83] Examples include the work by Holland and co-workers which reported the synthesis of three-coordinate iron(II) fluoride β-diketiminate complexes. These complexes feature short Fe–F bonds (1.8079(15)-1.9751(12) Å) which are thermally robust, however, in the presence of triethylsilane, acting as a fluoride acceptor and a hydride donor, were found to be efficient precatalysts in the

hydrodefluorination of fluoroarenes and fluoroalkenes *via* an iron hydride intermediate.[84] However, the analogous cobalt complexes were not effective in this reaction, possibly a result of the higher coordination number (four-coordinate *vs.* three coordinate) and also, the cobalt hydride complex was shown to be unlikely to form due to the rapid elimination of H_2.[85]



Scheme 1.6 Catalytic carbodiimide formation using an Fe(I) dinitrogen complex.

The iron(I) dinitrogen complex (Scheme 1.6) was found to be an efficient precatalyst in asymmetric carbodiimide formation from the reaction of an isocyanide and azide under mild conditions (5 mol% of precatalyst, 45-80 °C).[86]

Holland has also reported a cobalt(II) complex supported by a bulky β-diketiminate ligand which catalysts the isomerisation of terminal alkenes to 2-alkenes with Z-stereochemistry, the more challenging to access kinetic product.[87] This catalyst was successful for a variety of alkene substrates including 1-hexene, silanes, ketals and protected alcohols.[87]

Work by Webster and Hannedouche have demonstrated versatility of three-coordinate iron(II) complexes bearing β-diketiminate ligand in catalysing numerous reactions such as

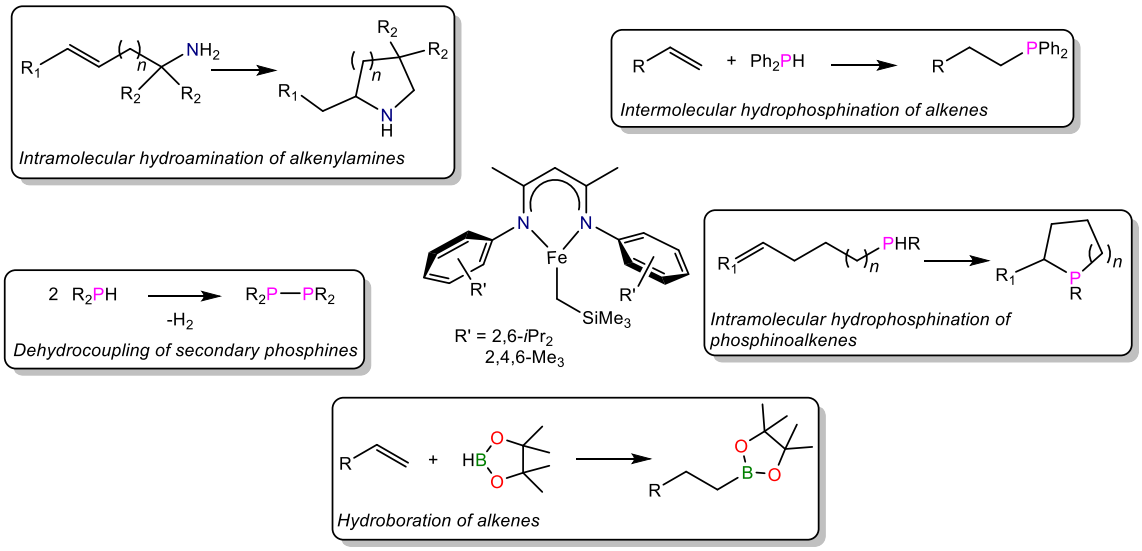
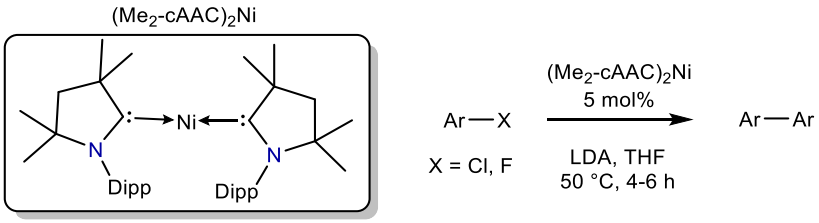


Figure 1.10 Three-coordinate Fe(II) complex which has been used to catalyse a variety of reactions.

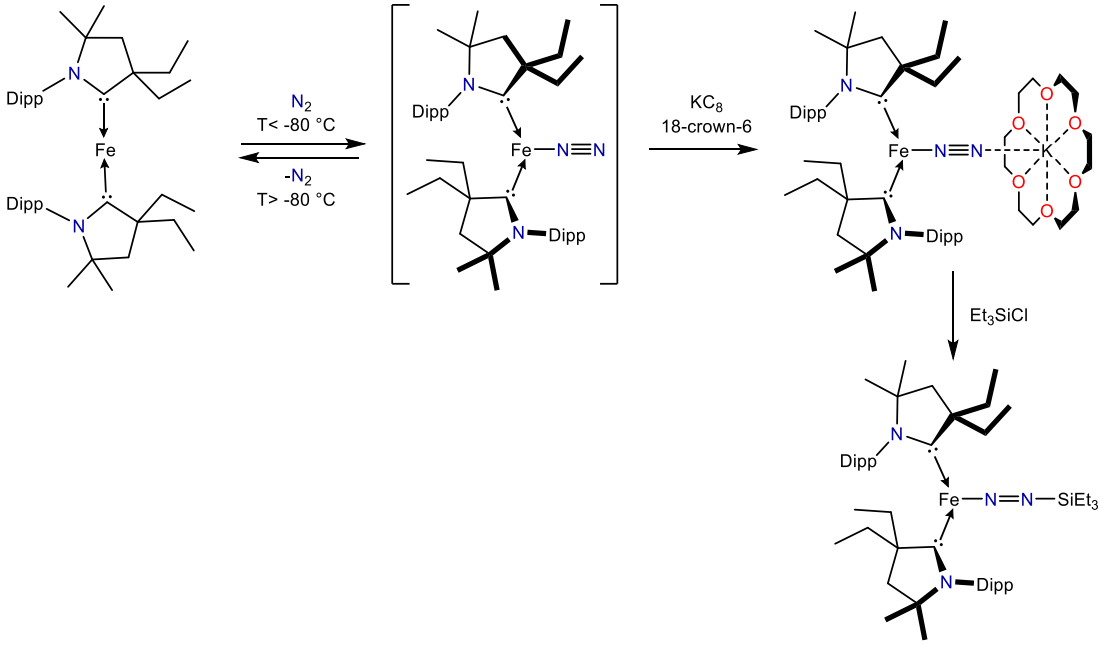
intramolecular and intermolecular hydrophosphination alkenes,[88,89] hydroamination of alkenylamines,[90] hydroboration of alkenes[91] and dehydrocoupling reactions[89] (Figure 1.10).

Cyclic alkyl(amino) carbene (cAAC) ligands, which are strong σ-donors and π-acceptors, have been used to isolate low-coordinate, electron rich transition metal centres which exhibit catalytic activity for a variety of organic transformations.[92,93]

The nickel complex $(Me_2\text{-cAAC})_2Ni$ was found to be catalytic active in the homocoupling of various unactivated aryl chlorides/fluorides where the resulting biaryls were obtained in good yields at moderate temperature (50 °C) (Scheme 1.7).[94]



Scheme 1.7 Homocoupling of aryl halides facilitated by $(Me_2\text{-cAAC})_2Ni$.



Scheme 1.8 Reduction of $(Et_2\text{-}cAAC)_2Fe$ and subsequent trapping with Et_3SiCl.

The related two-coordinate iron complex $(Et_2\text{-}cAAC)_2Fe^0$ effectively catalyses the formation of $N(SiEt_3)_3$ though the reaction of dinitrogen with Et_3SiCl in the presence of KC_8 (Scheme 1.8).[95] The two-coordinate complex reversibly binds dinitrogen at low temperature (< –80 °C) resulting in the three-coordinate N_2 complex $(Et_2\text{-}cAAC)_2Fe^0(N_2)$ which was trapped *via* one electron reduction using KC_8 to yielding the corresponding anion $[(Et_2\text{-}cAAC)_2Fe^0(N_2)]^-$ featuring an activated dinitrogen unit. This complex was subsequently trapped with silylating reagent, Et_3SiCl, to form the diazenido product $[(Et_2\text{-}cAAC)_2Fe^0(N_2SiEt_3)]$. When using Me_3SiCl as the silylating agent, the presumed diazenido product $[(Et_2\text{-}cAAC)_2Fe^0(N_2SiMe_3)]$ rapidly decomposed to the $(Et_2\text{-}cAAC)_2Fe^0$ on workup.

The two-coordinate complex $(Et_2\text{-}cAAC)_2Fe^0$ was also found to catalytically convert N_2 to ammonia with an excess of KC_8, $HBAr^F_{24}{\cdot}2Et_2O$ (BAr^F_{24} = $B[3,5\text{-}(CF_3)C_6H_3]_4$) (50 eq.) resulting in the formation of 3.3 ± 1.1 equivalents of NH_3 per iron centres at –95 °C. Low temperatures are required as the degree of N_2 binding to $(Et_2\text{-}cAAC)_2Fe^0$ at room temperature is minimal.[95]

Herein, an assortment of first row, low-coordinate transition metal complexes have been explored and discussed as their use as catalysts in a wide variety of reactions. The utilisation of bulky ligands has allowed the stabilisation of these highly reactive first row transition metal centres to offer complementary reactivity compared to their heavier d-block counterparts. The field is relatively underdeveloped where further research needs to be undertaken in order to improve these systems. As such, there are no examples in the literature of the use of low-coordinate open shell *m*-terphenyl transition metal complexes which have been used as catalysts in organic transformations.

1.5 Aims

This research project aims to expand the knowledge of low-coordinate transition metal complexes utilising the very bulky *m*-terphenyl framework and to study these complexes with respect to catalysis and reactivity towards small molecules.

Chapter II explores of the synthesis of low-coordinate transition metal complexes. The homoleptic complexes are synthesised *via* salt metathesis reactions between the aryl lithium halide and a transition metal dihalide, where depending on the steric demands of flanking aryl, the two- or three-coordinated complexes are afforded. Initial coordination chemistry of these complexes is explored with acetonitrile in order to assess the limits of the steric pocket in which the metal resides.

Chapters III-V investigates the catalytic abilities of two- and three-coordinate transition metal complexes (mainly manganese and iron) towards the cyclotrimerisation of isocyanates, hydrophosphination of isocyanates and the dehydrocoupling of amine boranes. Chapter VI builds upon the reactivity of iron(II) *m*-terphenyl complexes towards carbon monoxide whereby the reaction leads to unprecedented formation of squaraine molecules and diiron carboxylate complex from CO bond scission.

1.6 References

1 C. M. Lukehart, *Fundamental Transition Metal Organometallic Chemistry*, Brooks/Cole Publishing Company, California, 1984.

2 F. G. A. Stone, *Nature*, 1971, **232**, 534–539.

3 W. C. Zeise, *Pogg. Ann. Phys. Chem.*, 1827, **9**, 632.

4 M. Black, R. H. B. Mais and P. G. Owston, *Acta Crystallogr. Sect. B Struct. Crystallogr. Cryst. Chem.*, 1969, **25**, 1753–1759.

5 L. Mond, C. Langer and F. Quincke, *J. Chem. Soc., Trans.*, 1890, **57**, 749–753.

6 E. Frankland, *Ann. Chem.*, 1849, **71**, 171–213.

7 S. Dietmar, *Organometallics*, 2001, **20**, 2940–2955.

8 V. C. R. Grignard, *Acad. Sci.*, 1900, **130**, 1322–1324.

9 G. Wilkinson, M. Rosenblum, M. C. Whiting and R. B. Woodward, *J. Am. Chem. Soc.*, 1952, **74**, 2125–2126.

10 T. J. Kealy and P. L. Pauson, *Nature*, 1951, **168**, 1039–1040.

11 J. J. Eisch, *Organometallics*, 2012, **31**, 4917–4932.

12 F. H. Jardine, J. A. Osborn and G. Wilkinson, *J. Chem. Soc. A*, 1967, 1574–1578.

13 D. Evans, J. A. Osborn and G. Wilkinson, *J. Chem. Soc. A.*, 1966, 3133–3142.

14 J. A. Osborn, F. H. Jardine, J. F. Young and G. Wilkinson, *J. Chem. Soc. A*, 1966, 1711–1732.

15 A. H. Hoveyda and A. R. Zhugralin, *Nature*, 2007, **450**, 243–251.

16 R. R. Schrock, *Angew. Chem. Int. Ed.*, 2006, **45**, 3748–3759.

17 R. H. Grubbs, *Angew. Chem. Int. Ed.*, 2005, **45**, 3760–3765.

18 Y. Chauvin, *Angew. Chem. Int. Ed.*, 2006, **45**, 3741–3747.

19 W. Cabri and I. Candiani, *Acc. Chem. Res.*, 1995, **28**, 2–7.

20 D. Haas, J. M. Hammann, R. Greiner and P. Knochel, *ACS Catal.*, 2016, **6**, 1540–1552.

21 V. B. Phapale and D. J. Cárdenas, *Chem. Soc. Rev.*, 2009, **38**, 1598–1607.

22 F.-S. Han, *Chem. Soc. Rev.*, 2013, **42**, 5270–5298.

23 N. Miyaura and A. Suzuki, *J. Chem. Soc., Chem. Commun.*, 1979, 866–867.

24 I. P. Beletskaya and A. V. Cheprakov, *Chem. Rev.*, 2000, **100**, 3009–3066.

25 P. P. Power, *Chem. Rev.*, 2012, **112**, 3482–3507.

26 D. L. Kays, *Dalton Trans.*, 2011, **40**, 769–778.

27 F. A. Cotton, *Chem.Rev.*, 1955, **55**, 551–594.

28 R. R. Schrock and G. W. Parshall, *Chem. Rev.*, 1976, **76**, 243–268.

29 G. Yagupsky and G. Wilkinson, *J. Chem. Soc., Chem Commun.*, 1970, **24**, 1369–1370.

30 M. R. Collier, M. F. Lappert and M. M. Truelock, *J. Organomet. Chem.*, 1970, **25**, 36–38.

31 A. Shortland and M. Yagupsky, *J. Chem. Soc., Dalton Trans.*, 1972, 533–542.

32 M. R. Collier, M. F. Lappert and R. Pearce, *J. Chem. Soc., Dalton Trans.*, 1973, 445–451.

33 N. H. Buttrus, C. Eaborn, P. B. Hitchcock, J. D. Smith and A. C. Sullivan, *J. Chem. Soc., Chem. Commun.*, 1985, 1380–1381.

34 P. P. Power, *J. Organomet. Chem.*, 2004, **689**, 3904–3919.

35 H. Bürger and U. Wannagat, *Monatsh.*, 1963, **94**, 1007–1012.

36 H. Bürger and U. Wannagat, *Monatsh.*, 1964, **95**, 1099–1102.

37 H. Chen, R. a Bartlett, H. V. R. Dias, M. M. Olmstead and P. P. Power, *J. Am. Chem. Soc.*, 1989, **111**, 4338–4345.

38 R. A. Bartlett and P. P. Power, *J. Am. Chem. Soc.*, 1987, **109**, 7563–7564.

39 R. A. Andersen, K. Faegri, J. C. Green, A. Haaland, M. F. Lappert, W. P. Leung and K. Rypdal, *Inorg. Chem.*, 1988, **27**, 1782–1786.

40 R. Fischer, H. Görls, M. Friedrich and M. Westerhausen, *J. Organomet. Chem.*, 2009, **694**, 1107–1111.

41 S. Gambarotta, C. Floriani, A. Chiesivilla and C. Guastini, *J. Chem. Soc., Chem. Commun.*, 1983, 1128–1129.

42 E. Solari, F. Musso, E. Gallo, C. Floriani, N. Re, A. Chiesivilla, C. Rizzoli, A. Chiesi-Villa and C. Rizzoli, *Organometallics*, 1995, **14**, 2265–2276.

43 H. Müller, W. Seidel and H. Görls, *J. Organomet. Chem.*, 1994, **445**, 113–136.

44 W. Seidel, H. Müller and H. Görls, *Angew. Chem. Int. Ed.*, 1995, **34**, 325–327.

45 K. H. Theopold, J. Silvestre, E. K. Byrne and D. S. Richeson, *Organometallics*, 1989, **8**, 2001–2009.

46 R. J. Wehmschulte and P. P. Power, *Organometallics*, 1995, **14**, 3264–3267.

47 D. L. Kays and A. R. Cowley, *Chem. Commun.*, 2007, **58**, 1053–1055.

48 D. L. Kays, in *Organometallic Chemistry: Volume 36*, The Royal Society of Chemistry, 2010, vol. 36, pp. 56–76.

49 G. W. Rabe, R. D. Sommer and A. L. Rheingold, *Organometallics*, 2000, **19**, 5537–5540.

50 B. Schiemenz and P. P. Power, *Organometallics*, 1996, **15**, 958–964.

51 R. Wolf, M. Brynda, C. Ni, G. J. Long and P. P. Power, *J. Am. Chem. Soc.*, 2007, **129**, 6076–6077.

52 R. Wolf, C. Ni, T. Nguyen, M. Brynda, G. J. Long, A. D. Sutton, R. C. Fischer, J. C. Fettinger, M. Hellman, L. Pu and P. P. Power, *Inorg. Chem.*, 2007, **46**, 11277–11290.

53 C.-J. F. Du, H. Hart and K.-K. D. Ng, *J. Org. Chem*, 1986, **51**, 3162–3165.

54 A. Saednya and H. Hart, *Synthesis*, 1996, 1455–1458.

55 K. Ruhlandt-Senge, J. J. Ellison, R. J. Wehmschulte, F. Pauer and P. P. Power, *J. Am. Chem. Soc.*, 1993, **115**, 11353–11357.

56 S. Hino, M. M. Olmstead, J. C. Fettinger and P. P. Power, *J. Organomet. Chem.*, 2005, **690**, 1638–1644.

57 J. J. Ellison and P. P. Power, *J. Organomet. Chem.*, 1996, **526**, 263–267.

58 A. D. Sutton, T. Ngyuen, J. C. Fettinger, M. M. Olmstead, G. J. Long and P. P. Power, *Inorg. Chem.*, 2007, **46**, 4809–4814.

59 T. Nguyen, A. D. Sutton, M. Brynda, J. C. Fettinger, G. J. Long and P. P. Power, *Science*, 2005, **310**, 877–847.

60 T. Nguyen, W. A. Merrill, C. Ni, H. Lei, J. C. Fettinger, B. D. Ellis, G. J. Long, M. Brynda and P. P. Power, *Angew. Chem. Int. Ed.*, 2008, **47**, 9115–9117.

61 H. Lei, B. D. Ellis, C. Ni, F. Grandjean, G. J. Long, P. P. Power and Missouri, *Inorg. Chem.*, 2008, **47**, 10205–10207.

62 H. Lei, J. C. Fettinger and P. P. Power, *Inorg. Chem.*, 2012, **51**, 1821–1826.

63 C. Ni, B. D. Ellis, J. C. Fettinger, G. J. Long and P. P. Power, *Chem. Commun.*, 2008, 1014–1016.

64 C. Ni, J. C. Fettinger, G. J. Long, M. Brynda and P. P. Power, *Chem. Commun.*, 2008, 6045–6047.

65 C. Ni, B. D. Ellis, T. A. Stich, J. C. Fettinger, G. J. Long, R. D. Britt and P. P. Power, *Dalton Trans.*, 2009, **2**, 5401–5405.

66 C. Ni, J. C. Fettinger, G. J. Long and P. P. Power, *Dalton Trans.*, 2010, **39**, 10664–10670.

67 C. Ni, G. J. Long and P. P. Power, *Organometallics*, 2009, **28**, 5012–5016.

68 C. Ni, T. A. Stich, G. J. Long and P. P. Power, *Chem. Commun.*, 2010, **46**, 4466–4468.

69 C. Ni and P. P. Power, *Chem. Commun.*, 2009, 5543–5545.

70 B. Zhou, M. S. Dennlng, D. L. Kays and J. M. Goicoechea, *J. Am. Chem. Soc.*, 2009, **131**, 2802–2803.

71 B. M. Gridley, A. J. Blake, A. L. Davis, W. Lewis, G. J. Moxey and D. L. Kays, *Chem. Commun.*, 2012, **48**, 8910–8912.

72 R. M. Bullock, Ed., *Catalysis without Precious Metals*, Wiley-VCH, Weinheim, 2010.

73 S. Enthaler, K. Junge and M. Beller, *Angew. Chem. Int. Ed.*, 2008, **47**, 3317–3321.

74 B. Su, Z. C. Cao and Z. J. Shi, *Acc. Chem. Res.*, 2015, **48**, 886–896.

75 A. Mukherjee, A. Nerush, G. Leitus, L. J. W. Shimon, Y. B. David, N. A. E. Jalapa and D. Milstein, *J. Am. Chem. Soc.*, 2016, **138**, 4298–4301.

76 D. A. Valyaev, G. Lavigne and N. Lugan, *Coord. Chem. Rev.*, 2016, **308**, 191–235.

77 I. Bauer and H. Knölker, *Chem. Rev.*, 2015, **115**, 3170–3387.

78 J. Yang and T. D. Tilley, *Angew. Chem. Int. Ed.*, 2010, **49**, 10186–10188.

79 M. I. Lipschutz and T. D. Tilley, *Chem. Commun.*, 2012, **48**, 7146–7148.

80 M. I. Lipschutz and T. D. Tilley, *Angew. Chem. Int. Ed.*, 2014, **53**, 7290–7294.

81 M. I. Lipschutz, T. Chantarojsiri, Y. Dong and T. D. Tilley, *J. Am. Chem. Soc.*, 2015, **137**, 6366–6372.

82 Y. Liu and L. Deng, *J. Am. Chem. Soc.*, 2017, **139**, 1798–1801.

83 R. L. Webster, *Dalton Trans.*, 2017, **46**, 4483–4498.

84 J. Vela, J. M. Smith, Y. Yu, N. A. Ketterer, C. J. Flaschenriem, R. J. Lachicotte and P. L. Holland, *J. Am. Chem. Soc.*, 2005, **127**, 7857–7870.

85 K. Ding, T. R. Dugan, W. W. Brennessel, E. Bill and P. L. Holland, *Organometallics*, 2009, **28**, 6650–6656.

86 R. E. Cowley, M. R. Golder, N. A. Eckert, M. H. Al-Afyouni and P. L. Holland, *Organometallics*, 2013, **32**, 5289–5298.

87 C. Chen, T. R. Dugan, W. W. Brennessel, D. J. Weix and P. L. Holland, *J. Am. Chem. Soc.*, 2014, **136**, 945–955.

88 M. Espinal-Viguri, A. K. King, J. P. Lowe, M. F. Mahon and R. L. Webster, *ACS Catal.*, 2016, **6**, 7892–7897.

89 A. K. King, A. Buchard, M. F. Mahon and R. L. Webster, *Chem. Eur. J.*, 2015, **21**, 15960–15963.

90 E. Bernoud, P. Oulié, R. Guillot, M. Mellah and J. Hannedouche, *Angew. Chem. Int. Ed.*, 2014, **53**, 4930–4934.

91 M. Espinal-Viguri, C. R. Woof and R. L. Webster, *Chem. Eur. J.*, 2016, **22**, 11605–11608.

92 V. Lavallo, Y. Canac, C. Präsang, B. Donnadieu and G. Bertrand, *Angew. Chem. Int. Ed.*, 2005, **44**, 5705–5709.

93 S. Roy, K. C. Mondal and H. W. Roesky, *Acc. Chem. Res.*, 2016, **49**, 357–369.

94 K. C. Mondal, P. P. Samuel, Y. Li, H. W. Roesky, S. Roy, L. Ackermann, N. S. Sidhu, G. M. Sheldrick, E. Carl, S. Demeshko, S. De, P. Parameswaran, L. Ungur, L. F. Chibotaru and D. M. Andrada, *Eur. J. Inorg. Chem.*, 2014, 818–823.

95 G. Ung and J. C. Peters, *Angew. Chem. Int. Ed.*, 2015, **54**, 532–535.

Chapter II

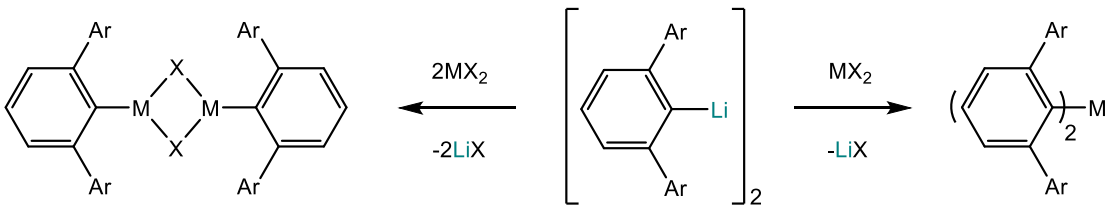
Low-Coordinate Complexes

2.1 Introduction

It has been documented that low-coordinate aryl complexes require ligands with significant steric bulk to prevent oligomerisation/polymerisation which can lead to coordination of other species which form donor-acceptor complexes.[1,2] Early attempts to synthesise open shell homoleptic complexes using aryl ligands resulted in the formation of oligomers, for example, when using the bulky aryl Mes resulted in the formation of Mn_3Mes_6 where the structure is a linear trimer linked by bridging Mes ligands.[3,4] Increasing the steric bulk by using 'supermesityl,' Mes*, allowed for the isolation of the homoleptic species $MMes^*_2$ (M = Mn, Fe).[5,6] However, it was not until *m*-terphenyl ligands were used that the monomeric homoleptic cobalt diaryl, $(2,6\text{-}Mes_2C_6H_3)_2Co$, was isolated by Kays.[7]

Very bulky *m*-terphenyl ligands have been shown to kinetically stabilise a variety of low-coordinate transition metal complexes which display some interesting and diverse reactivity where subtle changes in the ligand architecture dramatically alters the reactivity products obtained.[8,9]

Variation of the ratio of lithium *m*-terphenyl complex and the transition metal dihalide enables the synthesis of the heteroleptic species $[(2,6\text{-}Ar_2C_6H_3MX)_n$ (n = 1, 2) where the monomer is obtained if there is significant steric bulk from the ligand from the



Scheme 2.1 Synthesis of heteroleptic (left) and homoleptic (right) m-terphenyl complexes.

flanking aryl or buttressing groups][10] or homolepic [(2,6-$Ar_2C_6H_3)_2M$] species *via* salt elimination (Scheme 2.1). The heteroleptic complexes are viable precursors for the formation of metal–metal bonded species through the use of an appropriate reducing agent, for example KC_8, Na, and NaH. This methodology has been employed by Power and co-workers to stabilise the first homologous series of Group 12 metal–metal bonded complexes and the first quintuply bonded species in [2,6-$Dipp_2C_6H_3Cr]_2$.[11,12]

Low-coordinate open shell transition metal complexes with the highly anisotropic S = 3/2 spin state have been shown to exhibit interesting magnetic properties, where a recent example of a linear two-coordinate cobalt(II) imido complex, [(sIPr)CoNDmp] (where sIPr = 1,3-bis(2′,6′-diisopropylphenyl)-4,5-dihydro-imidazol-2-ylidene; Dmp = 2,6-$Mes_2C_6H_3$), and a linear iron(I) complex, [$Fe(C(SiMe_3)_3)_2$][K(2,2,2-crypt)], display single molecule magnetic (SMM) behaviour with high effective spin reversible barriers of 413 and 226 cm^{-1} respectively, under zero applied field.[13,14] These favourable magnetic properties arise from combination of the linear geometry about the metal centre where the weak field ligands define an axis for preferential alignment of spins which leads to unquenched orbital angular momentum.

Henceforth, this chapter encompasses the synthesis of novel low-coordinate transition metal complexes using the *m*-terphenyl framework with the aim to assess how the variation of the flanking aryls changes the subsequent reactivity and catalytic activity towards organic transformations. Preliminary investigations of the magnetic properties of these open shell systems has been investigated *via* the Evans method.[15,16]

2.2 Experimental

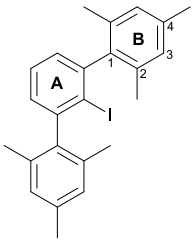
2.2.1 Ligand Synthesis

2.2.1.1 2,6-$Ar_2C_6H_3I$ (Ar = Mes, 2,4,6-$Me_3C_6H_2$, 1; 2,6-Xyl, 2,6-$Me_2C_6H_3$, 2; Tmp, 2,4,5-$Me_3C_6H_2$, 3)

Magnesium turnings (**1**, 6.63 g, 276 mmol; **2**, 7.14 g, 297 mmol; **3**, 3.32 g, 138 mmol) were activated by stirring in acetone (*ca.* 30 mL) in the presence of iodine (*ca.* 50 mg) for 1 h. The magnesium turnings were washed with acetone (*ca.* 3 × 10 mL) and dried after which THF (100 mL) was added. To this, the corresponding degassed bromoarene (**1**, 2-bromomesitylene, 50 g, 251 mmol; **2**, 2-bromo-1,3-dimethylbenzene, 50 g, 270 mmol; 1-bromo-2,4,5-trimethylbenzene, 25 g, 126 mmol) in THF (100 mL) was added dropwise over *ca.* 1 h. The reaction mixture was heated until the reaction maintained an exotherm and then heated at reflux overnight for 16 h. The reaction mixture was then filtered to give a clear brown solution of ArMgBr (**1**, 56.1 g, 251 mmol; **2**, 50.0 g, 270 mol; **3**, 27.5 g, 126 mmol) in THF. To a solution of 1,3-dichlorobenzene (**1**, 11.0 mL, 48.5 mmol; **2**, 11.9 mL, 104 mmol; **3**, 5.54 mL, 48.5 mmol) in THF (200 mL) at −78 °C, ^{n}BuLi (2.5 M solution in hexane) (**1**, 42.4 mL, 106 mmol; **2**, 46.5 mL, 114 mmol; **3**, 21.4 mL, 53.4 mmol) was added dropwise over *ca.* 30 mins with stirring resulting in a pale yellow solution. The reaction mixture was stirred for 1 h at −78 °C. The previously prepared ArMgBr (**1**, 56.1 g, 251 mmol; **2**, 28.2 g, 135 mmol; **3**, 28.1 g, 126 mmol) in THF (200 mL) was added dropwise over *ca.* 1 h with stirring whilst maintaining a constant temperature of −78 °C. The reaction mixture was allowed to warm to room temperature over 16 h, then heated at reflux for 3 h. The reaction mixture was cooled to 0 °C and iodine (**1**, 39.1 g, 154 mmol; **2**, 42.1 g, 166 mmol; **3**, 20 g, 78.8 mmol) was added over *ca.* 30 mins, resulting in a dark brown solution. To this, aqueous sodium sulfite (5 wt%,

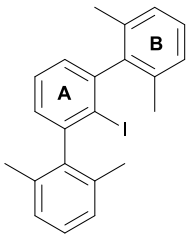
500 mL) was added and the mixture divided into two portions. To each portion, diethyl ether (300 mL) was added and the organic layer was washed with sodium sulfite (5 wt %, 3 × 200 mL) and brine (200 mL). The combined organic phases were dried over magnesium sulfate and the solvent was removed *in vacuo* resulting in a yellow oily solid. The crude product was recrystallised hot ethanol (250 mL) to give a yellow crystalline powder.

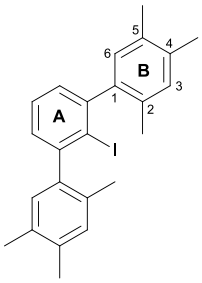
1 (17.8 g, 46%). ^{1}H NMR (400 MHz, $CDCl_3$, 25 °C): δ 7.47 (t, ^{3}J(H,H) = 7.5 Hz, 1H, Ph^{Ap}), 7.09 (d, ^{3}J(H,H) = 7.5 Hz, 2H, Ph^{Am}), 6.97 (s, 4H, Ph^{Bm}), 2.37 (s, 6H, Me^{4}), 2.00 (s, 12H, Me^{2}). $^{13}C\{^{1}H\}$ NMR (100 MHz, $CDCl_3$, 25 °C): δ 147.2 (Ph^{Aipso}), 142.1 (Ph^{Ao}), 137.2 (Ph^{Bipso}), 135.4 (Ph^{Bo}), 128.9 (Ph^{Bp}), 128.1 (Ph^{Am}), 127.8 (Ph^{Ap}), 107.6 (Ph^{Am}), 21.3 (Me^{4}), 20.3 (Me^{2}).



NMR data for **1** matched literature values.[17]

2 (19.2 g, 45%). ^{1}H NMR (400 MHz, $CDCl_3$, 25 °C): δ 7.50 (t, ^{3}J(H,H) = 7.6 Hz, 1H, Ph^{Ap}), 7.23 (t, ^{3}J(H,H) = 7.6 Hz, 2H, Ph^{Bp}), 7.14 (d, ^{3}J(H,H) = 7.6 Hz, 4H, Ph^{Bm}), 7.11 (d, ^{3}J(H,H) = 7.6 Hz, 2H, Ph^{Am}), 2.03 (s, 12H, Me). $^{13}C\{^{1}H\}$ NMR (100 MHz $CDCl_3$, 25 °C): δ 147.1 (Ar) 144.7 (Ar), 135.6 (Ar), 128.9 (Ar), 127.6 (Ar), 127.6 (Ar), 127.3 (Ar), 106.7 (*ipso*-Ar), 20.3 (Me). NMR data for **2** matched literature values.[18]

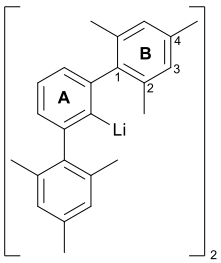




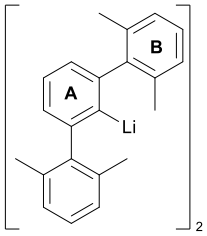
3 (7.98 g, 37%). ^{1}H NMR (400 MHz, $CDCl_3$, 25 °C): δ 7.38 (t, ^{3}J(H,H) = 7.4 Hz, 1H, Ph^{Ap}), 7.14 (d, ^{3}J(H,H) = 7.4 Hz, 2H, Ph^{Am}), 7.05 (s, 2H, Ph^{B3}), 6.92 (s, 2H, Ph^{B6}), 2.30 (s, 6H, Me^{4}), 2.27 (s, 6H, Me^{2}), 2.06 (s, 6H, Me^{5}). $^{13}C\{^{1}H\}$ NMR (100 MHz, $CDCl_3$, 25 °C): δ 147.6 (Ph^{Am}), 142.9 (Ph^{B2}), 136.0 (Ph^{B5}), 133.5 (Ph^{B4}), 132.7 (Ph^{B1}), 131.1 (Ph^{B3}), 130.1 (Ph^{B6}), 128.9 (Ph^{Am}), 127.7 (Ph^{Ap}), 106.9 (Ph^{Aipso}), 19.5 (Me^{4}), 19.3 (Me^{5}), 19.3 (Me^{2}). Elemental analysis for $C_{24}H_{25}I$ (440.37): calcd. C 65.46, H 5.72; found C 65.38, H 5.69. MS (ESI) *m/z*: calcd for $C_{24}H_{25}INa$ $[M+Na]^{+}$ 463.0893, found: 463.0886 (err [ppm] = 1.50). NMR data for **3** matched literature values.[19]

2.2.1.2 [2,6-Ar$_2$C$_6$H$_3$Li]$_2$ (Ar = Mes, 4; 2,6-Xyl, 5; Tmp, 6)[20]

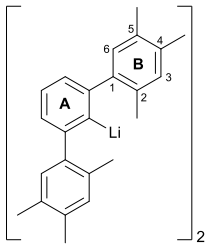
2,6-$Ar_2C_6H_3I$ (Ar = Mes, 8.00 g, 18.2 mmol, **4**; 2,6-Xyl, 8.00 g, 19.4 mmol; 6.88g, 14.9 mmol, **6**) was dried *in vacuo* overnight (*ca.* 16 h) after which hexane (*ca.* 100 mL) was added to give a pale yellow suspension. ^{n}BuLi (2.5 M solution in hexane, **4**, 8.7 mL, 21.8 mmol; **5**, 9.3 mL, 23.3 mmol; **6**, 7.0 mL, 17.9 mmol) was added dropwise with stirring at 0 °C and the reaction mixture was allowed to warm to room temperature overnight (*ca.* 16 h) forming a pale yellow suspension. This was filtered and dried to give $[2,6\text{-}Ar_2C_6H_3Li]_2$ as an off white powder.



4 (4.89 g, 84%). ^{1}H NMR (400 MHz, C_6D_6, 25 °C): δ 7.24 (t, ^{3}J(H,H) = 7.5 Hz, 1H, Ph^{Ap}), 6.84 (s, br, 4H, Ph^{Bm}), 6.82 (s, br, 2H, Ph^{Am}), 2.17 (s, 12H, Me^{4}), 1.83 (s, 24H, Me^{2}). $^{13}C\{^{1}H\}$ NMR (101 MHz, C_6D_6, 25 °C): δ 151.2 (Ph^{Aipso}), 143.7 (Ph^{Ao}), 136.7 (Ph^{Bipso}), 136.7 (Ph^{Bo}), 130.1 (Ph^{Bp}), 126.5 (Ph^{Am}), 124.1 (Ph^{Ap}), 21.9 (Me^{4}), 21.5 (Me^{2}). $^{7}Li\{^{1}H\}$ NMR (156 MHz, C_6D_6, 25 °C): δ 1.64 (s). NMR data for **4** matched literature values.[20]



5 (5.50 g, 97%). ^{1}H NMR (400 MHz, C_6D_6, 25 °C): δ 7.19 (t, ^{3}J(H,H) = 7.5 Hz, 1H. Ph^{Ap}), 7.03-6.94 (m, br, 6H, $Ph^{B(p+m)}$), 6.77 (d, ^{3}J(H,H) = 7.5 Hz, 2H, Ph^{Am}), 1.80 (s, 12H, Me).^{13}C{^{1}H} NMR (101 MHz, C_6D_6, 25 °C): δ 172.7 (Ph^{Aipso}), 152.0 (Ph^{Bipso}), 146.4 (Ph^{Ao}), 136.4 (Ph^{Bm}), 128.4 (Ph^{Bo}), 127.4 ($Ph^{B(C\text{-}H)}$) 126.4 (Ph^{Ap}), 123.6 (Ph^{Am}), 21.8 (Me). ^{7}Li{^{1}H} NMR (156 MHz, C_6D_6, 25 °C): δ 1.58 (s). NMR data for **5** matched literature values.[21]

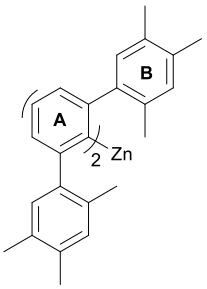


6 (4.14 g, 86%). ^{1}H NMR (400 MHz, THF-d_8, 25 °C): δ 7.07 (s, 2H, Ph^{B3}), 6.89 (s, 2H, Ph^{B6}), 6.81 (m, 3H, $Ph^{A(m+p)}$), 2.25 (s, 6H, Me), 2.21 (s, 6H, Me), 2.20 (s, 6H, Me). ^{13}C{^{1}H} NMR (100 MHz, THF-d^8, 25 °C): δ 156.3 (Ar), 152.9 (Ar), 151.3 (Ar), 132.9 (Ar), 132.7 (Ar), 132.3 (Ar), 132.2 (Ph^{B3}), 131.7 (Ph^{B6}), 123.2 (Ph^{Am}), 121.5 (Ph^{Ap}), 20.7 (Me), 19.5 (Me), 19.3 (Me). ^{7}Li{^{1}H} NMR (155 MHz, C_6D_6, 25 °C): δ 1.86 (s). Elemental analysis for $C_{24}H_{25}Li$ (320.40): calcd. C 89.97 H 7.86; found C 89.69 H 7.73. NMR data for **6** matched literature values.[19]

2.2.2 Two-Coordinate Complexes

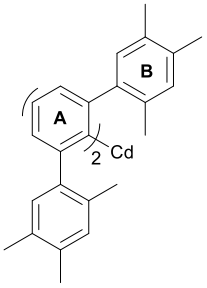
2.2.2.1 (2,6-Tmp$_2$C$_6$H$_3$)$_2$Zn (7)

To a mixture of **6** (200 mg, 0.312 mmol) and $ZnCl_2$ (42.5 mg, 0.312 mmol), were added toluene (20 mL) and THF (5 mL) resulting in a white suspension which was stirred for 16 h. The solvent was removed *in vacuo* resulting in a white solid which was extracted into hexane (3 × 10 mL), concentrated *in vacuo* and stored at −30 °C overnight. This resulted in the precipitation of colourless crystals suitable for X-ray diffraction (37.6 mg, 17 %). ^{1}H NMR (400 MHz, C_6D_6, 25 °C): δ 7.19 (d, br, ^3J(H,H) = 8.1 Hz, 4H, Ph^{Am}), 7.14 (t, br, ^3J(H,H) = 8.1 Hz, 2H, Ph^{Ap}), 6.90 (s, br, 8H, Ph$^{B(C\text{-}H)}$), 2.14 (s, 6H, Me), 2.10 (s, 6H, Me), 1.98 (s, br, 6H, Me). ^{13}C{^{1}H} NMR (100 MHz, C_6D_6, 25 °C): δ 153.7 (Ph^{Aipso}), 150.4 (Ph$^{B(C\text{-}quaternary)}$), 144.5 (Ph^{Bipso}), 134.8 (Ph$^{B(C\text{-}quaternary)}$), 133.9 (Ph^{Ao}), 133.0 (Ph$^{B(C\text{-}quaternary)}$), 132.3 (Ph$^{B(C\text{-}H)}$), 130.5 (Ph$^{B(C\text{-}H)}$), 126.9 (Ph^{Ap}), 126.1 (Ph^{Am}), 20.1 (Me), 19.4 (Me), 19.3 (Me). Elemental analysis for $C_{48}H_{50}Zn$ (692.31): calcd. C 83.28, H 7.28; found C 83.35, H 7.15. MS (EI) *m/z*: 690.3 [(2,6-Tmp$_2$C$_6$H$_3$)$_2$Zn]$^+$.



2.2.2.2 (2,6-Tmp$_2$C$_6$H$_3$)$_2$Cd (8)

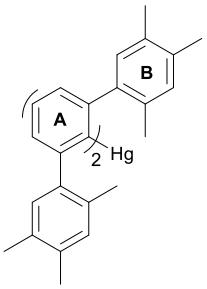
To a mixture of **6** (200 mg, 0.312 mmol) and CdI_2 (114 mg, 0.312 mmol), was added diethyl ether (20 mL) resulting in a white suspension. The reaction mixture was stirred for 16 h, the solvent removed *in vacuo* and the resulting in a grey solid which was extracted into hexane (3 × 10 mL) and toluene (10 mL). These solutions were concentrated *in vacuo* and stored at −30 °C. A white powder was obtained from the hexane extraction (72.0 mg, 31%). Crystals were grown from the toluene extraction however these crystals were too weak for X-ray diffraction. ^{1}H NMR (400 MHz, C_6D_6, 25 °C): δ 7.20 (d, br,



^{3}J(H,H) = 7.5 Hz, 4H, Ph^{Am}), 7.12 (t, br, ^{3}J(H,H) = 7.5 Hz, 2H, Ph^{Ap}), 7.01 (s, br, 4H, Ph$^{B(C\text{-}H)}$), 6.87 (s, br, 4H, Ph$^{B(C\text{-}H)}$), 2.08 (s, br, 24H, Me), 1.89 (s, br, 12H, Me).^{13}C{^{1}H} NMR (100 MHz, C_6D_6, 25 °C): δ 162.1 (Ph^{Aipso}), 150.2 (Ph^{Ao}), 145.7 (Ph^{Bipso}), 134.8 (Ph$^{B(C\text{-}quaternary)}$), 133.8 (Ph$^{B(C\text{-}quaternary)}$), 133.0 (Ph$^{B(C\text{-}quaternary)}$), 132.1 (Ph$^{B(C\text{-}H)}$), 130.5 (Ph$^{B(C\text{-}H)}$), 126.1 (Ph^{Ap}), 125.9 (Ph^{Am}), 19.9 (Me), 19.4 (Me), 19.3 (Me).^{113}Cd{^{1}H} NMR (88.8 MHz, C_6D_6, 25 °C): δ 421 (s), 429 (s). MS (EI) *m/z* : 740.3 [(2,6-Tmp$_2$C$_6$H$_3$)$_2$Cd]$^{+}$.

2.2.2.3 (2,6-Tmp$_2$C$_6$H$_3$)$_2$Hg (9)

To a mixture of **6** (270 mg, 0.422 mmol) and $HgBr_2$ (152 mg, 0.422 mmol), were added toluene (20 mL) and THF (5 mL) resulting in a white suspension which was stirred for 16 h. The solvent was removed *in vacuo* resulting in a white solid which was extracted into hexane (3 × 10 mL), concentrated *in vacuo* and stored at –30 °C overnight. This resulted in the precipitation of colourless crystals suitable for X-ray diffraction (34.0 mg, 10%).



^{1}H NMR (400 MHz, C_6D_6, 25 °C): δ 7.34 (d, ^{3}J(H,H) = 7.5 Hz, 4H, Ph^{Am}), 7.16 (t, ^{3}J(H,H) = 7.5 Hz, 2H, Ph^{Ap}), 7.07 (s, 4H, Ph$^{B(C\text{-}H)}$), 6.89 (s, 4H, Ph$^{B(C\text{-}H)}$), 2.19 (s, 3H, Me), 2.14 (s, 3H, Me), 2.07 (s, 3H, Me), 2.05 (s, 3H, Me), 2.00 (s, 6H, Ph$^{Bp\text{-}Me}$). ^{13}C{^{1}H} NMR (100 MHz, C_6D_6, 25 °C): δ 171.2 (Ph^{Aipso}), 147.4 (Ph^{Ao}), 142.4 Ph$^{B(C\text{-}quaternary)}$, 136.5 Ph$^{B(C\text{-}quaternary)}$, 134.7 Ph$^{B(C\text{-}quaternary)}$, 132.7 Ph$^{B(C\text{-}quaternary)}$, 132.5 (Ph$^{B(C\text{-}H)}$), 131.3 (Ph$^{B(C\text{-}H)}$), 128.5 (Ph^{Am}), 19.9 (Me), 19.3 (Me), 19.2 (Me). ^{199}Hg{^{1}H} NMR (72 MHz, C_6D_6, 25 °C): δ –629 (s), –649 (s). Elemental analysis for $C_{48}H_{50}Hg$ (828.36): calcd. C 69.67, H 6.09; found C 69.54, H 6.12. MS (EI) *m/z*: 828.4 [(2,6-Tmp$_2$C$_6$H$_3$)$_2$Hg]$^{+}$.

2.2.2.4 (2,6-Mes$_2$C$_6$H$_3$)$_2$Mn (10)[7]

To a mixture of **4** (500 mg, 0.780 mmol) and $MnBr_2$ (168 mg, 0.780 mmol), were added toluene (20 mL) and THF (5 mL) resulting in a clear pale yellow solution which was stirred at room temperature for 16 h. The solvent was removed *in vacuo* resulting in a pale yellow solid which was dried for 4 h. The product was extracted into toluene (3 × 10 mL), the solvent removed and dried resulting in a white powder (368 mg, 69%) Characterising data matched that in the literature.[7]

2.2.2.5 (2,6-Mes$_2$C$_6$H$_3$)$_2$Fe (11)[7]

To a mixture of **4** (500 mg, 0.780 mmol) and $FeCl_2(THF)_{1.5}$ (182 mg, 0.780 mmol), were added toluene (20 mL) and THF (5 mL) resulting in a clear brown solution which was stirred at room temperature for 16 h. The solvent was removed *in vacuo* resulting in a dark yellow solid which was dried at 60 °C for 5 h. The product was extracted into hexane (3 × 10 mL) and concentrated to *ca.* 10 mL and stored at −30 °C overnight. This resulted in the precipitation of a yellow crystalline solid (171 mg, 32%). Characterising data matched that in the literature.[7]

2.4.3.6 (2,6-Mes$_2$C$_6$H$_3$)$_2$Co (12)[7]

To a mixture of **4** (500 mg, 0.780 mmol) and $CoBr_2$(DME) (241 mg, 0.780 mmol), were added toluene (20 mL) and THF (5 mL) resulting in a clear blue solution. The reaction mixture was stirred at room temperature for 16 h, resulting in a deep red solution. The solvent was removed *in vacuo* and the product was extracted into hexane (3 × 10 mL), concentrated to *ca.* 10 mL *in vacuo* and stored at −30 °C overnight resulting in the

precipitation of a deep red crystalline solid (311 mg, 58%). Characterising data matched that in the literature.[7]

2.2.2.7 (2,6-(2,6-Xyl)$_2$C$_6$H$_3$)$_2$Mn (13)[19]

To a mixture of **5** (500 mg, 0.855 mmol) and $MnBr_2$ (184 mg, 0.855 mmol), were added toluene (20 mL) and THF (5 mL) resulting in a clear pale yellow solution which was stirred at room temperature 16 h. The solvent was removed *in vacuo* resulting in a pale yellow solid which was dried for 4 h. The product was extracted into toluene (3 × 10 mL) and concentrated to *ca.* 10 mL and stored at −30 °C overnight. This resulted in the precipitation of a white crystalline solid (144 mg, 27%). Characterising data matched that in the literature.[19]

2.2.2.8 (2,6-(2,6-Xyl)$_2$C$_6$H$_3$)$_2$Fe (14)[19]

To a mixture of **5** (500 mg, 0.855 mmol) and $FeCl_2(THF)_{1.5}$ (201 mg, 0.855 mmol), were added toluene (20 mL) and THF (5 mL) resulting in a clear dark yellow solution which was stirred at room temperature 16 h. The solvent was removed *in vacuo* resulting in a pale yellow solid which was dried for 4 h. The product was extracted into toluene (3 × 10 mL) and concentrated to *ca.* 10 mL and stored at −30 °C overnight. This resulted in the precipitation of a yellow crystalline solid (110 mg, 21%). Characterising data matched that in the literature.[19]

2.2.3 Three-Coordinate Complexes

2.2.3.1 (2,6-Tmp$_2$C$_6$H$_3$)$_2$Mn(THF) (15)

To a mixture of **6** (500 mg, 0.780 mmol) and $MnBr_2$ (168 mg, 0.780 mmol), were added toluene (20 mL) and THF (5 mL) with stirring resulting in a light yellow solution which was stirred for 16 h. The solvent was removed *in vacuo* resulting in an off white solid which was extracted into toluene (2 × 10 mL), concentrated *in vacuo* and stored at –30 °C for 1 day. This resulted in the precipitation of pale pink crystals suitable for X-ray diffraction (170 mg, 30%). ^{1}H NMR (400 MHz, C_6D_6, 25 °C): δ 15.78 (s, br, $\Delta\nu_{1/2}$ = 5000 Hz), 4.76 (s, br, $\Delta\nu_{1/2}$ = 695 Hz). UV/Vis (THF): strong absorption between 200 and 400 nm (ε > 900 dm^3 mol^{-1} cm^{-1}). Elemental analysis for $C_{52}H_{58}OMn$ (753.96): calcd. C 82.84, H 7.75; found C 82.66, H 7.55. μ_{eff} (Evans, C_6D_6, 25 ºC) = 5.59 μ_B. MS (EI) *m/z*: 682.3 [M+H–THF]$^+$.

2.2.3.2 (2,6-Tmp$_2$C$_6$H$_3$)$_2$Fe(THF) (16)

To a mixture of **6** (500 mg, 0.780 mmol) and $FeCl_2(THF)_{1.5}$ (182 mg, 0.780 mmol), were added toluene (20 mL) and THF (5 mL) with stirring resulting in a dark brown solution which was stirred for 16 h. The solvent was removed *in vacuo* resulting in a brown solid which was extracted into hexane (2 × 10 mL), concentrated *in vacuo* and stored at –30 °C for 1 day. This resulted in the precipitation of yellow crystals suitable for X–ray diffraction (150 mg, 25%). The ^{1}H NMR spectrum showed very broad signals which could not be readily assigned. UV/Vis (THF): strong absorption between 200 and 400 nm (ε > 1200 dm^3 mol^{-1} cm^{-1}) with peaks at λ_{max}/nm (ε/dm^3 mol^{-1} cm^{-3}) 385 (194). Elemental analysis for $C_{52}H_{58}OFe$ (754.86): calcd. C 82.74, H 7.74; found C 82.63, H 7.62. μ_{eff} (Evans, C_6D_6, 25 ºC) = 5.58 μ_B. MS (EI) *m/z*: 683.4 [M+H–THF]$^+$.

2.2.4 Four-Coordinate Complexes

2.2.4.1 (2,6-Mes$_2$C$_6$H$_3$)$_2$Mn(MeCN)$_2$ (17)

To a mixture of **4** (500 mg, 0.780 mmol) and $MnBr_2$ (168 mg, 0.780 mmol), were added toluene (20 mL) and THF (5 mL) resulting in a clear pale yellow solution which was stirred at room temperature for 16 h. The solvent was removed *in vacuo* resulting in a dark yellow solid which was dried for 4 h. The product was extracted into acetonitrile (2 × 20 mL) and concentrated to *ca.* 10 mL and stored at –30 °C for 4 days. This resulted in the precipitation of an off white crystalline solid (71.7 mg, 13%). ^{1}H NMR (400 MHz, C_6D_6, 25 °C): δ 25.7 (s, br, $\Delta\nu_{1/2}$ = 2021 Hz), 16.5 (s, br, $\Delta\nu_{1/2}$ = 1120 Hz), 8.8 (s, br, $\Delta\nu_{1/2}$ = 1191 Hz). UV/Vis (THF): strong absorption between 200 and 300 nm (ε > 2000 dm^3 mol^{-1} cm^{-1}). Elemental analysis for $C_{52}H_{56}N_2Mn$ (763.97): calcd. C 81.75 H 7.39 N, 3.67; found C 81.61, H 7.44, N 3.53. μ_{eff} (Evans, C_6D_6, 25 ºC) = 4.21 $\mu_{B.}$ MS (EI) *m/z*: 681.6 $[M–(MeCN)_2]^+$.

2.2.2.2 (2,6-Mes$_2$C$_6$H$_3$)$_2$Fe(MeCN)$_2$ (18)

To a mixture of **4** (500 mg, 0.780 mmol) and $FeCl_2(THF)_{1.5}$ (182 mg, 0.780 mmol), were added toluene (20 mL) and THF (5 mL) resulting in a clear brown solution which was stirred at room temperature for 16 h. The solvent was removed *in vacuo* resulting in a dark yellow solid which was dried for 4 h. The product was extracted into acetonitrile (2 × 20 mL) and concentrated to *ca.* 10 mL and stored at –30 °C for 5 days. This resulted in the precipitation of a yellow crystalline solid (147 mg, 25%). ^{1}H NMR (400 MHz, C_6D_6, 25 °C): δ 31.5 (s,br, $\Delta\nu_{1/2}$ = 272 Hz), –11.3 (s, br, $\Delta\nu_{1/2}$ = 54 Hz), –35.0 (s, br, $\Delta\nu_{1/2}$ = 1223 Hz), –54.3 (s, br, $\Delta\nu_{1/2}$ = 248 Hz). UV/Vis (THF): strong absorption between 200 and 350 nm (ε > 9700 dm^3 mol^{-1} cm^{-1}) with peaks at λ_{max}/nm (ε/dm^3 mol^{-1} cm^{-3}) 385

(4890). Elemental analysis for $C_{52}H_{56}N_2Fe$ (764.88): calcd. C 81.66, H 7.38, N 3.66; found C 81.44, H 7.26, N 3.52. μ_{eff} (Evans, C_6D_6, 25 ºC) = 5.17 μ_B. MS (EI) *m/z*: 682.3 $[M–(MeCN)_2]^+$.

2.3 Results and Discussion

2.3.1 Ligand Synthesis

2.3.1.1 m-Terphenyl Iodides

A series of *m*-terphenyl ligand precursors with different steric bulk were synthesised with the aim to evaluate how altering the steric bulk of the flanking aryls affects the bonding, geometric environment and resulting reactivity of the low-coordinate transition metal complexes. The flanking group of the *m*-terphenyl was either substituted with either a Mes, 2,6-xylyl (2,6-Xyl), or the asymmetric 2,4,5-$Me_3C_6H_2$ (Tmp) substituent (Figure 2.1) which were prepared though a one-pot procedure as outlined by Hart and co-workers.[17]

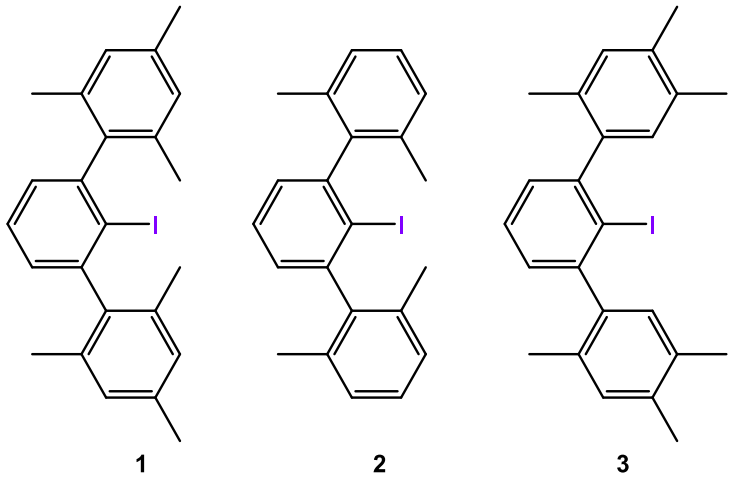
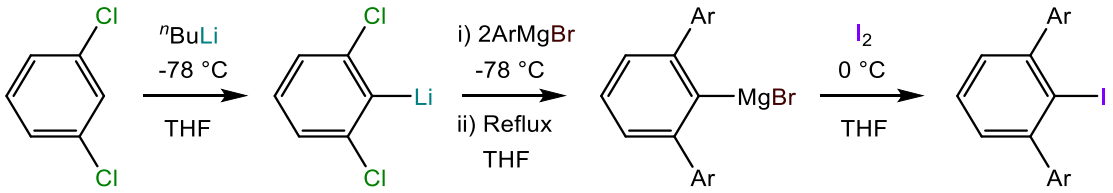


Figure 2.1 m-Terphenyl ligand precursors synthesised with Mes, 2,6-Xyl and Tmp substituents.

The respective aryl Grignard reagents were synthesised first *via* a typical route where a solution of the aryl bromide in THF was added dropwise to a suspension of activated magnesium turnings in THF with heating. After filtration the solution of the aryl Grignard, ArMgBr (Ar = Mes **1**; 2,6-Xyl, **2**; Tmp, **3**), was obtained. The *m*-terphenyl iodides were synthesised *via* a minor modification to the literature[17] where 1,3-dichlorobenzene was lithiated in the *ortho* position with the use of ^{n}butyllithium

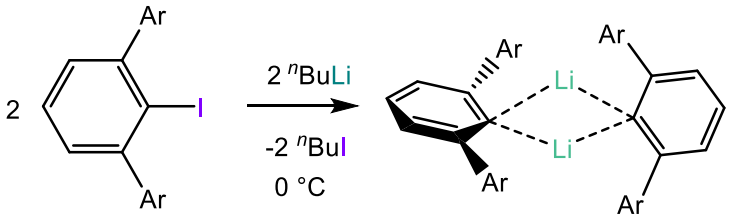


Scheme 2.2 Synthesis of m-terphenyl iodides where Ar = Mes, 1; 2,6-Xyl, 2; Tmp, 3.

(2.5 M solution in hexane) whilst maintaining a constant temperature of −78 °C and was held at this temperature for an hour. Two equivalents of the previously prepared aryl Grignard reagent was added dropwise at −78 °C and allowed to warm to room temperature overnight (*ca.* 16 h), heated at reflux, cooled to 0 °C and quenched with an excess of iodine (Scheme 2.2). After a standard aqueous workup and recrystallisation in hot ethanol, **1-3** were isolated in moderate yields (37-46%). The purity of **1-3** were confirmed with the use of ^{1}H and ^{13}C{^{1}H} NMR spectroscopy where values for **1**,[17] **2**[18] and **3**[19] matched those in the literature.

2.3.1.2 m-Terphenyl Lithium Complexes

The synthesis the *m*-terphenyl lithium complexes [2,6-$Ar_2C_6H_3Li]_2$ (where Ar = Mes, **4**; 2,6-Xyl, **5**; Tmp, **6**) were achieved *via* the addition of *n*-butyllithium (2.5 M solution in hexane) to a suspension of the *m*-terphenyl iodides (**1**-**3**) in hexane at 0 °C (Scheme 2.3).



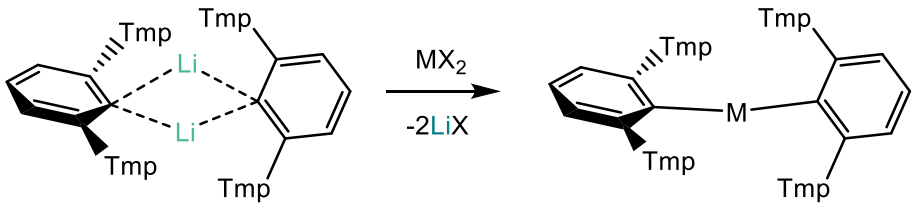
Scheme 2.3 Synthesis of m-terphenyl lithium dimers 4-6.

After filtration the lithium complexes were isolated in excellent yields (84-97%) and their purity was established through the use of ^{1}H and $^{13}C\{^{1}H\}$, $^{7}Li\{^{1}H\}$ NMR spectroscopy where values for **4**-**6** matched those in the literature.[19–21]

2.3.2 Two-Coordinate Complexes

2.3.2.1 Disubstitution of Group 12 Halides

The reaction between one equivalent of the lithium dimer $[2,6\text{-}Tmp_2C_6H_3Li]_2$ (**6**) and the group 12 transition metal halides $ZnCl_2$, CdI_2 and $HgBr_2$ in a mixture of toluene and THF (**7** and **9**) or diethyl ether (**8**) followed by removal of volatiles *in vacuo* and extraction into *iso*-hexane yielded the two-coordinate complexes in moderate yields according to Scheme 2.4.



Scheme 2.4 Synthesis of diaryl complexes $(2,6\text{-}Tmp_2C_6H_3)_2M$ [M = Zn (7), Cd (8), Hg (9)].

Despite multiple attempts in numerous solvents, single crystals suitable for X-ray diffraction experiments for the cadmium complex **8** could not be obtained. Crystals suitable for X-ray diffraction for **7** and **9** were grown from saturated solutions in *iso*-hexane at –30 °C which revealed the monomeric two-coordinate homoleptic complexes $(2,6\text{-}Tmp_2C_6H_3)_2M$ (M = Zn, **7**; Hg, **9**) with the absence of any coordinating solvents, presumably due to the combination of the steric demands of the *m*-terphenyl ligands and the fact that Zn is small due to d-block contraction and that mercury complexes prefer linear two-coordinate geometry due to relativistic effects.[22] Complexes

7-9 have been characterised by NMR spectroscopy, mass spectroscopy and elemental analysis, and the solid state structures for **7** and **9** have been determined by single crystal X-ray diffraction.

The NMR data for **7-9** are more complicated than those seen for Group 12 diaryl complexes in the literature which feature symmetrical *m*-terphenyl ligands[23] due to the asymmetric nature of the Tmp substituent. The ^{1}H NMR spectrum for **7** shows three singlets at 1.98, 2.10 and 2.14 ppm indicating three methyl environments of the Tmp substituent where the peak at 1.98 ppm is significantly broad. In the aromatic region, a slightly distorted doublet and triplet with a broad singlet are observed which correspond to the *meta* and *para* protons on the central aryl ring, and the C*H* protons on the flanking aryls respectively. This is also observed in the ^{1}H NMR spectrum for the corresponding cadmium complex **8** which suggests that there is some fluxionality in solution which possibly indicates the presence of conformational isomers in solution. This is further supported by the presence of two distinct chemical shifts in the ^{113}Cd{^{1}H} NMR spectrum at 421 and 429 ppm for **8** and two peaks in the ^{119}Hg{^{1}H} NMR spectrum at –629 and –649 ppm for **9** which are similar to other bis *m*-terphenyl cadmium and mercury complexes as seen in the literature.[23–25] The broad peaks observed in the ^{1}H NMR spectra suggests the flanking Tmp substituent is rotating in solution however, the multiple signals observed in the ^{113}Cd{^{1}H} and ^{119}Hg{^{1}H} NMR spectra indicates multiple isomers are present in solution. Such conformational flexibility has also been observed for the related group 12 bis *m*-terphenyl complexes with flanking aryl Naph flanking groups. The complexes (2,6-Naph$_2$C$_6$H$_3$)$_2$M(OEt$_2$) (where M = Cd or Hg) both crystallise in the *syn*/*syn* conformation, however in solution there are multiple isomers present as evidenced by the presence of multiple overlapping resonances in both the ^{1}H and ^{13}C{^{1}H} NMR spectra as well as four distinct resonances in both the ^{113}Cd{^{1}H} (422 to 442 ppm)

and $^{119}Hg\{^{1}H\}$ NMR (–648 to –600 ppm) spectra.[25] The $^{13}C\{^{1}H\}$ NMR spectra for complexes **7**-**9** exhibit broad peaks which also suggests fluxionality in solution. The ^{1}H NMR spectrum for the mercury complex **9** is slightly different than those of **7** and **8**. The aliphatic region exhibits five singlets where the *ortho*- and *meta*-methyl groups of the Tmp substituent are inequivalent (2.05-2.19 ppm) with a sharp peak at 2.00 ppm from the *para*-methyl group. The characteristic *m*-terphenyl doublet (7.34 ppm) and triplet (7.16 ppm) are also observed due to the *meta*- and *para*-hydrogens on the central aryl ring respectively. Variable temperature NMR was carried out in order deconvolute the ^{1}H spectrum. Samples of **7**-**9** in benzene-d_6 were heated from 25 °C to 50 °C however the ^{1}H signals were still very broad and was not possible to identify each specific signal.

2.3.2.1.1 Crystallographic Analysis

As a consequence of the steric demands of the Tmp substituted *m*-terphenyl ligand the zinc (**7**) and mercury (**9**) complexes are monomeric in the solid state (Figure 2.2) where the nearest M···M separations are *d*(Zn···Zn) = 9.3 Å and *d*(Hg···Hg) = 8.6 Å.

Selected bond lengths and angles are shown in Table 2.1 for **7** and **9**. The solid state structures of these complexes feature the metal centres bound to two *m*-terphenyl ligands where the orientation of the flanking Tmp substituents are in the *anti*-configuration [*i.e.* C(15):C(24) and C(37):C(48) are on opposite sides with respect to the central aryl ring]. Complex **7** crystallises in the tetragonal space group $P4_32_12$ with one molecule in the asymmetric unit. The Zn–C bond lengths in **7** are identical [Zn–C(1) = 1.950(3) Å, Zn–C(25) = 1.949(3) Å] and are within the range of other two-coordinate *m*-terphenyl diaryl zinc complexes seen in the literature [$(2,6\text{-}Ar_2C_6H_3)_2Zn$ where Ar = 2,6-Xyl, Zn–C = 1.949(4) and 1.944(4) Å; Ar = 3,5-Xyl, 3,5-Xylyl, $3,5\text{-}Me_2C_6H_3$, Zn–C = 1.9362(13) and

1.9402(13); Ar = Pmp, pentamethylphenyl, Me_5C_6, Zn–C = 1.939(3) and 1.939(3) Å, Naph, Zn–C = 1.946(2) and 1.955(2) Å].[23,25] The almost linear C–M–C angle of 175.07(12)° in **7** is similar to the aforementioned 2,6-Xyl and Pmp substituted *m*-terphenyl zinc complexes [178.7(2)° and 175.78(12)° respectively][23] whereas the 3,5-Xyl and Naph substituted *m*-terphenyl zinc complexes [171.18(15)° and 168.27(9)° respectively] deviate more from linearity.[23,25] This is possibly a consequence of a lesser amount of steric bulk imposed by the 3,5-Xyl and Naph flanking aryls which in turn allows for a greater degree of rotation. It has also been proposed that for the Naph substituted *m*-terphenyl zinc complex an intramolecular CH···π interaction from a flanking aryl to an opposing naphthyl group also the contributes to the bending of this angle.[24,25] A weak secondary metal-ligand interaction between the Zn and C on the flanking aryl is suggested by the C(36)···Zn(1) contact of 2.986(9) Å which is within the combined Van der Waals radii of these atoms of 3.8 Å,[26] bringing the aryl-proton in close proximity to the metal centre.

The mercury complex **9** crystallises in the orthorhombic space group $Pca2_1$ comprising of one molecule in the asymmetric unit. The C–Hg–C angle of 176.3(2)° is very similar to the 3,5-Xyl substituted *m*-terphenyl complex: $(2,6\text{-}(3,5\text{-}Xyl)_2C_6H_3)_2Hg$, 176.4(2)°, whereas the analogous mercury complexes with 2,6-Xyl, Pmp, Mes and Naph flanking aryls afford a more linear C–M–C bond angle [177.1(1)-180°].[25,27] The Hg–C bond

	7 ***M = Zn***	***9*** ***M = Hg***
M(1)–C(1)	1.950(3)	2.090(5)
M(1)–C(25)	1.949(3)	2.085(5)
C(1)–M(1)–C(25)	175.07(12)	176.3(2)
C(1)plane···C(25)plane	127.29(6)	130.4(8)

Table 2.1 Selected bond lengths (Å) and angles (°) for $(2,6\text{-}Tmp_2C_6H_3)_2M$ where M = Zn (7) and Hg (9).

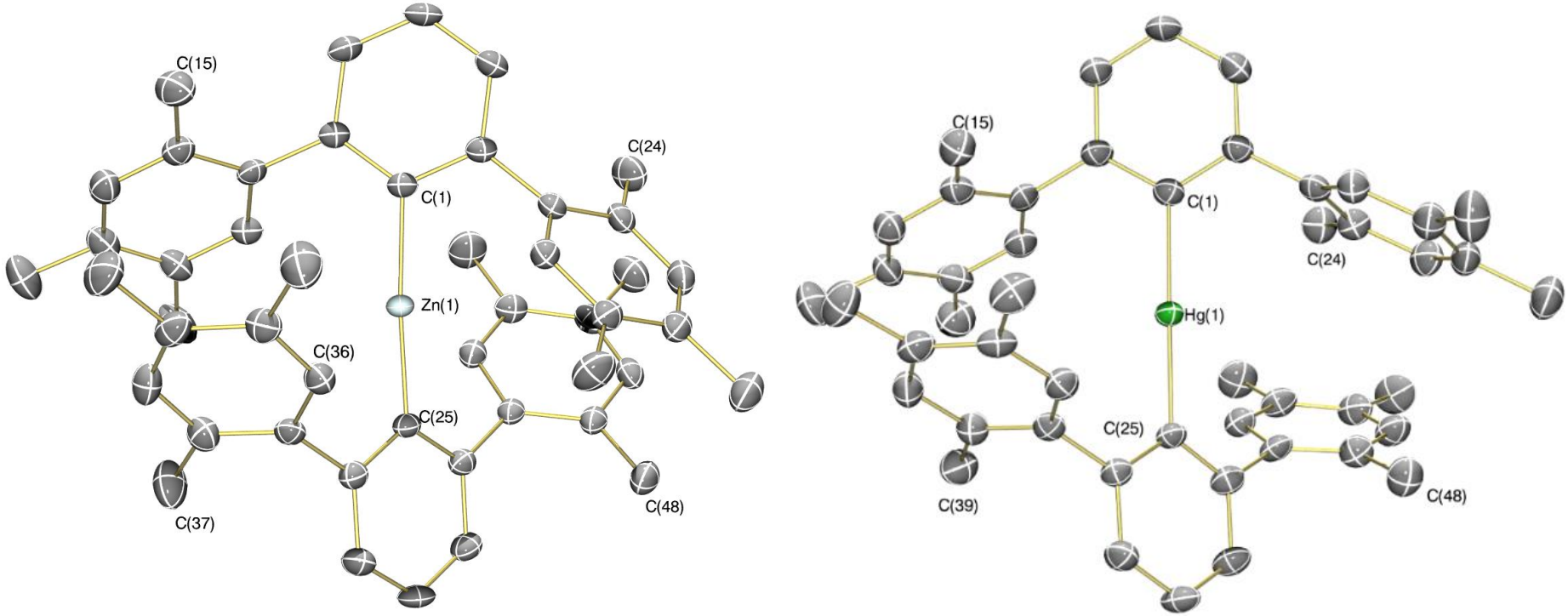


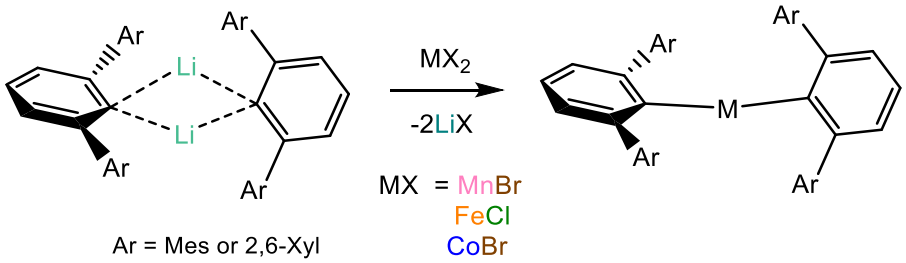
Figure 2.2 Crystal structures of 7 and 9. Thermal ellipsoids are set at the 50% probability level and hydrogen atoms omitted for clarity.

lengths in **9** [2.090(5) and 2.085(5) Å] which are close in value to the sum of the covalent radii of Hg and C (2.08 Å)[28] and are also similar to the aforementioned related bis *m*-terphenyl mercury complexes.[23,27,28] It could be possible that there is a weak secondary metal-ligand interaction from the C(41)···Hg(1) contact of 3.524(6) Å which is well within the sum of the Van der Waals radii of these two atoms of 3.75 Å.[26]

It is also important to highlight that the angle between the planes of the two central aryl rings in **7** and **9** are rather close in value at 127.29(6)° and 130.4(8)° respectively [Table 2.1, C(1)plane···C(25)plane]. These values are much larger than those of related two-coordinate bis *m*-terphenyl zinc and mercury diaryl complexes where the aryl rings are orientated almost perpendicular [Zn, 83.6(2)-89.07(10)°; Hg, 78.46(18)-86.03(19)°].[23,25] This is most likely due to the reduced steric strain of the Tmp substituent which allows for greater flexibility *versus* 2,6-Xyl, Mes and Pmp where it has been suggested that the maximum steric bulk is provided by substituents in the *ortho* position of the flanking aryls.[29]

2.3.2.2 Disubstitution of Transition Metal Halides

The open shell two-coordinate transition metal complexes **10**-**14** were synthesised according to modified literature procedures.[7,19] The reaction between the lithium aryl (**4** or **5**) and the corresponding transition metal dihalide in a mixture of toluene and THF gave the homoleptic transition metal complexes with concomitant precipitation of the lithium halide according to Scheme 2.5. Extraction into an appropriate non polar solvent [either hexanes (**11** and **12**) or toluene (**10**, **13**, **14**)] and storage of saturated solutions at –30 °C resulted in the precipitation of pure product as either a white (**10** and **13**) yellow (**11** and **14**) or red (**12**) crystalline solid.



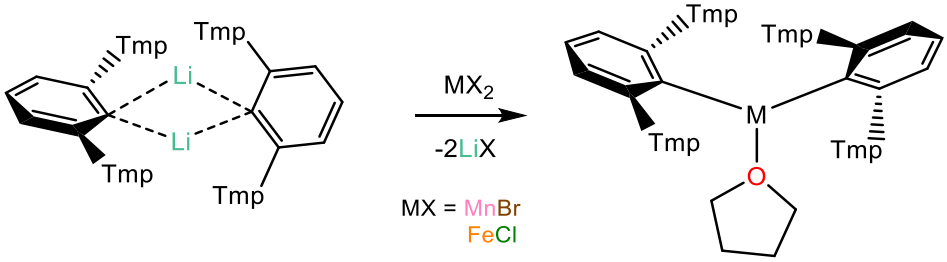
Scheme 2.5 Disubstitution of first row transition metals: Ar = Mes, M = Mn (10), Fe (11), and Co (12); Ar = 2,6-Xyl, M = Mn (13) and Fe (14).

These highly air- and moisture-sensitive compounds are stable for extended periods of time under an inert atmosphere and were isolated in low to good yields (27-69%) where their characterising data match those as seen in the literature.[7,19] Their catalytic activity and reactivity towards small molecules is explored and discussed in Chapters III to VI.

2.3.3 Three-Coordinate Complexes

2.3.3.1 Disubstitution of Transition Metal Halides

The reaction between one equivalent of the lithium dimer [2,6-TmpC_6H_3Li]$_2$ (**6**) and one equivalent of the corresponding transition metal dihalide [$MnBr_2$ and $FeCl_2(THF)_{1.5}$] in a mixture of toluene and THF at room temperature yields the three-coordinate complexes (2,6-Tmp$_2C_6H_3$)$_2$M(THF) [M = Mn (**15**), Fe (**16**)], with concomitant formation of the lithium halide according to Scheme 2.6.



Scheme 2.6 Synthesis of three-coordinate diaryl complexes (2,6-Tmp$_2C_6H_3$)$_2$M(THF), M = Mn (15) and Fe (16).

Attempts to synthesise the analogous cobalt complex using similar methodology in numerous solvent systems at various temperatures lead to an intractable mixture of solids. This could be a result of insufficient steric protection from the Tmp substituent in stabilising the highly reactive Co(II) centre. Complexes **15** and **16** were isolated as pale pink (**15**) or yellow (**16**) highly air- and moisture-sensitive crystals. They have been characterised (through mass spectrometry, UV/Vis spectroscopy and elemental analysis) and their solid state structures have been determined *via* X-ray crystallography. The elemental analyses for both complexes **15** and **16** agree well with the crystallographic formulation. The ^{1}H NMR spectra for **15** and **16** showed very broad signals which could not be readily assigned indicating the presence of paramagnetic ion. The effective magnetic moment (μ_{eff}) of **15** and **16** were measured *via* the Evans' method[15,16] where μ_{eff} = 5.59 μ_B (**15**) and 5.58 μ_B (**16**) at 25 °C.

The value of 5.59 μ_B for the manganese complex **15** is slightly lower than the spin-only contribution of five unpaired electrons on a high spin Mn(II) centre but close in value to related manganese complexes featuring *m*-terphenyl ligands [(2,6-$Mes_2C_6H_3)_2$Mn μ_{eff} = 5.89 μ_B; (2,6-$Naph_2C_6H_3)_2$Mn·OEt_2 = 5.52 μ_B).[7,24]

The theoretical spin only contribution for a high spin d^6 configuration for Fe(II) is 4.90 μ_B which is significantly lower than the measured value of 5.58 μ_B for **16**. This is similar to related three-coordinate iron(II) complexes featuring ring expanded *N*-heterocyclic carbene (NHC) ligands Fe[(7-DiPP)X_2][30] where [7-DiPP = 1,3-Bis(2,6-diisopropylphenyl)-4,5,6,7-tetrahydro-3H-[1,3]diazepin-1-ium; X = Br, Cl] of 6.0 μ_B and 5.9 μ_B but higher than Fe(II) *m*-terphenyl complexes [(2,6-$Mes_2C_6H_3)_2$Fe μ_{eff} = 4.90 μ_B; (2,6-$Naph_2C_6H_3)_2$Fe(THF) μ_{eff} = 4.90 μ_B)].[7,24]

3.3.3.2 Crystallographic Analysis

Crystals suitable of **15** and **16** for X-ray diffraction for were grown from saturated solutions from either toluene (**15**) or *iso*-hexane (**16**) at –30 °C. **15** and **16** are monomeric in the solid state where the nearest M···M separations are *d*(Mn···Mn) = 9.8 Å and *d*(Fe···Fe) = 9.8 Å. The molecular structures of **15** and **16** (Figure 2.3) display a distorted trigonal planar geometry [Σ(angles at M): 360.0° (**15**) and 359.9° (**16**)] around the metal centre with the coordination sites occupied by two *m*-terphenyl ligands, both in a *syn* conformation, and a THF molecule. This is contrary to that observed for the related two-coordinate compounds (2,6-$Ar_2C_6H_3$)M (Ar = Mes; Dipp; M = Mn, Fe),[7,24,31] and is presumably due to the more sterically demanding Mes and Dipp substituents. Three-coordinate monomeric d-block diaryl complexes have been observed previously when the *m*-terphenyl ligand features an asymmetric flanking substituent, for example in (2,6-$Naph_2C_6H_3)_2$ML (L = OEt_2, M = Mn,[24] Co,[8] Cd,[25] Hg;[25] L = THF, M = Fe[24]) where the flanking aryls on opposing *m*-terphenyl ligands are orientated such that a steric pocket is formed through which an Et_2O or THF molecule can coordinate. The M−O bond lengths in **15** and **16** are both within the combined Van der Waals radii of the two elements

	15 ***M = Mn*** ***n = 1'***	***16*** ***M = Fe*** ***n = 25***
M(1)–C(1)	2.1395(11)	2.073(2)
M(1)–C(*n*)	2.1395(12)	2.0734(19)
M(1)–O(1)	2.1303(13)	2.0583(14)
C(1)–M(1)–C(*n*)	138.13(6)	133.89(8)
C(1)–M(1)–O(1)	110.93(3)	115.22(7)
C(*n*)–M(1)–O(1)	110.93(3)	110.83(7)
C(1)plane···C(*n*)plane	78.77(6)	83.91(8)

Table 2.2 Selected bond lengths (Å) and angles (°) for (2,6-$Tmp_2C_6H_3)_2$M(THF) where M = Mn (15) and Fe (16). Symmetry operation: ' = $^3/_2$ – x, 1 – y, + z.

(Mn−O = 3.6 Å, Fe−O = 3.6 Å)[26] and are also close in value to related complexes containing oxygen donor atoms, for example, [MesMn(THF)(μ_2-Mes)]$_2$ [Mn−O = 2.2467(14) Å],[32] Mn[CH(SiMe$_3$)$_2$]$_2$(THF) [Mn−O = 2.19(2) Å],[33] Fe[(N(SiMe$_3$)$_2$]$_2$(THF) [Fe−O = 2.071(6) Å],[34] (pyac)Fe(THF)Cl (Fe−O = 2.029(3) Å)[35] (pyac = 1,5,9-trimesityldipyrromethene) and [ClFe(THF)Bp^{Ph}] [Fe−O = 2.0604(17) Å][36] (Bp^{Ph} = diphenylbis(pyrazolyl)borate).

Unsurprisingly, the C−Mn−C angle of 138.13(6)° (Table 2.2) in **15** is comparatively smaller than seen in related two-coordinate *m*-terphenyl complexes: (2,6-Mes$_2$C$_6$H$_3$)$_2$Mn [C−Mn−C = 166.41(3), 173.00(13)°][7] and (2,6-Dipp$_2$C$_6$H$_3$)$_2$Mn [C−Mn−C = 160.19(9)°][31] and is considerably larger than the value of 120° expected for a trigonal planar complex. This observation is consistent with the steric repulsion imposed by the two bulky *m*-terphenyl ligands. There are few examples in the literature of monomeric three-coordinate bis(aryl) complexes with Mn(II) atoms. These complexes display either distorted trigonal planar geometry, for example in the cationic complex [Li(THF)$_4$]$_2$[MnMes$_3$][37] and in the manganese complex featuring an NHC ligand: Mn(IPr)(Mes)$_2$ (IPr = 1,3-bis(2,6-diisopropylphenyl)-imidazol-2-yl-idene)[38] or T-shaped geometry which is observed in the aforementioned complex (2,6-Naph$_2$C$_6$H$_3$)$_2$MnOEt$_2$[24] and in {Li(THF)}2,6-Dipp$_2$C$_6$H$_3$Mn(μ-I)(C$_6$H$_2$-2,4,6-^{i}Pr$_3$) isolated by Power and co-workers.[31] The angle between planes of the two central aryl rings in **15** [C(1)plane···C(25)plane = 78.77(6)°, Table 2.2] is within the range of related two-coordinate bis *m*-terphenyl complexes (72.57-88.38°) but larger than the three coordinate (2,6-Naph$_2$C$_6$H$_3$)$_2$MnOEt$_2$ at 62.115(5)°.[7,24,31]

The Mn−C distances in **15** [2.1395(12) and 2.1395(11) Å] are slightly longer than in related Mn(II) *m*-terphenyl complexes (2,6-Ar$_2$C$_6$H$_3$)$_2$Mn(OEt$_2$)$_n$ [*n* = 0, Ar = Mes, Dipp;

n = 1, Naph; Mn−C = 2.066(5)-2.107(2) Å][7,24,31] but are closer in value to previously discussed $[Li(THF)_4]_2[MnMes_3]$ [Mn−C = 2.137(6), 2.142(6) and 2.144(6) Å], all of which are larger than the combined covalent radii for Mn and C atoms (1.96 Å).[26] These larger Mn−C distance is indicative that the bonding has less covalent character and is more ionic than seen in the aforementioned Mn(II) *m*-terphenyl complexes.

The analogous three-coordinate iron complex $(2,6\text{-}Tmp_2C_6H_3)_2Fe(THF)$ (**16**) is one of a few examples of crystallographically verified three-coordinate diaryls with an Fe(II) centre in the literature, the second only to feature *m*-terphenyl ligands.[24] Three-coordinate Fe(II) complexes have been isolated previously by utilisation of bulky ligands such as NHCs,[30,39–42] cAACs[43] and aryls.[44]

As mentioned previously, the geometry around the metal centre in **16** can be described as distorted trigonal planar, similar to other three-coordinate bis aryl iron(II) complexes such as $FeMes_3$,[45] $Fe(IPr)(Mes)_2$ and $Fe(IPr)(2,6\text{-}Xyl)_2$.[39] The Fe–C bond lengths are statistically indistinguishable at 2.073(2) Å and 2.0734(19) Å which are slightly longer than observed for the previously mentioned two-coordinate Fe(II) *m*-terphenyl complexes [2.028(2)-2.059(2) Å][7,19,46] but are closer in value to the three-coordinate complex $(2,6\text{-}Naph_2C_6H_3)_2Fe(THF)$ [Fe−C 2.066(5), 2.071(5) Å].[24] The C−Fe−C angle is more acute compared with the other Fe(II) *m*-terphenyl complexes[7,19,24,46] presumably due to the additional coordination of the THF molecule.

The nearest metal ligand interactions occur between the metal and the *ortho*-CH of the flanking aryl at 2.983(1) and 2.857(8) Å for **15** and **16** respectively, which are within the sum of the Van der Waals radii of the individual atoms. These are similar to related diaryl complexes, however, if said interactions exist they are indeed very weak and could be due to packing forces in the solid state.

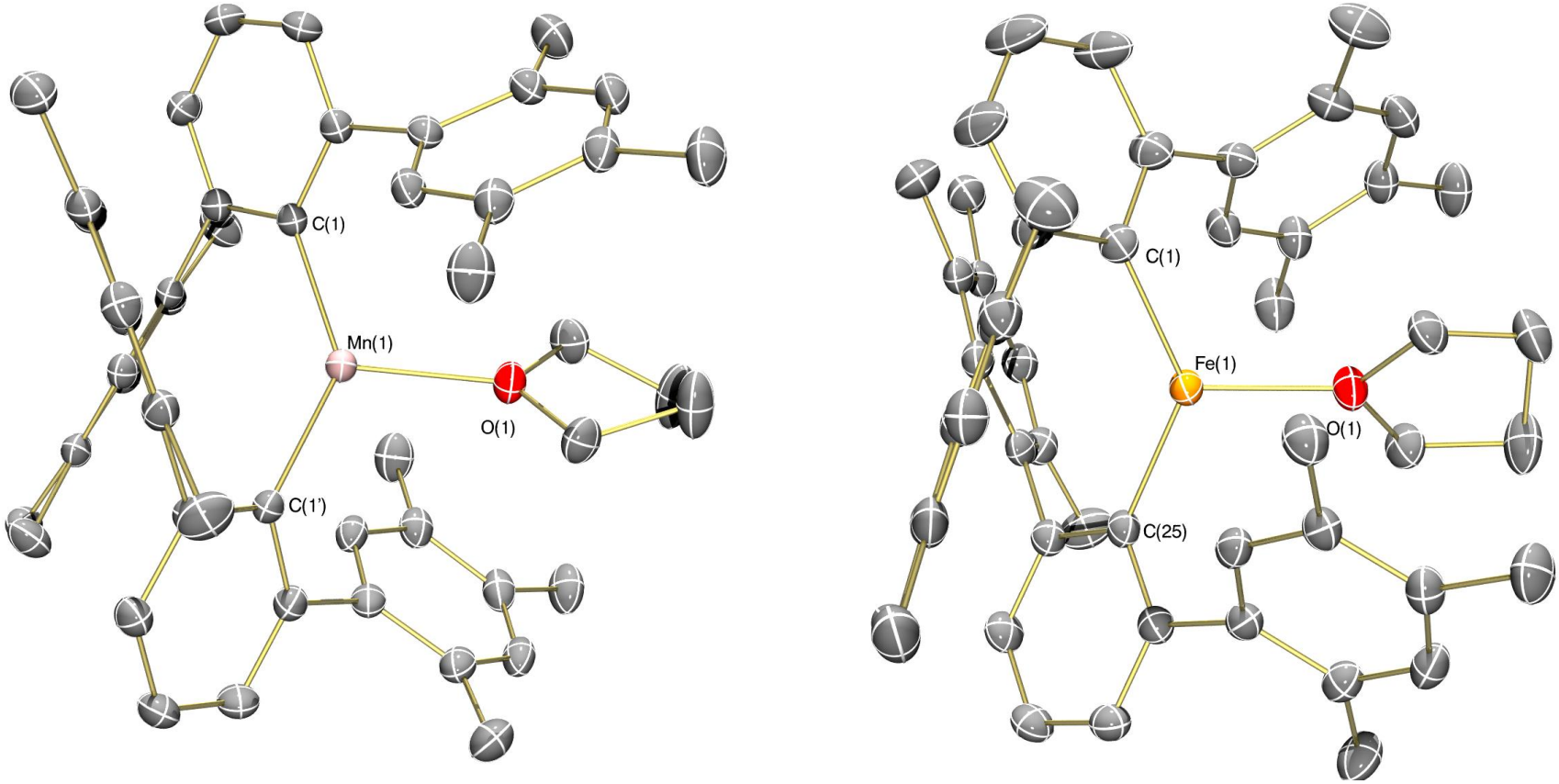
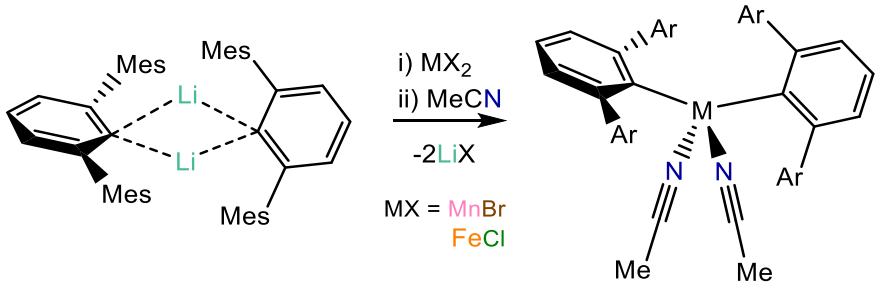


Figure 2.3 Crystal structures of 15 and 16. Thermal ellipsoids are set at the 50% probability level. Hydrogen atoms and minor disordered components omitted for clarity Symmetry operation: ' = $^{3}/_{2}$ – x, 1 – y, + z.

2.3.4 Four-Coordinate Complexes

As the study of the reactivity of transition metal *m*-terphenyl complexes was the main focus of this work, preliminary investigations with acetonitrile were undertaken in order to examine whether other substrates could penetrate the coordination sphere. The diaryl complexes **10** and **11**, were synthesised *in situ* by reaction of the lithium salt **4** with the corresponding transition metal dihalide (Scheme 2.7).



Scheme 2.7 Synthesis of four-coordinate diaryl complexes (2,6-$Mes_2C_6H_3)_2M(MeCN)_2$, M = Mn (17) and Fe (18).

After removal of volatiles *in vacuo* the resulting solids were dried after which acetonitrile was added. Subsequent workup resulted in the precipitation of fine needle shaped crystals which X-ray diffraction experiments revealed the structures to be the four-coordinate diaryl complexes: (2,6-$Mes_2C_6H_3)_2M(MeCN)_2$ [M = Mn (**17**) and Fe (**18**)].

17 and **18** have been characterised by mass spectrometry, UV/Vis spectroscopy and elemental analysis. The mass spectra (EI) of **17** and **18** only show the fragment ion of the diaryl complex: $[M(2,6\text{-}Mes_2C_6H_3)_2]^+$ with the absence of the coordinating acetonitrile molecules, however the elemental analyses agree well with the formulation shown by crystallographic analysis. The ^1H NMR spectra display very broad singlets which cannot be resolved indicating the presence of unpaired electrons. Their effective magnetic moments were calculated *via* the Evans method and were found to be 4.21 μ_B (**17**) and 5.17 μ_B (**18**). The μ_{eff} for iron complex **18** agrees with the spin only value for 4 unpaired

electrons (4.90 μ_B) but the value for **17** is considerably lower than spin only values for five unpaired electrons (5.92 μ_B). This significantly lower value could be an indication of spin orbit coupling, which is not observed for the corresponding diaryl complex (2,6-$Mes_2C_6H_3)_2Mn$, thereby reducing the effective magnetic moment.[7,47]

The UV/Vis spectrum of **17** and **18** in THF exhibit strong absorptions around 200-350 nm, which is consistent with the related species (2,6-$Ar_2C_6H_3)_2M$ (Ar = Mes, Dipp; M = Mn, Fe), which also feature strong absorption between 200-400 nm.[7,31,46]

3.3.4.1 Crystallographic Analysis

Storage of saturated solutions of **17** and **18** in acetonitrile at –30 °C resulted in the precipitation of crystals suitable for X-ray diffraction experiments. The isomorphous, four-coordinate complexes **17** and **18** feature two *m*-terphenyl ligands and two acetonitrile molecules bound to the metal centre (Figure 2.4). These are monomeric in the solid state with the closest M···M separations of *d*(Mn···Mn) = 11.4 Å and *d*(Fe···Fe) = 12.7 Å for **17** and **18** respectively (selected bond lengths and angles for **17** and **18** are shown in Table 2.3). The geometry of **17** and **18** can be described as seesaw by using Equation 2.1 as outlined by Houser and co-workers,[48] with the four-coordinate geometry index values, τ_4, of 0.71 and 0.72 respectively.

Both **17** and **18** crystallise in the monoclinic space group C2/*c* with half the molecule in the asymmetric unit with two disordered solvent molecules of crystallisation. The

$$\tau_4 = \frac{360° - (\alpha + \beta)}{141°}$$

Equation 2.1 Geometry index for four-coordinate complexes. τ_4 = four-coordinate index, α and β are the two largest angles in the four-coordinate species (°).[48]

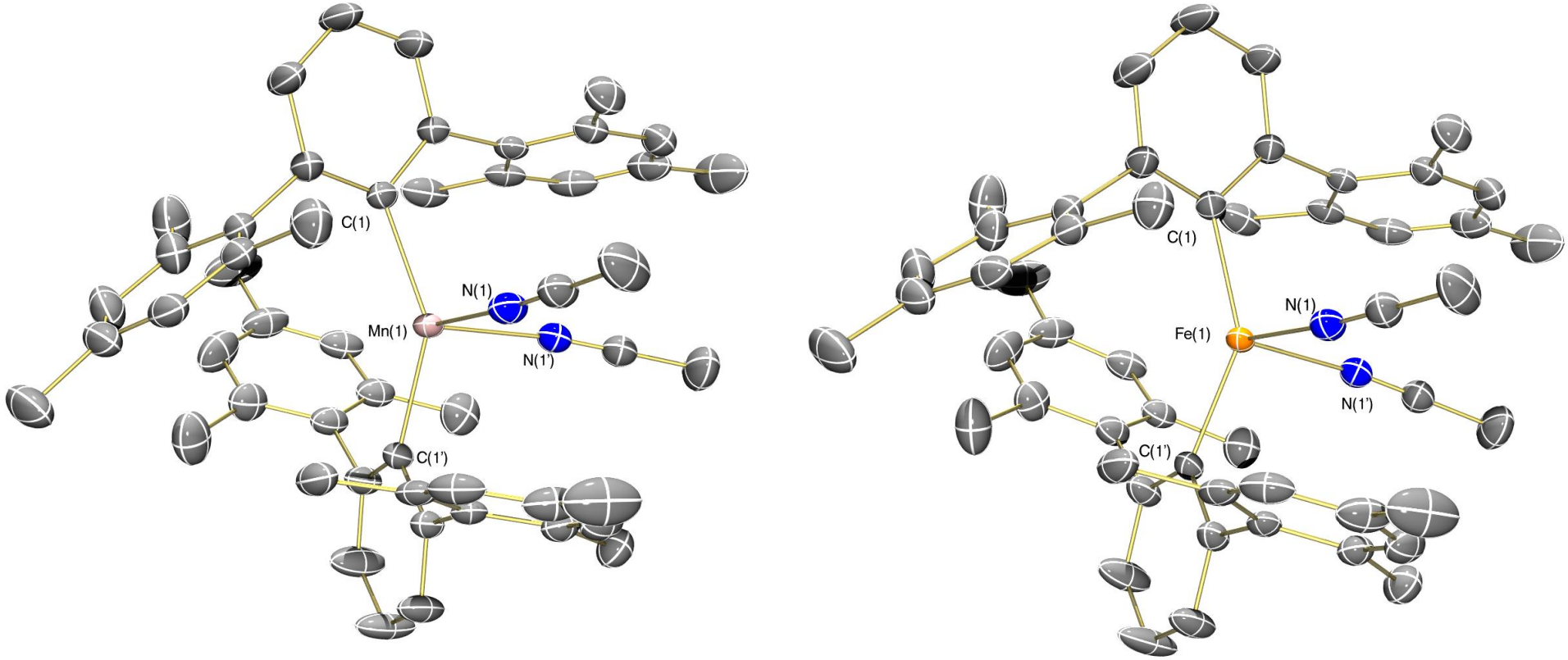


Figure 2.4 Crystal structures of 17 and 18. Thermal ellipsoids are set at the 50% probability level. Hydrogen atoms, solvent of recrystallisation and minor disordered components omitted for clarity. Symmetry operation: ' = 1– x, + y, ³⁄₂ – z.

m-terphenyl ligands are orientated almost orthogonal to each other [C(1)plane···C(1')plane angle *ca.* 84°] as a consequence of the steric bulk imposed by the *m*-terphenyl ligands. The M–C bonds in **17** and **18** are more elongated than in their corresponding diaryl counterparts (2,6-$Mes_2C_6H_3)_2M$ [M = Mn, 2.092(3)-2.098(3) Å; M = Fe, 2.037(3)-2.042(3) Å][7] presumably as a result of the coordination of the acetonitrile molecules. The C–M–C angles show significant distortion from linearity [C–M–C =146.36(7)° (**17**), 144.95(7)° (**18**)] which differ from the non-acetonitrile bound complexes by approximately 20°. The shift in the C–M–C angle suggests that there is a certain degree of flexibility in the bulky terphenyl ligand (2,6-$Mes_2C_3H_3^-$). The Fe–N distance in **18** [2.1457(13) Å] is slightly longer than those seen in other iron(II) complexes with coordinating nitrile molecules, for example in $L^{Me}Fe(NC^tBu)_2$, Fe–N = 2.074(2) Å (where L^{Me} = 2,4-bis(2,6-diisopropylphenylimido)-3-pentyl)[49] and Fe(L2)$(MeCN)_2$]OTf, Fe–N = 1.929(5) and 1.938 Å (L2 = *N,N'*-bis(2-pyridylmethyl)ethylenediamine)[50] but is closer in value to [Fe(6-Me_3TPA)$(CH_3CN)_2$]$(ClO_4)_2$, Fe–N = 2.17(2) Å (6-Me_3TPA = *tris*[(6-methyl-2-pyridyl)methyl]amine)[51] where the longer bond indicates a weaker donor-acceptor relationship at the very sterically crowded centre.

A similar observation can be made for the analogous manganese complex **17** with the Mn–N distance of 2.2347(13) Å which is elongated in comparison to other manganese(II) complexes bearing coordinated acetonitriles such as [Mn(Py_2N_2)$(MeCN)_2$]$(PF_6)_2$ [Mn–N = 2.174(2), 2.184(2) Å] (*N,N'*-dimethyl-2,11-diaza[3,3](2,6)pyridinophane),[52] [($Py_2N^tBu_2$)Mn$(MeCN)_2$]$(PF_6)_2$ [Mn–N = 2.152(12), 2.211(2) Å] ($Py_2N^tBu_2$ = *N,N'*-ditert-butyl-2,11-diaza[3,3](2,6)pyridinophane)[53] and [(Py_2NH_2)Mn$(MeCN)_2$]$(PF_6)_2$ [Mn–N = 2.2000(18), 2.1978(18) Å] [$PyNH_2$ = 2,6-bis(bromomethyl)pyridine, 2,11-

diaza[3,3](2,6)pyridinophane],[53] which are all shorter than those in **17**, presumably as a consequence of the steric hindrance of the bulky *m*-terphenyl ligand.

	17 ***M = Mn***	***18*** ***M = Fe***
M(1)–C(1)	2.1805(14)	2.1254(14)
M(1)–N(1)	2.2347(13)	2.1457(13)
N(1)–C(25)	1.136(2)	1.138(2)
C(1)–M(1)–C(1')	146.34(8)	144.95(8)
C(1)–M(1)–N(1)	91.76(5)	92.36(5)
C(1')–M(1)–N(1)	113.86(5)	114.11(5)
C(1)plane···C(1')plane	84.70(5)	84.90(8)

Table 2.3 Selected bond lengths (Å) and angles (°) for M(2,6-$Mes_2C_6H_3)_2(MeCN)_2$ where M = Mn (17) and M = Fe (18). Symmetry operation: ' = 1– x, + y, $^3/_2$ – z.

2.4 Conclusions

A series of *m*-terphenyl ligands have been synthesised with varying steric bulk though substitution of the flanking aryl with either a Mes, 2,6-Xyl or Tmp substituent. The synthesis of the iodides were achieved using the method outlined by Hart and co-workers[17] in good to excellent yields. The *m*-terphenyl iodides (**1**-**3**) were then metallated with use of *n*-butyllithium to yield the *m*-terphenyl lithium dimers (**4**-**6**).

Salt metathesis reactions between $[2,6\text{-}Tmp_2C_6H_3Li]_2$ (**6**) and transition metal dihalides resulted in the synthesis of novel two- and three-coordinate transition metal complexes. Three-coordinate transition metal *m*-terphenyl complexes have previously been isolated with an asymmetric Naph substituent with either a molecule of Et_2O or THF where the flanking groups of the *m*-terphenyl ligand are in various conformations.[24,25] The group 12 transition metal complexes **7**-**9** exhibit fluxionality in solution with the broadening of NMR spectra and presence of multiple peaks in the $^{113}Cd\{^1H\}$ and $^{199}Hg\{^1H\}$ NMR spectra. The solid state structures of **7** and **9** were determined *via* X-ray crystallography and show the ligands orientated in the *anti*-configuration. The analogous reaction with transition metals iron and manganese resulted in the isolation of three-coordinate trigonal planar complexes, with coordination of a THF molecule to the metal centre. The flanking Tmp substituents of the *m*-terphenyl are in the *syn*-conformation in the solid state, unlike that observed for the group 12 complexes. The electronic configurations are likely to be high-spin with the effective magnetic moments of **15** and **16** as determined *via* Evans' method, indicate five and four unpaired electrons.

Preliminary investigations with acetonitrile and two-coordinate transition metal complexes **10** and **11** were undertaken in order to examine whether other substrates could coordinate to the transition metal. *In situ* reactions resulted in the isolation of the four-

coordinate seesaw complexes **17** and **18** with two *m*-terphenyl ligands and two acetonitrile molecules bound to the metal centre. This demonstrates that the steric demands imposed by the *m*-terphenyl ligand are not such that prevent small molecules to reach the metal centre.

2.5 Future Work

Future work will involve expanding the library of *m*-terphenyl complexes through substitution of flanking aryls, altering the sterics, and through substitution on back of the central aryl ring with electron donating or withdrawing groups, thereby altering the electronic properties. This would allow for further study of how the *m*-terphenyl ligand effects the structural geometry of the transition metal which could have further implications on the reactivity towards small molecules, catalytic applications (see Chapters IV-VI) and magnetic properties.

DFT calculations on the complexes bearing the asymmetric Tmp substituent (**7**-**9**) would further enhance the understanding of the conformational isomerism observed in solution and help verify whether the most stable conformer is that observed in the solid state.[25]

Characterisation of the electronic structure of the iron and manganese complexes (**15**, **16, 17** and **18**) has been undertaken *via* Evans' method however, further, more rigorous approach using SQUID measurements and EPR spectroscopy should be undertaken to fully elucidate the electronic structure. This would also enable the temperature dependency of the magnetic moments of such species to be investigated and the spin states of the complexes. This could also be complimented with cyclic voltammetry measurements of these species to investigate their chemical redox properties. Mössbauer spectroscopy measurements on the iron complexes would also enable the understanding of the electronic properties and allow for the study of how the different ligand environment affects the metal centre.

The coordination chemistry of the two- and three-coordinate transition complexes could be expanded to larger molecules, for example, pyridine, 2,2'-bipyridine (bipy), and phenanthroline in order to probe the flexibility of the *m*-terphenyl ligands further.

2.6 References

1 D. L. Kays, *Dalton Trans.*, 2011, **40**, 769–778.

2 P. P. Power, *J. Organomet. Chem.*, 2004, **689**, 3904–3919.

3 S. Gambarotta, C. Floriani, A. Chiesivilla and C. Guastini, *J. Chem. Soc., Chem. Commun.*, 1983, 1128–1129.

4 E. Solari, F. Musso, E. Gallo, C. Floriani, N. Re, A. Chiesivilla, C. Rizzoli, A. Chiesi-Villa and C. Rizzoli, *Organometallics*, 1995, **14**, 2265–2276.

5 W. Seidel, H. Müller and H. Görls, *Angew. Chem. Int. Ed.*, 1995, **34**, 325–327.

6 R. J. Wehmschulte and P. P. Power, *Organometallics*, 1995, **14**, 3264–3267.

7 D. L. Kays and A. R. Cowley, *Chem. Commun.*, 2007, **58**, 1053–1055.

8 B. M. Gridley, A. J. Blake, A. L. Davis, W. Lewis, G. J. Moxey and D. L. Kays, *Chem. Commun.*, 2012, **48**, 8910–8912.

9 D. L. Kays, in *Organometallic Chemistry: Volume 36*, The Royal Society of Chemistry, 2010, vol. 36, pp. 56–76.

10 R. Wolf, C. Ni, T. Nguyen, M. Brynda, G. J. Long, A. D. Sutton, R. C. Fischer, J. C. Fettinger, M. Hellman, L. Pu and P. P. Power, *Inorg. Chem.*, 2007, **46**, 11277–11290.

11 T. Nguyen, A. D. Sutton, M. Brynda, J. C. Fettinger, G. J. Long and P. P. Power, *Science*, 2005, **310**, 877–847.

12 Z. Zhu, M. Brynda, R. J. Wright, R. C. Fischer, W. A. Merrill, E. Rivard, R. Wolf, J. C. Fettinger, M. M. Olmstead and P. P. Power, *J. Am. Chem. Soc.*, 2007, **129**, 10847–10857.

13 X.-N. Yao, J.-Z. Du, Y.-Q. Zhang, X.-B. Leng, M.-W. Yang, S.-D. Jiang, Z.-X. Wang, Z.-W. Ouyang, L. Deng, B.-W. Wang and S. Gao, *J. Am. Chem. Soc.*, 2017, **139**, 373–380.

14 J. M. Zadrozny, D. J. Xiao, M. Atanasov, G. J. Long, F. Grandjean, F. Neese and J. R. Long, *Nat. Chem.*, 2013, **5**, 577–581.

15 D. F. Evans, *J. Chem. Soc.*, 1959, 2003–2005.

16 E. M. Schubert, *J. Chem. Educ.*, 1992, **69**, 62.

17 A. Saednya and H. Hart, *Synthesis*, 1996, 1455–1458.

18 S. Duttwyler, Q. Q. Do, A. Linden, K. K. Baldridge and J. S. Siegel, *Angew. Chem. Int. Ed.*, 2008, **47**, 1719–1722.

19 T. J. Blundell, PhD Thesis, The University of Nottingham, 2015.

20 K. Ruhlandt-Senge, J. J. Ellison, R. J. Wehmschulte, F. Pauer and P. P. Power, *J.*

Am. Chem. Soc., 1993, **115**, 11353–11357.

21 S. Hino, M. M. Olmstead, J. C. Fettinger and P. P. Power, *J. Organomet. Chem.*, 2005, **690**, 1638–1644.

22 G. Meyer and P. Nockemann, *Z. Anorg. Allg. Chem.*, 2003, **629**, 1447–1461.

23 T. J. Blundell, F. R. Hastings, B. M. Gridley, G. J. Moxey, W. Lewis, A. J. Blake and D. L. Kays, *Dalton Trans.*, 2014, **43**, 14257–14264.

24 B. M. Gridley, PhD Thesis, The University of Nottingham, 2013.

25 B. M. Gridley, G. J. Moxey, W. Lewis, A. J. Blake and D. L. Kays, *Chem. Eur. J.*, 2013, **19**, 11446–11453.

26 S. S. Batsanov, *Inorg. Mater.*, 2001, **37**, 871–885.

27 M. Niemeyer and P. P. Power, *Organometallics*, 1997, **16**, 3258–3260.

28 P. Pyykkö and M. Atsumi, *Chem. Eur. J.*, 2009, **15**, 186–197.

29 R. C. C. Smith, T. Ren and J. D. D. Protasiewicz, *Eur. J. Inorg. Chem.*, 2002, 2779–2783.

30 J. J. Dunsford, D. J. Evans, T. Pugh, S. N. Shah, N. F. Chilton and M. J. Ingleson, *Organometallics*, 2016, **35**, 1098–1106.

31 C. Ni, J. C. Fettinger, G. J. Long and P. P. Power, *Dalton Trans.*, 2010, **39**, 10664–10670.

32 R. Fischer, H. Görls, M. Friedrich and M. Westerhausen, *J. Organomet. Chem.*, 2009, **694**, 1107–1111.

33 P. B. Hitchcock, M. F. Lappert, W.-P. Leung and N. H. Buttrus, *J. Organomet. Chem.*, 1990, **394**, 57–67.

34 M. M. Olmstead, P. P. Power and S. C. Shoner, *Inorg. Chem.*, 1991, **30**, 2547–2551.

35 E. R. King and T. A. Betley, *Inorg. Chem.*, 2009, **48**, 2361.

36 M. Wagner, C. Limberg and B. Ziemer, *Eur. J. Inorg. Chem.*, 2008, 3970–3976.

37 R. A. Bartlett, M. M. Olmstead, P. P. Power and S. C. Shoner, *Organometallics*, 1988, **7**, 1801–1806.

38 R. A. Musgrave, R. S. P. Turbervill, M. Irwin and J. M. Goicoechea, *Angew. Chem. Int. Ed.*, 2012, **51**, 10832–10835.

39 R. A. Musgrave, R. S. P. Turbervill, M. Irwin, R. Herchel and J. M. Goicoechea, *Dalton Trans.*, 2014, **43**, 4335–4344.

40 R. A. Layfield, J. J. W. McDouall, M. Scheer, C. Schwarzmaier and F. Tuna, *Chem. Commun.*, 2011, **47**, 10623–10625.

41 W.-T. Lee, I.-R. Jeon, S. Xu, D. A. Dickie and J. M. Smith, *Organometallics*,

2014, **33**, 5654–5659.

42 T. Pugh and R. A. Layfield, *Dalton Trans.*, 2014, **43**, 4251–4254.

43 G. Ung and J. C. Peters, *Angew. Chem. Int. Ed.*, 2015, **54**, 532–535.

44 A. Klose, E. Solari, C. Floriani, A. Chiesi-Villa, C. Rizzoli, N. Re, A. Chiesivilla, C. Rizzoli and N. Re, *J. Am. Chem. Soc.*, 1994, **116**, 9123–9135.

45 H. Müller, W. Seidel and H. Görls, *Z. Anorg. Allg. Chem.*, 1996, **622**, 1269–1273.

46 C. Ni and P. P. Power, *Chem. Commun.*, 2009, 5543–5545.

47 P. P. Power, *Chem. Rev.*, 2012, **112**, 3482–3507.

48 L. Yang, D. R. Powell and R. P. Houser, *Dalton Trans.*, 2007, 955–964.

49 R. E. Cowley, G. J. Christian, W. W. Brennessel, F. Neese and P. L. Holland, *Eur. J. Inorg. Chem.*, 2012, 479–483.

50 S. Kundu, E. Matito, S. Walleck, F. F. Pfaff, F. Heims, B. Rábay, J. M. Luis, A. Company, B. Braun, T. Glaser and K. Ray, *Chem. Eur. J.*, 2012, **18**, 2787–2791.

51 Y. Zang, J. Kim, Y. Dong, E. C. Wilkinson, E. H. Appelman and L. Que, *J. Am. Chem. Soc.*, 1997, **119**, 4197–4205.

52 W.-T. Lee, S. Xu, D. A. Dickie and J. M. Smith, *Eur. J. Inorg. Chem.*, 2013, 3867–3873.

53 W. T. Lee, S. B. Muñoz, D. A. Dickie and J. M. Smith, *Angew. Chem. Int. Ed.*, 2014, **53**, 9856–9859.

Chapter III

Catalytic Cyclotrimerisation of Isocyanates

3.1 Introduction

The cyclotrimerisation of isocyanates is a direct and an atom-economical approach for the synthesis of isocyanurates. The commercial importance of isocyanurates is well known as they are commonly used as additives in polyurethane foams, coating materials and composites in order to enhance their physical properties.[1,2] Moreover, the incorporation of isocyanurates into polymers and coatings increases crosslink density and improves mechanical properties, thermal and chemical resistance, as well as flame retardation due to their outstanding thermal stability.[3–7] They are also used as key components in such diverse applications as microporous materials,[8,9] selective ion-bonding,[10] medicines and drug delivery (Figure 3.1).[11–14] Isocyanurates functionalised by donor arms at the periphery have also been shown to exhibit remarkable nonlinear optical properties.[15]

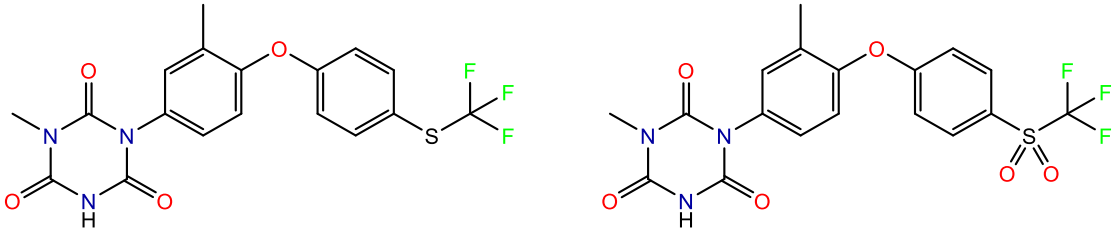


Figure 3.1 Chemical structure of Toltrazuril (left) and Ponazuril (right) which are used to treat coccidiosis in small animals.[11,12]

There are numerous examples of precatalysts which have previously been used for the cyclooligomerisation of isocyanates including Lewis bases (e.g. amines,[16] phosphines,[17–21] NHCs[22]), rare-earth (Figure 3.2)[23–25] and main group complexes.[26–29] There are few examples of transition metal species which have been used for this purpose with palladium(0) complexes currently dominating this area.[30,31]

A key early example included the use of copper(II) and nickel(II) halides which were effective in the cyclotrimerisation of methyl- and ethyl isocyanate.[32] Low-valent manganese and iron complexes have also been shown to catalyse the conversion of

isocyanates to carbodiimides, yielding low amounts (less than 15%) of cyclooligomerisation side products.[33–36]

Despite the plethora of existing cyclotrimerisation methodologies, the current technologies often suffer from issues such as low catalyst activity, by-product formation, long reaction times, high reaction temperatures or difficulty with product separation. Furthermore, there is significant concern for the replacement of noble metal catalysts by more economical, environmentally friendly catalysts based on earth-abundant metals such as manganese, iron and cobalt.[37–40] With this in mind, this Chapter explores and investigates the catalytic activity of low coordinate *m*-terphenyl transition metal complexes towards the cyclotrimerisation of isocyanates.

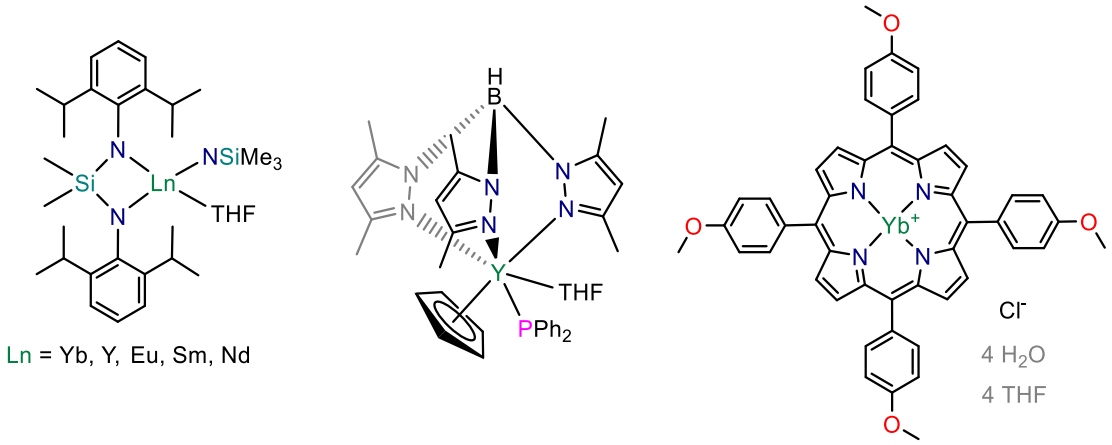


Figure 3.2 Rare-earth complexes which catalyse the cyclotrimerisation of isocyanates.[23–25]

.

3.2 Experimental

3.2.1 Initial Assessments

To a solution of precatalyst **10**, **11** or **12** (**10**, 0.213 g, 0.312 mmol; **11**, 0.213 g, 0.312 mmol; **12**, 0.214 g, 0.312 mmol) in toluene (*ca.* 20 mL) was added ethylisocyanate (1.0 mL, 1.5 M solution in toluene, 1.5 mmol) and stirred at room temperature overnight. The solvent was removed *in vacuo* and the resulting residue extracted into hexane (10 mL) concentrated to *ca*. half volume and placed in the freezer which led to the precipitation of colourless crystals. X-ray diffraction experiments revealed the structure to be the cyclotrimerisation product 1,3,5-tri(ethyl)-isocyanurate.

3.2.2 Standard Procedure for the Catalytic Cyclotrimerisation of Isocyanates

In a Young's NMR tube 0.5 to 10 mol% of precatalyst **10**, **11**, **15**, or **16** were dissolved in C_6D_6 (0.6 mL). The corresponding isocyanate was then added. The reaction was either carried out at room temperature and monitored by ^{1}H NMR spectroscopy or heated to 60 °C; the samples were maintained at 60 °C for 14 h and ^{1}H NMR spectroscopy was performed at the final time. Conversion was quantified by integration of ^{1}H NMR spectra of isocyanate *vs*. isocyanurate. See Table 3.1 for quantities of precatalyst and isocyanate used.

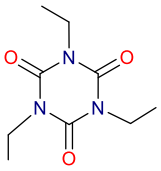
Precatalyst			***RNCO***		
Cat (mol%)	***mg***	***mmol***	***R***	***mmol***	***µL***
10 (5)	10.0	0.0147	Et	0.294	23
			^{n}Pr		28
			^{n}Hx		37
			Bn		36
11 (5)	10.0	0.0147	Et	0.294	23
			^{n}Pr		28
			^{n}Hx		37
			Bn		36
15 (5)	10.0	0.0133	Et	0.266	21
			^{n}Pr		25
			^{n}Hx		39
			Bn		33
15 (2)	5.0	0.00663	Et	0.322	26
15 (0.5)	5.0	0.00663	Et	1.33	105
16 (5)	10.0	0.0132	Et	0.264	21
			^{n}Pr		25
			^{n}Hx		39
			Bn		33

Table 3.1 Quantities of precatalyst and isocyanate used in reactions.

3.2.3 Standard procedure for the Synthesis of Cyclotrimerisation Products 19a-d

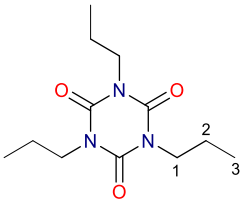
5 mol% of **10** (30.0 mg, 0.0440 mmol) and the corresponding isocyanate (RNCO, 0.88 mmol; R = Et, 70 µL; R = ^{n}Pr, 83 µL; R = ^{n}Hex, 128 µL; R = Bn, 109 µL) were dissolved in toluene (5 mL) and stirred at room temperature for 3 h (**19a**) or heated at 60 °C for 14 h (**19b-c**). The solvent was removed *in vacuo* and the residue was dissolved in dichloromethane and filtered through a short silica column. Elimination of the volatiles *in vacuo* enabled the isolation of the corresponding isocyanurates.

3.2.3.1 1,3,5-Tri(ethyl)-isocyanurate (19a)



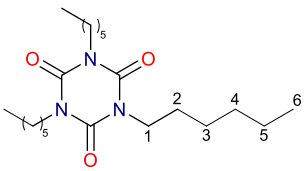
The isocyanurate was identified by comparison of its spectroscopic data with those reported in the literature.[13] Selected spectroscopic data: ^{1}H NMR (400 MHz, $CDCl_3$, 25 °C): δ 3.95 (q, ^{3}J(H,H) = 7.1 Hz, 2H, CH_2), 1.25 (t, ^{3}J(H,H) = 7.1 Hz, 3H, CH_3).^{13}C{^{1}H} NMR (101 MHz, $CDCl_3$, 25 °C): δ 148.8 (*C*=O), 38.3 (*C*H_2), 13.3 (*C*H_3). MS (GC-EI) *m/z*: calcd. for $C_9H_{15}N_3O_3$ $[M]^+$ 213.1108, found: 213.1106 (err [ppm] = 0.94).

3.2.3.2 1,3,5-Tri(n-propyl)-isocyanurate (19b)



The isocyanurate was identified by comparison of its spectroscopic data with those reported in the literature.[16] Selected spectroscopic data: ^{1}H NMR (400 MHz, $CDCl_3$, 25 °C): δ 3.88-3.81 (m, 2H, CH_2^1), 1.74-1.62 (m, 2H, CH_2^2), 0.94 (t, ^{3}J(H,H) = 7.5 Hz, 3H, CH_3^3).^{13}C{^{1}H} NMR (101 MHz, $CDCl_3$, 25 °C): δ 149.2 (*C*=O), 44.6 (*C*H_2^1), 21.3 (*C*H_2^2), 11.2 (*C*H_3^3). MS (GC-EI) *m/z*: calcd. for $C_{12}H_{21}N_3O_3$ $[M]^+$ 255.1577, found: 255.1572 (err [ppm] = 2.17).

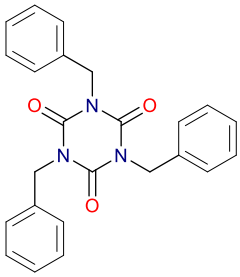
3.2.3.3 1,3,5-Tri(n-hexyl)-isocyanurate (19c)



The isocyanurate was identified by comparison of its spectroscopic data with those reported in the literature.[41] Selected spectroscopic data: ^{1}H NMR (500 MHz, $CDCl_3$, 25 °C): δ 3.96-3.77 (m, 2H, CH_2^1), 1.66-1.58 (m, 2H, CH_2^2), 1.40-1.24 (m, 6H, CH_2^{3+4+5}), 0.94-0.79 (m, 3H, CH_3^6). ^{13}C{^{1}H} NMR (126 MHz, $CDCl_3$, 25 °C): δ 149.2 (*C*=O), 43.2

(CH_2[1]), 31.5 (CH_2), 27.9 (CH_2[2]), 26.5 (CH_2), 22.7 (CH_2), 14.2 (CH_3[6]). MS (ESI) *m/z*: calcd for $C_{21}H_{39}N_3O_3$ $[M+H]^+$ 382.3064, found: 382.3070 (err [ppm] = 1.60).

3.2.3.4 1,3,5-Tri(benzyl)-isocyanurate (19d)

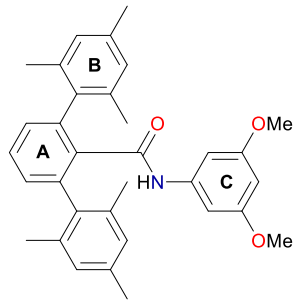


The isocyanurate was identified by comparison of its spectroscopic data with those reported in the literature.[41] Selected spectroscopic data: ^{1}H NMR (500 MHz, $CDCl_3$, 25 °C): δ 7.49 (d, ^3J(H,H) = 7.1 Hz, 2H, Ph^o), 7.42-7.27 (m, 3H, Ph^{m+p}), 5.07 (s, 2H, CH_2).^{13}C{^{1}H} NMR (126 MHz, $CDCl_3$, 25 °C): δ 149.2 (*C*=O), 135.9 (Ph^i), 129.2 (Ph^o), 128.8 (Ph^m), 128.3 (Ph^p), 46.4 (CH_2). MS (ESI) *m/z*: calcd for $C_{24}H_{21}N_3O_3Na$ $[M+Na]^+$ 422.1475, found 422.1468 (err [ppm] = 1.60).

3.2.4 Stoichiometric Reaction of 3,5-Dimethoxyphenyl Isocyanate with 11 to Form Carboxamide, 2,6-$Mes_2C_6H_3C(O)NH$-3,5-$(OMe)_2C_6H_3$ (20)

3,5-Dimethoxyphenyl isocyanate, (8.0 mg, 0.045 mmol) was added to a yellow solution of (2,6-$Mes_2C_6H_3)_2Fe$ (**11**) (30.5 mg, 0.045 mmol) in toluene (4 mL). The reaction was monitored by solution IR spectroscopy. After stirring for 12 h at room temperature no reaction had been observed, so the solution was heated to 60 °C and stirred for 16 h, whereupon the solution became dark red and a complete consumption of the isocyanate was observed *via* IR spectroscopy. The solvent was removed under vacuum to yield a yellow solid and dissolved in "wet" Et_2O and filtered through a short silica column. The solvent was then evaporated to yield a colourless crystalline solid. ^{1}H NMR indicated a mixture 42:58 of **20** and protonated ligand (2,6-$Mes_2C_6H_4$) respectively. Single crystals

for X-ray diffraction studies were grown from a saturated hexane solution at –30 °C. ^{1}H



NMR (400 MHz, $CDCl_3$, 25 °C): δ 7.56 (t, ^{3}J(H,H) = 7.6 Hz, 1H, Ph^{Ap}), 7.21 (d, ^{3}J(H,H) = 7.6 Hz, 2H, Ph^{Am}), 6.96 (s, 4H, Ph^{Bm}), 6.11 (t, ^{4}J(H,H) = 2.3 Hz, 1H, Ph^{Cp}), 5.97 (d, ^{4}J(H,H) = 2.3 Hz, 2H, Ph^{Co}), 5.32 (s, 1H, N*H*), 3.65 (s, 6H, OCH_3), 2.30 (s, 6H, CH_3^{Bp}), 2.12 (s, 12H, CH_3^{Bo}). ^{13}C{^{1}H} NMR (101 MHz, $CDCl_3$, 25 °C): δ 166.2 (*C*=O), 160.8 (Ph^{Cm}), 141.1 (Ph^{Bo}), 139.2 (Ph^{Ao}), 138.9 (Ph^{Bi}), 138.7 (Ph^{Ci}), 137.2 (Ph^{Bp}), 135.9 (Ph^{Ai}), 130.0 (Ph^{Ap}), 129.2 (Ph^{Am}), 128.2 (Ph^{Bm}), 99.5 (Ph^{Co}), 96.9 (Ph^{Cp}), 55.4 (OCH_3), 21.2 (CH_3^{Bp}), 20.8 (CH_3^{Bo}). MS (ESI) *m/z*: calcd for $C_{33}H_{34}NO$ $[M–H]^-$ 492.2544, found 492.2538 (err [ppm] = 1.20). IR (Toluene) $\bar{\nu}$/cm^{-1}: 3557 (s, N–H), 1676 (s, C=O).

3.2.5 Catalyst Poisoning Tests

3.2.5.1 Mercury Drop Test

In two separate Young's NMR tubes was added **10** (5.0 mg, 0.5 mol%) in C_6D_6 (0.6 mL) and to one, a drop of mercury was added. Ethyl isocyanate (116 µL, 1.47 mmol) was added to each tube and the reactions were monitored by ^{1}H NMR spectroscopy. Both reactions were found to reach >90% conversion after 2 days at room temperature.

3.2.5.2 Radical Trap Test

In two separate Young's NMR tubes was added **15** (10.0 mg, 5 mol%) in C_6D_6 (0.6 mL) and to one, an excess of cumene ($C_6H_5CH(CH_3)_2$) was added (9.3 µL, 0.0665 mmol). *n*-Propyl isocyanate (25 µL, 0.266 mmol) was added to each tube and the reactions were

monitored by ^{1}H NMR. Both reactions were found to reach >80% conversion after 7 h at room temperature.

3.2.6 General Procedure for Kinetic NMR Experiments

In a Young's NMR tube the precatalyst **10** was dissolved in C_6D_6 so that the total volume was 600 µL and was frozen at –30 °C. Ethyl isocyanate was then added and the sample was frozen to –78 °C to prevent the reaction from proceeding. The sample was transferred to the NMR spectrometer and monitored directly at 25 °C. Conversion was quantified by integration of ^{1}H NMR spectra.

3.2.7 Cyclotrimerisation with Mixed Isocyanates

In a Young's NMR tube was added **10** (10.0 mg, 5 mol%) in C_6D_6 (0.6 mL). The isocyanates were added and the reactions were monitored by ^{1}H NMR and GC-MS after 16 h at room temperature. See Table 3.2 for quantities and ratios of the isocyanates used.

Ratio EtNCO:RNCO	***EtNCO***		***RNCO***		
	µL	***mmol***	***R***	***µL***	***mmol***
1:2	23	0.294	^{p}Tol	74	0.588
2:1	47	0.588	^{p}Tol	37	0.294
1:2	23	0.294	^{i}Pr	58	0.588
2:1	47	0.588	^{i}Pr	29	0.294

Table 3.2 Reactions performed with a mixture of isocyanates with the manganese(II) precatalyst 10 present, where RNCO is an isocyanate with a substrate that does not undergo catalytic cyclotrimerisation with only the precatalyst present.

3.3 Results and Discussion

3.3.1 Preliminary Testing

Initial reactions of the manganese, iron, and cobalt precatalysts **10-12** with an excess of ethyl isocyanate were performed in toluene and stirred overnight at room temperature. After subsequent workup, colourless crystals were isolated which X-ray diffraction measurements showed the structure to be the cyclotrimerisation product, triethyl isocyanurate. This prompted the investigation as to whether the reaction was catalytic. Using ethyl isocyanate as a model substrate, an initial assessment of the catalytic activity of a range of *m*-terphenyl transition metal complexes (Mn: **10**, **15**; Fe: **11**, **14**, **16**; Co: **12**) were trialled at room temperature, monitored *via* ^{1}H NMR spectroscopy (Table 3.3).

Entry	***Cat. (mol%)***	***Time (h)***	***Conversion (%)***
1	**12** (10)	24	85
2	**14** (10)	24	66
3	**11** (5)	5	95
4	**16** (5)	14	97
5	**10** (5)	2.5	98
6	**15** (5)	1	97

Table 3.3 Reaction conditions: room temperature (20 °C ± 2), 0.6 mL of C_6D_6. Conversion determined by ^{1}H NMR spectroscopy.

When the cobalt precatalyst **12** was employed at 10 mol% catalyst loading the room temperature reaction had only reached 24% conversion after 7 h. After 24 h, there was a significant amount of black precipitate observed in the reaction solution and had reached 85% conversion suggesting that the catalyst was decomposing to an as yet unidentified,

catalytically inactive species (Table 3.3, entry 1). Assessment of the iron(II) complexes showed that the 2,6-Xyl substituted *m*-terphenyl complex **14** was much slower than the analogous Mes (**11**) or Tmp (**16**) substituted *m*-terphenyl complexes. The reaction of **14** at 10 mol% catalyst loading reached only 66% conversion after 24 h at room temperature whereas **11** and **16** at a lower catalyst loading (5 mol%) had reached >95% after 5 and 14 h respectively (Table 3.3, entries 2-4). The two manganese catalysts **10** and **15** showed excellent performance with high conversions to the isocyanurate after very short periods of time at room temperature (Table 3.3, entries 5 and 6). With this information, the study of the catalytic cyclotrimerisation was limited to the two- and three-coordinate manganese and iron precatalysts (2,6-$Mes_2C_6H_3)_2M$ (M = Mn, **10**; Fe, **11**) and (2,6-$Tmp_2C_6H_3)_2M(THF)$ (M = Mn, **15**; Fe, **16**) with the aim to evaluate how catalytic activity is affected as a consequence of changing the ligand environment and transition metal in these complexes.

3.3.2 Catalytic Cyclotrimerisation of Primary Alkyl Isocyanates

The catalytic activity of complexes **10**, **11**, **15** and **16** as precatalysts for the cyclotrimerisation of isocyanates were carried out in C_6D_6 at room temperature or at 60 °C and monitored *via* ^{1}H NMR. The samples which were heated were maintained at 60 °C for 14 h after which, ^{1}H NMR spectroscopy was performed at the final time. The conversions of starting isocyanates to the corresponding isocyanurate were quantified by integration of ^{1}H NMR spectra where these results are summarised in Table 3.4. The three-coordinate manganese precatalyst **15** performed remarkably well with EtNCO from 5-0.5% catalyst loading at room temperature where high conversion to the isocyanurate was observed in relatively short times (Table 3.4, entries 1-3). A significant decrease in

rate was observed when using the analogous three-coordinate iron complex **16** where the reaction reaches 97% after 24 h however, when increasing the reaction temperature to 60 °C high conversions are achieved after just 14 h (Table 3.4, entries 4 and 5). The two-coordinate complexes **10** and **11** also performed well at room temperature with EtNCO. Whilst the two manganese complexes **15** and **10** reached completion in comparable times, a notable difference was seen for the two iron complexes **16** and **11**.

Indeed, this is clearly evident in the calculated turnover frequency (TOF) for the room temperature cyclotrimerisation of ethyl isocyanate (Table 3.4, entries 2, 4, 6 and 7). The three coordinate manganese precatalyst, **15**, had the highest TOF of 81.6 h^{-1}, followed by complex **10**. The worst performing precatalyst was complex **11**.

When the chain length of the substrate is increased from ethyl to *n*-propyl and *n*-hexyl it became necessary to increase the temperature to 60 °C to achieve high conversions after 14 h (Table 3.4, entries 8-16). The cyclotrimerisation of benzyl isocyanate was also successful for all, however when using precatalyst **16**, the reaction only reached 65% conversion after 14 h. Notably, no dimerisation of the isocyanates to uretdiones, a common by-product, were observed in these reactions.[22,24,28] These reactions are also scalable where the isocyanurates **19a-d** were isolated by reaction of **11** (5 mol%) with the corresponding isocyanate in toluene and purified *via* passage through a short silica column using dichloromethane as an eluent.

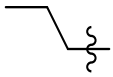
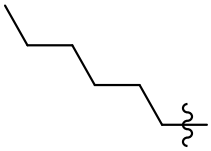
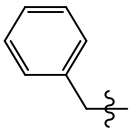
Entry	***Isocyanate RN=C=O***	***Cat. (mol%)***	***Product***	***T (°C)***	***Time (h)***	***Conversion (%)***	***TOF (h^{-1})***
1		**15** (5)	**19a**	rt	1	97	-
2		**15** (2)	**19a**	rt	2.8	98	81.6
3		**15** (0.5)	**19a**	rt	5	98	-
4		**16** (5)	**19a**	rt	24	97	4.6
5	R = Et	**16** (2)	**19a**	60	14	94	-
6		**10** (5)	**19a**	rt	2.5	98	26.7
7		**11** (5)	**19a**	rt	6.5	99	1.5
8		**15** (5)	**19b**	rt	14	96	-
9		**15** (5)	**19b**	60	14	98	-
10		**16** (5)	**19b**	60	14	88	-
11	R = ^{n}Pr	**10** (5)	**19b**	60	14	94	-
12		**11** (5)	**19b**	60	14	>99	-
13		**15** (5)	**19c**	60	14	97	-
14		**16** (5)	**19c**	60	14	98	-
15		**10** (5)	**19c**	60	14	99	-
16	R = ^{n}Hx	**11** (5)	**19c**	60	14	99	-
17		**15** (5)	**19d**	60	14	99	-
18		**16** (5)	**19d**	60	14	65	-
19		**10** (5)	**19d**	60	14	>99	-
20	R = Bn	**11** (5)	**19d**	60	14	>99	-

Table 3.4 Reaction conditions: 0.6 mL of C_6D_6. Conversion determined by ^{1}H NMR spectroscopy.- rt = room temperature (20 °C ± 2). TOF = Turnover frequency (h^{-1}).

3.3.3 Reactions with Aromatic, Secondary and Tertiary Alkyl Isocyanates

After the successful use of **10**, **11**, **15** and **16** as precatalysts for the cyclotrimerisation of primary aliphatic isocyanates, the scope of this reaction was extended to a variety of aliphatic and aryl isocyanates with precatalysts **10** and **11** (Table 3.5).

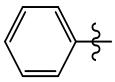
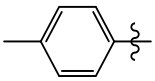
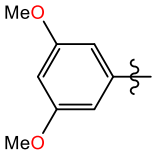
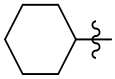
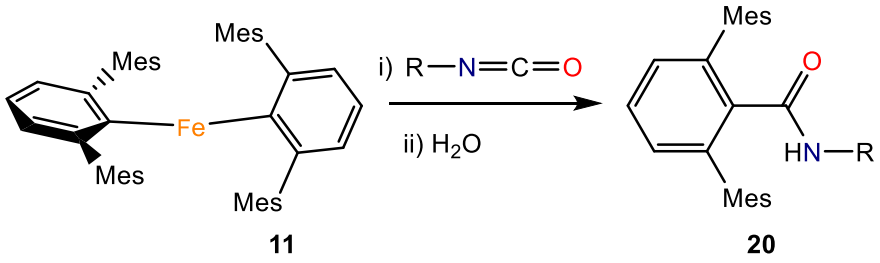
Entry	***Isocyanate RN=C=O***	***Cat. (mol%)***	***T (°C)***	***Time (h)***	***Conversion (%)***
1		**10** (5)	60	48	0
2	R = Ph	**11** (5)	60	48	0
3		**10** (10)	50	48	0
4	R = ^{p}Tol	**11** (10)	50	48	0
5		**10** (5)	60	48	0
6	R = 3,5-(OMe)$_2$Ph	**11** (5)	60	48	0
7		**10** (5)	60	48	0
8	R = Cy	**11** (5)	60	48	0
9		**10** (5)	60	48	0
10	R = ^{i}Pr	**11** (5)	60	48	0
11		**10** (5)	80[(a)]	48	0
12	R = ^{t}Bu	**11** (5)	80[(a)]	48	0

Table 3.5 Reaction conditions: 0.6 mL of C_6D_6. Conversions determined by ^{1}H NMR spectroscopy. (a) Reactions performed in toluene-d_8.

No cyclotrimerisation was observed *via* NMR spectroscopy when aromatic isocyanates (phenyl-, *p*-tolyl and 3,5-dimethoxyphenyl isocyanate) were used as substrates, even when the reactions were heated to temperatures 50 °C or higher for 48 h (Table 3.5, entries 1-6). This was also seen when secondary and tertiary isocyanates were used (Table 3.5, entries 7-12), possibly due to the incremented steric bulk of the substrates which could prevent access to the metal centre. However, subsequent experiments suggest that there is possible formation of an metal-amidate complex when using these isocyanates thereby preventing formation of the active catalyst (*infra vide*). Therefore, the lack of catalytic activity is due to an electronic rather than a steric effect.

3.3.4 Reaction of 3,5-Dimethoxyphenyl Isocyanate with 11

To gain information regarding the absence of catalytic activity observed for aryl isocyanates with these *m*-terphenyl precatalysts, a stoichiometric reaction between **11** and one equivalent of 3,5-dimethoxyphenyl isocyanate in toluene was performed according to Scheme 3.1. Due to the paramagnetic nature of **11** it was not possible to observe intermediates *via* NMR and therefore the reaction was monitored by performing solution IR spectroscopy on aliquots of the reaction mixture. No reaction was observed after stirring for 12 h at room temperature, subsequently raising the temperature to 60 °C for 16 h results in a colour change from light yellow to dark red with the appearance of new peaks in the IR spectra. Whilst no peaks were found in the aromatic isocyanurate region (*ca.* 1693-1770 cm^{-1}),[13,15,30] the appearance of a strong peak at 1676 cm^{-1} which can plausibly be assigned to the formation of an Fe-amidate and species resulting from the insertion of the 3,5-dimethoxyphenyl isocyanate into the Fe–C bond.[42–45]



Scheme 3.1 Insertion of one equivalent of RN=C=O (R = 3,5-(OMe)$_2$C$_6$H$_3$) into the Fe–C bond of complex 11 followed by hydrolysis.

Although this species could not be isolated, it was hydrolysed leading to the *in situ* formation of the amide species **20** which has been characterised by IR NMR spectroscopy, mass spectrometry and single crystal X-ray diffraction. That there is no reaction towards isocyanates indicates that this putative Fe-amidate species is deactivated towards further insertion of an external isocyanate therefore preventing the catalysis from proceeding. The IR spectrum shows peaks at 3557 and 1676 cm^{-1} corresponding to the N–H and C=O moieties respectively and accurate mass measurements of **20** also agree well with theoretical values. The ^{1}H NMR features the characteristic triplet, doublet and singlet in the aromatic reaction from protons on the central aryl and from the Mes substituent of the *m*-terphenyl ligand 2,6-Mes$_2$C$_6$H$_3^-$. There are also two peaks in the methyl region (2.30 and 2.12 ppm) corresponding to the *meta* and *para* methyl groups of the Mes moiety. The aryl-C*H* protons on the 3,5-methoxyphenyl moiety are shifted slightly upfield from the free isocyanate with a four-bond coupling constant of 2.3 Hz. The N*H* peak occurs at 5.32 ppm which is slightly lower than related compounds.[46–48] The solid state structure of **20** (Figure 3.3) was obtained *via* X-ray diffraction of single crystals grown from storage of a saturated hexane solution at –30 °C. A list of bond lengths and angles are given in Table 3.6. **20** is the second reported crystallographically characterised 2,6-disubstitued aryl benzamide with the previous example synthesised by Wan *et al.*, which features a4-methoxy aryl flanking group and a quinolone moiety

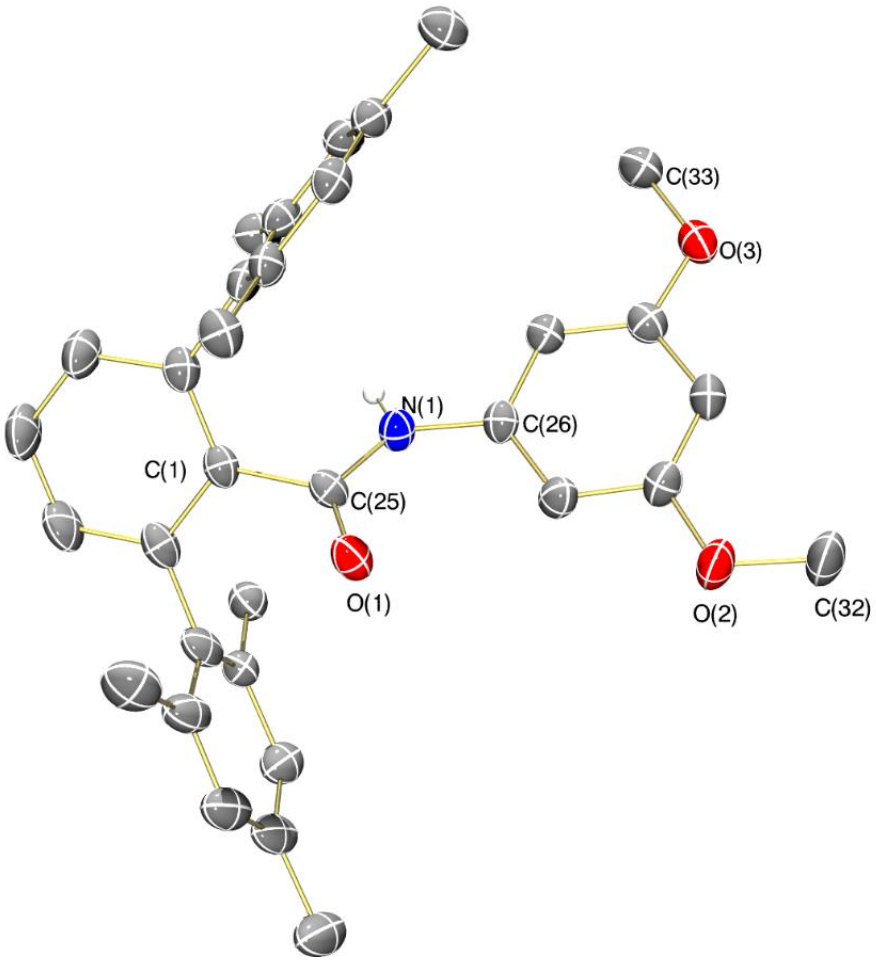


Figure 3.3 Crystal structure of 20. Thermal ellipsoids are set at the 50% probability level. Hydrogen atoms [except H(1)], minor disorder components and solvent of recrystallisation omitted for clarity.

attached to the nitrogen.[47] The C–C distances between the central aryl and the carbonyl moiety are very similar [1.502(3) Å *vs.* 1.509(3) Å in **20**] and have identical C=O distances. The plane between the two aryls (C(1)plane···C(26)plane) however are significantly different where the aryls in the aforementioned structure are orientated almost orthogonal to each other [*ca.* 84° *vs.* 145.16(6)° in **20**] presumably as a result of crystal packing. Hunter *et al.* have synthesised a series of similar amide compounds with various substituents in the *para*-position of the benzoyl moity where the solid state structures feature linear H-bonded chains where the molecules are arranged in a 'head-to-head fashion'. This is contrary to what is observed in **20** which has no H-bonds between

adjacent molecules as a result of the steric bulk imposed by the bulky Mes flanking groups.[49]

	20
C(1)–C(25)	1.509(3)
O(1)–C(25)	1.220(3)
N(1)–C(25)	1.364(3)
N(1)–C(26)	1.414(3)
C(1)plane···C(26)plane	145.16(6)

Table 3.6 Selected bond lengths (Å) and angles (°) for amide species 23.

3.3.5 Mechanistic Studies

To gain insight to the mechanism of the cyclotrimerisation of aliphatic isocyanates a series of experiments were undertaken. The reaction of *n*-PrNCO and the two manganese precatalysts **10** and **15** at 5 mol% were monitored using NMR spectrometry at 60 °C and room temperature, respectively. These samples were prepared by dissolving the precatalyst in C_6D_6, cooling the solution to –30 °C after which the isocyanate was added and was quickly cooled to –78 °C to prevent the reaction from proceeding. The samples were then transferred directly into the NMR spectrometer and a ^{1}H NMR spectrum was then taken in numerous time intervals. From the plot of conversion *vs*. time (Figure 3.4) no induction period was observed indicating that the reaction most likely proceeds though a homogenous mechanism. Furthermore the mercury drop test was performed which is a common method in the literature whereby Hg(0) will make an amalgam with the metal therefore deactivating the heterogeneous catalyst but will not affect the activity of a homogeneous catalyst.[50,51] To this end, two samples were prepared with **10** (0.5 mol%) and ethyl isocyanate in C_6D_6, with one sample containing a drop of mercury which were

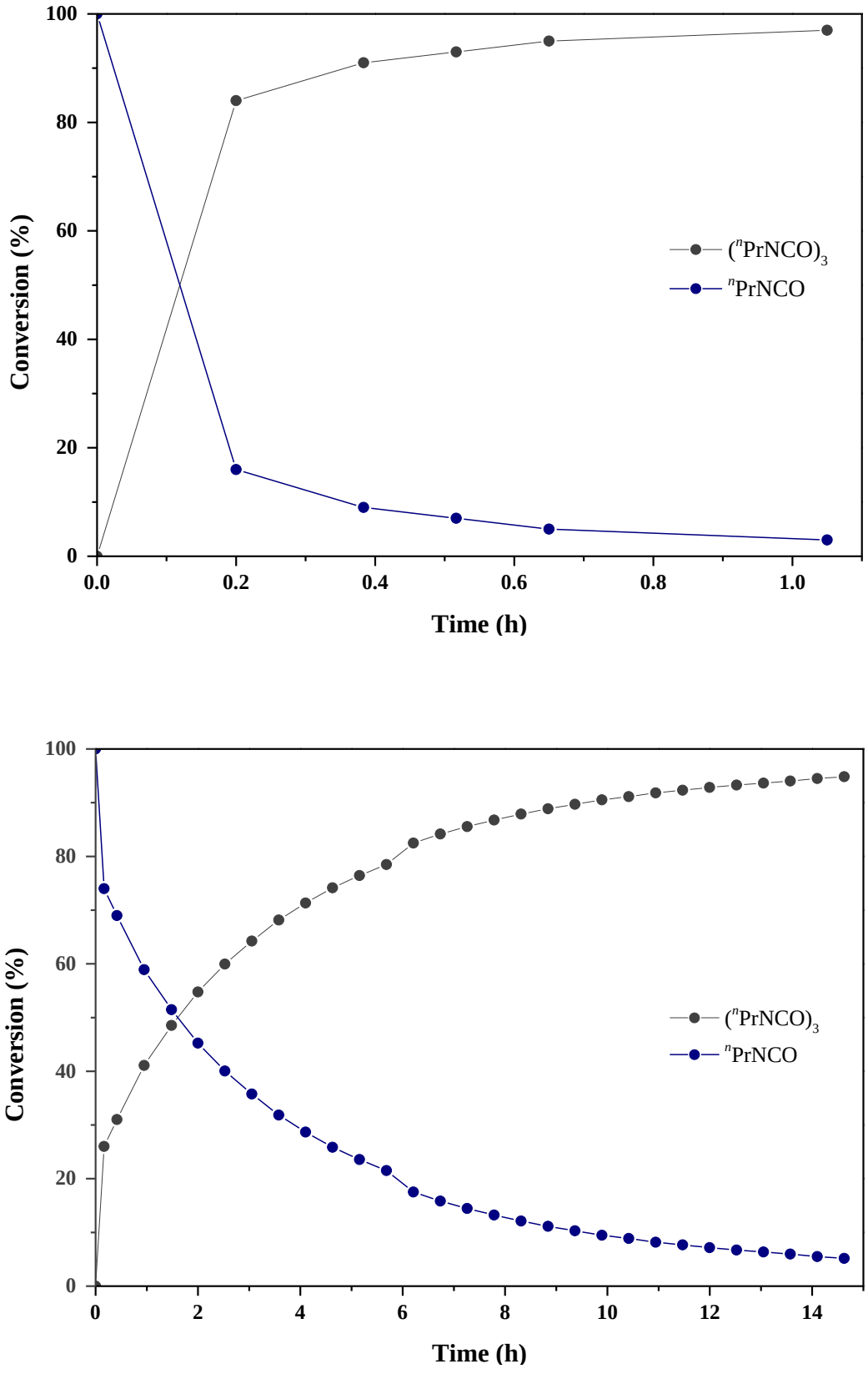


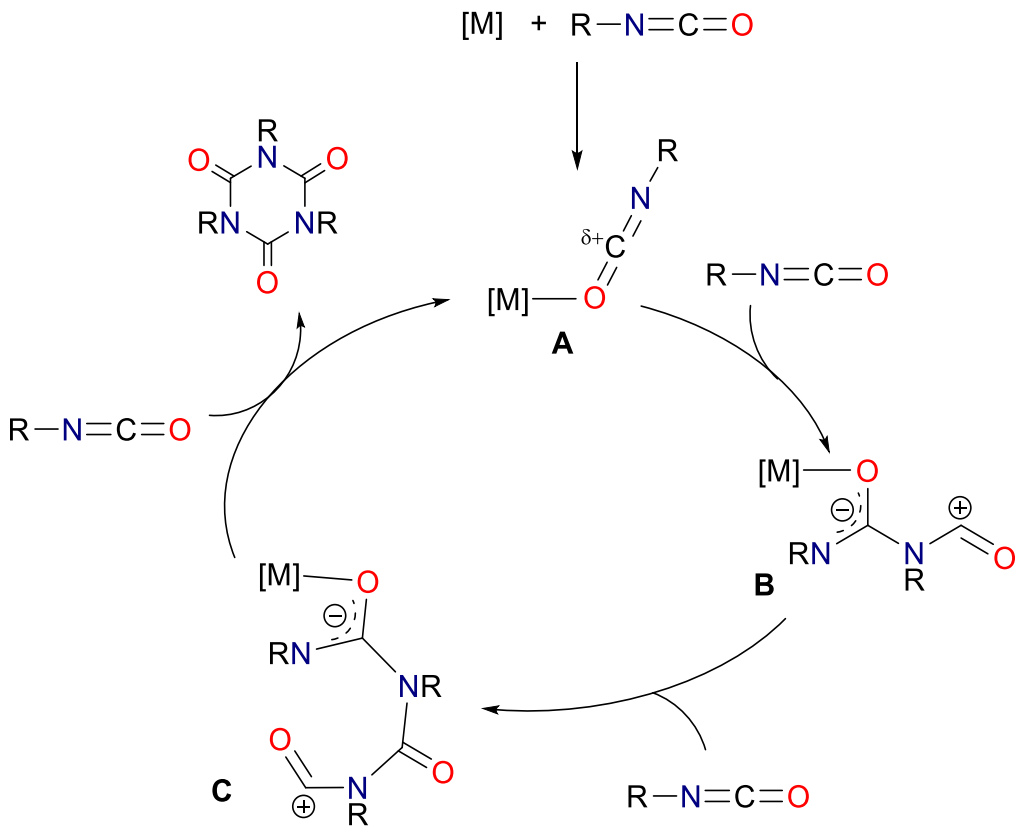
Figure 3.4 Conversion (%) vs. time (h) for the cyclotrimerisation of n-PrNCO with 5 mol% of 15 at room temperature (top) and 10 at 60 °C (bottom) in C_6D_6

followed simultaneously by ^{1}H NMR. The rate of the reaction catalysis was found to be unaffected further supporting the theory of a homogenous mechanism. The catalysis was also carried out in the presence of the radical trap cumene where two samples of **15** (5 mol%) and *n*-propyl isocyanate in C_6D_6 were prepared with one containing an excess of cumene. The reactions were followed simultaneously by ^{1}H NMR and were both found to reach >80% conversion after 7 h at room temperature with no observable decrease in reaction rate leading to the conclusion that the reaction is not radical mediated.

3.3.5.1 Proposed Mechanism

With the experimental observations indicating that the catalytic cyclotrimerisation of primary aliphatic isocyanates is homogeneous and not radical mediated this led to the proposed mechanism as shown in Scheme 3.2. Considering the inherent coordinative unsaturated nature and the +II oxidation state of the precatalysts **10**, **11**, **15** and **16**, it is reasonable to assume that the precatalysts act as Lewis acids,[52] in a similar manner to that postulated for Yb complexes.[25] Initially, the isocyanate coordinates to the metal centre to give **A** where this coordination renders the carbon atom of the isocyanate more electrophilic. Following this, an outer-sphere attack of the nucleophilic nitrogen of an incoming isocyanate at the electropositive carbon yields intermediate **B**.[30,53] Subsequently, nucleophilic attack of a free isocyanate on the coordinated linear dimer (**B**) results in the formation of **C**. Finally, ring closure to give the cyclotrimer, which is displaced by a new isocyanate moiety therefore regenerating the catalyst **A**. Previous calculations on a Pd(0) cyclotrimerisation catalyst by Paul *et al.* have found that the C=N coordination mode is slightly more stable than C=O, but both states lie close in energy.[31] This coordination renders the carbon atom more electrophilic. It is also proposed that the

coordination of the isocyanate to the metal centre results in an increase of the nucleophilic character of the coordinated isocyanate. Therefore, the stepwise formation of the cyclotrimer would take place by nucleophilic attack of the coordinated isocyanate onto a free isocyanate.[31]



Scheme 3.2 Proposed catalytic cycle for the cyclotrimerisation of isocyanates catalysed by Mn(II) (10 and 15) and Fe(II) (11 and 16) complexes.

It could also be possible that the mechanism operates through a metallacyclic intermediate where upon two isocyanate molecules coordinate to the metal centre, dimerise and form a metallacycle though an oxidative coupling reaction. A successive concerted oxidative coupling of another isocyanate followed by reductive elimination yields the cyclotrimer.[31] This process would require the oxidation state of metal to change from M(II) to M(IV) which seems unlikely to occur in these systems due to the already electron deficient Mn and Fe metal centres.

The proposed mechanism is consistent with the substantial difference in the catalytic activity of the manganese and iron complexes which is most probably due to the more Lewis acidic manganese(II) centre compared to the iron(II) centre.

3.3.5.2 Cyclotrimerisation with Mixed Isocyanates

The mechanism proposed in Scheme 3.2 suggests that the steric demands about the metal centre decrease as the linear chain grows further away. Therefore, it should be possible for the unreactive isocyanates (aryl and secondary or tertiary alkyl isocyanates, see Table 3.5) to react after the coordination of the first or second isocyanate (Scheme 3.2, intermediates **B** and **C**) producing mixed cyclotrimers. Preliminary cross coupling reactions were carried out with isocyanate mixtures (Table 3.2) with precatalyst **10** (5 mol%) in C_6D_6 at room temperature. After 16 h the ^{1}H NMR spectra showed multiple resonances suggesting formation of mixed cyclotrimers which was confirmed by subsequent GC-MS measurements of the reaction mixtures (Table 3.7 and Table 3.8). The reaction of ethyl and *p*-tolyl isocyanate (1:2) yielded mixed trimers with some selectivity with the isocyanurate $(EtNCO)_2(^pTolNCO)$ being the major product with a large amount of unreacted ^{p}TolNCO in the reaction mixture.

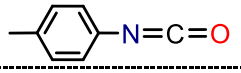
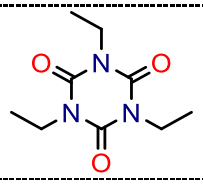
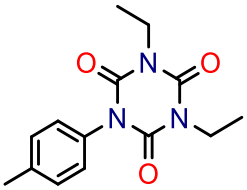
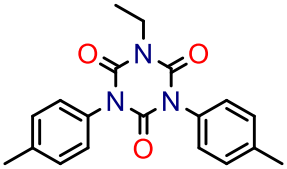
Entry	*Compound*	*m/z*	*Normalised Area (%) EtNCO:^{p}TolNCO*	
			1:2	*2:1*
1		133.05	66	12
2		213.11	7	51
3		275.13	17	33
4		337.14	10	4

Table 3.7 GC-MS results for the reaction of EtNCO with ^{p}TolNCO (1:2 and 2:1 ratio) with 10 (5 mol%).

Furthermore, when ethyl isocyanate was in excess (2:1) the isocyanurate $(EtNCO)_3$ was the major product. There was no formation of the isocyanurate $(^{p}TolNCO)_3$ observed in both cases. The reaction of ethyl and *iso*-propyl isocyanate in either 1:2 or 2:1 molar ratio showed the same trend where triethyl isocyanurate (**19a**) is the major product with decreasing amounts of the mono-, di- and tri-substituted *iso*-propyl isocyanurate (Table 3.8, entries 2-4) with the proportion of the mixed isocyanurates being higher when *iso*-propyl isocyanate was in excess. Note that *n*-propyl isocyanate eluted along with the solvent and therefore was not seen in the GC-MS trace. The presence of the more reactive monomer in this case does not promote the formation of $(^{p}TolNCO)_3$ or $(^{i}PrNCO)_3$ which has been previously been observed by Moritsugu and co-workers with mixed isocyanate systems.[4]

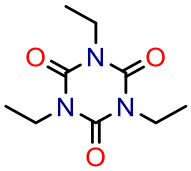
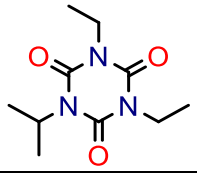
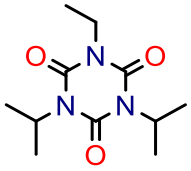
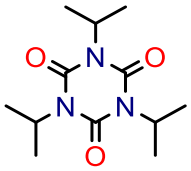
Entry	***Compound***	***m/z***	***Normalised Area (%) EtNCO:^{i}PrNCO***	
			1:2	***2:1***
1		213.11	88	64
2		227.16	10	29
3		241.18	>1	6
4		255.19	>0.1	1

Table 3.8 GC-MS results for the reaction of EtNCO with ^{i}PrNCO (1:2 and 2:2 ratio) with 10 (5 mol%).

3.3.5.3 Kinetic Studies

Kinetic experiments for reagent order determination were performed at variable concentrations of precatalyst (**10**) and isocyanate (EtNCO), whilst keeping the other reagent concentration constant. The samples were prepared by cooling the precatalyst (**10**) in C_6D_6 to –30 °C then adding the isocyanate and quickly cooling the reaction mixture to –78 °C to prevent the reaction from initiating. The samples were transferred into the NMR spectrometer and monitored *in situ* by ^{1}H NMR at 25 °C and the ethyl isocyanate concentration was obtained *via* monitoring the CH_2 signal from the starting isocyanate relative to the isocyanurate. The initial rates of the reaction were derived from least squares fit from the plot of ethyl isocyanate concentration *vs.* time for various precatalyst concentrations and ethyl isocyanate concentration (Figure 3.5) and are shown in Table 3.9. The plot of ln(initial reaction rate) *vs.* ln(concentration) for precatalyst **10** and ethyl isocyanate (Figure 3.6) shows a first-order relationship with respect to both precatalyst and ethyl isocyanate concentration.

Entry	***[10] mM***	***Rate mMmin^{-1}***
1	9.78	1.61
2	14.7	3.49
3	19.5	4.18
4	24.5	5.63
5	29.3	6.13

Entry	***[EtNCO] M***	***Rate mMmin^{-1}***
1	0.4	4.26
2	0.5	5.18
3	0.6	6.24
4	0.7	6.25
5	0.8	7.22

Table 3.9 Initial rates obtained when concentration of 10 (left) and ethyl isocyanate concentration (right) is varied in C_6D_6 (0.6 mL) at 25 °C.

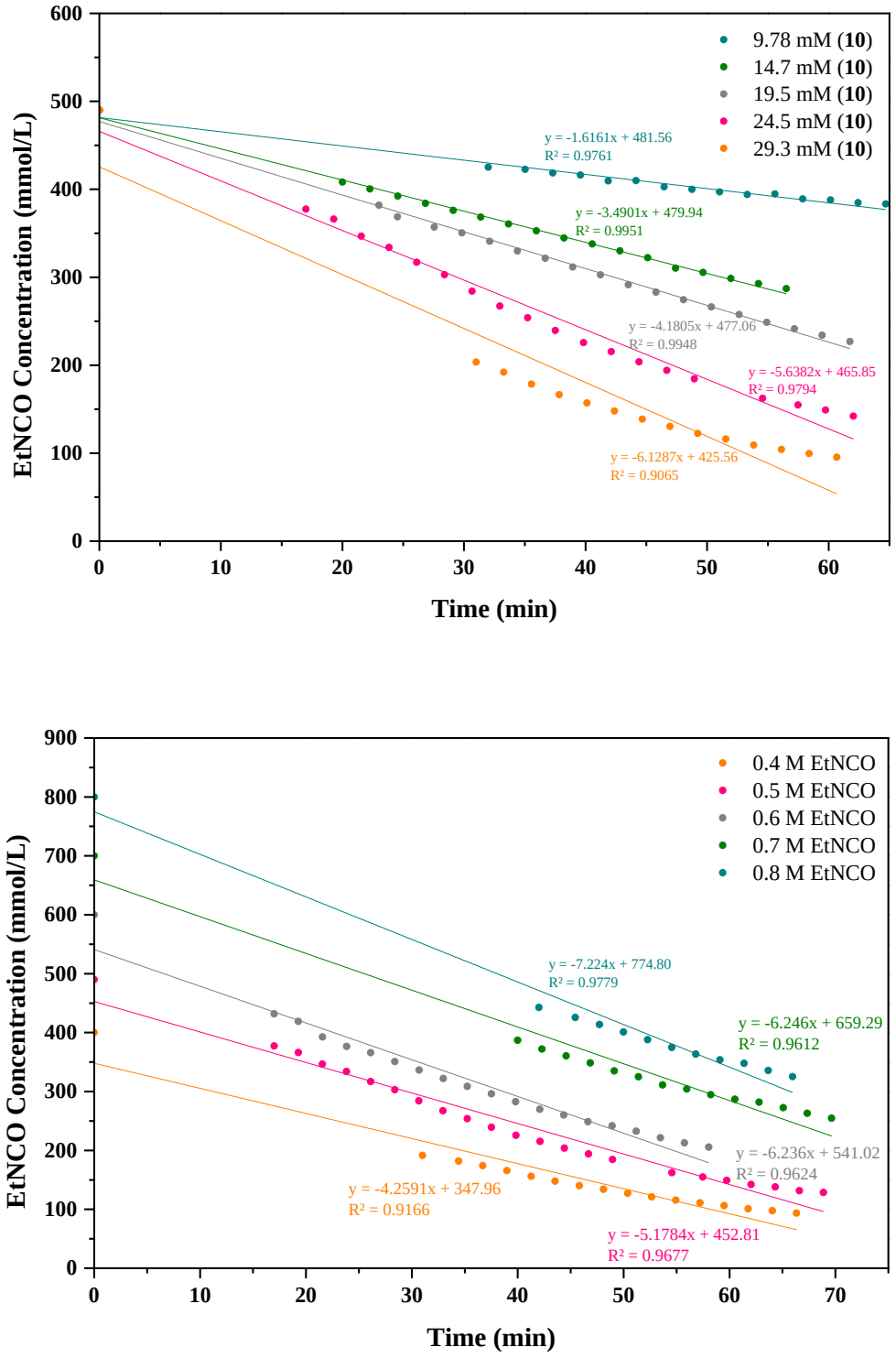


Figure 3.5 Initial rate graphs of EtNCO concentration vs. time when catalyst concentration 10 is varied (top) and when EtNCO concentration is varied (bottom).

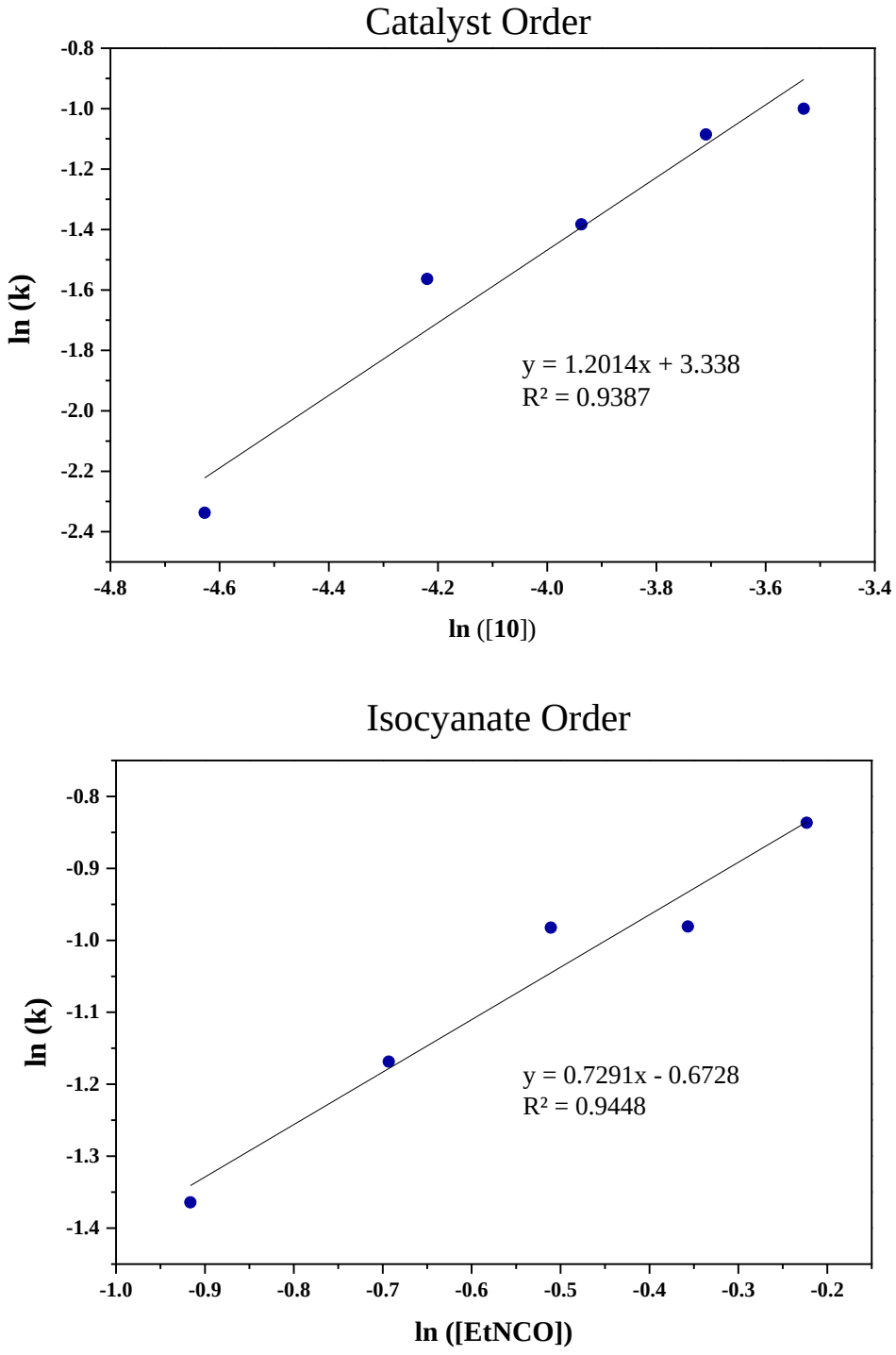


Figure 3.6 Plot of ln(initial rate) vs. ln(concentration) when precatalyst concentration 10 is varied (top) and when EtNCO concentration is varied (bottom) both showing first-order kinetics.

3.4 Conclusions

Two- and three-coordinate Mn(II) and Fe(II) *m*-terphenyl complexes **10**, **11**, **15**, and **16** were found to be efficient precatalysts for the cyclotrimerisation of primary aliphatic isocyanates under mild conditions. The rate of the reaction decreased as the chain length of the primary alkyl isocyanate increased (ethyl, *n*-propyl, *n*-hexyl) and was found necessary to heat the reaction to 60 °C to achieve high conversions after 14 h. Initial assessments of other two-coordinate *m*-terphenyl complexes (**12** and **14**) were found to perform inferior than the aforementioned complexes and were therefore not assessed further.

The scope of the reaction was extended to secondary and tertiary aliphatic isocyanates and aromatic isocyanates using precatalysts **10** and **11** but were not successful even after heating the reaction mixtures at temperatures upwards of 50 °C for 48 h. *In situ* IR spectroscopy studies on a stoichiometric reaction of the iron precatalyst **11** and 3,5-dimethoxyphenyl isocyanate suggested the formation of an Fe-amidate species resulting from the insertion of the 3,5-dimethoxyphenyl isocyanate into the Fe–C bond. This complex prevents formation the active catalyst (Scheme 3.2, **A**) therefore inhibiting the cyclotrimerisation of the isocyanate thus providing an insight into the apparent lack of catalytic activity when using aryl isocyanates. Subsequent hydrolysis of this compound allowed for the isolation of the novel amide species **20** further supporting the proposed formation of the Fe-amidate species.

Experimental observations suggested that the catalysis is homogeneous, not radical mediated and most likely proceeds *via* a Lewis acid type mechanism with coordination of an isocyanate to the metal centre which undergoes successive addition of an external isocyanate. Preliminary results with isocyanate mixtures showed the formation of mixed

isocyanurates, further supporting the proposed mechanism, with possibility of the selective synthesis of cross-coupled isocyanurates.

Kinetic experiments were performed at variable concentrations of precatalyst (**10**) and isocyanate (EtNCO) and using the initial rates method, analysis of the rate order reveals first-order behaviour with respect to both the precatalyst and the isocyanate.

3.5 Future Work

DFT calculations on the mechanism would be of utmost importance to help elucidate which coordination mode between the isocyanate to the transition metal centre is more favourable (C=N *vs.* C=O). It could also be possible that the coordinated isocyanate is more nucleophilic and therefore attacks an external isocyanate as suggested by Paul *et al.* with Pd(0) complexes.[31] These calculations could also provide an insight into why the isocyanurate is obtained from the reaction mixture and not any other cyclic oligomers: $(RNCO)_n$ (where n = 2, 4, 5 *etc.*), or a linear chain polymer. Calculations could also confirm that the formation of an metal-amido species is energetically more favourable than the coordination of the isocyanate to the transition metal centre when using secondary, tertiary or aromatic isocyanates.

The scope of the reaction with isocyanates mixes could be explored further with other isocyanates in different ratios in the presence of various precatalysts to produce mixed/asymmetric isocyanurates. These asymmetrically-substituted isocyanurates have been shown to be of interest through their pharmaceutical and agricultural utility.[11,12]

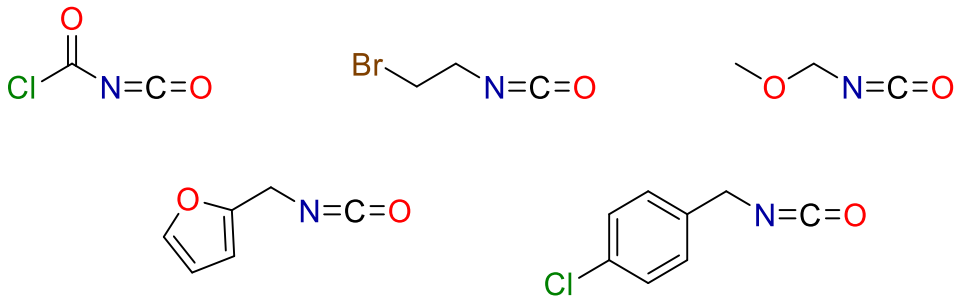


Figure 3.7 Commercial isocyanates containing heteroatoms.

As this catalysis has been shown to be successful in the cyclotrimerisation of primary aliphatic isocyanates, it would be beneficial to investigate whether the reaction is heteroatom tolerant (Figure 3.7). Expanding up on this, it would also be interesting to investigate whether these two- and three-coordinate precatalysts are effective for the

cyclotrimerisation of isothiocyanates (RNCS) or alkynes of which have great importance in drug development,[54] biological molecular recognition[55] and energetic materials.[56]

3.6 References

1 J. M. Kenny, L. Torre and L. M. Chiacchiarelli, *J. Appl. Polym. Sci.*, 2015, **132**, 42750–42750.

2 G. Wegener, M. Brandt, L. Duda, J. Hofmann, B. Klesczewski, D. Koch, R. J. Kumpf, H. Orzesek, H. G. Pirkl, C. Six, C. Steinlein and M. Weisbeck, *Appl. Catal. A Gen.*, 2001, **221**, 303–335.

3 M. Sun, X. Zhang, W. Chen and L. Feng, *J. Appl. Polym. Sci.*, 2016, **133**, 43327.

4 M. Moritsugu, A. Sudo and T. Endo, *J. Polym. Sci. A*, 2013, **51**, 2631–2637.

5 M. Moritsugu, A. Sudo and T. Endo, *J. Polym. Sci. A*, 2012, **50**, 4365–4367.

6 T. S. Leu, *J. Appl. Polym. Sci.*, 2006, **102**, 2470–2480.

7 M. S. Khajavi, M. G. Dakamin and H. Hazarkhani, *J. Chem. Res.*, 2000, 145–147.

8 Y. Zhang, S. N. Riduan and J. Y. Ying, *Chem. Eur. J.*, 2009, **15**, 1077–1081.

9 E. Preis, N. Schindler, S. Adrian and U. Scherf, *ACS Macro Lett.*, 2015, **4**, 1268–1272.

10 M. Mascal, I. Yakovlev, E. B. Nikitin and J. C. Fettinger, *Angew. Chem. Int. Ed.*, 2007, **46**, 8782–8784.

11 A. Bosco, L. Rinaldi, G. Cappelli, A. Saratsis, L. Nisoli and G. Cringoli, *Vet. Parasitol.*, 2015, **212**, 408–410.

12 P. Gibbons, D. Love, T. Craig and C. Budke, *Vet. Parasitol.*, 2016, **218**, 1–4.

13 J. Tang, T. Mohan and J. G. Verkade, *J. Org. Chem.*, 1994, **59**, 4931–4938.

14 A. P. Murray, M. J. Miller and N. S. Hall, *J. Org. Chem.*, 2003, **68**, 191–194.

15 G. Argouarch, R. Veillard, T. Roisnel, A. Amar, H. Meghezzi, A. Boucekkine, V. Hugues, O. Mongin, M. Blanchard-Desce and F. Paul, *Chem. Eur. J.*, 2012, **18**, 11811–11827.

16 Y. Taguchi, I. Shibuya, T. Tsuchiya and K. Yonemoto, *Bull. Chem. Soc. Jpn.*, 1990, **63**, 3486–3489.

17 D. Heift, Z. Benkő, H. Grützmacher, A. R. Jupp and J. M. Goicoechea, *Chem. Sci.*, 2015, **6**, 4017–4024.

18 J. N. Gibb and J. M. Goodman, *Org. Biomol. Chem.*, 2013, **11**, 90–7.

19 S. M. Raders and J. G. Verkade, *J. Org. Chem.*, 2010, **75**, 5308–5311.

20 J. Tang and J. G. Verkade, *Angew. Chem. Int. Ed.*, 1993, **32**, 896–898.

21 Z. Pusztai, G. Vlád, A. Bodor, I. T. Horváth, H. J. Laas, R. Halpaap and F. U. Richter, *Angew. Chem. Int. Ed.*, 2006, **45**, 107–110.

22 H. A. Duong, M. J. Cross and J. Louie, *Org. Lett.*, 2004, **6**, 4679–4681.

23 W. Yi, J. Zhang, L. Hong, Z. Chen and X. Zhou, *Organometallics*, 2011, **30**, 5809–5814.

24 X. Zhu, J. Fan, Y. Wu, S. Wang, L. Zhang, G. Yang, Y. Wei, C. Yin, H. Zhu, S. Wu and H. Zhang, *Organometallics*, 2009, **28**, 3882–3888.

25 W. Wong, L. Zhang, W. Wong, F. Xue and T. C. W. Mak, *J. Am. Chem. Soc., Dalton. Trans.*, 1999, 615–622.

26 M. K. Barman, A. Baishya, T. Peddarao and S. Nembenna, *J. Organomet. Chem.*, 2014, **772**–**773**, 265–270.

27 L. Orzechowski and S. Harder, *Organometallics*, 2007, **26**, 2144–2148.

28 S. R. Foley, Y. Zhou, G. P. A. Yap and D. S. Richeson, *Inorg. Chem.*, 2000, **39**, 924–929.

29 S. R. Foley, G. P. A. Yap and D. S. Richeson, *Organometallics*, 1999, **18**, 4700–4705.

30 S. G. Lee, K.-Y. Choi, Y.-J. Kim, S. Park and S. W. Lee, *Dalton Trans.*, 2015, **44**, 6537–6545.

31 S. Moulin, O. Piechaczyk, P. Le Floch, J. A. Osborn and F. Paul, *J. Am. Chem. Soc.*, 2007, **129**, 7294–7304.

32 J. F. Villa and H. B. Powell, *Syn. React. Inorg. Met. Org. Chem.*, 1976, **6**, 59–63.

33 M. I. Lipschutz, T. Chantarojsiri, Y. Dong and T. D. Tilley, *J. Am. Chem. Soc.*, 2015, **137**, 6366–6372.

34 G. Ung and J. C. Peters, *Angew. Chem. Int. Ed.*, 2015, **54**, 532–535.

35 M. I. Lipschutz and T. D. Tilley, *Angew. Chem. Int. Ed.*, 2014, **53**, 7290–7294.

36 J. Yang and T. D. Tilley, *Angew. Chem. Int. Ed.*, 2010, **49**, 10186–10188.

37 D. A. Valyaev, G. Lavigne and N. Lugan, *Coord. Chem. Rev.*, 2016, **308**, 191–235.

38 J. R. Carney, B. R. Dillon and S. P. Thomas, *Eur. J. Org. Chem.*, 2016, 3912–3929.

39 B. Su, Z. C. Cao and Z. J. Shi, *Acc. Chem. Res.*, 2015, **48**, 886–896.

40 S. Enthaler, K. Junge and M. Beller, *Angew. Chem. Int. Ed.*, 2008, **47**, 3317–3321.

41 M. Ozaki, Y. Obora, Y. Tada and Y. Ishii, *J. Organomet. Chem.*, 2013, **741**–**742**, 109–113.

42 A. Kumar, S. De, A. G. Samuelson and E. D. Jemmis, *Organometallics*, 2008, **27**, 955–960.

43 Y. Yamamoto and A. Wojcicki, *J. Chem. Soc., Chem. Commun.*, 1972, 1088–1089.

44 W. J. Evans, J. R. Walensky and J. W. Ziller, *Organometallics*, 2010, **29**, 945–950.

45 P. Braunstein and D. Nobel, *Chem. Rev.*, 1989, **89**, 1927–1945.

46 C.-J. F. Du, H. Hart and K.-K. D. Ng, *J. Org. Chem*, 1986, **51**, 3162–3165.

47 Y. Liu, Y. Zhang, M. Huang and J.-P. Wan, *RSC Adv.*, 2015, **5**, 46192–46196.

48 Y. Kametani, T. Satoh, M. Miura and M. Nomura, *Tetrahedron Lett.*, 2000, **41**, 2655–2658.

49 H. Adams, P. L. Bernad, G. A. Hembury, C. A. Hunter, J. F. McCabe, D. S. Eggleston, R. C. Haltiwanger, D. J. Livingstone, K. D. M. Harris and B. M. Kariuki, *Chem. Commun.*, 2001, 1500–1501.

50 A. A. Mikhailine, M. I. Maishan, A. J. Lough and R. H. Morris, *J. Am. Chem. Soc.*, 2012, **134**, 12266–12280.

51 J. A. Widegren and R. G. Finke, *J. Mol. Catal. A Chem.*, 2003, **198**, 317–341.

52 M. D. Greenhalgh, A. S. Jones and S. P. Thomas, *ChemCatChem*, 2015, **7**, 190–222.

53 A. K. F. Rahman and K. M. Nicholas, *Tetrahedron Lett.*, 2007, **48**, 6002–6004.

54 T. J. Ritchie, S. J. F. MacDonald, R. J. Young and S. D. Pickett, *Drug Discov. Today*, 2011, **16**, 164–171.

55 L. M. Salonen, M. Ellermann and F. Diederich, *Angew. Chem. Int. Ed.*, 2011, **50**, 4808–4842.

56 L. Türker and S. Variş, *Polycycl. Aromat. Compd.*, 2009, **29**, 228–266.

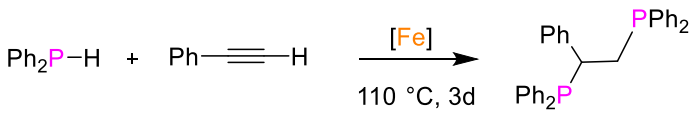
Chapter IV

Hydrophosphination of Isocyanates

4.1 Introduction

Organophosphorus compounds are a vital class of chemicals with extensive applications such as organocatalysis, as ligands for transition metal complexes, and as building blocks for medicinal and supramolecular chemistry.[1,2] Classic synthetic methodologies for phosphine preparation have major drawbacks; including poor functional group tolerance, side-product formation, the use of protecting groups and stoichiometric amounts of additives, which is a significant disadvantage for atom economy.[3] Hence, there is a growing requirement to develop atom-economical routes in the preparation of functionalised phosphines.

Hydrophosphination reactions are an attractive synthetic route to phosphine products, proceeding *via* P–H bond addition across a C–C/X (X = O, N, S) multiple bond.[4–6] This reaction can be synthetically challenging as a result of the coordination capability of both starting phosphine and products to the soft metal centre thereby inhibiting the catalyst. This issue is a significance challenge in the double hydrophosphination of alkynes whereby the reaction product binds stronger than a monodentate ligand because of the chelate effect. Nakazawa and co-workers circumvented this issue by utilising precatalysts with a hard iron(II) centre in thereby preventing product coordination to the catalyst (Scheme 4.1).[7]



Scheme 4.1 The first catalytic double hydrophosphination of alkynes using iron(II) precatalysts ([Fe]).[7]

The hydrophosphination of olefins and alkynes has been extensively explored in the last decade, [5,8–15] whereas the hydrophosphination of heterocumulene substrates has been less explored, with examples of precatalysts for these reactions limited to rare-earth,[16–23] alkali

metal,[24] and group 2 complexes.[25,26] The hydrophosphination of organic isocyanates, yielding phosphinocarboxamide products, are limited to a few recent examples, all of which are catalysed by f-block or rare earth complexes as shown in Figure 4.1.[16,17,19,21] A significant issue with the hydrophosphination of isocyanates is that of competing side reactions, such as the cyclotrimerisation of isocyanates to isocyanurates and catalyst incompatibility towards heteroatom-containing substrates. This has been documented for the hydrophosphination of aromatic isocyanate substrates using a yttrium precatalyst (Figure 4.1, bottom left).[19]

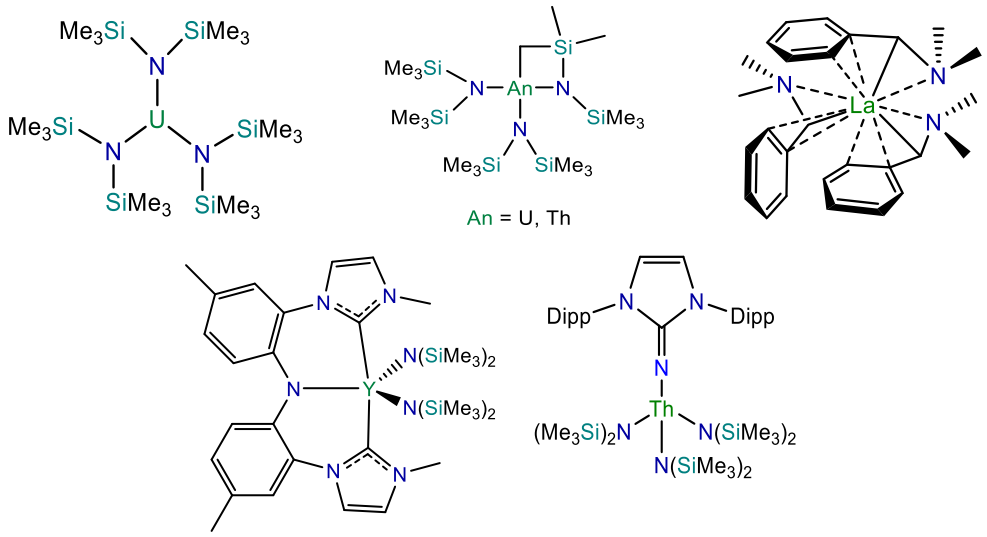


Figure 4.1 Rare earth and f-block precatalysts for the hydrophosphination of isocyanates in the literature.[16,17,19,21]

This chapter explores the catalytic activity of two and three coordinate iron(II) *m*-terphenyl complexes in hydrophosphination of isocyanates producing phosphinocarboxamides, and the diinsertion product, phosphino*di*carboxamides, a new family of derivatised phosphines currently absent in the literature. Preliminary assessments in the coordination chemistry of the novel phosphinodicarboxamides is also explored with dichloro(*p*-cymene) ruthenium dimer.

4.2 Experimental

4.2.1 Standard Procedure for the Catalytic Hydrophosphination of Isocyanates

In a Young's NMR tube 5 mol% of the precatalyst (**11**: 10.0 mg, 0.0147 mmol; **16**: 10.0 mg, 0.0132 mmol) was dissolved in C_6D_6 (0.6 mL) with the corresponding isocyanate and Ph_2PH (1:1 or 2:1 of RNCO:Ph_2PH). The reaction was either carried out at room temperature and monitored by ^1H and $^{31}P\{^1H\}$ NMR spectroscopy or heated to 60 °C; the samples were maintained at 60 °C for 16 h and ^1H and $^{31}P\{^1H\}$ NMR spectroscopy were performed at the final time. Conversion was quantified by integration of ^1H and $^{31}P\{^1H\}$ NMR spectra. For the catalysis with 2 mol% (**11**: 5.0 mg, 0.00733 mmol; **16**: 5.0 mg, 0.00662 mmol) and 0.5 mol% (**11**: 5.0 mg, 0.00733 mmol) of precatalyst **11** and **16** were used.

4.2.2 Standard Procedure for in situ NMR Reaction Monitoring for the Catalytic Hydrophosphination of Isocyanates

In a Young's NMR tube 5 mol% of precatalyst (**11**: 10.0 mg, 0.0147 mmol; **16**: 10.0 mg, 0.0132 mmol) were dissolved in C_6D_6 (0.6 mL) with the corresponding isocyanate. The solution was cooled to –30 °C after which the phosphine was added and the sample cooled to –78 °C to prevent the reaction from initiating. The sample was transferred to the NMR spectrometer and monitored directly at 25 °C or heated to 60 °C. Conversion was quantified by integration of ^1H and $^{31}P\{^1H\}$ NMR spectra.

4.2.3 Standard Procedure for the Catalytic Hydrophosphination of Isocyanates in THF

In a Young's NMR tube 5 mol% of the precatalyst (**11**: 10.0 mg, 0.0147 mmol) was dissolved in THF (0.6 mL) with the corresponding isocyanate (0.293 mmol) and Ph_2PH (51 µL, 0.293 mmol) with a C_6D_6 insert. The reaction was either carried out at room temperature or heated to 60 °C and monitored by ^1H and $^{31}P\{^1H\}$ NMR spectroscopy. Conversion was quantified by integration of the $^{31}P\{^1H\}$ NMR spectrum.

4.2.4 Catalytic Hydrophosphination of Isocyanates with Additives

4.2.4.1 In situ NMR Reaction Monitoring for the Catalytic Hydrophosphination of Isocyanates with Additives

In a Young's NMR tube 5 mol% of the precatalyst **11** (10.0 mg, 0.0147 mmol) was dissolved in C_6D_6 (0.6 mL) with CyNCO (38 µL, 0.294 mmol) and the corresponding additive (see Table 4.1 below). The solution was cooled to –30 °C after which Ph_2PH (51 µL, 0.294 mmol) was added and the sample cooled to –78 °C to prevent the reaction from initiating. The sample was then transferred to the NMR spectrometer and monitored directly at 25 °C. Conversion was quantified by integration of ^1H and $^{31}P\{^1H\}$ NMR spectra.

Additive	***Quantity***
CS_2 (0.05 M in toluene)	29 µL, 0.00147 mmol
Hg	*ca.* 1 drop
Cumene	10 µL, 0.0735 mmol

Table 4.1 Additive and quantities used in the in situ NMR reaction monitoring experiments.

4.2.4.2 Catalytic Hydrophosphination of Isocyanates with Weak Base/Acid

In a Young's NMR tube 5 mol% of the precatalyst **11** (10.0 mg, 0.0147 mmol), the corresponding isocyanate, Ph_2PH (51 µL, 0.294 mmol) and the additive (see Table 4.2 below) were dissolved in C_6D_6 (0.6 mL). The reactions were kept at room temperature and monitored by ^1H and $^{31}P\{^1H\}$ NMR at the final time. Conversion was quantified by integration of ^1H and $^{31}P\{^1H\}$ NMR spectra.

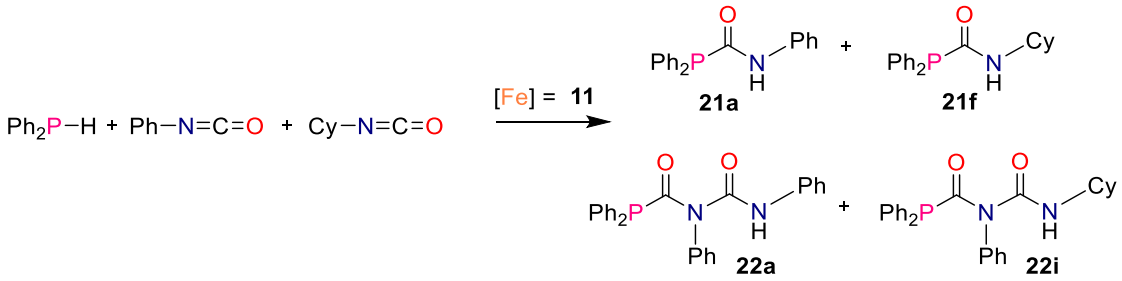
Additive	***RNCO***		***Solvent***	***Time (h)***	***Conv. (%)***
NEt_3 (41 µL, 0.294 mmol)	3,5-$(OMe)_2$ C_6H_3	(105 mg, 0.588 mmol)	C_6D_6 (0.6 mL)	16	>99
$Et_3N{\cdot}HCl$ (40.4 mg, 0.294 mmol)	3,5-$(OMe)_2$ C_6H_3	(105 mg, 0.588 mmol)	C_6D_6 (0.6 mL), THF-d_8 (*ca.* 2 drops)	16	>99
	3,5-$(OMe)_2$ C_6H_3	(105 mg, 0.588 mmol)	C_6D_6 (0.6 mL), THF-d_8 (*ca.* 2 drops)	16	19
	Ph	(64 µL, 0.588 mmol)	C_6D_6 (0.6 mL), THF-d_8 (*ca.* 2 drops)	16	>99
	Cy	(75 µL, 0.588 mmol)	C_6D_6 (0.6 mL), THF-d_8 (*ca.* 2 drops)	48	0

Table 4.2 Additive and quantities used in the catalytic hydrophosphination of isocyanates with a weak base (NEt_3) or weak acid ($Et_3N{\cdot}HCl$).

4.2.5 Hydrophosphination with Isocyanate Mixtures

In a Young's NMR tube 5 mol% of the precatalyst (**11**: 10.0 mg, 0.0147 mmol) was dissolved in C_6D_6 (0.6 mL) in a glove box with Ph_2PH (51 µL, 0.293 mmol), PhNCO (32 µL, 0.293 mmol) and CyNCO (37 µL, 0.293 mmol). The reaction was carried out at room temperature and monitored by ^1H and $^{31}P\{^1H\}$ NMR spectroscopy. After 16 h at room temperature catalysis was completed (>99% conversion) and the formation of **21a**, **21f**, **22a** and **22i** was observed by NMR with a ratio of 26/27/30/17 (**21a**/**21f**/**22a**/**22i**).

Selected spectroscopic data for phosphinocarboxamide **22i**: ^{1}H NMR (400 MHz, C_6D_6, 25 ºC): δ 9.22 (s, 1H, N*H*), 7.63-6.82 (Ar), 3.93 (CH_2), 1.97-1.87 (m, CH_2), 1.49-1.45 (m, CH_2), 1.18 (m, CH_2), 1.11-1.04 (m, CH_2). ^{31}P{^{1}H} NMR (162 MHz, C_6D_6, 25 ºC): δ 7.8 (s, 1P, Ph_2P). MS (ESI) *m/z*: calcd. $C_{26}H_{28}N_2O_2P$ $[M+H]^+$ 431.1883, found: 431.1883 (err [ppm] = 0.1).



Scheme 4.2 Hydrophosphination of mixture of phenyl and cyclohexyl isocyanate with diphenylphosphine (1:1:1) using 11. A combination of four products are obtained 21a/21f/22a/22i

4.2.6 Scale up of Hydrophosphination Products 21 and 22

4.2.6.1 Synthesis of 21a, c, and d

5 mol% of **11** (30.0 mg, 0.0441 mmol), Ph_2PH (153 µL, 0.880 mmol) and the isocyanate (0.880 mmol) were dissolved in THF (1.5 mL) and stirred at 60 °C for 3 days (**21a** and **21c**) or 2 days (**21d**). The solvent was removed *in vacuo* and the solid was washed with cold *iso*-hexane (3 × 5 mL) and dried under vacuum affording the corresponding pure phosphinocarboxamide as a white powder (**21a**: 190 mg, 71%; **21c**: 184 mg, 57%; **21d**: 217 mg, 64%).

4.2.6.2 Synthesis of 21f-h

5 mol% of **11** (30.0 mg, 0.0441 mmol), Ph_2PH (153 µL, 0.880 mmol) and the isocyanate (0.880 mmol) were dissolved in toluene (5 mL) and stirred at room temperature (**21f**) or at 60 °C (**21g** and **21h**) for 16 h. The solvent was removed *in vacuo* and the oily residue was extracted into *n*-pentane (2 × 10 mL) and stored at –30 °C for one day. This resulted in the precipitation of white crystalline solid of the corresponding pure phosphinocarboxamide (**21f**: 153 mg, 56%; **21g**: 137 mg, 57%; **21h**: 168 mg, 67%).

4.2.6.3 Synthesis of 22a-d

5 mol% of **11** (30.0 mg, 0.0441 mmol), Ph_2PH (153 µL, 0.880 mmol) and the isocyanate (1.76 mmol) were dissolved in toluene (5 mL) and stirred at room temperature for 16 h. The solvent was removed *in vacuo* and the oily residue was washed with *n*-pentane (2 × 10 mL) and dried for *ca.* 6 h. enabling the isolation of the corresponding pure phosphinodicarboxamide (**22a**: 186 mg, 50%; **22b**: 220 mg, 55%; **22c**: 304 mg, 65%, **22d**: 406 mg, 79%).

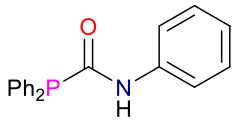
4.2.6.4 Large Scale Synthesis of 22a

5 mol% of **11** (102 mg, 0.150 mmol), Ph_2PH (522 µL, 3.00 mmol), PhNCO (653 µL, 6.00 mmol) and $Et_3N{\cdot}HCl$ (404 mg, 2.93 mmol) were dissolved in toluene (6 mL) and stirred at room temperature for 16 h. The solvent was removed *in vacuo* and the product was extracted into toluene (20 mL) and the solvent removed yielding a white solid which was dried for *ca.* 3 h. The solid was washed with *iso*-hexane (3 × 10 mL) and dried for *ca.* 6 h

enabling the isolation of a while solid of the corresponding phosphinocarboxamide (**22a**: 936 mg, 74%).

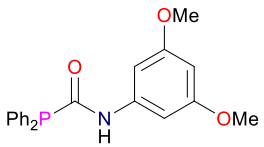
4.2.7 Spectroscopic Data

4.2.7.1 $Ph_2PC(=O)NH(Ph)$ (21a)



White solid: 190 mg, 71%.^{1}H NMR (400 MHz, C_6D_6, 25 ºC): δ 7.64-7.52 (m, 4H, PPh_2^{o}), 7.35 (d, ^{3}J(H,H) = 8.0 Hz, 2H, Ph^{o}), 7.24 (d, ^{3}J(H,P) = 7.6 Hz, 1H, N*H*), 7.07-7.01 (m, 6H, PPh_2^{m+p}), 6.98 (t, ^{3}J(H,H) = 7.9 Hz, 2H, Ph^{m}), 6.82 (t, ^{3}J(H,H) = 7.4 Hz, 1H, Ph^{p}). $^{13}C\{^{1}H\}$ NMR (101 MHz, C_6D_6, 25 ºC): δ 175.2 (d, ^{1}J(C,P) = 15 Hz, *C*=O), 138.5 (Ph^{i}), 134.8 (d, ^{2}J(C,P) =19 Hz, PPh_2^{o}), 134.3 (d, ^{1}J(C,P) = 10 Hz, PPh_2^{i}), 129.9 (PPh_2^{m}), 129.3 (Ph^{m}), 129.2 (PPh_2^{p}), 124.6 (Ph^{p}), 119.4 (Ph^{o}). $^{31}P\{^{1}H\}$ (162 MHz, C_6D_6, 25 ºC) δ –0.2 (s, 1P, Ph_2P). MS (ESI) *m/z*: calcd. for $C_{19}H_{17}NOP$ $[M+H]^+$ 306.1039, found: 306.1042 (err [ppm] = 1.00). IR (ATR) $\bar{\nu}$/cm^{-1} 3244 (N–H), 1645 (C=O). ^{1}H NMR and IR data matched previous reported literature.[21]

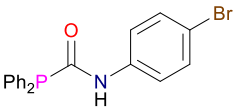
4.2.7.2 $Ph_2PC(=O)NH[3,5\text{-}(OMe)_2C_6H_3]$ (21c)



White solid: 184 mg, 57%.^{1}H NMR (400 MHz, C_6D_6, 25 ºC): δ 7.57 (td, ^{3}J(H,H) = 6.9, ^{3}J(H,P) = 6.9, ^{4}J(H,H) = 2.9 Hz, 4H, PPh_2^{o}), 7.37 (s, 1H, N*H*), 7.18-6.94 (m, 6H, PPh_2^{m+p}), 6.91-6.75 (m, 2H, Ph^{Ao}), 6.34 (s, 1H, Ph^{Ap}), 3.27 (s, 6H, O*C*H_3). $^{13}C\{^{1}H\}$ NMR (101 MHz, C_6D_6, 25 ºC): δ 175.5 (d, ^{1}J(C,P) = 16 Hz, *C*=O), 161.8 (Ph^{m}), 140.4 (d, ^{3}J(C,P) = 5 Hz, Ph^{i}), 134.7 (d, ^{1}J(C,P) = 19 Hz, PPh^{i},), 134.2 (d, ^{2}J(C,P) = 11 Hz, PPh_2^{o}), 129.9 (PPh_2^{p}), 129.2 (d, ^{3}J(C,P) = 7 Hz, PPh_2^{m}), 97.9 (Ph^{o}), 97.6 (Ph^{p}), 55.0 (O*C*H_3). $^{31}P\{^{1}H\}$ (162 MHz,

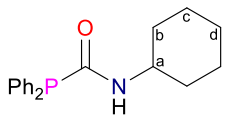
C_6D_6, 25 ºC): δ 0.8 (s, 1P, Ph_2P). MS (ESI) *m/z*: calcd. for $C_{21}H_{21}NO_3P$ $[M+H]^+$ 366.1257, found: 366.1254 (err [ppm] = 1.00). IR (ATR) $\bar{\nu}$/cm^{-1} 3278 (N–H), 1630 (C=O).

4.2.7.3 $Ph_2PC(=O)NH(4\text{-}BrC_6H_4)$ (21d)



White solid: 217 mg, 64%. ^{1}H NMR (400 MHz, C_6D_6, 25 ºC): δ 7.62-7.45 (m, 4H, PPh_2^o), 7.09-7.01 (m, 9H, N*H*, PPh_2^{m+p}, Ph^o), 6.96 (d, ^3J(H,H) = 8.6 Hz, 2H, Ph^m). ^{13}C{^{1}H} NMR (151 MHz, C_6D_6, 25 ºC): δ 175.4 (d, ^1J(C,P) = 16 Hz, *C*=O), 137.3 (Ph^i), 134.8 (d, ^2J(C,P) = 19 Hz, PPh_2^o), 134.0 (d, ^1J(C,P) = 10 Hz, PPh^i), 132.1 (Ph^o), 130.0 (PPh^p), 129.2 (d, ^3J(C,P) = 5 Hz PPh^m), 121.1 (Ph^m), 117.1 (Ph^p). ^{31}P{^{1}H} (162 MHz, C_6D_6, 25 ºC): δ 0.2 (s, 1P, Ph_2P). MS (ESI) *m/z*: calcd. for $C_{19}H_{15}BrNNaOP$ $[M+Na]^+$ 405.9967, found: 405.9966 (err [ppm] = 0.10). IR (ATR) $\bar{\nu}$/cm^{-1} 3244 (N–H), 1645 (C=O). ^{1}H NMR and IR data matched previous reported literature.[21]

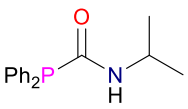
4.2.7.4 $PPh_2C(O)NH(Cy)$ (21f)



White solid: 153 mg, 56%. ^{1}H NMR (800 MHz, C_6D_6, 25 ºC): δ 7.67 (td, ^3J(H,H) = 7.4 Hz, ^3J(H,P) = 1.4 Hz, 4H, PPh_2^o), 7.12-7.02 (m, 6H PPh_2^{m+p}), 5.44 (br d, ^3J(H,P) 4.1 Hz, 1H, N*H*), 3.95 (dddd, *J* = 14.2, 10.2, 7.8, 3.9 Hz, 1H, CH^a), 1.63 (dt, ^2J(H,H) = 12.9 Hz, ^3J(H,H) = 4.3 Hz, 2H, C$H^{b'}$), 1.27 (dt, ^2J(H,H) = 13.7, ^2J(H,H) = 4.2 Hz, 2H, C$H^{c'}$), 1.23 (dt, ^2J(H,H) = 12.8 Hz, ^2J(H,H) = 4.2 Hz, 1H, C$H^{d'}$), 1.07-0.98 (m, 2H, C$H^{c''}$), 0.79 (ddt, ^2J(H,H) = 11.6 Hz, ^2J(H,H) = 11.6 Hz, 3.6, 1H, C$H^{d''}$), 0.74-0.65 (m, 2H, C$H^{b''}$). ^{13}C{^{1}H} NMR (101 MHz,

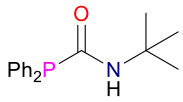
C_6D_6, 25 ºC): δ 174.9 (d, ^1J(C,P) 12 Hz, *C*O), 135.4 (d, ^1J(C,P) = 12 Hz, PPh_2^i), 134.7 (d, ^2J(C,P) = 19 Hz, PPh_2^o), 129.6 (PPh_2^p), 129.0 (d, ^3J(C,P) = 6.6 Hz, PPh_2^m), 48.7 (*C*H), 32.8 (C^bH_2), 25.6 (C^dH_2), 24.7 (C^cH_2). $^{31}P\{^1H\}$ (162 MHz, C_6D_6, 25 ºC): δ –4.3 (s, 1P, Ph_2P). ^{15}N NMR (81 MHz, C_6D_6, 25 ºC): δ 111.2 (1N, *N*H). Elemental analysis for $C_{19}H_{22}NOP$ (311.36): calcd. C 73.29, H 7.12, N 4.50; found: C 73.16, H 7.00, N 4.58. MS (ESI) *m/z*: calcd. for $C_{19}H_{23}NOP$ $[M+H]^+$ 312.1512, found: 312.1526 (err [ppm] = 4.60). IR (ATR) $\bar{\nu}$/cm^{-1} = 3244 (N–H), 1645 (C=O). ^1H NMR and IR data matched previous reported literature.[21]

4.2.7.5 $PPh_2C(O)NH(^iPr)$ (21g)



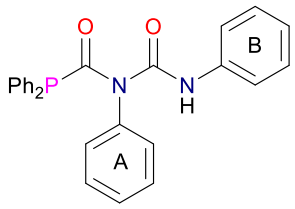
White crystalline solid: 137 mg, 57%. ^1H NMR (800 MHz, C_6D_6, 25 ºC): δ 7.64 (ddd, ^3J(H,H) = 7.5 Hz, ^3J(H,P) = 7.5 Hz, ^4J(H,P) = 1.5 Hz, 4H PPh_2^o), 7.07 (t, ^3J(H,H) = 7.4 Hz, 4H PPh_2^m), 7.06-7.03 (m, 2H, PPh_2^p), 5.35 (s, 1H, N*H*), 4.14 (oct, ^3J(H,H) = 6.8 Hz, 1H, C*H*), 0.72 (d, ^3J(H,H) = 6.6 Hz, 6H, CH_3). $^{13}C\{^1H\}$ (101 MHz, C_6D_6, 25 ºC): δ 175.0 (d, ^1J(C,P) = 13 Hz, *C*O), 135.2 (d, ^1J(C,P) = 12 Hz, PPh_2^i), 134.6 (d, ^2J(C,P) = 19 Hz, PPh_2^o), 129.6 (s, PPh_2^p), 129.0 (d, ^3J(C,P) = 7 Hz, PPh_2^m), 42.1 (*C*H), 22.3 (CH_3). $^{31}P\{^1H\}$ (162 MHz, C_6D_6, 25 ºC): δ –4.0 (s, 1P, Ph_2P).^{15}N NMR (81 MHz, C_6D_6, 25 ºC): δ 113.5 (1N, *N*H). MS (ESI) *m/z*: calcd. for $C_{16}H_{19}NOP$ $[M+H]^+$ 272.1199 found: 272.1205 (err [ppm] = 2.40). IR (ATR) $\bar{\nu}$/cm^{-1} 3258 (N–H), 1641 (C=O).

4.2.7.6 $PPh_2C(O)NH(^tBu)$ (21h)



White crystalline solid: 168 mg, 67%. ^{1}H NMR (800 MHz, C_6D_6, 25 ºC): δ 7.64 (ddd, ^3J(H,H) = 7.5 Hz, ^3J(H,P) = 7.5 Hz, ^3J(H,P) = 1.7 Hz, 4H, PPh_2^o), 7.07 (t, ^3J(H,H) = 7.4 Hz, 4H PPh_2^m), 7.05-7.02 (m, 2H, PPh_2^p), 5.42 (s, 1H, N*H*), 1.12 (s, 9H, C*H*$_3$). ^{13}C{^{1}H} (101 MHz, C_6D_6, 25 ºC): δ 175.3 (d, ^1J(C,P) = 13 Hz, *C*O), 135.6 (d, ^1J(C,P) = 12 Hz, PPh_2^i), 134.6 (d, ^2J(C,P) = 19 Hz, PPh_2^o), 129.5 (s, PPh_2^p), 129.0 (d, ^3J(C,P) = 7 Hz, PPh_2^m), 52.5 (d, ^3J(C,P) = 3 Hz, (*C*(CH$_3$)$_3$), 28.6 (*C*H$_3$). ^{31}P{^{1}H} (162 MHz, C_6D_6, 25 ºC): δ –2.7 (s, 1P, Ph_2P). ^{15}N NMR (81 MHz, C_6D_6, 25 ºC): δ 117.6 (1N, *N*H). Elemental analysis for $C_{17}H_{20}NOP$ (285.327): calcd. C 71.56, H 7.07, N 4.91; found: C 71.63 H 6.93, N 5.01. MS (ESI) *m/z*: calcd for $C_{17}H_{21}NOP$ $[M+H]^+$ 286.1355, found: 286.1372 (err [ppm] = 5.90). IR (ATR) $\bar{\nu}$/cm^{-1} 3310 (N–H), 1632 (C=O).

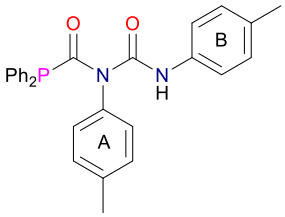
4.2.7.7 $PPh_2C(O)N(Ph)C(O)NH(Ph)$ (22a)



White solid: 186 mg, 50%. ^{1}H NMR (800 MHz, C_6D_6, 25 ºC): δ 11.57 (s, 1H, N*H*), 7.67 (d, ^3J(H,P) = 7.9 Hz, 2H, Ph^{Bo}), 7.31 (t, ^3J(H,P) = 7.8 Hz, ^3J(H,H) = 7.8 Hz, 4H, PPh^o), 7.13-6.97 (m, 8H, PPh_2^{m+p} + Ph^{Bm}), 6.92 (t, ^3J(H,H) = 7.3 Hz, 1H, Ph^{Ap}), 6.87-6.82 (m, 3H, Ph^{Bp} + Ph^{Am}), 6.80 (d, ^3J(H,H) = 7.9 Hz, 2H, Ph^{Ao}). ^{13}C{^{1}H} (101 MHz, C_6D_6, 25 ºC): δ 184.9 (d, ^1J(C,P) = 29 Hz, P*C*=O), 151.2 (*C*=O), 138.7 (Ph^{Bi}), 136.5 (d, ^3J(C,P) = 4 Hz, Ph^{Ai}), 135.1 (d, ^2J(C,P) = 21 Hz, PPh_2^o), 133.3 (d, ^1J(C,P) = 8 Hz, PPh_2^i), 132.3 (d, ^4J(C,P) = 4 Hz, Ph^{Ao}), 129.9 (PPh_2^p), 129.4 (Ph^{Bm}), 129.2 (Ph^{Ap}), 128.8 (PPh_2^m), 128.7 (Ph^{Am}), 124.2 (Ph^{Bp}), 120.1 (Ph^{Bo}). ^{31}P{^{1}H} (162 MHz, C_6D_6, 25 ºC): δ 8.3 (s, 1P, Ph_2P). ^{15}N NMR (81 MHz, C_6D_6, 25 ºC): δ 116.7 (1N, *N*H). MS (ESI) *m/z*: calcd. for

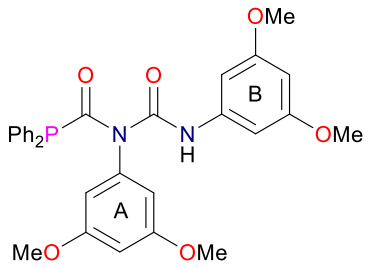
$C_{26}H_{22}N_2O_2P$ $[M+H]^+$ 425.1413, found: 425.1414 (err [ppm] = 0.10). IR (ATR) $\bar{\nu}$/cm^{-1} 3259 (N–H), 1718 (PC=O), 1588 (C=O).

4.2.7.8 $PPh_2C(O)N(^pTol)C(O)NH(^pTol)$ (22b)



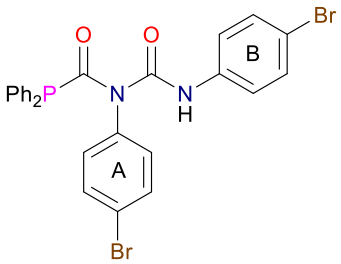
White solid: 220 mg, 55%. ^{1}H NMR (400 MHz, C_6D_6, 25 ºC): δ 11.58 (s, 1H, N*H*), 7.63 (d, ^3J(H,H) = 8.2 Hz, 2H, Ph^{Bo}), 7.35 (td, ^3J(H,H) = 8.1, ^3J(H,P) = 8.1, ^4J(H,H) =1.6 Hz, 4H, $PPh_2{}^o$), 7.06-6.98 (m, 6H, $PPh_2{}^{m+p}$), 6.88 (d, ^3J(H,H) = 8.2 Hz, 2H, Ph^{Bm}), 6.73 (dd,^3J(H,H) = 8.1 Hz, ^5J(H,P) = 1.5 Hz, 2H, Ph^{Ao}), 6.67 (d, ^3J(H,H) = 8.1 Hz, 2H, Ph^{Am}), 2.02 (s, 3H, C$H_3{}^B$), 1.97 (s, 3H, C$H_3{}^A$). ^{13}C{^{1}H} (101 MHz, C_6D_6, 25 ºC): δ 184.9 (d, ^1J(C,P) = 28 Hz, P*C*=O), 151.3 (*C*=O), 138.8 (Ph^{Ap}), 136.3 (Ph^{Bp}), 135.1 (d, ^2J(C,P) = 21 Hz, $PPh_2{}^o$), 134.0 (Ph^{Ai}), 133.6 (d, ^1J(C,P) = 8 Hz, $PPh_2{}^i$), 133.4 (Ph^{Bi}), 132.1 (d, ^4J(C,P) = 3 Hz, Ph^{Ao}), 130.0 (Ph^{Bm}), 129.2 ($PPh_2{}^p$), 129.1 (Ph^{Ao}), 128.7 (d, ^3J(C,P) = 8 Hz, $PPh_2{}^m$), 120.2 (Ph^{Bo}), 21.1 (*C*H$_3{}^A$), 20.8 (*C*H$_3{}^B$). ^{31}P{^{1}H} (162 MHz, C_6D_6, 25 ºC): δ 8.0 (s, 1P, Ph_2P). Elemental analysis for $C_{28}H_{25}N_2O_2P$ (452.494): calcd. C 74.32, H 5.57, N 6.19; found: C 74.01, H 5.39, N 6.07. MS (ESI) *m/z*: calcd. for $C_{28}H_{26}N_2O_2P$ $[M+H]^+$ 453.1726, found: 453.1731 (err [ppm] = 1.10). IR (ATR) $\bar{\nu}$/cm^{-1} 3202 (N–H), 1716 (PC=O), 1536 (C=O).

4.2.7.9 $PPh_2C(O)N(3,5\text{-}(OMe)_2C_6H_3)C(O)NH(3,5\text{-}(OMe)_2C_6H_3)$ (22c)



White solid: 304 mg, 65%. ^{1}H NMR (400 MHz, C_6D_6, 25 ºC): δ 11.74 (s, 1H, N*H*), 7.43-7.34 (m, 4H, PPh_2^o), 7.22 (d, ^4J(H,H) = 2.3 Hz, 2H, Ph^{Bo}), 7.06-6.96 (m, 6H, PPh_2^{m+p}), 6.53 (t, ^4J(H,H) = 2.3 Hz, 1H, Ph^{Ap}), 6.42 (t, ^4J(H,H) = 2.3 Hz, 1H, Ph^{Bp}), 6.19 (dd, ^4J(H,H) = 2.3 Hz, ^5J(H,P) = 1.3 Hz, 2H, Ph^{Ao}), 3.30 (s, 6H, OCH_3^B), 3.09 (s, 6H, OCH_3^A). ^{13}C{^{1}H} (101 MHz, C_6D_6, 25 ºC): δ 184.9 (d, ^1J(C,P) = 30 Hz, P*C*=O), 162.0 (Ph^{Bm}), 160.9 (Ph^{Am}), 151.1 (*C*=O), 140.5 (Ph^{Bi}), 138.2 (d, ^3J(C,P) = 4 Hz, Ph^{Ai}), 135.1 (d, ^2J(C,P) = 21 Hz, PPh_2^o),133.8 (d, ^1J(C,P) = 9 Hz, PPh_2^i), 129.8 (PPh_2^p), 128.8 (d, ^3J(C,P) = 8 Hz, PPh_2^m), 110.4 (d, ^4J(C,P) = 4 Hz, Ph^{Ao}), 102.8 (Ph^{Ap}), 98.4 (Ph^{Bo}), 97.8 (Ph^{Bp}), 54.9 (OCH_3^B), 54.9 (OCH_3^A).^{31}P{^{1}H} (162 MHz, C_6D_6, 25 ºC): δ 7.7 (s, 1P, Ph_2P). Elemental analysis $C_{30}H_{29}N_2O_6P$: calcd. C 66.17, H 5.37, N 5.14; found: C 65.89, H 5.25, N 5.07. MS (ESI) *m/z*: calcd. for $C_{30}H_{30}N_2O_6P$ $[M+H]^+$ 545.1836, found: 545.1822 (err [ppm] = 2.50). IR (ATR) $\bar{\nu}$/cm^{-1} 3161 (N–H), 1719 (PC=O), 1544 (C=O).

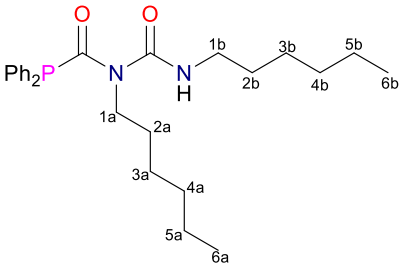
4.2.7.10 $PPh_2C(O)N(4\text{-}BrC_6H_4)C(O)NH(4\text{-}BrC_6H_4)$ (22d)



White solid: 406 mg, 79%.^{1}H NMR (400 MHz, C_6D_6, 25 ºC): δ 11.41 (s, 1H, N*H*), 7.52 (m, 4H, PPh_2^o), 7.30 (d, ^3J(H,H) = 9.0 Hz, 2H, Ph^{Bm}), 7.13 (d, ^3J(H,H) = 9.0 Hz, 2H, Ph^{Bo}), 7.09-6.97 (m, 6H, PPh_2^{m+p}), 6.92 (d, ^3J(H,H) = 8.6 Hz, 2H, Ph^{Am}), 6.40 (dd, ^3J(H,H) = 8.6 Hz, ^5J(H,P) = 1.5 Hz, 2H, Ph^{Ao}). ^{13}C{^{1}H} (101 MHz, C_6D_6, 25 ºC): δ 185.0 (d, ^1J(C,P) = 31 Hz, P*C*=O), 150.8 (*C*=O), 137.1 (Ph^{Bi}), 135.1 (d, ^2J(C,P) = 21 Hz, PPh_2^o), 134.7 (d, ^3J(C,P) = 4 Hz, Ph^{Ai}), 134.6 (Ph^{Ap}), 134.0

(PPh_2^i), 133.4 (d, ^4J(C,P) = 4 Hz, Ph^{Ao}), 132.1 (Ph^{Bo}), 131.3 (Ph^{Am}), 129.8 (PPh_2^p), 128.8 (d, ^3J(C,P) = 8 Hz, PPh_2^m), 121.3 (Ph^{Bm}), 116.6 (Ph^{Bp}). $^{31}P\{^1H\}$ (162 MHz, C_6D_6, 25 ºC): δ 8.8 (s, 1P, Ph_2P). MS (ESI) *m/z*: calcd. for $C_{26}H_{19}Br_2N_2O_2P$ $[M+H]^+$ 580.9642, found: 580.9624 (err [ppm] = 3.20). IR (ATR) $\bar{\nu}$/cm^{-1} 3268 (N–H), 1717 (PC=O), 1594 (C=O).

4.2.7.11 $PPh_2C(O)N(^nHx)C(O)NH(^nHx)$ (22e)

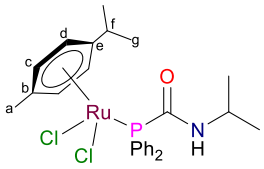


22e was prepared *in situ* by addition of Ph_2PH (51 µL, 0.293 mmol) and ^{n}HxNCO (85 µL, 0.586 mmol) to a solution of **11** (10 mg, 5 mol%) in C_6D_6 (0.6 mL). After 16 h at r.t the solution was studied by NMR spectroscopy. Selected spectroscopic data: ^{1}H NMR (400 MHz, C_6D_6, 25 ºC): δ 9.22 (s, 1H, N*H*), 7.55-7.45 (m, 4H, PPh_2^o), 7.07-6.99 (m, 6H, PPh_2^{m+p}), 4.03 (t, 2H, ^3J(H,H) = 4.6 Hz, CH_2^{1a}), 3.25 (q, 2H, ^3J(H,H) = 4.2 Hz, CH_2^{1b}), 1.64 (m, 2H, CH_2^{2a}), 1.34 (br t, ^3J(H,H) = 5.6 Hz, CH_2^{2b}), 1.17-1.04 (m, 12H, $CH_2^{3a,4a,5a}$ + $CH_2^{3b,4b,5b}$), 0.81 (m, 4H, CH_3^{6a+6b}). $^{13}C\{^1H\}$ NMR (101 MHz, C_6D_6, 25 °C): δ 182.8 (d, ^1J(C,P) = 25 Hz, P*C*=O), 154.4 (*C*O), 135.0 (d, ^2J(C,P) = 20 Hz, PPh_2^o), 133.4 (d, ^1J(C,P) = 7 Hz, PPh_2^i), 46.2 (d, ^4J(C,P) = 19 Hz, CH_2^{1a}), 40.6 (CH_2^{1b}), 28.2 (CH_2^{2a+2b}), 26.6 (CH_2), 22.5 (CH_2), 14.4(CH_3^{6a+6b}). $^{31}P\{^1H\}$ (162 MHz, C_6D_6, 25 ºC): δ 8.4 (s, 1P, Ph_2P). MS (ESI) *m/z*: calcd. for $C_{26}H_{38}N_2O_2P$ $[M+H]^+$ 441.2665, found: 441.2677 (err [ppm] = 2.60).

4.2.8 Coordination of Phosphinocarboxamides to Dichloro(p-cymene) Ruthenium

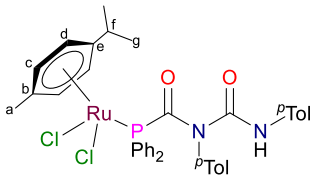
4.2.8.1 Synthesis of [Ru(p-cym){PPh$_2$C(O)NH(^{i}Pr)}Cl$_2$] (23)

To a mixture of **21g** (12.0 mg, 0.0442 mmol) and [Ru(*p*-cym)Cl$_2$]$_2$ (13.5 mg, 0.0221 mmol) was added dichloromethane (4 mL) and the red solution stirred for 3 days. The solvent was removed *in vacuo* and the product dried for 6 h. The product was extracted into toluene (4 mL) and stored at –30 °C for 1 week resulting in the precipitation of a red crystalline solid (5 mg, 39%). Crystals suitable for XRD were grown from a solution of



23 in C_6D_6 at room temperature. ^{1}H NMR (400 MHz, C_6D_6, 25 ºC): δ 8.63 (d, ^3J(H,P) = 7.4, 1H, N*H*), 8.20-8.02 (m, 4H, PPh^o), 7.14-6.94 (m, 6H, PPh^{m+p}), 4.75 (d, ^3J(H,H) = 6.1, 2H, *p*-cym^c), 4.70 (dd, ^3J(H,H) = 6.1 Hz, ^4J(H,H) = 1.3 Hz, 2H, *p*-cym^d), 4.05 (m, 1H, ^{i}Pr^{CH}), 2.56 (hept, ^3J(H,H) = 7.0 Hz, 1H, *p*-cym^f), 1.51 (s, 3H, *p*-cym^a), 1.04 (d, ^3J(H,H) = 6.6 Hz, 6H, ^{i}Pr^{CH_3}), 0.82 (d, ^3J(H,H) = 7.0 Hz, 6H, *p*-cym^g). ^{13}C{^{1}H} (101 MHz, C_6D_6, 25 ºC): δ 167.4 (d, ^1J(C,P) = 55 Hz, *C*=O), 134.8 (d, ^2J(C,P) = 9 Hz, PPh^o), 133.7 (d, ^1J(C,P) = 43 Hz, PPh^i).130.7 (d, ^4J(C,P) = 2 Hz, PPh^p), 128.2 (d, ^3J(C,P) = 10 Hz, PPh^m), 109.7 (*p*-cym^b), 95.2 (*p*-cym^e), 89.7 (d, ^2J(C,P) = 4 Hz, *p*-cym^d), 86.0 (d, ^2J(C,P) = 6 Hz, *p*-cym^c), 43.6 (d, ^3J(C,P) = 6 Hz, ^{i}Pr^{CH}), 30.3 (*p*-cym^f), 22.2 (*p*-cym^g), 21.7 (*i*-Pr^{CH_3}), 17.3 (*p*-cym^a). ^{31}P{^{1}H} (162 MHz, C_6D_6, 25 ºC): δ 29.8 (s, 1P, Ph$_2$*P*).

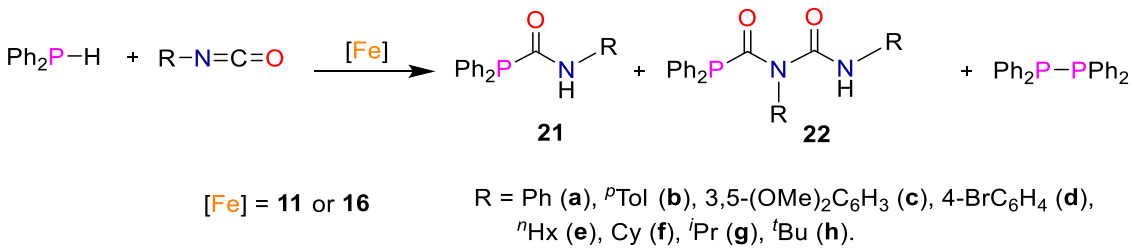
4.2.8.2 Synthesis of [Ru(p-cym){PPh$_2$C(O)N(^{p}Tol)C(O)NH(^{p}Tol)}Cl$_2$] (24)



To a mixture of **22c** (57.3 mg, 0.126 mmol) and [Ru(*p*-cym)Cl$_2$]$_2$ (38.6 mg, 0.066 mmol) was added dichloromethane (4 mL) and the red solution stirred overnight. The solvent was removed *in vacuo* and the oily residue dried for 6 h. The oil was triturated with *iso*-hexane (4mL) and the solvent removed to give a red solid. This was extracted into toluene (4 mL) and layered with *iso*-hexane (2 mL) and stored at –30 °C for 1 week resulting in the precipitation of a red crystals suitable for XRD. The remaining solid was an intractable mixture of products *via* analysis by ^{1}H and ^{31}P{^{1}H} NMR.

4.3 Results and Discussion

The catalytic hydrophosphination of isocyanates using two- and three-coordinate iron(II) precatalysts **11** and **16** were investigated under mild conditions (25 °C or 60 °C) and monitored *via* ^{1}H and $^{31}P\{^{1}H\}$ NMR in C_6D_6 (Scheme 4.3).



Scheme 4.3 Hydrophosphination of isocyanates with diphenylphosphine catalysed by Fe(II) m-terphenyl complexes (11 and 16).

Initially, diphenyl phosphine was reacted with one equivalent of phenyl isocyanate in C_6D_6 in the presence of 5 mol%. After 16 h at room temperature the solution underwent a colour change from yellow to dark red with formation of two phosphorus-containing products as observed by ^{1}H and $^{31}P\{^{1}H\}$ NMR in a relative ratio of 59:41 (98% conversion). Further analysis revealed that the major product was [$Ph_2PC(=O)N(H)Ph$] (**21a**), while the second product was [$Ph_2C(=O)N(Ph)C(=O)N(H)Ph$] (**22a**), resulting from the double insertion of two isocyanate molecules into the P–H bond of Ph_2PH (Scheme 4.3). These diinsertion processes are incredibly rare, and indeed, this is the first example of a diinsertion of an isocyanate into a phosphine.[27]

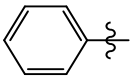
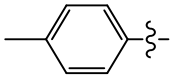
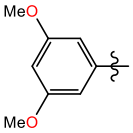
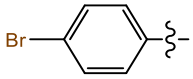
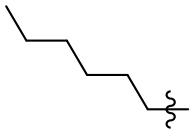
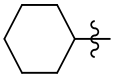
Entry	Isocyanate RN=C=O	Cat. (mol %)	RNCO: Ph_2PH	T (°C)	Time (h)	Conv. (%)	21/22/$(Ph_2P)_2$	TOF (h^{-1})
1		**11** (5)	1:1	25	16	98	59/41/0	-
2		**11** (5)	2:1	25	15	95	33/67/0	2.5
3	R = Ph	**11** (2)	2:1	25	21	>99	20/80/0	-
4		**16** (5)	2:1	25	6	96	35/65/0	6.7
5		**11** (5)	2:1	25	16.5	95	27/72/1	3.8
6		**16** (5)	2:1	25	4.8	94	36/63/1	7.3
7	R = ^{p}Tol	**11** (2)	2:1	25	19	71	2/98/0	-
8		**11** (5)	2:1	25	12	95	43/57/0	3.0
9	R = 3,5-$(OMe)_2C_6H_3$	**16** (5)	2:1	25	3	99	46/54/0	17.8
10		**11** (5)	2:1	25	15	99	30/70/0	-
11	R = 4-BrC_6H_4	**16** (5)	2:1	25	4	99	27/71/2	-
12		**11** (5)	1:1	25	15	99	13/26/5/56[a]	-
13		**11** (5)	2:1	25	15	99	8/39/3/49[a]	-
14	R = ^{n}Hx	**16** (5)	2:1	25	15	99	12/36/7/46[a]	-
15		**11** (5)	1:1	25	16	90	93/0/6/1[b]	1.4
16	R = Cy	**16** (5)	1:1	25	8	89	95/0/5	16.0
17		**11** (5)	1:1	25	16	55	91/5/4	-
18		**11** (5)	1:1	60	1.6	89	96/0/4	22.4
19	R = ^{i}Pr	**16** (5)	1:1	60	1	92	97/0/3	55.3
20		**11** (5)	1:1	60	16	70	91/0/9	-
21		**11** (5)	2:1	60	16	99	92/0/8	-
22	R = ^{t}Bu	**16** (5)	1:1	60	16	77	86/0/14	-

Table 4.3 Reaction conditions: 0.6 mL of C_6D_6. Conversions and ratios of products determined by ^{1}H and $^{31}P\{^{1}H\}$ NMR spectroscopies. [a] ($^{n}HxNCO)_3$ ratio, [b] unidentified $^{31}P\{^{1}H\}$ resonance.

In order to optimise the formation of the diinsertion product **22a**, the ratio of PhNCO:Ph_2PH was changed from 1:1 to 2:1 (Table 4.3, entries 1-2), resulting in an increase in the ratio of **22a** (67%) with respect to **21a** (33%). Upon lowering the catalyst loading to 2 mol%, the reaction reached high conversion after 21 h with a higher proportion of the diinsertion product **22a** (Table 4.3, entry 3). Three-coordinate iron complex **16** shows a higher activity than **11**; high conversion is achieved in a significantly shorter time (Figure 4.2;16 h [top] *vs.* 6 h [bottom]) with a similar product distribution (Table 4.3, entry 4).

Very similar behaviour is observed when using *p*-TolNCO (Table 4.3, entries 5 and 6) with 5 mol% of precatalyst. However, when the precatalyst is lowered to 2 mol% of **11**, and monitored after a similar time, the diinsertion product is favoured in a larger ratio than observed when using PhNCO (Table 4.3, entry 7). Reactions with isocyanates featuring functional groups proceed in a similar manner, with excellent conversions for substrates which bear either electron donating or withdrawing groups (Table 4.3, entries 8-11). When 3,5-$(OMe)_2C_6H_3NCO$ is used, the hydrophosphination proceeds with a higher reaction rate and a small decrease in the amount of the diinsertion product, whereas the reaction of 4-BrC_6H_4NCO yields the diinsertion product in higher quantity.

The scope of the reaction was extended to aliphatic isocyanate subustrates. When the reaction was performed with ^{n}HxNCO, the hydrophosphination competes with the cyclotrimerisation reaction leading to a mixture of $[^{n}HxNCO]_3$ (**19c**, see Chapter III), $[Ph_2PC(=O)N(H)^{n}Hx]$ (**21e**) and $[Ph_2PC(=O)N(^{n}Hx)C(=O)N(H)^{n}Hx]$ (**21e**) (Table 4.3, entries 12-14). Increasing the stoichiometry from 1:1 to 2:1 (RNCO:Ph_2PH) when using **11** at 5 mol% increased the proportion of diinsertion product obtained.

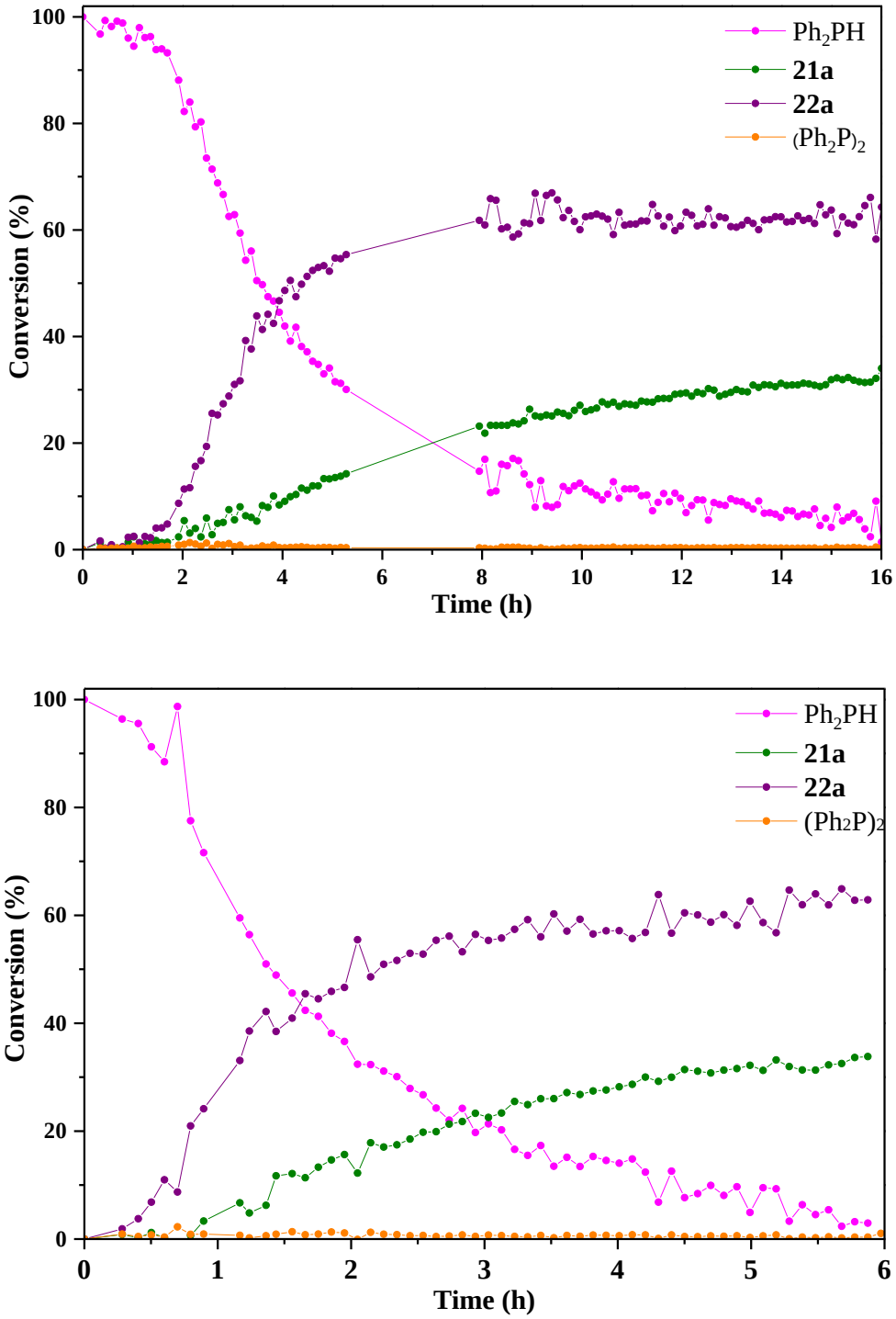


Figure 4.2 Conversion (%) vs. time (hour) for the hydrophosphination of PhNCO with 5 mol% cat. of 11 (top) or 16 (bottom) in C_6D_6 at 25 °C.

Reactions with more sterically bulky secondary and tertiary isocyanates (RNCO; R = cyclohexyl, *iso*-propyl and *tert*-butyl), where precatalysts **11** and **16** are ineffective

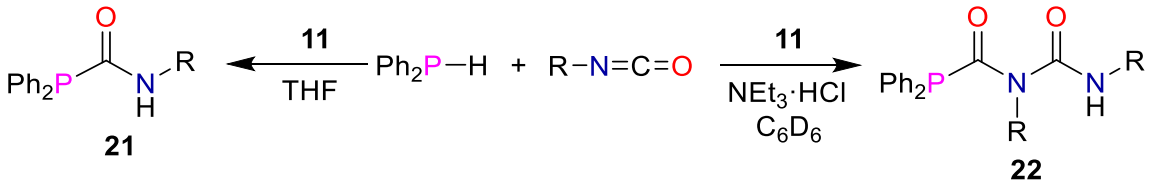
precatalysts for the cyclotrimersation of isocyanates (Chapter III, Table 3.5), afforded almost exclusively the monoinsertion products **21f-h** (Table 4.3, entries 15-22). When using *iso*-propyl or *tert*-butyl isocyanate, the temperature was raised to 60 °C in order to reach reasonable conversions in 16 h, however, this increase in temperature was accompanied by an increase in the dehydrocoupling product $(Ph_2P)_2$. Interestingly, when changing the stoichiometry from 1:1 to 2:1 of ^{t}BuNCO:Ph_2PH when using **11** the reaction reached higher conversion after 16 h at 60 °C. Previous attempts to catalyse the hydrophosphination reaction of ^{t}BuNCO with Ph_2PH were low yielding (<20%).[21]

TOF values calculated clearly show that precatalyst **16** is more active than **11** in the hydrophosphination of aromatic and aliphatic isocyanates (Table 4.3).

Collectively, these results indicate that the observed selectivity between the catalysis of the mono- and diinsertion of isocyanates into Ph_2PH may be governed by steric factors obtaining preferentially the diinsertion product for less bulky isocyanates (R = Ph, ^{p}Tol, 3,5-$(OMe)_2C_6H_3$ and 4-BrC_6H_4) and the monoinsertion product for secondary and tertiary aliphatic isocyanates.

4.3.1 Product Selectivity

Through small changes of the reaction conditions, the selectivity of the hydrophosphination products obtained in the reaction (mono *vs.* diinsertion) can be controlled as outlined in Scheme 4.4.



Scheme 4.4 Hydrophosphination products obtained with using THF (left) or NEt_3·HCl in C_6D_6 (right) with 11 (5 mol%).

When the solvent was replaced with THF, a significant change in the selectivity of the reaction was observed where the mono insertion product (**21**) was obtained almost exclusively (Table 4.4Table). A decrease in the catalyst activity was also observed, for example, the reaction of PhNCO with Ph_2PH (1:1) in the presence of 5 mol% of **11** at room temperature only reached 40% conversion after 16 h while the equivalent reaction in C_6D_6 reached 98% conversion (Table 4.4, entry 1; Table 4.3, entry 1).

Entry	***Isocyanate RN=C=O***	***Cat. (mol %)***	***RNCO: Ph_2PH***	***T (°C)***	***Time (h)***	***Conv. (%)***	***21/22/$(Ph_2P)_2$***
1	Ph	**11** (5)	1:1	25	16	40	97/0/3
2		**11** (5)	1:1	60	32	80	100/0/0
3	3,5-$(OMe)_2C_6H_3$	**11** (5)	1:1	60	32	66	99/1/0
4	4-BrC_6H_3	**11** (5)	1:1	60	24	50	98/0/2

Table 4.4 Reaction conditions: 0.6 mL of THF. Conversions and ratios of products determined by $^{31}P\{^1H\}$ NMR spectroscopy.

With this decrease in catalyst activity, the reactions were heated to 60 °C in order to achieve moderate conversions (Table 4.4, entries 2-4). When the reaction was performed in the presence of a weak base (Table 4.5, entry 1) no significant changes were observed. However, the addition of a weak acid, NEt_3·HCl, to the reaction mixture afforded the diinsertion product (**22**) in high selectivity.

Entry	*Isocyanate RN=C=O*	*Cat. (mol %)*	*RNCO: Ph_2PH*	*Time (h)*	*Additive*	*Conv. (%)*	*21/22/$(Ph_2P)_2$*
1		**11** (5)	2:1	16	NEt_3	>99	37/63/0
2	3,5-$(OMe)_2$Ph	**11** (5)	2:1	16	NEt_3·HCl	>99	3/97/0
3		None	2:1	16	NEt_3·HCl	19	94/0/1
4	Ph	**11** (5)	2:1	16	NEt_3·HCl	>99	1/99/0
6	Cy	**11** (5)	1:1	48	NEt_3·HCl	0	-

Table 4.5 Reaction conditions: 25 ºC, 0.6 mL of C_6D_6. Conversions and ratio of products determined by ^1H and $^{31}P\{^1H\}$ NMR spectroscopies. Several drops of THF-d_8 were added to solubilise NEt_3·HCl. [a] 5% unidentified $^{31}P\{^1H\}$ NMR resonance.

4.3.2 Mechanistic Studies

To investigate the faster rates for precatalyst **16** compared to **11** (Table 4.3) the hydrophosphination catalysis was monitored using ^1H and $^{31}P\{^1H\}$ NMR spectroscopy with CyNCO as a model substrate. In a Young's tap NMR tube, the precatalyst (**11** or **16**, 5 mol%) with CyNCO in C_6D_6 was cooled to –30 °C after which Ph_2PH was added and the NMR tube quickly cooled to –78 °C to prevent the reaction from proceeding. The NMR tube was transferred into the spectrometer and the reaction monitored *via* ^1H and $^{31}P\{^1H\}$ NMR spectroscopies.

When using **11**, an induction period of around 2 h was observed (Figure 4.3, top), indicating that the two-coordinate complex **11** is not the true catalyst and that a transformation takes place before the catalysis begins. No induction period is observed for **16**, where the catalysis starts immediately after substrate addition (Figure 4.3, bottom). It is likely that the same initial reaction takes place for **16** but the labile THF ligand is easily displaced making this step considerably faster.

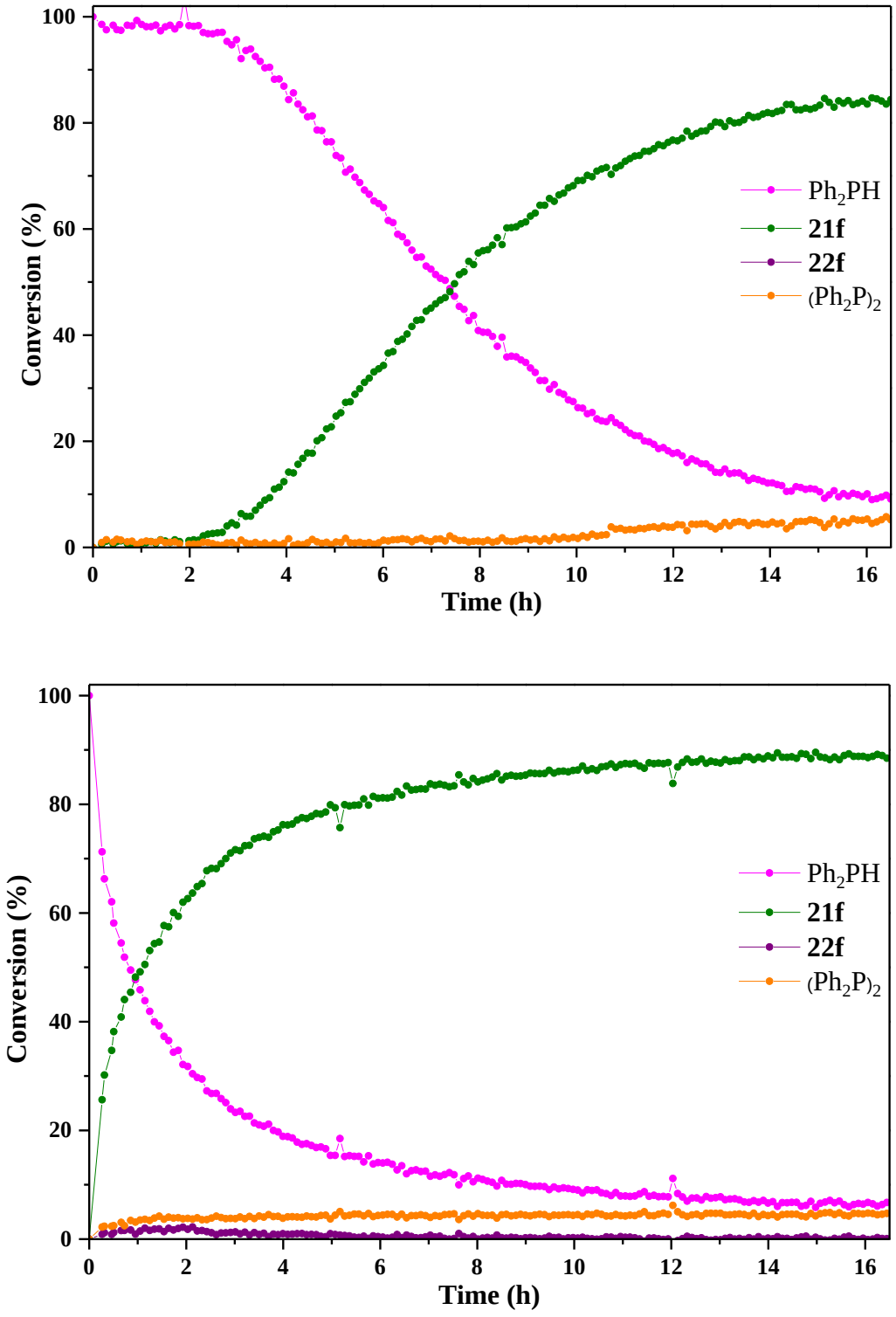


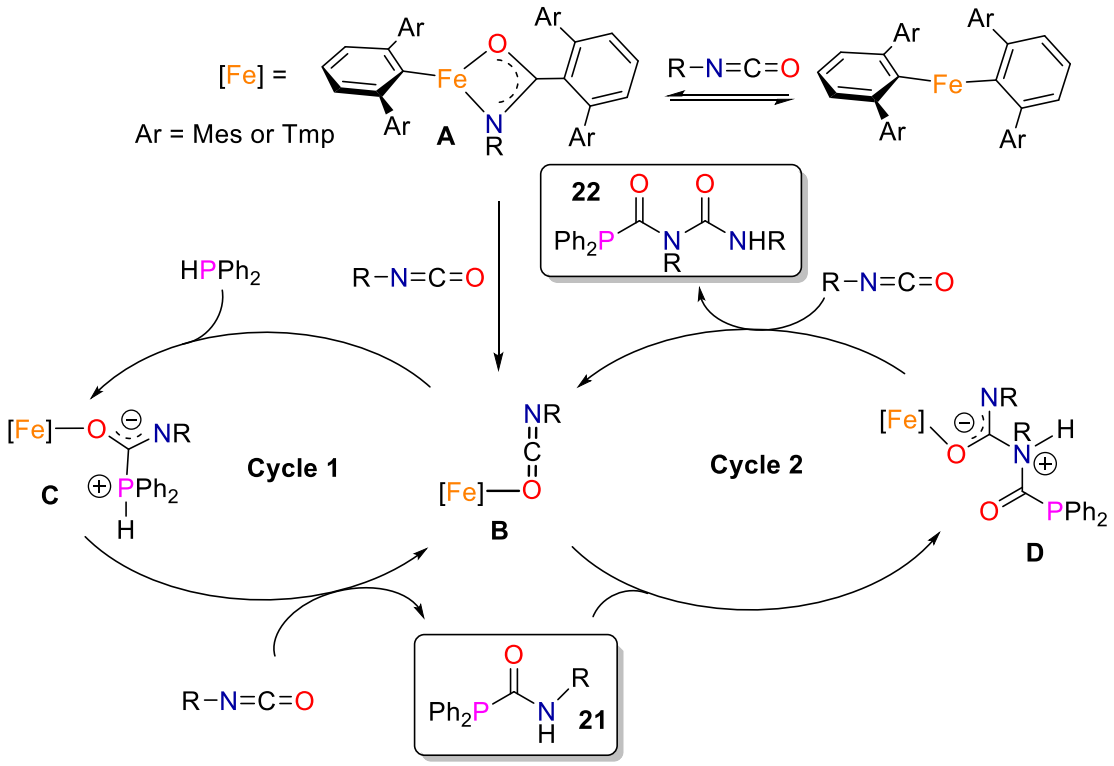
Figure 4.3 Conversion (%) vs. time (hour) for the hydrophosphination of CyNCO with 5 mol% cat. of 11 (top) or 16 (bottom) in C_6D_6 at 25 °C.

Surprisingly, when complex **11** was reacted separately with either Ph_2PH or CyNCO no reaction was observed after 48 h at room temperature by NMR and IR spectroscopy. As soon as the other substrate is added the formation of product **21f** is observed. Stoichiometric studies were not conclusive as IR spectroscopy shows several peaks in the amide region, but indicates that the active catalyst is an iron amidate complex (Scheme 4.5, **A**). The formation of this species could be an equilibrium; therefore, both Ph_2PH and CyNCO are needed to drive the reaction to **A**. However, the possibility that both substrates are required for precatalyst activation cannot be ruled out. A similar observation has also been made by Hill *et al.* in the hydrophosphination of carbodiimides.[26]

Catalyst poisoning tests on the reaction of **11** with CyNCO and Ph_2PH were undertaken and this was monitored *in situ*. The catalysis in the presence of 1 drop of mercury or with an excess of CS_2 proceeded unhindered indicating that the catalysis homogeneous and that the reaction is not catalysed by iron metal or trace iron nanoclusters in suspension.[28,29] The reaction appears to not be radical mediated where the catalysis in unaffected in the presence of a radical trap cumene.[30]

4.3.2.1 Proposed Mechanism

Experimental observations suggest the catalysis operates through a homogenous mechanism which does not appear to be radical mediated therefore plausible mechanism is proposed in Scheme 4.5.



Scheme 4.5 Proposed mechanism for the formation of the mono- (21) and diinsertion (22) products in the hydrophosphination of isocyanates

First, insertion of an isocyanate into the Fe–C bond forms an iron amidate complex **A** as evidenced though IR spectroscopy. It is likely that the metal centre acts as a Lewis acid due to the relatively high +II oxidation state and its coordinative unsaturation. Hence, coordination of an isocyanate molecule to forms the active species **B** which is activated towards nucleophilic attack of a phosphine leading to P–C bond formation and generation of intermediate **C**. Similar substrate coordination followed by outer-sphere attack of a phosphine have been proposed.[12,15,31,32] A 1,3-proton shift, followed by addition of a new molecule of isocyanate regenerates the active species **B** with displacement of the mono product **21**. When the phosphinocarboxamide (**21**) produced in Cycle 1 contains a smaller R group, the reaction can proceed into Cycle 2 *via* nucleophilic attack on **B** with the subsequent formation of **D**. Proton transfer followed by displacement of the

phosphinodicarboxamide (**22**) by an incoming isocyanate molecule results in the regeneration of **B**.

To provide further support for the proposed mechanism a mixture of PhNCO and CyNCO were reacted with diphenylphosphine (1:1:1) where a combination of four products **21a**/**21f**/**22a**/**22i** were obtained (Scheme 4.2). The diinsertion product **22i** [$Ph_2PC(=O)N(Ph)C(=O)NH(Cy)$] results from the coordination of CyNCO to the iron amidate complex (**A**) to form **B** which then undergoes nucleophilic attack of [$Ph_2PC(=O)N(H)Ph$] (**21a**) which is in agreement with the proposed mechanism.

When coordinating solvents such as THF are used, solvation of intermediate **B** can occur blocking the income of a phosphinocarboxamide molecule (**21**) therefore enforcing the monoinsertion pathway (Cycle 1) and blocking Cycle 2. The weak acid (NEt_3·HCl) likely aids the protonolysis step in Cycle 2 (**D** to **B**); a rate limiting step for hydroamination reactions.[33,34]

An alternative mechanism similar to those reported for rare-earth precatalysts[16,17,21] where the Ph_2PH attacks the metal centre first through protolytic cleavage of the amide ligand has been dismissed due to the lack of evidence of the formation of (2,6-$MesC_6H_3$)C(=O)NH(R) *via* ^{1}H NMR or IR spectroscopy.

4.3.3 Scale up of Hydrophosphination Products 21 and 22

The mono- and diinsertion products were successfully scaled up and isolated in moderate to good yields (50-79%). The mono-insertion products or phosphinocarboxamides, **21a**,**c**,**d**, were synthesised by reaction of the corresponding isocyanate with diphenyphospine (1:1) in the presence of precatalyst **11** (5 mol%) in THF. After removal of volatiles, the white solid was washed with cold *iso*-hexane and dried yielding pure

products. The other phosphinocarboxamides (**21f-h**) were obtained by the reaction of the isocyanate, phosphine (1:1) in the presence of precatalyst **11** (5 mol%) in toluene either at room temperature (**21f**) or 60 °C (**21g**, **21h**). Subsequent removal of solvent afforded an oily residue after which the product was extracted into *n*-pentane. Storage at –30 °C overnight resulted in the precipitation of pure product.

The diinsertion products, or phosphinodicarboxamides, **22a-d**, were obtained in a similar manner with reaction of the isocyanate and phosphine (2:1) in the presence of **11** (5 mol%) in toluene overnight. Removal of the volatiles and washing of the remaining residue with *n*-pentane enabled isolation of the corresponding pure phosphinodicarboxamide. A large scale (3 mmol of phosphine) reaction for the synthesis of phosphinodicarboxamide **22a** was also performed where PhNCO, Ph_2PH, and **11** with the addition of $Et_3N{\cdot}HCl$ (ensuring formation of **22a** over **21a**) which were stirred in toluene at room temperature after which the solvent was removed and solid dried. The product was extracted into toluene, solvent removed and the white solid washed with *iso*-hexane resulting in the isolation of the corresponding phosphinocarboxamide in high yield.

4.3.3.1 Spectroscopic Analysis

The phosphinocarboxamides (PCAs, **21a**,**c-h**) and phosphinodicarboxamides (PDCAs, **22a-d**) were fully characterised by multinuclear NMR and IR spectroscopy and mass spectrometry where selected data are shown in Table 4.6. ^{1}H and IR data for compounds **21a**,**d**,**f** agree well with those reported in the literature.[21] The N*H* resonances in the ^{1}H NMR spectra occur at *ca.* 7 ppm for the aryl PCAs (**21a**,**c**,**d**) whereas the alkyl PCAs (**21f-h**) appear at *ca.* 5 ppm. This trend is also observed for the corresponding aryl/alkyl

PDCAs (**22a**-**d** *vs.***22e**,**i**) which appear at approximately 11 and 9 ppm respectively. The $^{31}P\{^{1}H\}$ NMR spectra feature a singlet between –4.3 to 0.8 ppm for the PCAs (**21**) whereas the PDCAs (**22**) are shifted downfield in the range between 7.7 and 8.8 ppm. A similar observation can be seen in the $^{13}C\{^{1}H\}$ NMR spectra where the signal corresponding to the P*C*=O carbon appears as a doublet where the PDCAs (**22**) (183.6-184.9 ppm; ^{1}J(C,P) = 25-31 Hz) are shifted downfield with respect to the PCAs (**21**) (174.9-175.5 ppm; ^{1}J(C,P) = 12-16 Hz) indicating stronger multiple bond character of the carbonyl. This is also observed in the IR spectra where the bands corresponding to the PC=O stretches are higher in the PDCAs (**22**) (*ca.* 1718 *vs.* 1640 cm^{-1}). Selected ^{15}N chemical shifts for the *N*H moiety were obtained *via* a ^{1}H, ^{15}N HSQC which were found to range between 111.2-117.6 ppm.

	Isolated Yield (%)	***^{31}P (ppm)***	***$^{13}C_{PCO}$ (ppm)***	***^{1}J(C,P) (Hz)***	***$^{1}H_{NH}$ (ppm)***	***$^{15}N_{NH}$ (ppm)***	***$\bar{\nu}_{PCO}$ (cm^{-1})***	***$\bar{\nu}_{NCONH}$ (cm^{-1})***
21a	71	–0.2	175.2	15	7.24	-	1688[a]	-
21c	57	0.8	175.5	16	7.37	-	1630	-
21d	64	0.2	175.4	16	7.00	-	1630[a]	-
21f	56	–4.3	174.9	12	5.44	111.2	1645	-
21g	57	–4.0	175.0	13	5.35	113.5	1641	-
21h	67	–2.7	175.3	13	5.42	117.6	1632	-
22a	50	8.3	184.9	29	11.57	116.7	1718	1588
22b	55	8.0	184.9	28	11.58	-	1716	1536
22c	65	7.7	184.9	30	11.74	-	1719	1544
22d	79	8.8	185.0	31	11.41	-	1717	1594
22e	-	8.4	182.8	25	9.22	-	-	-
22i	-	7.8	183.6	27	9.22	-	-	-

Table 4.6 Selected spectroscopic data for phosphinocarboxamides (21) and phosphinodicarboxamides (22). [a] values from the literature.[21]

4.3.3.2 Crystallographic Analysis

The molecular structures of the hydrophosphination products were determined by X-ray crystallography where crystals for compounds **21a**,**c**,**d**,**f-h** and **22a**,**b** were obtained by either slow diffusion of *n*-pentane into C_6D_6 at room temperature or from storage of a saturated solution in *n*-pentane at room temperature or –30 °C. The crystal structures of the PCAs and PDCAs are shown in Figure 4.4 and Figure 4.5 with relevant bond distances and angles shown in Table 4.7 and Table 4.8 respectively.

All the hydrophosphination products and crystallised with one molecule in the asymmetric unit with the exception of **21h** which featured two molecules in the asymmetric unit with a hydrogen bond acceptor/donor interaction between the two independent molecules at a distance of 2.147(18) Å. Similar hydrogen bond acceptor/donor interactions are observed between adjacent molecules in the crystal structures of **21a**,**c**,**d**,**f**,**g** which vary between 1.84(4)-2.071(19) Å. The solid state structures of **22a** and **22c** feature an intramolecular hydrogen bond between the amide proton and the phosphorus carbonyl of 1.94(6) and 1.884(9) Å respectively.

The phosphorus atoms in these structures displays a pyramidal environment where the sum of the three angles about P(1) fall in the range of 299.12-303.36° and 304.8-305.18° for PCAs and PDCAs respectively, lower than the expected 328.5° for a tetrahedron due to the repulsion from the lone pair of electrons. The P–C distances to the carbonyl carbon are all statistically equivalent (*ca.* 1.88 Å), with the exception of **21c** which is slightly longer. These distances are slightly longer than the sum of the single bond covalent radii (1.86 Å)[35,36] but well within the sum of the Van der Waals radii.[37]

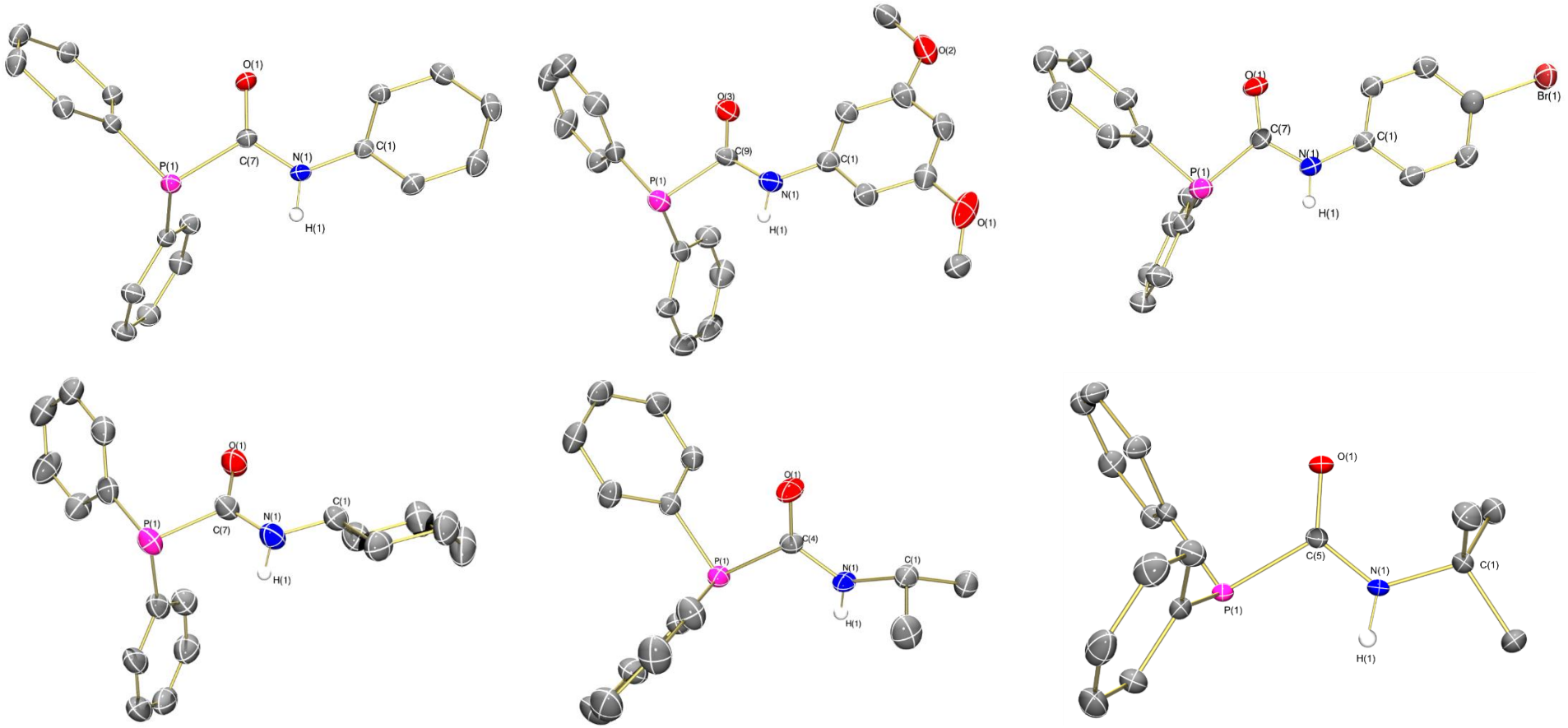


Figure 4.4 Crystal Structures of the PCAs. Top left to right: 21a, c, d. Bottom left to right: 21f, g, h. Thermal ellipsoids are set at the 50% probability level. Hydrogen atoms [with the exception of H(1)] and minor disorder components of the molecule have been omitted for clarity.

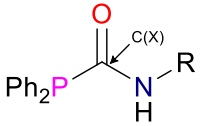
	***21a*** ***X = 7***	***21c*** ***X = 9***	***21d*** ***X = 7***	***21f*** ***X = 7***	***21g*** ***X = 4***	***21h*** ***X = 5***
P(1)–C(X)	1.8882(14)	1.902(5)	1.885(5)	1.8855(19)	1.8855(14)	1.8943(13), 1.8886(13)[a]
C(X)–O(1)	1.2254(17)	1.364(7)	1.220(6)	1.225(3)	1.2288(17)	1.2316(15), 1.2288(15)[a]
N(1)–C(1)	1.4184(18)	1.423(6)	1.407(6)	1.466(2)	1.4699(18)	1.4839(16), 1.4846(17)[a]
N(1)–H(1)	0.846(19)	0.8800	0.86(3)	0.91(3)	0.80(2)	0.864(18), 0.843(19)[a]
H(1)···O(2)	-	-	-	-	-	2.147(18)
C(Ar)–P(1)–C(X)	102.08(6)	98.1(2)	101.6(2)	98.79(9)	97.63(6)	97.74(6), 100.75(5)[a]
	99.72(6)	98.4(2)	99.7(2)	99.00(9)	99.03(6)	99.77(5), 99.82(6) [a]
C(Ar)–P(1)–C(Ar)	101.56(6)	104.2(2)	101.8(2)	103.50(9)	102.46(6)	103.68(6), 100.57(6)[a]

Table 4.7 Selected bond lengths (Å) and angles (°) for the PCAs 21a,c,d,f-h. [a] two molecules in asymmetric unit where chemically equivalent bond distances and angles are shown.

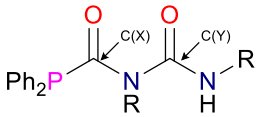
	***22a*** ***X = 13*** ***Y = 20***	***22c*** ***X = 13*** ***Y = 21***
P(1)–C(X)	1.889(5)	1.885(3)
C(X)–O(1)	1.237(6)	1.224(3)
C(X)–N(1)	1.369(6)	1.398(4)
C(Y)–O(2)	1.196(6)	1.219(4)
N(2)–H(2)	0.882	0.864(18)
H(2)···O(1)	1.94(6)	1.884(9)
C(Ar)–P(1)–C(X)	98.0(2)	99.17(13)
	101.94(19)	102.02(14)
C(Ar)–P(1)–C(Ar)	104.9(2)	103.99(13)

Table 4.8 Selected bond lengths (Å) and angles (°) of the PDCAs 22a and 22c.

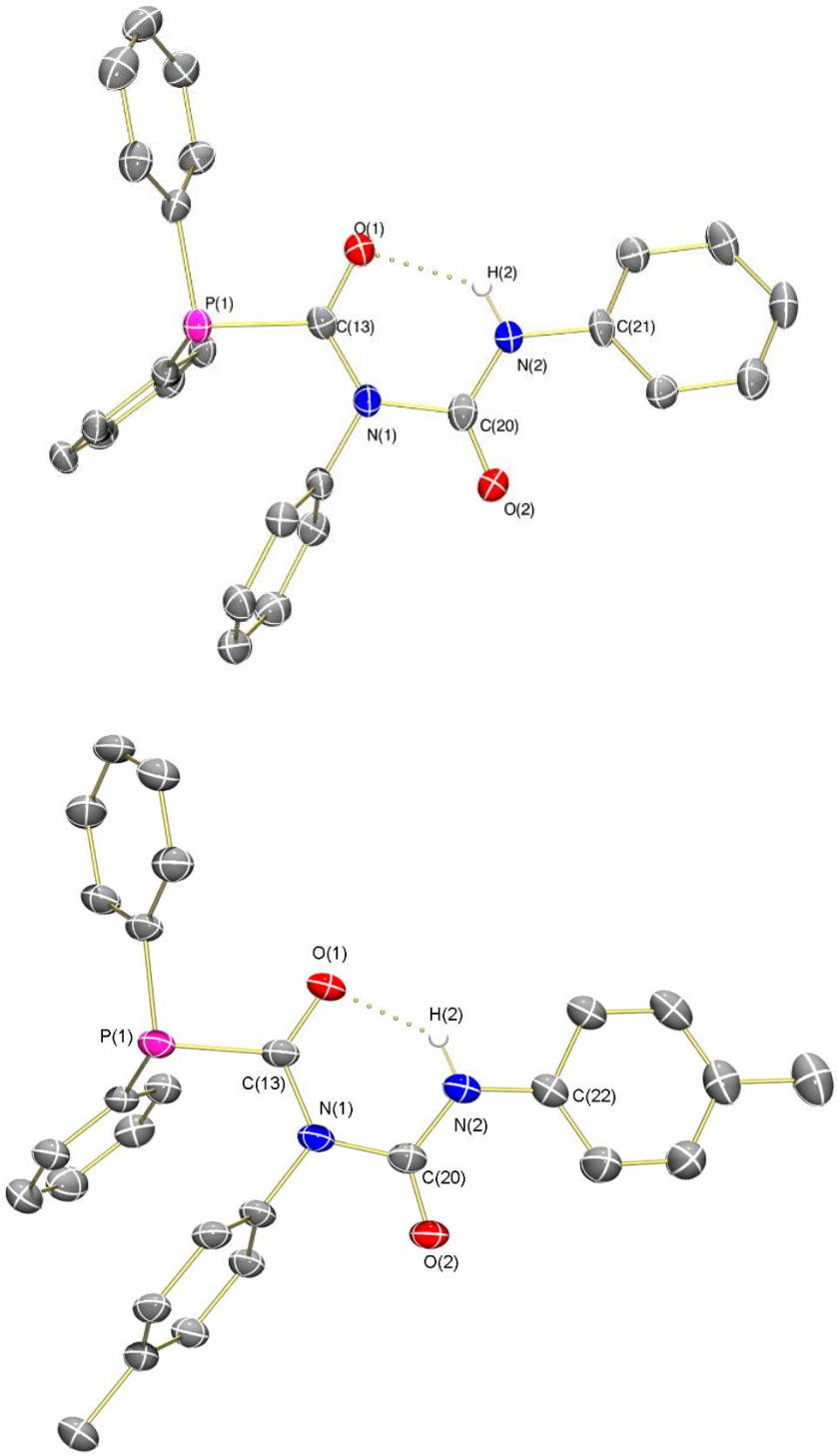
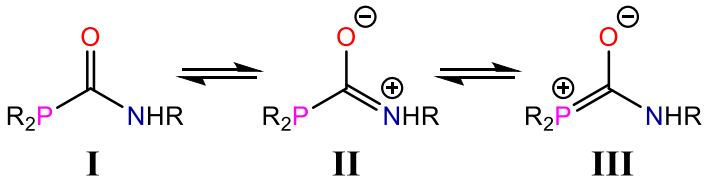


Figure 4.5 Crystal Structures of the PDCAs 22a (top) and 22c (bottom). Thermal ellipsoids are set at the 50% probability level. Hydrogen atoms [with the exception of H(2)] and solvent of recrystallisation molecules omitted for clarity.

The carbonyl distances (C=O) in the PCAs (**21a**,**c**,**d**,**f**,**g**) are slightly longer than those found in the PDCAs (**22a**,**c**) [Table 4.8, C(Y)–O(2)] indicating stronger multiple bond character of PDCAs *vs.* PCAs which agrees with experimental observations (see Section 4.3.3.1). The C–N distances in **21a**,**c**,**d**,**f**,**g** are longer than those seen in the literature (1.329(2)-1.371(4) Å)[38–40] which is indicative of the C–N bond possessing more single bond character. These experimental observations suggest that the most significant resonance form is **I** for the PCAs **21a**,**c**,**d**,**f**,**g**, whereas in literature resonance form **II** is observed (Scheme 4.6).[38–41]

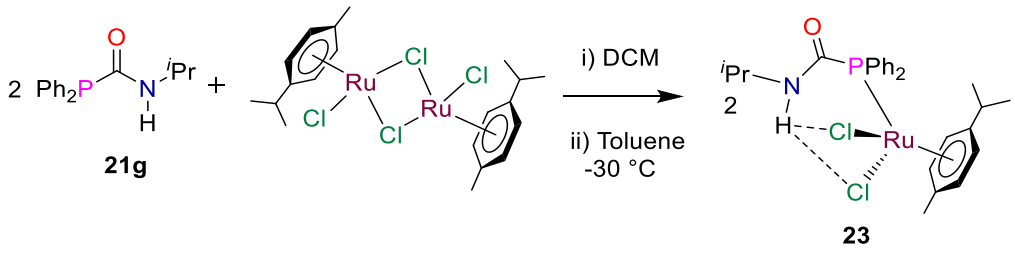


Scheme 4.6 Possible resonance forms for PCAs

4.3.4 Coordination of 21g and 22a to Dichloro(p-cymene) Ruthenium

Phosphines bearing carboxamide amide moieties have been described as an 'inconspicuous gem' by Štěpnička, where the combination of hard (N or O) and soft (P) donors on the molecule gives rise to the potential of these as use as hemilable donors.[1] These compounds have been shown to have applications in coordination chemistry,[1,38,41] biomedicine,[42,43] enantioselective catalysis[44,45] and supramolecular and self-assembled arrays.[46] Indeed, a recent report by Nakazawa and co-works found that reaction between a ferrocene derivative bearing a PCA moiety, Fe(η-$C_5H_4NHC(O)PPh_2)_2$ with $PtX_2(PPh_3)_2$ (X = Cl, Br) allowed for the unprecedented selective synthesis of M_4L_6 cage complex, facilitated by hydrogen bond between PCA moiety and the halide ion.[47]

With this in mind, preliminary investigations into the coordination capabilities of PCAs and PDCAs to dichloro(*p*-cymene) ruthenium dimer, $[Ru(p\text{-cym})Cl_2]_2$, were performed following a modified procedure as outlined by Goicoechea and co-workers.[38]



Scheme 4.7 Coordination of phosphinocarboxamide 21g to Ru(p-cym)Cl₂ .

A solution of $[Ru(p\text{-cym})Cl_2]_2$ and **21g** in a 1:2 ratio in dichloromethane was stirred at room temperature overnight, after removal of solvent, extraction into toluene resulted in the precipitation of pure product of **23** (Scheme 4.7). Analysis by X-ray diffraction revealed the solid state structure of **23** (Figure 4.6) which was in good agreement with ^{1}H, $^{13}C\{^{1}H\}$ and $^{31}P\{^{1}H\}$ NMR spectra.

The ^{1}H NMR shows signals for the PCA ligand in **23** which are shifted with respect to free ligand (**21g**) where the N*H* proton is shifted significantly downfield (8.63 *vs.* 5.35 ppm) due to the hydrogen bond donor interaction with the Cl atoms. This is also reflected in the $^{31}P\{^{1}H\}$ NMR which features a singlet at 29.8 ppm, a difference of *ca.* 34 ppm when compared to **21g** (Table 4.6). The C=O is shifted slightly upfield in the $^{13}C\{^{1}H\}$ NMR spectra with respect to **21g** indicating less multiple bond character of the carbonyl after coordination to the metal.

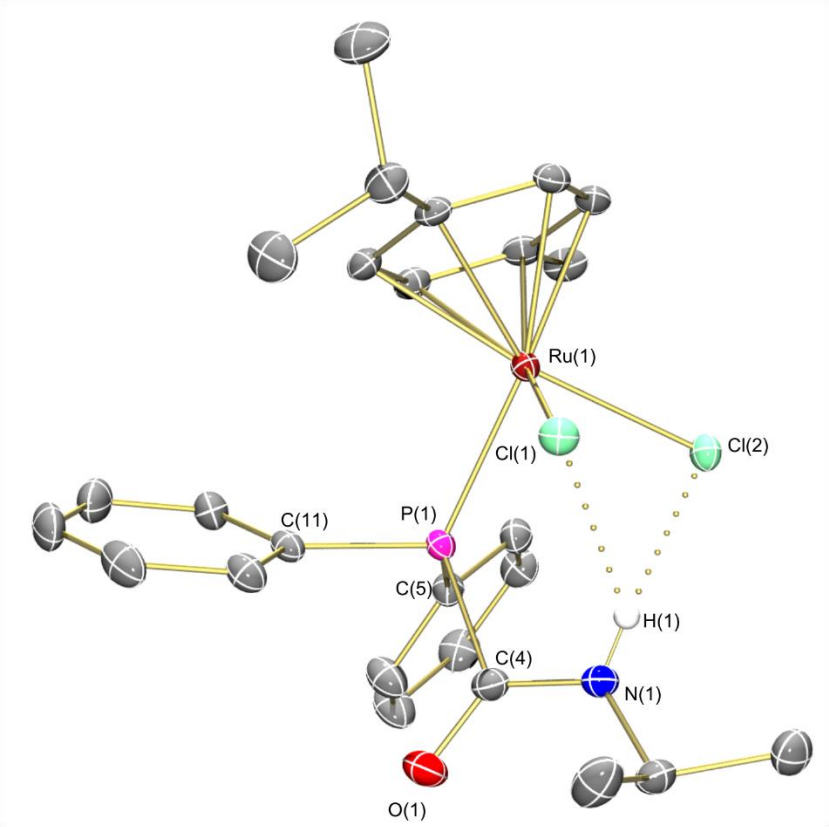


Figure 4.6 Crystal Structure of 23. Thermal ellipsoids are set at the 50% probability level. Hydrogen atoms [with the exception of H(1)] and solvent of recrystallisation molecules omitted for clarity.

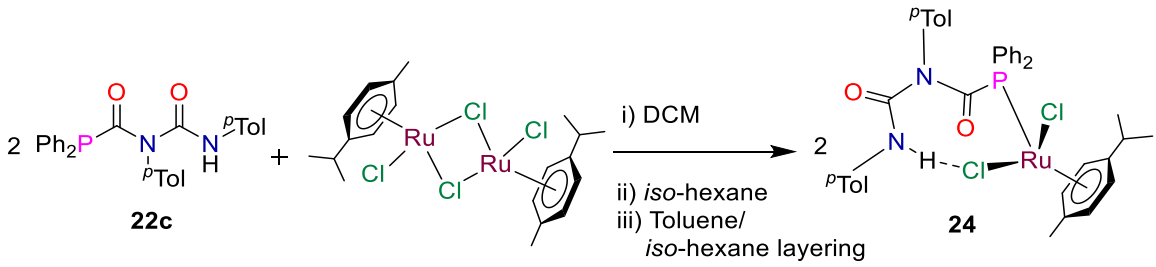
The molecular structure of **23** (Figure 4.6) features a ruthenium metal centre which is bonded to two chloride ions, the phosphorus atom from the PCA with an η^6 interaction with the *p*-cymene moiety. Selected bond distances and angles are shown in Table 4.9. The Ru–Cl and Ru–P bond lengths in **23** are within the sum of the Van der Waals radii between the two elements[37] and are similar to the related compound [Ru(*p*-cym){$PH_2C(O)NHCy$}Cl_2].[38]

The chloride ions form a hydrogen bond with the N*H* moiety of the PCA moiety of *ca.* 2.58 Å. The phosphorus atom features a distorted tetrahedral geometry where the C–P–C angles are less than the ideal 109° for a tetrahedron whereas the Ru–P–C angles are larger. The P–C, bond in **23** is slightly longer and the C–O and C–N bonds are slightly shorter than those found in **21g**.

	23
Ru(1)–Cl(1)	2.4115(5)
Ru(1)–Cl(2)	2.4183(5)
Ru(1)–P(1)	2.3476(5)
P(1)–C(4)	1.902(2)
C(4)–O(1)	1.217(3)
N(1)–C(1)	1.328(3)
N(1)–H(1)	0.80(3)
Cl(1)···H(1)	2.58(3)
Cl(1)···H(1)	2.57(3)
C(11)–P(1)–C(4)	100.55(9)
C(5)–P(1)–C(4)	99.83(9)
C(11)–P(1)–C(5)	105.02(9)
C(4)–P(1)–Ru(1)	120.52(6)
C(5)–P(1)–Ru(1)	117.60(7)
C(11)–P(1)–Ru(1)	110.96(6)

Table 4.9 Selected bond lengths (Å) and angles (°) of 23.

The analogous reaction of **22c** with $[Ru(p\text{-cym})Cl_2]_2$ (2:1) in dichloromethane over night at room temperature yielded an oily solid after removal of the solvent. This was triturated with *iso*-hexane and the resulting red solid was extracted into toluene, layered with *iso*-hexane which enabled crystallisation of a small quantity of **24** (Scheme 4.8). Analysis *via* $^{31}P\{^{1}H\}$ NMR suggested there was a mixture of species in solution with multiple peaks in the region of *ca.* 90-8 ppm. This was also reflected in the ^{1}H NMR spectrum which showed multiple overlapping peaks which hampered useful structural interpretation of **24**; presumably the sample of **22c** contained impurities prior to the reaction.



Scheme 4.8 Coordination of phosphinodicarboxamide 22c to Ru(p-cym)Cl₂

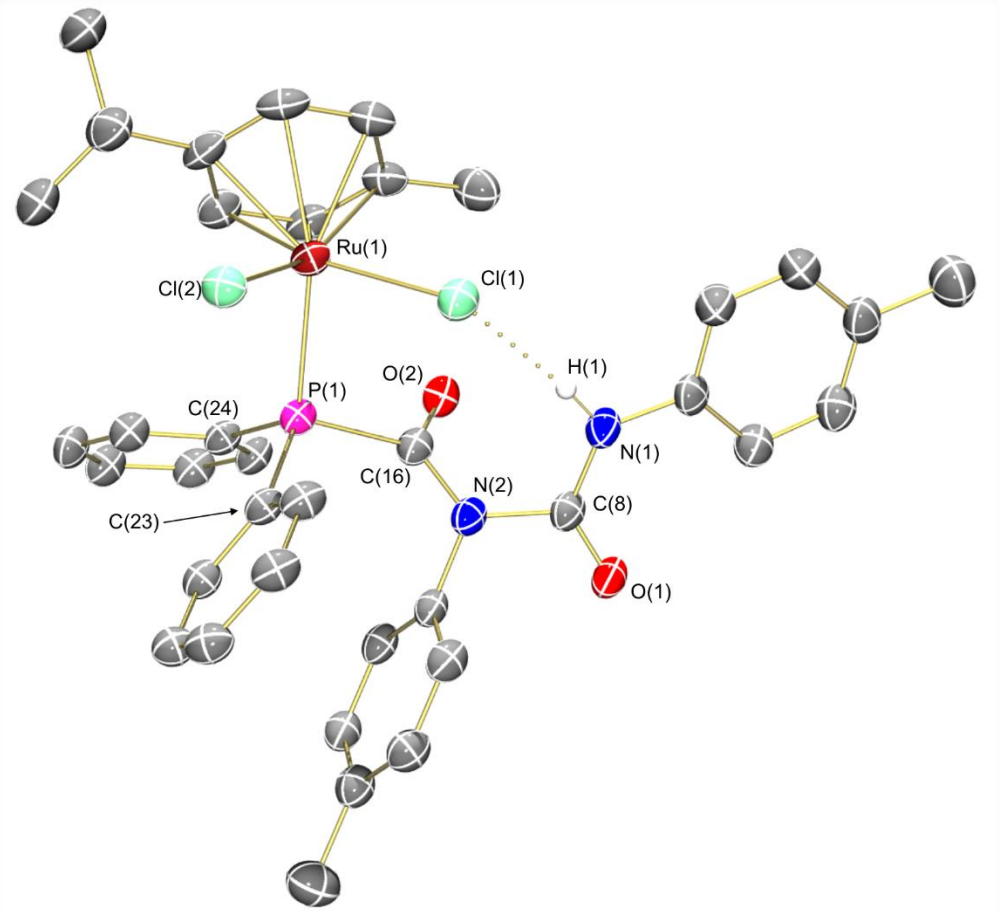


Figure 4.7 Crystal Structure of 24. Thermal ellipsoids are set at the 50% probability level. Hydrogen atoms [with the exception of H(2)] and solvent of recrystallisation molecules omitted for clarity.

It is also possible that there are enantiomeric isomers of **24** present in solution arising from the chirality at the Ru centre which could result in multiple resonances in the $^{31}P\{^{1}H\}$ NMR spetrum. Never the less, analysis by X-ray crystallography allows for comparison between the starting PDCA (**22c**) and the coordination product. The molecular structure of **24** crystallised in the monoclinic space group of $P2_1/c$ with one molecule of toluene in the asymmetric unit (Figure 4.7). The structure is very similar to that of **23** where the ruthenium centre is bonded to the *p*-cymene in an η^6 fashion, two chloride ions and the phosphorus atom from the PDCA moiety. The Ru–Cl and Ru–P bond distances are similar to those in **23** which also features a hydrogen bond interaction between one of the chloride ions and the N*H* proton (Table 4.10). The core of the PCDA in **24** is twisted somewhat compared

	24
Ru(1)–Cl(1)	2.4302(11)
Ru(1)–Cl(2)	2.3974(10)
Ru(1)–P(1)	2.3635(10)
P(1)–C(16)	1.898(4)
N(2)–C(16)	1.385(5)
C(8)–O(1)	1.213(5)
C(16)–O(2)	1.208(5)
N(1)–H(1)	0.874(3)
Cl(1)···H(1)	2.438(5)
C(23)–P(1)–C(16)	109.58(19)
C(24)–P(1)–C(16)	102.49(18)
C(24)–P(1)–C(23)	104.52(19)
C(16)–P(1)–Ru(1)	104.45(13)
C(23)–P(1)–Ru(1)	120.11(13)
C(24)–P(1)–Ru(1)	114.33(13)

Table 4.10 Selected bond lengths (Å) and angles (°) of 24.

to **22c** (Figure 4.8) which seems to be as a result of the π···π stacking interaction between the phosphorus aryl and the *p*-tolyl moiety and the hydrogen bonding interaction between the amide proton and chloride atoms (Figure 4.7). The phosphorus atom features a tetrahedral geometry where the C–P–C angles are slightly lower than idealised angle of 109° for a tetrahedron whereas the Ru–P–C angles are larger. The carbonyl (C–O) bond distances in **24** are slightly shorter that those in **23** [1.208(5), 1.213(5) *vs.* 1.224(3), 1.219(4) Å].

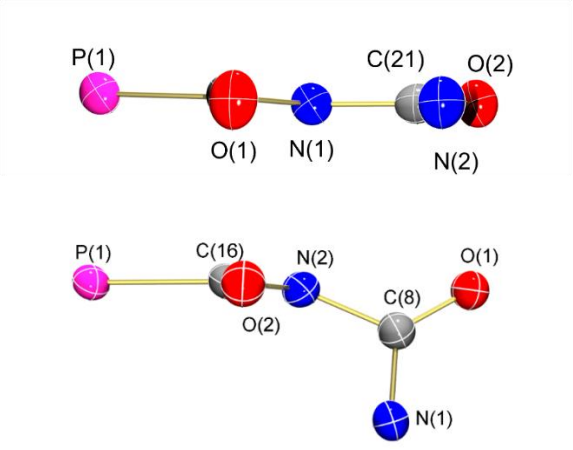


Figure 4.8 Core of PDCA in 22c (top) and 24 (bottom).

4.4 Conclusions

Two- and three-coordinate iron complexes, **11** and **16** respectively, were found to be efficient precatalysts for the hydrophosphination of isocyanates producing mono (PCA) and/or diinsertion (PDCA) products where the PDCAs are a new family of functionalised phosphines. This work represents the first example of an iron system to catalyse this reaction and also, the first example of the diinsertion process in the hydrophosphination of isocyanates.

The product obtained seems to be dominated by sterics of the isocyanate: bulky secondary and tertiary alkyl isocyanates produce almost exclusively the mono-insertion product (PCAs) whereas the less bulky aryl isocyanates (aryl and primary alkyl isocyanates) produce a mixture. When increasing the ratio of isocyanate to phosphine from 1:1 to 2:1 the corresponding PDCA is obtained in greater quantity.

Simple changes in the reaction conditions allows for control of the selectivity of hydrophosphination products obtained: the addition of a weak acid enables isolation of the PDCA. Changing the solvent from C_6D_6 to THF allows for the isolation of the PDA almost exclusively. The addition of a weak base did not significantly alter the reaction.

A plausible mechanism for the homogeneous catalysis is proposed in Scheme 4.5 where initial coordination of the isocyanate to the Lewis acidic iron centre is activated towards nucleophilic attack of the phosphine after which a 1,3-proton shift followed by displacement by an isocyanate generates the PCA (Cycle 1). If the isocyanate is less bulky the reaction can proceed through to Cycle 2 where the PCA reacts with the active species **B**, 1,3-proton shift followed by displacement of an isocyanate allows gives the PDCA. This agrees with experimental observations: the addition of the weak acid likely aids the 1,3-proton shift for species **D** and when the solvent is changed from C_6D_6 to THF

results in solvation of the PCA which therefore cannot react with species **B**. The increase in reaction rates when using **16** over **11** is possibly due to rapid formation for the iron amidate species **A** (Scheme 4.5) where the labile THF ligand and less bulky Tmp substituent in **16** facilitates this formation. Also, when using isocyanate mixtures (1:1:1 of Ph_2PH:CyNCO:PhNCO) a combination of four products are obtained (Scheme 4.2) where the PDCA product **22i**, [$Ph_2PC(=O)N(Ph)C(=O)NH(Cy)$] results from the coordination of CyNCO with nucleophilic attack of [$Ph_2PC(=O)N(H)Ph$].

The hydrophosphination products were scaled up successfully leading to good yields of the PCAs (**21a**,**c**,**d**,**f-h**) and PDCAs (**22a-d**) and were fully spectroscopically characterised. The crystal structures of all PCAs and the PDCAs **22a**,**b** were analysed *via* X-ray crystallography.

Initial coordination chemistry of PCA and PCDA was investigated with [Ru(*p*-cym)Cl_2]$_2$ leading to the isolation of coordination products **23** and **24**. The solid state structures show coordination of the PCA and PCDA to the ruthenium centre *via* the phosphorus lone pair. **23** and **24** feature intramolecular hydrogen bond interactions between the NH and Cl moieties. This interaction with the combination of the π···π stacking of the *p*-tolyl and a phosphorus-aryl substituent in **24** results in a significant twisting of the PDCA core (Figure 4.8) which highlights the flexibility of the PDCA ligand.

4.5 Future Work

The possible application of the PDCAs, a new class of functionalised phosphines, will be interesting to explore. The combination of the hard and soft donors present the potential to allow for the simultaneous coordination of two different transition metal centres in the synthesis of heterobimetallic complexes which may have applications in cooperative catalysis.[48] This could be achieved by first coordination of the phosphine to one transition metal centre, subsequent deprotonation at the NH moiety then a salt metathesis reaction with another transition metal halide.

It would also be useful to isolate intermediates by performing a stoichiometric reaction at low temperatures. This would allow further understanding of the mechanism and to help verify the proposed mechanism.

The scope of the hydrophosphination reaction could also be extended to other commercially available phosphines such as Cy_2PH, $(t\text{-}Bu)_2PH$ and $(1\text{-}Ad)_2PH$. Other heterocumulenes could also be used in hydrophosphination reactions such as carbodiimides and isothiocyanates which would be interesting to investigate whether diinsertion products are obtained. Other low-coordinate manganese, cobalt and zinc *m*-terphenyl complexes could also be investigated in this reaction to study how changing the metal centre affects the catalytic ability.

These systems could also be extended to other hydroelementation reactions such as hydroamination, hydrosilyation, hydroalkoxylation and hydrothiolation which are particularly attractive due to their atom economical routs to various families of organic compounds.[49]

4.6 References

1 P. Štěpnička, *Chem. Soc. Rev.*, 2012, **41**, 4273.

2 D. W. Allen, *Phosphines and related P–C bonded compounds*, 2016, vol. 45.

3 I. Wauters, W. Debrouwer and C. V. Stevens, *Beilstein J. Org. Chem.*, 2014, **10**, 1064–1096.

4 C. A. Bange and R. Waterman, *Chem. Eur. J.*, 2016, **22**, 12598–12605.

5 V. Koshti, S. Gaikwad and S. H. Chikkali, *Coord. Chem. Rev.*, 2014, **265**, 52–73.

6 L. Rosenberg, *ACS Catal.*, 2013, **3**, 2845–2855.

7 M. Kamitani, M. Itazaki, C. Tamiya and H. Nakazawa, *J. Am. Chem. Soc.*, 2012, **134**, 11932–11935.

8 J. P. W. Stelmach, C. A. Bange and R. Waterman, *Dalton Trans.*, 2016, **45**, 6204–6209.

9 A. M. Geer, Á. L. Serrano, B. De Bruin, M. A. Ciriano and C. Tejel, *Angew. Chem. Int. Ed.*, 2015, **54**, 472–475.

10 R. G. Belli, K. M. E. Burton, S. A. Rufh, R. McDonald and L. Rosenberg, *Organometallics*, 2015, **34**, 5637–5646.

11 P. E. Sues, A. J. Lough and R. H. Morris, *J. Am. Chem. Soc.*, 2014, **136**, 4746–4760.

12 F. Jérôme, F. Monnier, H. Lawicka, S. Dérien and P. H. Dixneuf, *Chem. Commun.*, 2003, 696–697.

13 E. Costa, P. G. Pringle and K. Worboys, *Chem. Commun.*, 1998, 49–50.

14 S. Sabater, J. A. Mata and E. Peris, *Organometallics*, 2013, **32**, 1112–1120.

15 L. Routaboul, F. Toulgoat, J. Gatignol, J. F. Lohier, B. Norah, O. Delacroix, C. Alayrac, M. Taillefer and A. C. Gaumont, *Chem. Eur. J.*, 2013, **19**, 8760–8764.

16 R. J. Batrice and M. S. Eisen, *Chem. Sci.*, 2016, **7**, 939–944.

17 I. S. R. Karmel, M. Tamm and M. S. Eisen, *Angew. Chem. Int. Ed.*, 2015, **54**, 12422–12425.

18 W. Ma, L. Xu, W.-X. Zhang and Z. Xi, *New J. Chem.*, 2015, **39**, 7649–7655.

19 X. Gu, L. Zhang, X. Zhu, S. Wang, S. Zhou, Y. Wei, G. Zhang, X. Mu, Z. Huang, D. Hong and F. Zhang, *Organometallics*, 2015, **34**, 4553–4559.

20 C. A. Busacca, J. A. Milligan, E. Rattanangkool, C. Ramavarapu, A. Chen, A. K. Saha, Z. Li, H. Lee, S. J. Geib, G. Wang, C. H. Senanayake and P. Wipf, *J. Org. Chem.*, 2014, **79**, 9878–9887.

21 A. C. Behrle and J. A. R. Schmidt, *Organometallics*, 2013, **32**, 1141–1149.

22 W.-X. Zhang and Z. Hou, *Org. Biomol. Chem.*, 2008, **6**, 1720–1730.

23 W. X. Zhang, M. Nishiura, T. Mashiko and Z. Hou, *Chem. Eur. J.*, 2008, **14**, 2167–2179.

24 F. Alonso, I. P. Beletskaya and M. Yus, *Chem. Rev.*, 2004, **104**, 3079–3159.

25 M. De Tullio, A. Hernán-Gómez, Z. Livingstone, W. Clegg, A. R. Kennedy, R. W. Harrington, A. Antinolo, A. Martínez, F. Carrillo-Hermosilla and E. Hevia, *Chem. Eur. J.*, 2016, **22**, 17646–17656.

26 M. R. Crimmin, A. G. M. Barrett, M. S. Hill, P. B. Hitchcock and P. A. Procopiou, *Organometallics*, 2008, **27**, 497–499.

27 Y. Sun, Z. Zhang, X. Wang, X. Li, L. Weng and X. Zhou, *Dalton Trans.*, 2010, **39**, 221–226.

28 J. A. Widegren and R. G. Finke, *J. Mol. Catal. A Chem.*, 2003, **198**, 317–341.

29 R. H. Crabtree, *Chem. Rev.*, 2012, **112**, 1536–1554.

30 K. J. Gallagher and R. Webster, *Chem. Commun.*, 2014, **50**, 12109–12111.

31 A. D. Sadow and A. Togni, *J. Am. Chem. Soc.*, 2005, **127**, 17012–17024.

32 M. A. Kazankova, M. O. Shulyupin and I. P. Beletskaya, *Synlett.*, 2003, **2**, 2155–2158.

33 B. M. Cochran and F. E. Michael, *J. Am. Chem. Soc.*, 2008, **130**, 2786–2792.

34 M. R. Douglass, C. L. Stern and T. J. Marks, *J. Am. Chem. Soc.*, 2001, **123**, 10221–10238.

35 P. Pyykkö and M. Atsumi, *Chem. Eur. J.*, 2009, **15**, 186–197.

36 B. Cordero, V. Gómez, A. E. Platero-Prats, M. Revés, J. Echeverría, E. Cremades, F. Barragán and S. Alvarez, *Dalton Trans.*, 2008, 2832–2838.

37 S. S. Batsanov, *Inorg. Mater.*, 2001, **37**, 871–885.

38 A. R. Jupp, G. Trott, É. Payen De La Garanderie, J. D. G. Holl, D. Carmichael and J. M. Goicoechea, *Chem. Eur. J.*, 2015, **21**, 8015–8018.

39 T. P. Robinson and J. M. Goicoechea, *Chem. Eur. J.*, 2015, **21**, 5727–5731.

40 A. R. Jupp and J. M. Goicoechea, *J. Am. Chem. Soc.*, 2013, **135**, 19131–19134.

41 M. B. Geeson, A. R. Jupp, J. E. McGrady and J. M. Goicoechea, *Chem. Commun.*, 2014, **50**, 12281–12284.

42 C. Fernandes, J. D. G. Correia, L. Gano, I. Santos, S. Seifert, R. Syhre, R. Bergmann and H. Spies, *Bioconjug. Chem.*, 2005, **16**, 660–668.

43 L. Meléndez-Alafort, A. Nadali, G. Pasut, E. Zangoni, R. De Caro, L. Cariolato, M. C. Giron, I. Castagliuolo, F. M. Veronese and U. Mazzi, *Nucl. Med. Biol.*, 2009, **36**, 57–64.

44 M. Leautey, P. Jubault, X. Pannecoucke and J.-C. Quirion, *Eur. J. Org. Chem.*, 2003, 3761–3768.

45 F. Sladojevich, A. Trabocchi, A. Guarna and D. J. Dixon, *J. Am. Chem. Soc.*, 2011, **133**, 1710–1713.

46 D. T. Seidenkranz, J. M. McGrath, L. Zakharov and M. D. Pluth, *Chem. Commun.*, 2017, **53**, 561–564.

47 M. Ito, M. Iseki, M. Itazaki and H. Nakazawa, *Chem. Commun.*, 2016, **52**, 7205–7208.

48 P. Buchwalter, J. Rosé and P. Braunstein, *Chem. Rev.*, 2015, **115**, 28–126.

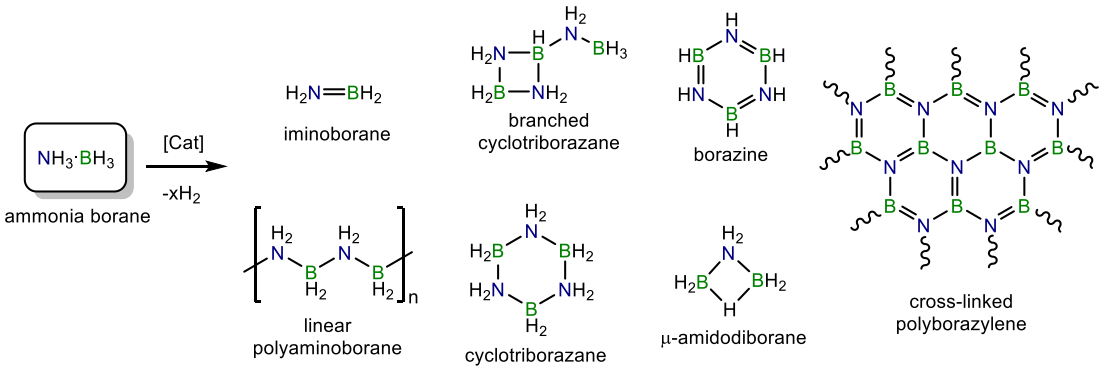
49 X. Zeng, *Chem. Rev.*, 2013, **113**, 6864–6900.

Chapter V

Dehydrocoupling of Amine-Boranes

5.1 Introduction

Dehydrocoupling reactions involve the formation of element-element bonds with the sole by-product being the formation of H_2 gas.[1] The catalytic dehydrocoupling on amine-boranes ($R_2NH{\cdot}BH_3$ where R = H or alkyl) has attracted much attention due to their potential use as a chemical hydrogen storage material as ammonia borane, $NH_3{\cdot}BH_3$, has a high hydrogen content by mass (19.6%).[2,3] Amine-boranes have further uses such as reagents for hydrogen transfer to organic and inorganic substrates,[4–6] and as precursors to BN-based ceramics and polymeric materials.[7–9]



Scheme 5.1 Catalytic dehydrocoupling of ammonia borane with possible boron nitrogen intermediates and products.

Catalytic dehydrocoupling of amine-boranes can be easily monitored through convenient use of ^{11}B NMR spectroscopy and can yield a variety of products as shown in Scheme 5.1,[10] and has been explored extensively through use of group 1[11], group 2,[12–15] group 3,[16] group 4[7,15,17,18], precious metals (*e.g* Ru,[19] Rh,[20,21] Ir,[7] Pd,[22]), rare earth,[23] main group[24] and frustrated Lewis pair[25] based catalysts. Nishibayashi and co-workers have also reported the use of heterobimetallic complexes which catalyse the dehydrogenation of $Me_2NH{\cdot}BH_3$ where it is proposed that the two metal centres cooperatively participate in the catalysis.[26]

There are numerous examples of first row transition metal catalysts which have been used in the dehydrocoupling of amine-boranes such as Cr,[27] Fe,[28–33] Co,[34,35] Ni.[36,37] However, the only manganese based example is limited to the half sandwich carbonyl complex, $CpMn(CO)_3$, by Shimoi and co-workers, which suffers from long reaction times and requires photoinitiation.[27]

Herein, the catalysis of the dehydrocoupling of amine-boranes using two- and three-coordinate transition metal *m*-terphenyl complexes is described, with the main focus being the use of manganese(II) complexes.

5.2 Experimental

5.2.1 Catalytic Dehydrocoupling of NH_3·BH_3

In a Young's NMR tube 10 mol% of precatalyst **10**, (10.0 mg, 0.0147 mmol) and NH_3·BH_3 (4.7 mg, 0.147 mmol) were dissolved in THF (0.6 mL) with a C_6D_6 insert. The reactions were kept at room temperature and monitored by ^{11}B NMR spectroscopy. Conversion was quantified by integration of ^{11}B NMR spectra.

5.2.2 Catalytic Dehydrocoupling of NH_3·BH_3, with Hydrogen Acceptor

In a Young's NMR tube 10 mol% of precatalyst **10** or **11**, (10.0 mg, 0.0147 mmol), NH_3·BH_3 (4.7 mg, 0.147 mmol) and 3,3-dimethyl-1-butene (2 eq., 38 µL, 0.294 mmol; or 25 eq., 475 µL, 3.68 mmol) were dissolved in THF (0.6 mL) with a C_6D_6 insert. The reactions were kept at room temperature and monitored by ^{11}B NMR spectroscopy. Conversion was quantified by integration of ^{11}B NMR spectra.

5.2.3 Standard Procedure for the Catalytic Dehydrocoupling of Me_2NH·BH_3

In a Young's NMR tube 5 or 2 mol% of precatalyst **10**, **13** or **15** and Me_2NH·BH_3 were dissolved in C_6D_6 (0.6 mL). The reactions were either carried out at room temperature or heated to 60 °C for 16 h in a sealed NMR tube (closed system). Conversion was quantified by integration of ^{1}H and ^{11}B NMR spectra. See Table 5.1 for quantities of reagents used.

Precatalyst			***$Me_2NH{\cdot}BH_3$***	
Cat. (mol%)	***mg***	***mmol***	***mg***	***mmol***
10 (5)	10.0	0.0147	17.3	0.294
10 (2)	5.0	0.00733	21.5	0.367
13 (5)	10.0	0.0160	18.9	0.320
13 (2)	5.0	0.00799	23.7	0.400
15 (5)	10.0	0.0133	15.7	0.266
15 (2)	5.0	0.00663	19.7	0.322

Table 5.1 Quantities of precatalyst and $Me_2NH{\cdot}BH_3$ used in reactions.

5.2.4 In situ NMR Reaction Monitoring for the Catalytic Dehydrocoupling of $Me_2HN{\cdot}BH_3$

In a Young's NMR tube 5 mol% of precatalyst **10**, **13** or **15** was dissolved in C_6D_6 (0.4 mL) and cooled to –30 °C after which $Me_2NH{\cdot}BH_3$ in C_6D_6 (0.2 mL) was added and the sample cooled to –78 °C to prevent the reaction from initiating. The sample was transferred to the NMR spectrometer and monitored directly at 60 °C. Conversion was quantified by integration of ^{1}H and ^{11}B NMR spectra. See Table 5.1 for quantities of reagents used.

5.2.5 Catalyst Poisoning Tests

5.2.5.1 Mercury Drop Test

In a Young's NMR tube was added 5 mol% of precatalyst **10**, **13** or **15** and $Me_2NH{\cdot}BH_3$ in C_6D_6 (0.6 mL) with mercury (*ca.* 1 drop). The reaction mixture was heated at 60 °C for 16 h and were monitored by ^{1}H and ^{11}B NMR spectroscopy at the final time. See Table 5.1for quantities of reagents used.

5.2.5.2 CS_2

In a Young's NMR tube 5 mol% of precatalyst **10** or **13** was dissolved in C_6D_6 (0.4 mL) with CS_2 (0.05 M in toluene; **10**: 29 µL, 0.00147 mmol; **13**: 32 µL, 0.0016 mmol) and cooled to –30 °C after which $Me_2NH{\cdot}BH_3$ in C_6D_6 (0.2 mL) was added and the sample cooled to –78 °C to prevent the reaction from initiating. The sample was transferred to the NMR spectrometer and monitored directly at 60 °C. Conversion was quantified by integration of ^1H and ^{11}B NMR spectra. See Table 5.1 for quantities of reagents used.

5.2.5.3 Radical Trap Test

In a Young's NMR tube 5 mol% of precatalyst **10** or **13** was dissolved in C_6D_6 (0.4 mL) with cumene (**10**: 10 µL, 0.0735 mmol; **13**: 11 µL, 0.0800 mmol) and cooled to –30 °C after which $Me_2NH{\cdot}BH_3$ in C_6D_6 (0.2 mL) was added and the sample cooled to –78 °C to prevent the reaction from initiating. The sample was transferred to the NMR spectrometer and monitored directly at 60 °C. Conversion was quantified by integration of ^1H and ^{11}B NMR spectra. See Table 5.1 for quantities of reagents used.

5.3 Results and Discussion

5.3.1 Catalytic Dehydrocoupling of NH_3·BH_3, by Manganese(II) and Iron(II) Precatalysts

An initial assessment of the catalytic ability of the mesityl-substituted *m*-terphenyl complexes of manganese and iron (**10** and **11** respectively) in the dehydrocoupling of NH_3·BH_3 were undertaken. These reactions were performed in a sealed Young's NMR tube in THF with a C_6D_6 and were followed by ^{11}B NMR spectroscopy at room temperature (Table 5.2). The manganese catalyst **10** in the relatively high catalyst loading of 10 mol% had only reached 4% conversion to products in 6 h (entry 1). Upon the addition of a hydrogen acceptor 3,3-dimethyl-1-butene (2 equivalents) with 10 mol% of **10** or **11**, very low conversions to dehydrocoupled products were observed (entries 2 and 3).

Entry	*Cat.(mol %)*	*Additive*	*T (°C)*	*Time (h)*	*Conv. (%)*
1	**10** (10)	None	r.t.	6	4
2	**10** (10)	2 eq. 	r.t.	24	16
3	**11** (10)	2 eq. 	r.t.	30	27
4	**10** (10)	25 eq. 	r.t.	65	12

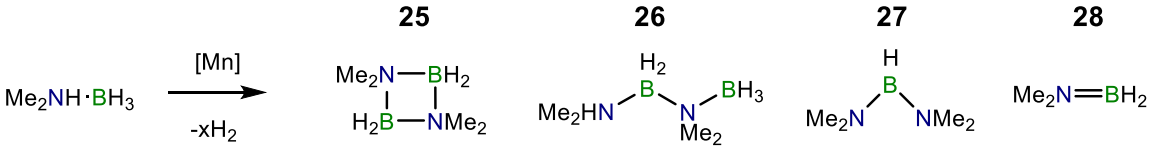
Table 5.2 Dehydrocoupling of ammonia borane H_3N·BH_3 with 10 and 11. Reaction conditions: room temperature (20 ℃ ± 2), 0.6 mL of THF with C_6D_6 insert. Conversion determined by ^{11}B NMR spectroscopy.

Increasing the amount of hydrogen acceptor to 25 equivalents with respect to ammonia borane did not aid the progress of the reaction (entry 4). In all cases, a significant amount of black precipitate was observed indicating that the catalyst was decomposing into an unidentified inactive species. With this in mind, it is evident that these two-coordinate species are unsuitable for the catalytic dehydrocoupling of ammonia borane and therefore were not explored further.

5.3.2 Catalytic Dehydrocoupling of $Me_2NH{\cdot}BH_3$ by Manganese(II) Precatalysts

The activity of two- and three-coordinate manganese(II) complexes (**10**, **13** and **15**) were explored in the dehydrocoupling of $Me_2NH{\cdot}BH_3$, in order to investigate how the ligand environment affects the catalytic activity of the complex and distribution of products obtained. All reactions were performed in C_6D_6 at either room temperature or 60 °C and were monitored after 16 h by ^1H and ^{11}B NMR spectroscopy. Upon addition of $Me_2NH{\cdot}BH_3$ to the precatalyst, bubbles of hydrogen appeared in the NMR tube suggesting an immediate reaction. However, in the case of **15**, after the addition of dimethylamine borane to precatalyst **15**, the reaction mixture turned dark black.

Numerous products (**25**-**28**) were observed in the ^1H and ^{11}B NMR spectra of the reactions as shown in Scheme 5.2, with the corresponding ^{11}B NMR shifts displayed



Scheme 5.2 Products obtained from dehydrocoupling of $Me_2NH{\cdot}BH_3$ using Mn(II) precatalysts 10, 13 and 15.

in Table 5.3. As there is an overlap between the chemical shifts of the BH_3 moiety in the linear diborazane Me_2NH-BH_2-Me_2N-BH_3 (**26**) and in $Me_2NH{\cdot}BH_3$ (δ_B –13.1 ppm, Table 5.3, entries 1 and 3) the presence of **26** is confirmed from the triplet from the BH_2 moiety in **26** at 2.3 ppm.[38] This has been accounted for when calculating the conversion (%) to products when **26** is present in the reaction mixture.

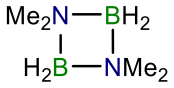
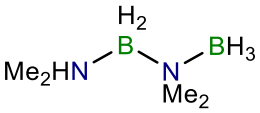
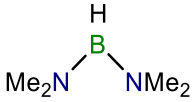
Entry		*Compound*	*^{11}B NMR δ (ppm)*
1		$Me_2NH{\cdot}BH_3$	–13.1 (q, ^1J(B,H) = 97 Hz, *B*H_3)
2	**25**		5.6 (t, ^1J(B,H) = 113 Hz, *B*H_2)
3	**26**		2.3 (t, ^1J(B,H) = 109 Hz, *B*H_2), –13.1, (q, ^1J(B,H) = 97 Hz, *B*H_3)
4	**27**		29.1 (d, ^1J(B,H) = 131 Hz, *B*H)
5	**28**	$Me_2N{=}BH_2$	38.5 (t, ^1J(B,H) = 128 Hz, *B*H_2)

Table 5.3 ^{11}B NMR shifts for dimethylamine borane and the corresponding dehydrocoupling products from reactions catalysed by 10, 13 and 15.

5.3.2.1 Closed Reaction System

The manganese precatalysts **10**, **13**, and **15** were employed at a 5 mol% catalyst loading at room temperature in a sealed NMR tube (closed system). After 16 h the progress of the reactions were monitored by ^{1}H and ^{11}B NMR spectroscopies. All three precatalysts gave poor conversion to products (Table 5.4, entries 1-3) affording **26** as the major product in all cases. Upon increase of reaction temperature to 60 °C, after 16 h the ^{1}H and ^{11}B NMR spectra showed complete consumption of $Me_2NH{\cdot}BH_3$ to products where the major product in all cases is the cyclic dimer$(Me_2N–BH_2)_2$ (**25**) (Table 5.4, entries 4-6).

Entry	*Cat. (mol%)*	*Temp. (° C)*	*Additive*	*Conversion (%)*	*Product (%)*			
					25	***26***	***27***	***28***
1	**10** (5)	r.t.	-	33	10	84	3	3
2	**13** (5)	r.t.	-	15	24	76	0	0
3	**15** (5)	r.t	-	38	28	69	2	1
4	**10** (5)	60	-	100	98	0	2	0
5	**13** (5)	60	-	100	99	0	0	1
6	**15** (5)	60	-	100	98	0	1	1
7	**10** (2)	60	-	75	95	4	1	0
8	**13** (2)	60	-	94	98	1	1	0
9	**15** (2)	60	-	100	99	0	1	0
10	**10** (5)[a]	60	Hg	90	60	40	0	0
11	**13** (5)[b]	60	Hg	92	98	0	0	2
12	**15** (5)	60	Hg	29	83	14	1	2

Table 5.4 Reaction conditions: closed system, 16 h, 0.6 mL of C_6D_6. Conversion determined by ^1H and ^{11}B NMR spectroscopy. [a] reaction time = 4 h. [b] Reaction time = 2 h

Small quantities of the diaminoborane $HB(NMe_2)_2$ and the aminoborane $Me_2N{=}BH_2$ (**27** and **26** respectively, Scheme 5.2) were also observed in all reactions (*ca.* 2%). The higher proportion of **26** observed in the room temperature reactions compared to the reactions carried out at 60 °C indicates that **26** is likely an intermediate to the formation of the cyclic dimer **25**. This has also been observed in other dehydrocoupling reactions with dimethylamine borane using Ti(II),[38] Fe(II),[32] Sc(III)[16] and Rh(I)[21] catalytic systems. Upon lowering the catalyst loading from 5 to 2 mol% (Table 5.4, entries 7-9) moderate to excellent conversion to products were observed after 16 h at 60 °C where **25** is obtained

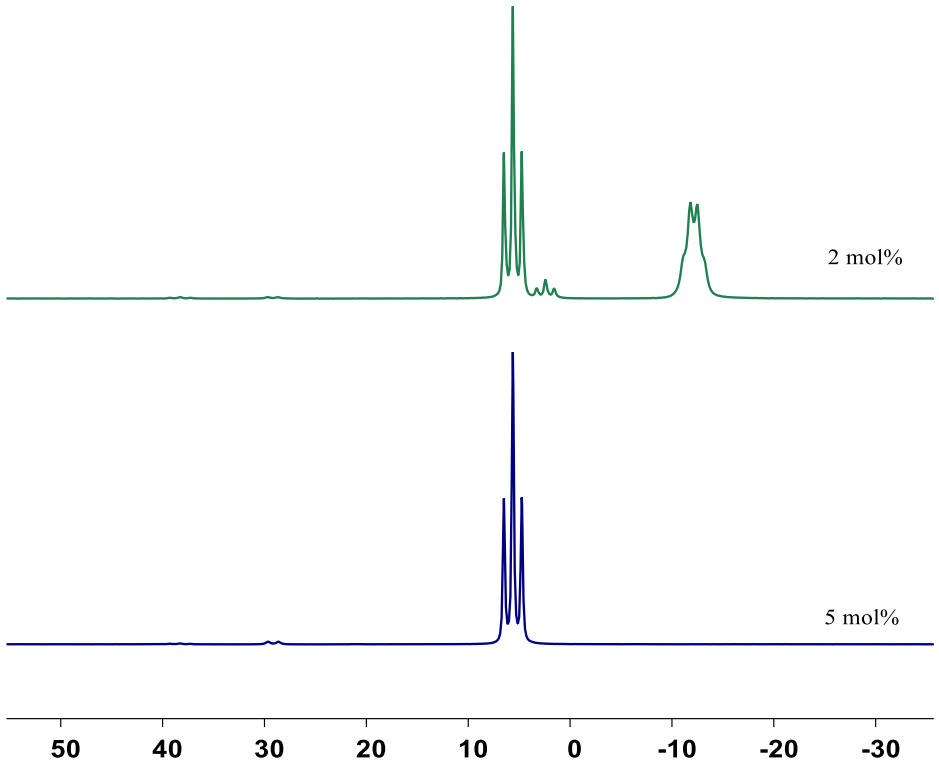


Figure 5.1 ^{11}B NMR spectra of the dehydrocoupling of dimethylamine borane with 10 at 2 mol% (above) or 5 mol% (below) catalyst loading.

almost exclusively (>94%). When precatalyst **10** was employed, the conversion dropped quite significantly from 100% to 75% as the catalyst loading was lowered from 5 to 2 mol% (Figure 5.1), accompanied by a larger amount of **26** (4%) compared to the analogous reaction with **13** and **15** (<1%) at 2 mol%.

5.3.2.2 In situ Reaction Monitoring

To gain further insight into the dehydrocoupling of dimethylamine borane with the manganese(II) precatalysts, the reactions using **10**, **13** and **15** at 5 mol% loading were monitored directly in the NMR spectrometer at 60 °C *via* ^{1}H and ^{11}B NMR spectroscopies. The ^{11}B NMR spectra were processed using back linear prediction to eliminate the broad peak arising from the borosilicate NMR tube. A consequence of this

processing method is that broad peaks can often be removed therefore the conversions were confirmed by comparison of ^{1}H and ^{11}B NMR spectra. Furthermore, as the precatalysts are paramagnetic and the spectra were recorded at 60 °C, significant broadening of the NMR spectra were also observed.

The samples were prepared by dissolving the precatalyst in C_6D_6 (0.4 mL) and cooled to –30 °C after which dimethylamine borane in C_6D_6 (0.2 mL) was added and quickly cooled to –78 °C to prevent the reaction from proceeding. The sample was transferred to the NMR spectrometer and heated to 60 °C and the reaction was monitored *via* ^{1}H and ^{11}B NMR.

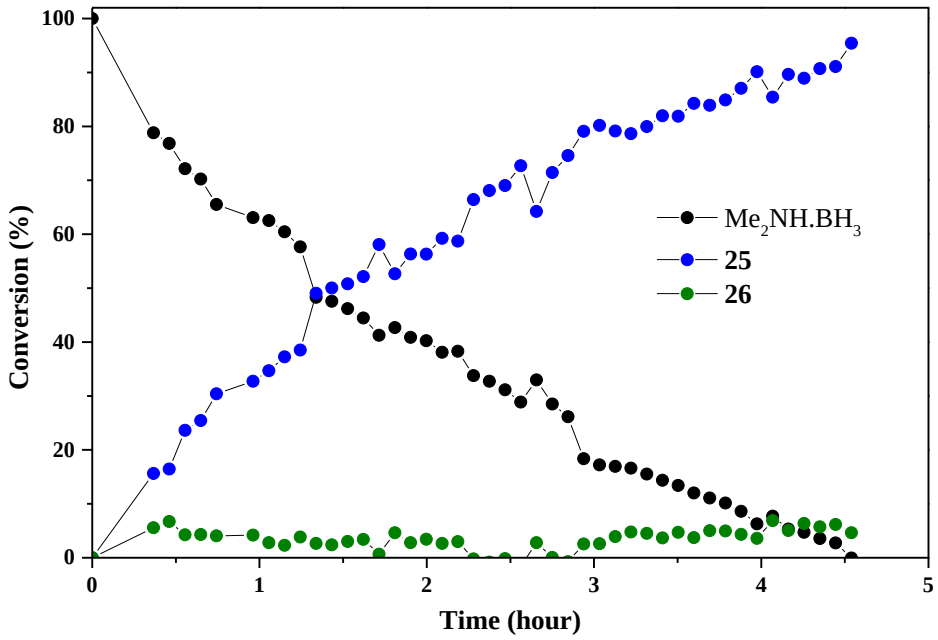


Figure 5.2 Conversion (%) vs. time (h) for the dehydrocoupling of $Me_2NH{\cdot}BH_3$ using 10 (5 mol%) at 60 °C followed by ^{11}B NMR. Products 27 and 28 were observed in small quantites (<4%) and omitted for clarity.

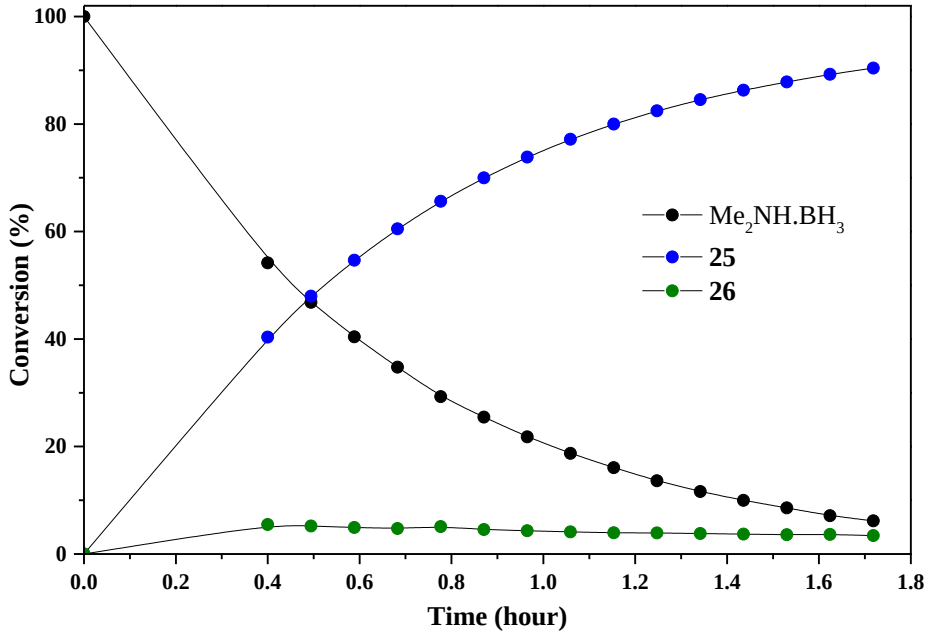


Figure 5.3 Conversion (%) vs. time (h) for the dehydrocoupling of $Me_2NH{\cdot}BH_3$ using 13 (5 mol%) at 60 °C followed by ^1H NMR. Products 27 and 28 were observed in the ^{11}B NMR spectra in small quantities (<2%).

When **10** was employed at 5 mol% catalyst loading, after *ca*. 4.5 h complete consumption of $Me_2NH{\cdot}BH_3$ was observed with formation of dimer **25** accompanied by small amounts of **26** (Figure 5.2). When **13** was used, however, the peaks corresponding to dimethylamine borane and the signal for the BH_3 unit for **26** were very broad it was therefore not possible to observe them in the ^{11}B NMR spectra, which is possibly a consequence of the interaction of the BH_3 unit with the paramagnetic manganese centre. In this case, the conversion was quantified solely by ^1H NMR by integration of the methyl peaks in $Me_2NH{\cdot}BH_3$, **25** and **26** occurring at δ_H = 1.87, 2.24 and 2.33 ppm respectively. The graph of conversion to products can be seen in Figure 5.3 which shows smooth conversion from $Me_2NH{\cdot}BH_3$ to the dimeric species **25** accompanied by very small amounts of **26**. When assessing the ^{11}B NMR spectra it can be seen that in the early stages in the reaction a small amount of **26** is observed at 2.3 ppm arising from the internal BH_2

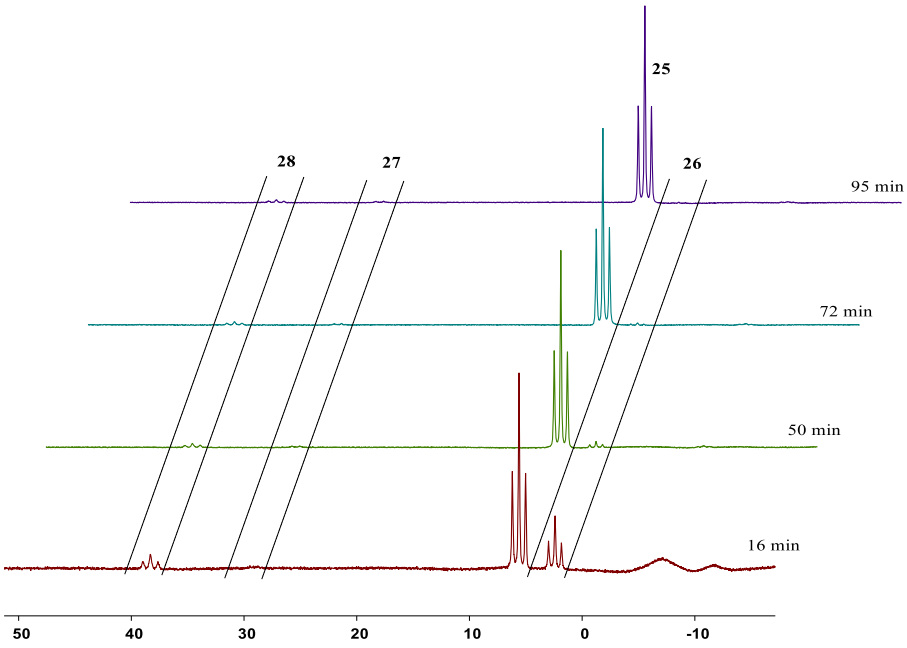


Figure 5.4 ^{11}B NMR spectra obtained from the dehydrocoupling of $Me_2NH{\cdot}BH_3$ using 13 (5 mol%) at 60 °C.

moiety of **26** which decreases with time to **25** (Figure 5.4). When monitoring **15** at 5 mol% catalyst loading with $Me_2NH{\cdot}BH_3$, the reaction reached full conversion after 14 h (Figure 5.5), which is significantly longer than that for the analogous reactions with **10** and **13**. In the case of **15**, free THF can been seen in the ^{1}H NMR spectra, so a likely first step of this reaction is disassociation of the coordinating THF ligand. Calculation of TOF (after 60% conversion of $Me_2NH{\cdot}BH_3$ to products at 60 °C) for each reaction revealed the best performing precatalyst is **13** (where TOF = 6.0, 19.4 and 7.1 h^{-1} for **10**, **13** and **15** respectively).

In all cases no induction period was observed suggesting that the catalysis is homogeneous.[39,40] However, the absence of the induction period could indicate that the nanoparticles (NPs) are formed immediately upon addition of the amine-borane; no induction period was similary reported by Morris *et al.* in the dehydrogenation of ammonia-borane by iron NPs.[41]

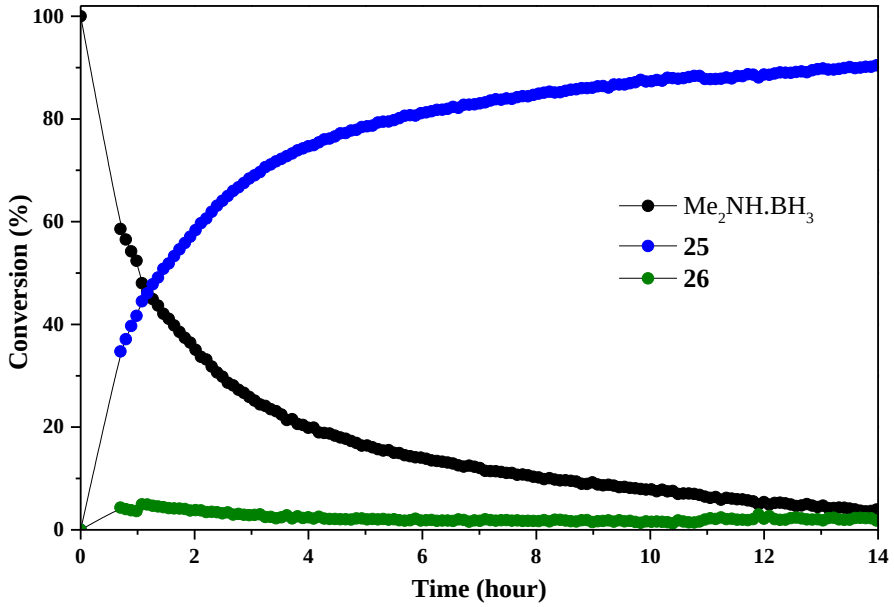


Figure 5.5 Conversion (%) vs. time (h) for the dehydrocoupling of $Me_2NH{\cdot}BH_3$ using 5 mol% of 15 at 60 °C followed by ^1H NMR. Products 27 and 28 were observed in small quantities (<4%) and not displayed for clarity.

5.3.2.3 Catalyst Poisoning Experiments

In order to assess whether the catalysis is homogeneous or heterogeneous the mercury drop test was undertaken using the three precatalysts at 5 mol% at 60 °C (Table 5.4, entries 10-12). The reactions using **10** and **13** in the presence of this additive reached similar conversions to those without mercury after 4 and 2 hours respectively indicating that these reactions are homogeneous. However, when using **15** the conversion from dimethylamine borane to products was significantly lower from 100% to 29% (Table 5.4, entries 6 and 12) suggesting that mercury had formed an amalgam with manganese particles which are the active catalyst in the reaction. It is of note that upon the addition of $Me_2NH{\cdot}BH_3$ to the precatalyst **15**, the reaction mixture instantly turns from a colourless solution to a black suspension, suggesting the possible formation of manganese particles.

Further catalyst poisoning tests were undertaken using precatalysts **10** and **13** at 5 mol% and monitored directly in the NMR spectrometer. To elucidate further if the reaction proceeds through a homogeneous reaction pathway CS_2 (10 mol% of precatalyst) was added into the reaction mixture which did not alter the reaction rate.[40,39] The presence of an excess of cumene, which acts as a radical trap,[42] had no effect on the reaction rate with using precatalysts **10** and **13** indicating that the reaction are not radical mediated.

5.3.3 Particle Size Measurements

5.3.3.1 Preliminary TEM Measurements

The observation of a colour change from colourless solution to dark black suspention on addition of dimethylamine borane to the precatalyst **15** and that the addition of mercury results in the significantly lowered reaction rate indicates that the active catalyst in the dehydrogenation of $Me_2NH{\cdot}BH_3$ is heterogeneous, which presented the possibility of manganese particles in the reaction mixture. To determine the morphology of the sample, *e.g.* aggregates of small particles or simply large particles, and chemical composition, samples of the reaction mixture were analysed transmission electron microscopy (TEM), scanning electron microscopy (STEM) and energy dispersive X-ray (EDX) spectroscopy. The reaction solution of **15** (5 mol% catalyst loading) and $Me_2NH{\cdot}BH_3$ in C_6D_6 (0.6 mL), after heating at 60 °C for 16 h, was diluted with *ca*. 2 mL of benzene. An aliquot of the reaction solution in benzene was opened up to air and spotted onto a copper-mounted carbon film and left at room temperature overnight. The TEM micrographs show large clusters of particles measuring *ca.* 1 μm in diameter (Figure 5.6, top). Energy-dispersive X-ray spectroscopy (EDX) spectroscopy determined that these particles comprised mainly of oxygen (43%) and manganese (38%) atoms (Figure 5.6, bottom).

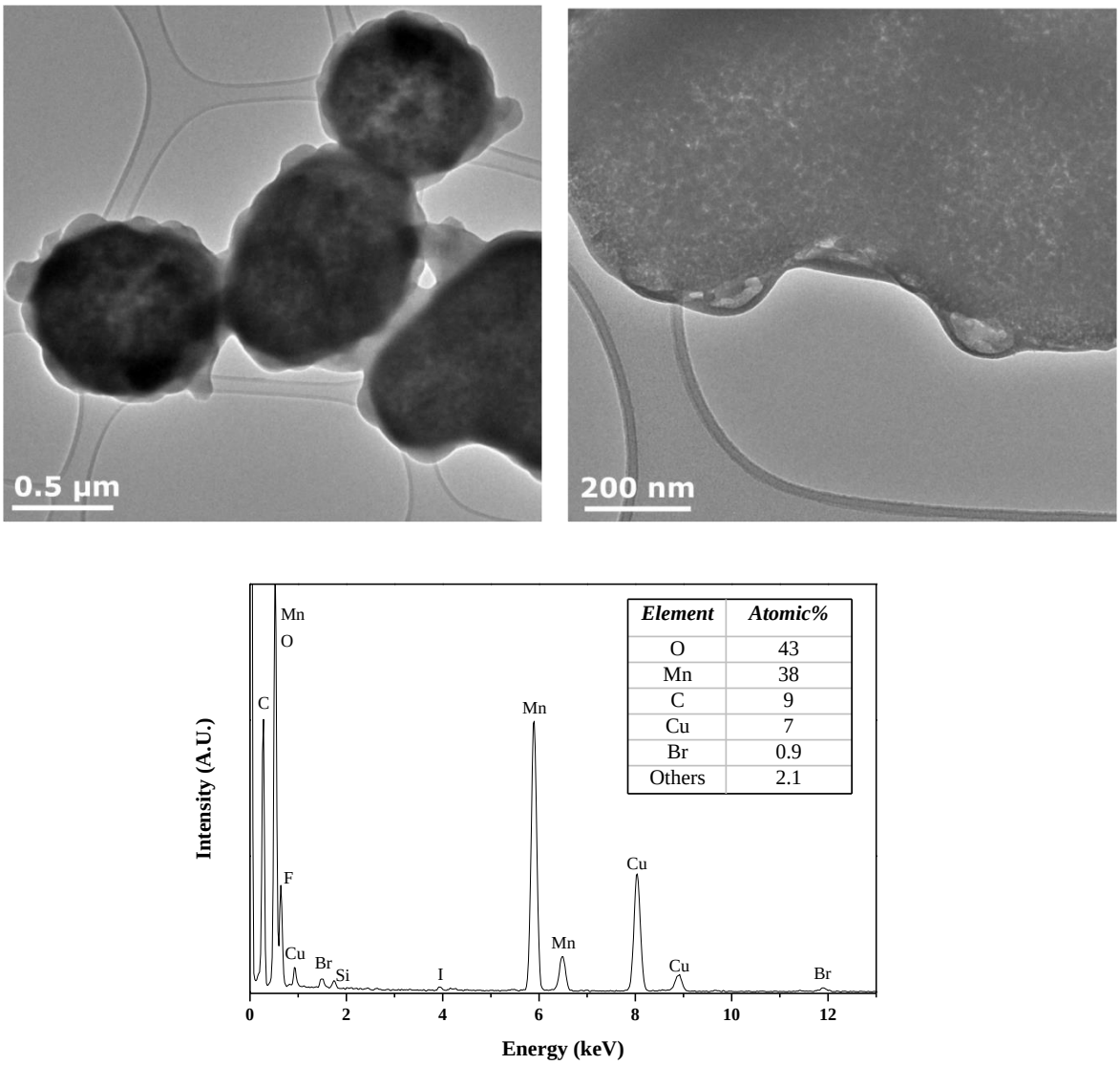


Figure 5.6 Top: TEM micrographs (bright field mode) micrograph of the NPs afforded during the reaction of $Me_2NH{\cdot}BH_3$ with 15 (5 mol%) in C_6D_6 after 16 h at 60 °C. Bottom: EDX spectrum of manganese NPs on TEM grid with the table atomic% of elements (inset). Copper, carbon and silicon peaks originate from the lacey carbon coated copper grid.

5.3.3.2 TEM Measurements under Inert Atmosphere

In order to rule out whether these particles are formed as a result of exposure to air/moisture, a new sample for TEM analysis was prepared under an inert atmosphere (dinitrogen) in a glove box. As before, the reaction solution of **15** (5 mol% catalyst loading) and $Me_2NH{\cdot}BH_3$ in C_6D_6 (0.6 mL), after heating at 60 °C for 16 h, was diluted with *ca*. 2 mL of benzene. An aliquot of this solution was spotted onto a copper-mounted carbon film and the solvent allowed to dry. Next, the grid was transferred to the TEM holder after which an air tight cover was placed on the holder. This cover was then removed and the TEM holder was quickly put inside the TEM

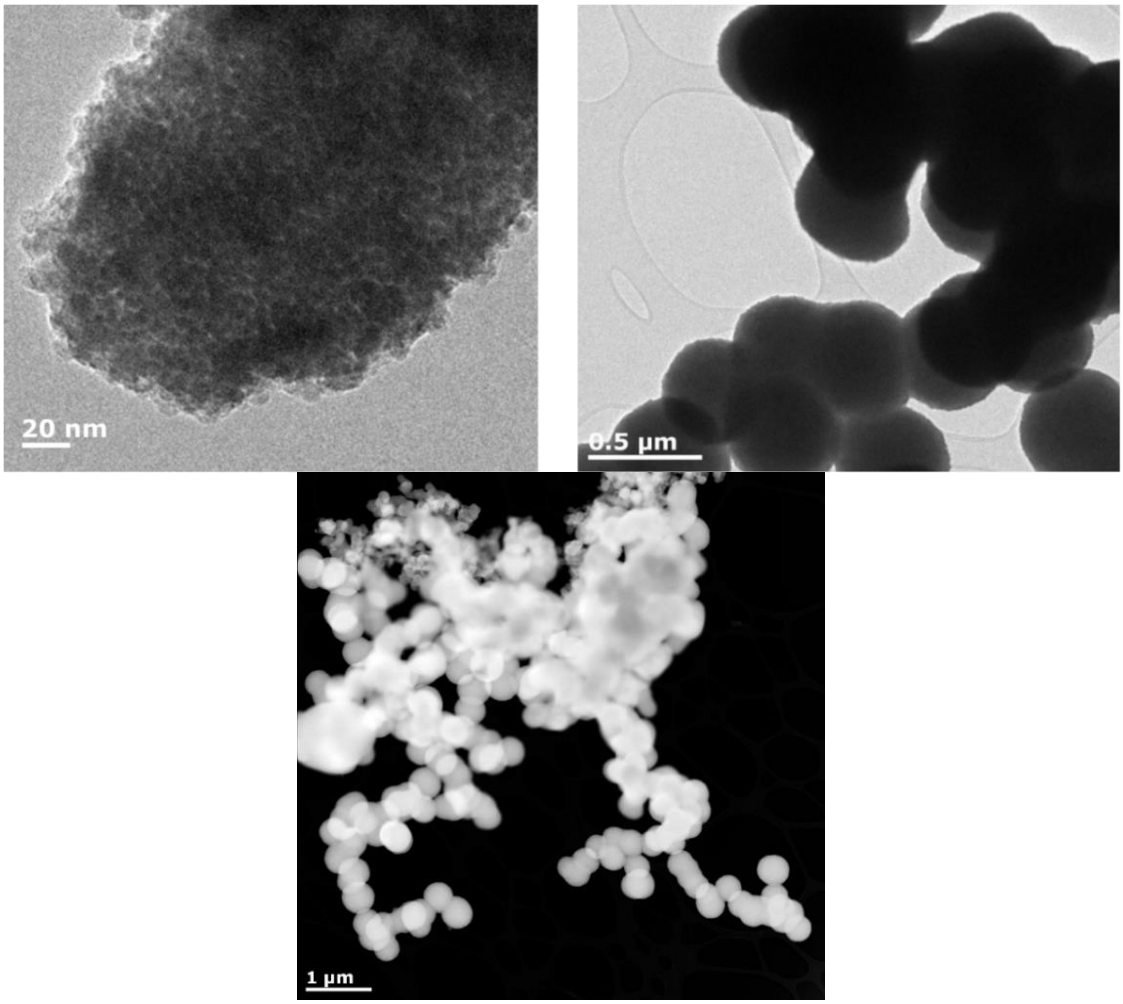


Figure 5.7 Bright field TEM (above) and dark field STEM (below) micrograph of the NPs affored during the reaction of $Me_2NH{\cdot}BH_3$ with 15 (5 mol%) in C_6D_6 after 16 h at 60 °C with minimal exposure to oxygen. Large sub-micron aggregates of small (ca. 10 nm) NPs are observed.

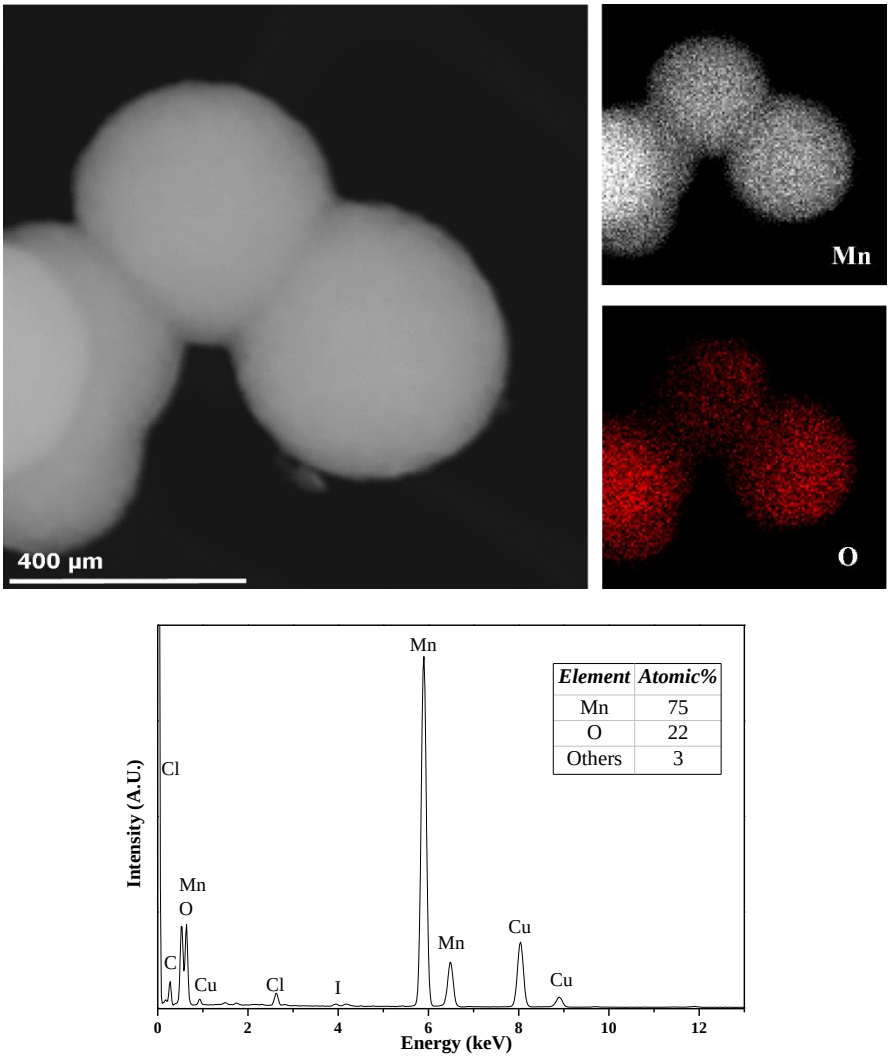


Figure 5.8 STEM micrograph (dark field, top left) with EDX spectroscopic mapping (top right) of Mn (white) and O (red). EDX spectrum (bottom) of manganese particles on TEM grid with the table of atomic% of elements (inset).

microscope, resulting in the exposure of the sample in air for *ca.* 5 seconds until high vacuum was achieved. TEM and scanning transmission electron microscopy (STEM) micrographs obtained (Figure 5.7) provides clear evidence for the formation of aggregation of small particles, as seen previously (see Figure 5.6). of *ca.* 10 nm nanoparticles assembled into sub-micron aggregates *ca.* 500 nm in diameter, consistent with the absence of an effective mechanism for stabilisation of discrete nanoparticles. The small nanoparticle size indicates a rapid decomposition of the manganese precatalyst **15** to Mn NPs. Furthermore, EDX spectroscopic analysis (Figure 5.8) confirmed the

presence of both manganese (75%) and oxygen (22%), with the apparent excess of manganese indicative of the formation of manganese nanoparticles passivated by a thin layer of a manganese oxide, an artefact of the unavoidable exposure of the sample to atmospheric oxygen during its introduction to the microscope.

5.3.3.3 DLS Measurements

To confirm that what is shown in the TEM and STEM micrographs is a true reflection of the NPs in solution, analysis of the post reaction mixture was undertaken using dynamic light scattering (DLS). DLS is a technique which measures the time-dependent fluctuations in scattered light intensity to determine size (as hydrodynamic diameter) and dispersity of particles as they move under Brownian motion in suspension. In this instance, it is used to determine the heterogeneity of a catalytic reaction by detection of metal colloid particles. After heating a mixture of **15** (5 mol%) and $Me_2NH{\cdot}BH_3$ in C_6D_6 (0.6 mL) at 60 °C for 16 h to ensure the formation of the catalytically active species, the solution was diluted with *ca*. 2 mL of benzene and transferred to a quartz cuvette and sealed under an inert atmosphere and analysed by DLS. These measurements indicated that large, sub-micron particles (*ca.* 800-900 nm in diameter) were present in the reaction mixture (Figure 5.9). However, the determined polydispersity index was high, indicative of a broad range of stable species in suspension, some larger than the limit of detection for the instrument and as such, the measured value is at best an estimate. The apparent offset in determined aggregate size *vs* TEM and STEM analysis is expected based on fundamental differences in how the absolute value of nanoparticle size is determined, where DLS typically overestimate nanoparticle size owing to the greater amount of light scattered by larger particles within the distribution.

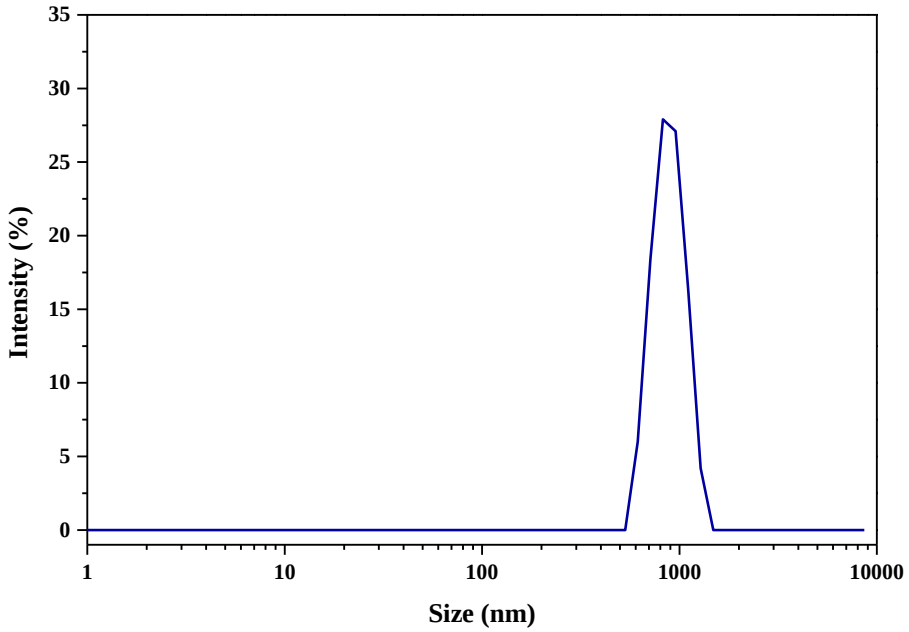
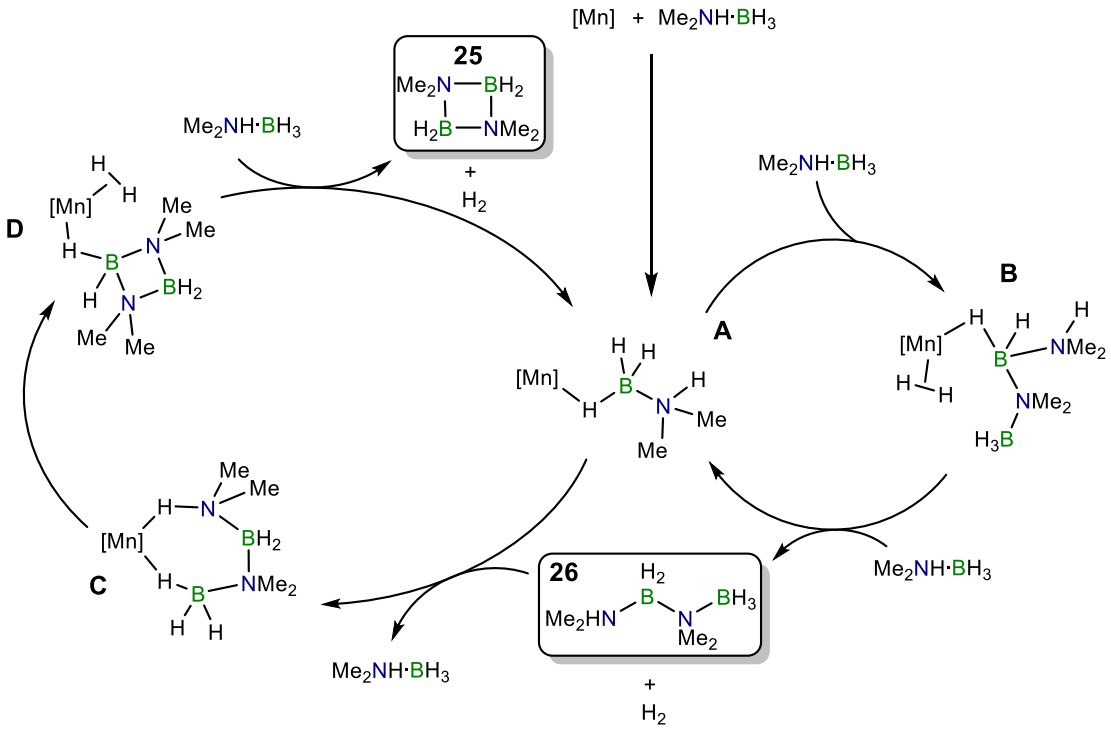


Figure 5.9 Particle size distribution from DLS measurements of the reaction mixture of $Me_2NH{\cdot}BH_3$ with 15 (5 mol%) in benzene after 16 h at 60 °C.

5.3.4 Proposed Catalytic Cycle

With the mechanistic observations for precatalysts **10** and **13** that the reaction is homogeneous and not radical mediated, a plausible two stage catalytic cycle for the homogenous reaction is proposed in Scheme 5.3. As discussed in Chapters III and IV, due to the inherent coordinative unsaturated nature and the +II oxidation state of the manganese centre in **10** and **13**, it is reasonable to assume that the precatalysts act as Lewis acids. Initially $Me_2NH{\cdot}BH_3$ coordinates to the metal centre though interaction of BH_3 unit to form **A**, similar to manganese half-sandwich complexes as investigated Shimoi.[27,43,44]Addition of another $Me_2NH{\cdot}BH_3$ results in an intermolecular coupling with formation of a new B–N bond between the two adducts at the metal centre (**B**).



Scheme 5.3 Proposed mechanism for homogeneous dehydrocoupling catalysis of dimethylamine borane. [Mn] = 10 or 13.

Subsequent displacement of **26** and H_2 by the addition of $Me_2NH{\cdot}BH_3$ regenerates the active species **A**. **26** then coordinates to the Mn centre forming **C** which then cyclises releasing another molecule of H_2 (**D**).

Displacement by another molecule of $Me_2NH{\cdot}BH_3$ reforms the active species **A** and releases **25** and a molecule of H_2. This two stage mechanism is similar to an Fe(II) system where the catalyst is photoactivated, and the extensively studied Ti(II) system by Manners and co-workers.[32,38]

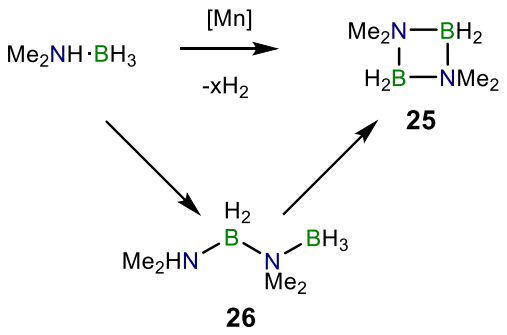
An important question still remains however: why do two mechanisms exist (homogeneous *vs.* heterogeneous) for precatalysts **10**, **13** and **15**? A similar observation has been observed for iron carbonyl complexes in the dehydrocoupling of $Me_2NH{\cdot}BH_3$ under photoirradiation using iron complexes $[CpFe(CO)_2]_2$ and $CpFe(CO)_2I$ where the latter operates through a homogeneous mechanism and the former a heterogeneous

mechanism.[32] The authors postulate that the low formal oxidation state of Fe(I) in the binuclear structure which already possess Fe(I)–Fe(I) interactions could aid the reduction to Fe nanoparticles in the presence of $Me_2NH{\cdot}BH_3$.[32]

In our system this is not the case as the manganese centres are all in the +II oxidation state however, the lower steric demands of the Tmp substituent *vs.* that of 2,6-Xyl and Mes, as the *ortho* substituents on the outer aromatic ring provide greater steric coverage to the metal centre,[45] could render the metal centre in **15** more susceptible to reduction. It is also well reported that amine-boranes are effective in the chemical synthesis of nanoparticles,[46] for example, $Me_2NH{\cdot}BH_3$ is an effective reducing reagent to form Sn, Fe, Ni, Pd and Pt nanoparticles.[41,47] This result is unexpected for manganese(II) due to its large negative reduction potential which has made chemical synthesis of Mn NPs *via* chemical reduction challenging.[48]

5.4 Conclusions

Preliminary investigations have shown the first examples of manganese(II) complexes are efficient precatalysts in the dehydrocoupling of dimethylamine borane. Using relatively low catalyst loadings (5 or 2 mol%) under mild conditions (60 °C) the cyclic dimer is selectively produced in good to excellent yields. At lower reaction temperatures (room temperature) a higher proportion of **26** is obtained suggesting that **26** is an intermediate to the cyclic dimer **25** (Scheme 5.4). *In situ* NMR reaction monitoring using catalyst loading of 5 mol% of **10**, **13** and **15** at 60 °C showed no induction period and revealed that the reactions reached completion after 4.7, 1.7 and 14 h, respectively. Catalyst poisoning experiments with **10** and **13** suggest that the reaction is homogeneous and not radical mediated.



Scheme 5.4 Catalytic dehydrocoupling of $Me_2NH{\cdot}BH_3$ to products 25 and 26.

However, in the case of **15**, the presence of *ca.* 1 drop of mercury caused the reaction rate to vastly reduce suggesting that the reaction is not homogeneous. Analysis by TEM, STEM and EDX spectroscopy confirmed the presence of small manganese NPs, assembled into sub-micron aggregates *ca.* 500 nm in diameter, which indicates a rapid decomposition of the manganese precatalyst **15** to Mn NPs. DLS analysis on the reaction

mixture when using **15** at 5 mol% suggested the presence of large, sub-micron particles (*ca.* 800-900 nm in diameter) present in the reaction mixture.

A two stage mechanism has been proposed (Scheme 5.3) for the homogeneous catalysis where the linear diborazane **26** is synthesised first through an intermolecular coupling of dimethylamine borane adducts, which is subsequently dehydrogenated in an "on metal" process to the linear dimer **25**.

5.5 Future Work

As the dehydrocoupling reactions were all performed as closed systems, it would be interesting to investigate how the reaction proceeds as an open system by using a gas burette where conversion is quantified by measuring the volume of H_2 gas evolved. The reaction rate could possibly be affected as a result of the build-up of hydrogen gas pressure in the sealed NMR tube thereby lowering the rate of reaction.

The scope of this catalysis could be extended further to other amine-boranes such as $^{i}Pr_2NH{\cdot}BH_3$, $MeBnNH{\cdot}BH_3$ and $MeNH_2{\cdot}BH_3$ and phosphine-boranes[49,50] such as $Me_3P{\cdot}BH_3$ and $Ph_2PH{\cdot}BH_3$. This would allow for further understanding of the mechanism of the reaction, *i.e* if the sterics of the amine-borane is a limiting factor to the reaction. Other low coordinate Fe(II) and Co(II) *m*-terphenyl complexes could be explored to enable the understanding of the role of the metal centre in these reactions.

As **26** has been suggested as a plausible intermediate to the dimeric species **25**, it would be useful to react independently synthesised **26** with the manganese complexes **10**, **13** and **15** in catalytic amounts. If product **25** is formed, this would enable further verification of the proposed mechanism in Scheme 5.3. Stoichiometric reactions with precatalysts and $Me_2NH{\cdot}BH_3$ could also enable the isolation of intermediates in the reaction which would enable further understanding into the mechanism.

It would also be beneficial to follow the reaction by IR spectroscopy in order to elucidate if the mechanism operates through a hydride intermediate. These intermediate may be very short lived therefore ultra-fast IR may need to be used.

5.6 References

1 R. L. Melen, *Chem. Soc. Rev.*, 2016, **45**, 775–788.

2 A. Staubitz, A. P. M. Robertson and I. Manners, *Chem. Rev.*, 2010, **110**, 4079–4124.

3 Z. Lu, B. L. Conley and T. J. Williams, *Organometallics*, 2012, **31**, 6705–6714.

4 E. M. Leitao, N. E. Stubbs, A. P. M. Robertson, H. Helten, R. J. Cox, G. C. Lloyd-Jones and I. Manners, *J. Am. Chem. Soc.*, 2012, **134**, 16805–16819.

5 Y. Jiang, O. Blacque, T. Fox, C. M. Frech and H. Berke, *Organometallics*, 2009, **28**, 5493–5504.

6 Y. Jiang and H. Berke, *Chem. Commun.*, 2007, 3571–3573.

7 A. Staubitz, M. E. Sloan, A. P. M. Robertson, A. Friedrich, S. Schneider, P. J. Gates, I. Manners and J. Schmedt auf der Guenne, *J. Am. Chem. Soc.*, 2010, **132**, 13332–13345.

8 H. C. Johnson, E. M. Leitao, G. R. Whittell, I. Manners, G. C. Lloyd-Jones and A. S. Weller, *J. Am. Chem. Soc.*, 2014, **136**, 9078–9093.

9 E. M. Leitao, T. Jurca and I. Manners, *Nat. Chem.*, 2013, **5**, 817–829.

10 A. Rossin and M. Peruzzini, *Chem. Rev.*, 2016, **116**, 8848–8872.

11 R. McLellan, A. R. Kennedy, S. A. Orr, S. D. Robertson and R. E. Mulvey, *Angew. Chem. Int. Ed.*, 2016, **56**, 1036–1041.

12 J. Spielmann, M. Bolte and S. Harder, *Chem. Commun.*, 2009, 6934–6936.

13 J. Spielmann, D. E. J. Piesik and S. Harder, *Chem. Eur. J.*, 2010, **16**, 8307–8318.

14 P. Bellham, M. D. Anker, M. S. Hill, G. Kociok-Köhn and M. F. Mahon, *Dalton Trans.*, 2016, **45**, 13969–13978.

15 D. J. Liptrot, M. S. Hill, M. F. Mahon and D. J. MacDougall, *Chem. Eur. J.*, 2010, **16**, 8508–8515.

16 M. S. Hill, G. Kociok-Köhn and T. P. Robinson, *Chem. Commun.*, 2010, **46**, 7587–7589.

17 K. Nomura and J. Liu, *Dalton Trans.*, 2011, **40**, 7783–7790.

18 M. Klahn, D. Hollmann, A. Spannenberg, A. Brueckner and T. Beweries, *Dalton Trans.*, 2015, **44**, 12103–12111.

19 N. Blaquiere, S. Diallo-Garcia, S. I. Gorelsky, D. A. Black and K. Fagnou, *J. Am. Chem. Soc.*, 2008, **130**, 14034–14035.

20 X. Zhang, Z. Lu, L. K. Foellmer and T. J. Williams, *Organometallics*, 2015, **34**, 3732–3738.

21 C. A. Jaska, K. Temple, A. J. Lough and I. Manners, *J. Am. Chem. Soc.*, 2003, **125**, 9424–9434.

22 S. Kim, W. Han, T. Kim, T. Kim, S. W. Nam and M. Mitoraj, *J. Am. Chem. Soc.*, 2010, **132**, 9954–9955.

23 P. Cui, T. P. Spaniol, L. Maron and J. Okuda, *Chem. Eur. J.*, 2013, **19**, 13437–13444.

24 M. M. Hansmann, R. L. Melen and D. S. Wright, *Chem. Sci.*, 2011, **2**, 1554–1559.

25 O. J. Metters, S. R. Flynn, C. K. Dowds, H. A. Sparkes, I. Manners and D. F. Wass, *ACS Catal.*, 2016, **6**, 6601–6611.

26 T. Miyazaki, Y. Tanabe, M. Yuki, Y. Miyake and Y. Nishibayashi, *Organometallics*, 2011, **30**, 2394–2404.

27 T. Kakizawa, Y. Kawano, K. Naganeyama and M. Shimoi, *Chem. Lett.*, 2011, **40**, 171–173.

28 C. Lichtenberg, L. Viciu, M. Adelhardt, J. Sutter, K. Meyer, B. de Bruin and H. Grützmacher, *Angew. Chem. Int. Ed.*, 2015, **54**, 5766–5771.

29 R. T. Baker, J. C. Gordon, C. W. Hamilton, N. J. Henson, P. H. Lin, S. Maguire, M. Murugesu, B. L. Scott and N. C. Smythe, *J. Am. Chem. Soc.*, 2012, **134**, 5598–5609.

30 A. Glüer, M. Förster, V. R. Celinski, J. Schmedt Auf Der Günne, M. C. Holthausen and S. Schneider, *ACS Catal.*, 2015, **5**, 7214–7217.

31 A. Schaefer, T. Jurca, J. Turner, J. R. Vance, K. Lee, V. A. Du, M. F. Haddow, G. R. Whittell and I. Manners, *Angew. Chem. Int. Ed.*, 2015, **54**, 4836–4841.

32 J. R. Vance, A. Schäfer, A. P. M. Robertson, K. Lee, J. Turner, G. R. Whittell and I. Manners, *J. Am. Chem. Soc.*, 2014, **136**, 3048–3064.

33 J. R. Vance, A. P. M. Robertson, K. Lee and I. Manners, *Chem. Eur. J.*, 2011, **17**, 4099–4103.

34 T.-P. Lin and J. C. Peters, *J. Am. Chem. Soc.*, 2013, **135**, 15310–15313.

35 J. K. Pagano, J. P. W. Stelmach and R. Waterman, *Dalton Trans.*, 2015, **44**, 12074–12077.

36 P. M. Zimmerman, A. Paul and C. B. Musgrave, *Inorg. Chem.*, 2009, **48**, 5418–5433.

37 A. P. M. Robertson, R. Suter, L. Chabanne, G. R. Whittell and I. Manners, *Inorg. Chem.*, 2011, **50**, 12680–12691.

38 M. E. Sloan, A. Staubitz, T. J. Clark, C. R. Russell, G. C. Lloyd-Jones and I. Manners, *J. Am. Chem. Soc.*, 2010, **132**, 3831–3841.

39 R. H. Crabtree, *Chem. Rev.*, 2012, **112**, 1536–1554.

40 J. A. Widegren and R. G. Finke, *J. Mol. Catal. A Chem.*, 2003, **198**, 317–341.

41 J. F. Sonnenberg and R. H. Morris, *ACS Catal.*, 2013, **3**, 1092–1102.

42 K. J. Gallagher and R. Webster, *Chem. Commun.*, 2014, **50**, 12109–12111.

43 Y. Kawano, K. Yamaguchi, S. Y. Miyake, T. Kakizawa and M. Shimoi, *Chem. Eur. J.*, 2007, **13**, 6920–6931.

44 T. Kakizawa, Y. Kawano and M. Shimoi, *Organometallics*, 2001, **20**, 3211–3213.

45 R. C. C. Smith, T. Ren and J. D. D. Protasiewicz, *Eur. J. Inorg. Chem.*, 2002, 2779–2783.

46 S. B. Kalidindi, U. Sanyal and B. R. Jagirdar, *ChemSusChem*, 2011, **4**, 317–324.

47 O. Lidor-Shalev and D. Zitoun, *RSC Adv.*, 2014, **4**, 63603–63610.

48 J. F. Bondi, K. D. Oyler, X. Ke, P. Schiffer and R. E. Schaak, *J. Am. Chem. Soc.*, 2009, **131**, 9144–9145.

49 H. Dorn, R. A. Singh, J. A. Massey, J. M. Nelson, C. A. Jaska, A. J. Lough and I. Manners, *J. Am. Chem. Soc.*, 2000, **122**, 6669–6678.

50 A. K. King, A. Buchard, M. F. Mahon and R. L. Webster, *Chem. Eur. J.*, 2015, **21**, 15960–15963.

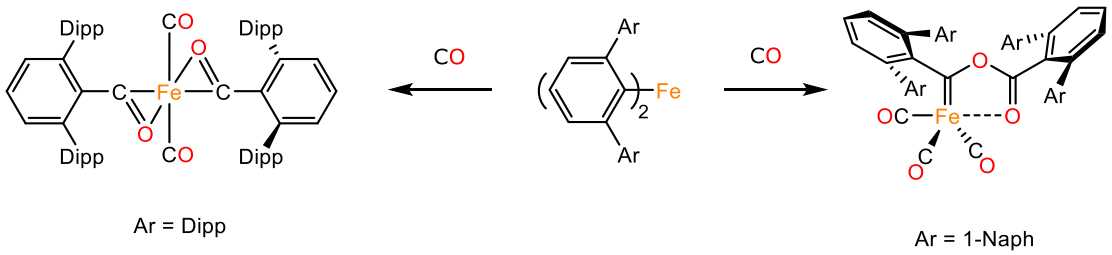
Chapter VI

Reductive Coupling of CO by Iron(II) Complexes

6.1 Introduction

Carbon monoxide is an important chemical feedstock in the Fischer-Tropsch process used to produce solvents, fuels and bulk chemicals in industry where CO is obtained either by coal, natural gas, biomass or carbon dioxide.[1] The Fischer-Tropsch process requires a heterogenous catalyst and high temperatures with the presence of additives (*e.g.* 0.5 wt.% K_2O) to maintain high activity and stability, reduction promotion and selectivity control.[2] As hydrocarbon reserves become more depleted, the generation of hydrocarbons through reactions such as Fischer-Tropsch will only become more industrially and economically important.[3]

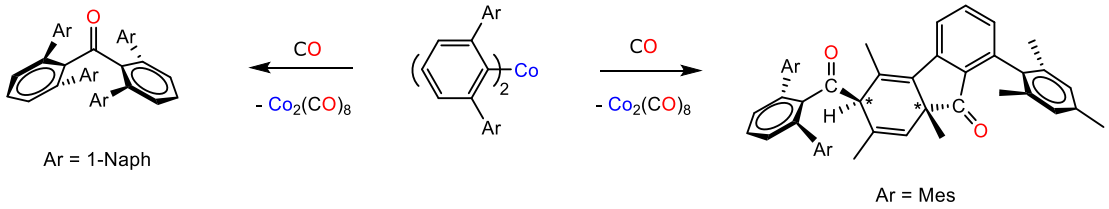
Direct CO homologation has significant challenges: the CO bond has a bond dissociation energy of 1076 kJ mol^{-1} and is the strongest bond between two elements, where complete bond-breaking requires six electrons.[4] In biological systems, molybdenum and vanadium nitrogenases use discrete proton and electron sources to efficiently convert carbon monoxide into hydrocarbons under mild conditions,[5] whilst in the Fischer-Tropsch process dihydrogen is used for carbon monoxide coupling under high temperatures and pressures.[6] Although the reductive coupling of two or more CO molecules has been demonstrated by alkaline earth,[7] p-block,[8–10] d-block,[11–17] and f-block complexes,[1,18–23] much less explored are simple compounds that can induce scission of the carbon-oxygen bonds to generate carbon-carbon bonds.[10,19,21,24–27] A notable example is a molybdenum arene complex which features a terphenyl diphosphine ligand which accommodates a broad range of binding modes to stabilise a range of highly reduced species.[24] This complex was capable of the conversion of CO to C_2O_1 products which is facilitated by silylation and reduction.



Scheme 6.1 Insertion products obtained from the reaction of iron(II) complexes with CO.

Previous reactivity of CO with transition metal *m*-terphenyl complexes has been shown to yield a variety of insertion products though alteration of the sterics of the ligand and by changing the metal centre as documented by Power and Kays.[28–31] The reaction of the iron(II) complex, (2,6-$Dipp_2C_6H_3)_2Fe$, with CO yields the η^2-acyl carbonyl complex: [2,6-$Dipp_2C_6H_3(\eta^2$-$CO)]_2Fe(CO)_2$, *via* CO insertion into the Fe–C bonds (Scheme 6.1 left).[28] When the iron diaryl features 1-Naph flanking groups, (2,6-$Naph_2C_6H_3)_2Fe\cdot THF$, the reaction with CO yields the iron metallacyclic carbene complex, $(CO)_3Fe$[C(2,6-$Naph_2C_6H_3$)OC(O)(2,6-$Naph_2C_6H_3$)]·OEt_2, an 18 electron air stable complex which features trigonal bipyramidal core geometry around the iron centre (Scheme 6.1, right).[31] The mechanism for the formation is thought to involve initial coordination of CO, 1,1-migratory insertion to yield the analogous bis(acyl) iron complex which cyclises to form the iron carbene complex.[31]

The reactivity of cobalt complexes has also been investigated. Treatment of the cobalt diaryls $Co(2,6\text{-}Ar_2C_6H_3)_2(OEt_2)_n$ (Ar = Mes, n = 0; Naph, n = 1) with dry CO produced sterically encumbered ketones as a result of CO insertion *via* M–C bond breaking and C–C bond forming reactions with concomitant elimination of $Co_2(CO)_8$.[30]



Scheme 6.2 Insertion products obtained from the reaction of cobalt(II) complexes with CO.

Reaction of the naphthyl substituted terphenyl complex with CO produces a rare example of a tetra *ortho*-substuted benzophenone (Scheme 6.2, left) whereas the reaction with the mesityl substituted *m*–terphenyl complex produced an organic fluorenone containing two stereogenic centres (Scheme 6.2, right).[30]

Herein, this chapter encompasses the reactivity of two coordinate bis iron(II) complexes with CO which form novel squarines and diironcarboxylate complexes from scission of the CO bond under ambient conditions in the absence of external reducing agents.

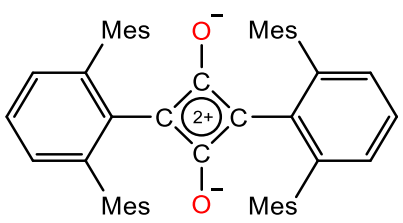
.

6.2 Experimental

6.2.1 Reaction of Iron Diaryls with CO

6.2.1.1 Reaction of 11 with CO

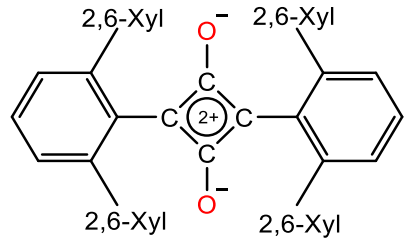
In a greaseless ampoule, a stirred solution of **11** (100 mg, 0.146 mmol) in toluene (5 mL) was exposed to an atmosphere of dry CO at room temperature whereupon an immediate colour change from yellow to red solution occurred. The reaction mixture was stirred for a further 6 days after which the solvent was removed *in vacuo* and the product extracted into hexane (20 mL), concentrated *in vacuo* and kept at –30 °C. This resulted in the precipitation of red needle crystals suitable for X-ray diffraction revealing the presence of a squaraine 1,3-(2,6-$Mes_2C_6H_3)_2C_4O_2$ (**29**$^{\mathbf{Mes}}$) (13.0 mg, 24%). ^{1}H NMR (400 MHz, C_6D_6, 25 ºC): δ 7.01 (t, ^3J(H,H) = 7.6 Hz, 2H, $C_6H_3{}^p$), 6.86 (s, 8H, C*H*-Mes), 6.79 (d, ^3J(H,H) = 7.6 Hz, 4H, $C_6H_3{}^m$), 2.19 (s, 12H, ^{p}C*H*$_3$-Mes), 1.98 (s, 24H, ^{o}C*H*$_3$-Mes). ^{13}C{^{1}H} (101 MHz, C_6D_6, 25 ºC): δ 269.7 (*C*O), 177.3 (*C*CO), 141.1 ($C_6H_3{}^o$), 137.0 (Mes^p), 136.8 (Mes^{ipso}), 136.6 (Mes^o), 133.7 ($C_6H_3{}^p$), 132.2 ($C_6H_3{}^{ipso}$), 129.3 ($C_6H_3{}^m$), 128.9 (Mes^m), 21.3 (^{p}*C*H$_3$-Mes), 21.0 (^{o}*C*H$_3$-Mes). UV/Vis (DCM) at λ_{max}/nm (ε/dm^3 mol^{-1} cm^{-3}): strong absorption between 200 and 300 nm (>8000), 480 (8904), 515 (9329), 742 (3110). MS (ESI) *m/z*: calcd. for $C_{52}H_{51}O_2$ $[M+H]^+$ 707.3883, found: 707.3871, (err [ppm] = 1.80). IR (Toluene) $\bar{\nu}$/cm^{-1}: 1673 (C–O).



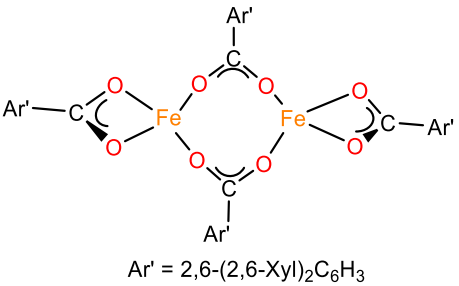
The corresponding diironcarboxylate complex (**30**$^{\mathbf{Mes}}$) was not isolated however, evidence for its formation can be seen *via in situ* reaction monitoring, see Section 6.3.3.1): IR (Toluene) $\bar{\nu}$/cm^{-1}: 1751 (C–O).

6.2.1.2 Reaction of 14 with CO

In a greaseless ampoule, a solution of **14** (73.1 mg, 0.117 mmol) in toluene (10 mL) was exposed to an atmosphere of dry CO at room temperature whereupon an immediate colour change from yellow to red solution occurred. The reaction mixture was stirred for a further 6 days after which the solvent was removed *in vacuo* and the product extracted into toluene (5 mL), and pentane was carefully layered (5 mL) and kept at room temperature. This resulted in the precipitation of orange crystals suitable for X-ray diffraction revealing the presence of a squaraine 1,3-[(2,6-(2,6-Xyl)$_2$C$_6$H$_3$]$_2$C$_4$O$_2$ (**29**$^{2,6\text{-Xyl}}$). The yield of **29**$^{2,6\text{-Xyl}}$ could not be accurately determined due to a mixture of paramagnetic species in the solid state that could not be separated. MS (ESI) *m/z*: calcd. for $C_{48}H_{42}O_2$ $[M]^-$: 649.3112, found: 649.3097, (err [ppm] = 1.50). IR (Toluene) $\bar{\nu}$/cm^{-1} 1675 (C–O) (as obtained *via in situ* reaction monitoring, see Section 6.3.3.1)



However, when a solution of **14** was exposed to CO and stirred for only 16 h, subsequent workup and extraction of the reaction mixture into hexane (2 × 10 mL) followed by storage at room temperature for 5 days allowed for the precipitation of red crystals suitable for X-ray diffraction revealing the presence of a diiron carboxylate complex [(2,6-Xyl$_2$C$_6$H$_3$CO$_2$)Fe(μ-CO$_2$C$_6$H$_3$-2,6-(2,6-Xyl)$_2$]$_2$ (**30**$^{2,6\text{-Xyl}}$). The yield of **30**$^{2,6\text{-Xyl}}$ could not be accurately determined due to a mixture of paramagnetic species in the solid state that could not be separated. IR (Toluene) $\bar{\nu}$/cm^{-1}: 1751 (C–O) (as obtained *via in situ* reaction monitoring, see Section 6.3.3.1).



6.2.2 Standard Procedures for Reaction Monitoring

6.2.2.1 Reaction Monitoring via IR Spectroscopy

In a greaseless ampoule a solution of **11** (72.2 mg, 0.106 mmol) or **14** (73.1 mg, 0.117 mmol) in toluene (8 mL) was exposed to an atmosphere of CO gas whereupon an immediate colour change from yellow to red was observed. Samples of the reaction solution (0.4 mL) were removed from the reaction vessel periodically under an atmosphere of CO and transferred to a separate ampoule after which the solvent was removed and the resulting red solid was dried for *ca.* 1h. The sample was dissolved in toluene (0.4 mL) under an argon atmosphere and transferred to a prepurged solution IR cell and the IR spectrum was recorded.

6.2.2.2 Reaction Monitoring via EPR Spectroscopy

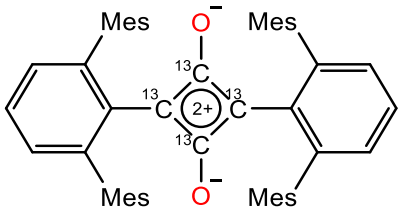
In a Young's tap modified quartz EPR tube was added **11** (20.0 mg, 0.0293 mmol) or **14** (20.0 mg, 0.0319 mmol) in toluene (*ca.* 0.4 mL) and exposed to an atmosphere of CO gas whereupon an immediate colour change from red to yellow was observed. The tube was repressurised with CO gas every 24 h and an EPR spectrum was taken periodically at room temperature and 77 K.

6.2.3 ^{13}CO Labelling Studies

6.2.3.1 Reaction of 11 with ^{13}CO

A stirred solution of **11** (40 mg, 0.0586 mmol) in toluene (8 mL) was exposed to an atmosphere of dry ^{13}CO (99%) at room temperature whereupon an immediate colour

change from yellow to red solution occurred. The reaction mixture was stirred for a further 6 days after which the solvent was removed *in vacuo* and the product extracted into hexane (20 mL), concentrated *in vacuo* and kept at –30 °C. This resulted in the precipitation of red needles of pure squaraine 1,3-(2,6-$Mes_2C_6H_3$)$_2$$^{13}C_4O_2$ (**^{13}C-29^{Mes}**).



^{1}H NMR (500 MHz, C_6D_6, 25 ºC) δ = 7.01 (t, ^3J(H,H) = 7.7 Hz, 2H, $C_6H_3^p$), 6.86 (s, 8H, C*H*-Mes), 6.79 (d, ^3J(H,H) = 7.7 Hz, 4H, $C_6H_3^m$), 2.19 (s, 12H, ^{p}CH_3-Mes), 1.98 (s, 24H, ^{o}CH_3-Mes). ^{13}C{^{1}H} (126 MHz, C_6D_6, 25 ºC) δ = 269.7 (t, ^1J(C,C) = 45 Hz, *C*O), 177.3 (t, ^1J(C,C) = 45 Hz, C_4ring), 141.1 ($C_6H_3^o$), 137.0 (Mes^p), 136.8 (Mes^{ipso}), 136.6 (Mes^o), 133.7 ($C_6H_3^p$), 132.2 ($C_6H_3^{ipso}$), 129.3 ($C_6H_3^m$), 128.9 (Mes^m), 21.3 (^{p}*C*H$_3$-Mes), 21.0 (^{o}*C*H$_3$-Mes). MS (ESI) *m/z*: calcd for ($C_{49}H_{53}O_3{}^{13}C_4$) [M+MeO]$^-$ 741.4134, found: 741.4118, (err [ppm] = 2.20). IR (Toluene) $\bar{\nu}$/cm^{-1}: 1638 (^{13}C–O).

The corresponding diironcarboxylate complex (**^{13}C-30^{Mes}**) was not isolated however, evidence for its formation can be seen *via in situ* reaction monitoring, see Section 6.3.4.2): IR (Toluene) $\bar{\nu}$/cm^{-1}: 1705 (^{13}C–O).

6.2.3.2 Reaction Monitoring via IR Spectroscopy

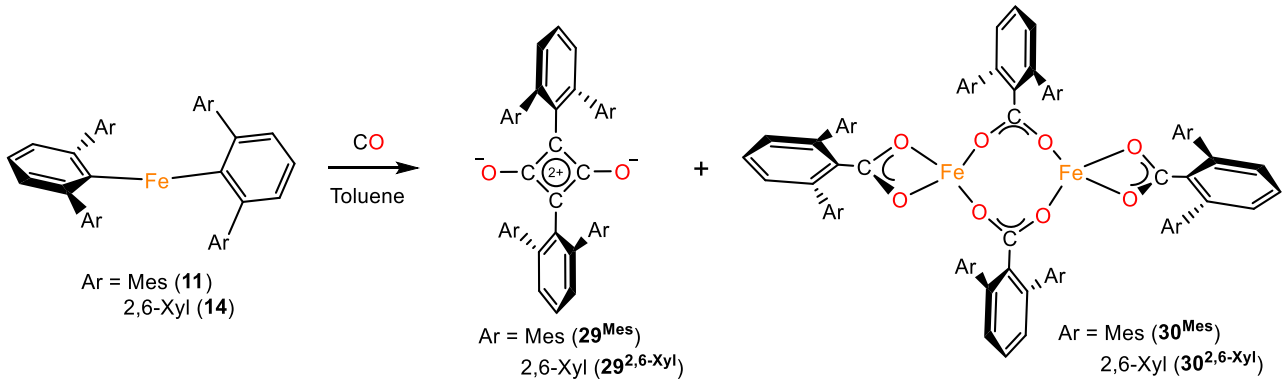
In a greaseless ampoule, **11** (40 mg, 0.0586 mmol) was dissolved in toluene (8 mL) under and argon atmosphere and sealed. The ampoule was connected to the ^{13}CO gas bottle (fitted with a low-pressure regulator) and the Schlenk line *via* a three-way glass stopcock. After cycling the connecting pipes the argon atmosphere was removed from ampoule and sealed under reduced pressure after which the three-way glass stopcock was moved to the two-way position connecting the ampoule and gas bottle. The Young's tap to the ampoule

and the gas bottle were opened exposing the solution of **11** in toluene to ^{13}CO gas where upon an immediate colour change from yellow to red was observed.

A sample of the reaction solution (0.4 mL) after 1 h and after 6 days was removed from the reaction vessel under an atmosphere of argon and transferred to a separate ampoule after which the solvent was removed and the resulting red solid was dried for *ca.* 1h. The sample was dissolved in toluene (0.4 mL) under an argon atmosphere and transferred to a prepurged solution IR cell and the IR spectrum was recorded. After each sample was taken the reaction vessel was re-pressurised with ^{13}CO gas as described previously.

6.3 Results and Discussion

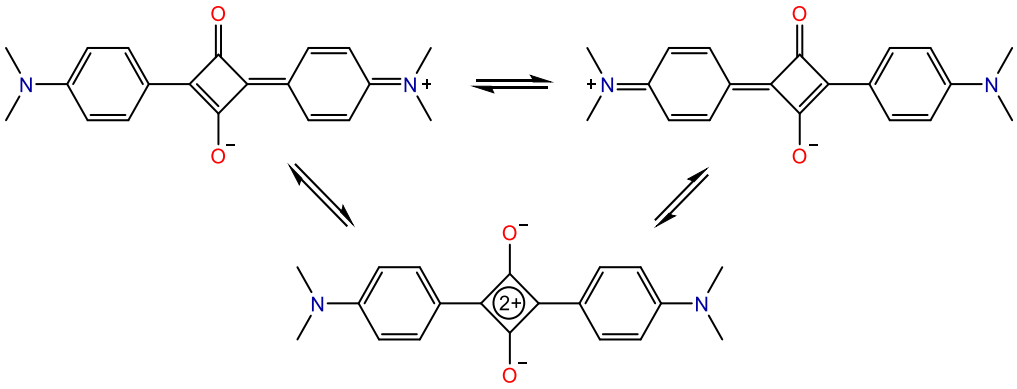
Yellow solutions of iron(II) diaryls **11** or **14** in toluene were exposed to an atmosphere of dry CO gas at room temperature whereupon an immediate colour change to a red solution was observed. Subsequent work up and crystallisation by either controlled cooling of a saturated hexane solution (**29**$^{\mathbf{Mes}}$) or by toluene/pentane layering (**29**$^{\mathbf{2,6\text{-}Xyl}}$) afforded red crystals of a squaraine molecule as identified by X-ray crystallography (Scheme 6.3). A diiron carboxylate complex (**30**$^{\mathbf{2,6\text{-}Xyl}}$) has also been isolated in the reaction of **14** with CO where X-ray crystallography verified its structure. It has not been possible to crystallographically characterise the analogous Mes substituted *m*-terphenyl iron carboxylate complex (**30**$^{\mathbf{Mes}}$) due to the preferential crystallisation of **29**$^{\mathbf{Mes}}$, however evidence for its formation has been observed through *in situ* reaction monitoring with IR spectroscopy (see Section 6.3.3.1 below). As both the squaraine and diironcarboxylate complex derive from the insertion of CO into the carbon-iron bond, it is significant to note that the squaraine molecule has an extra carbon (in the central C_4O_2 ring) and the iron carboxylate complex has an extra oxygen atom. Therefore, this indicates the CO triple bond, the strongest between two elements, has indeed been broken under ambient conditions.



Scheme 6.3 Reaction of iron(II) diaryls 11 and 14 with CO.

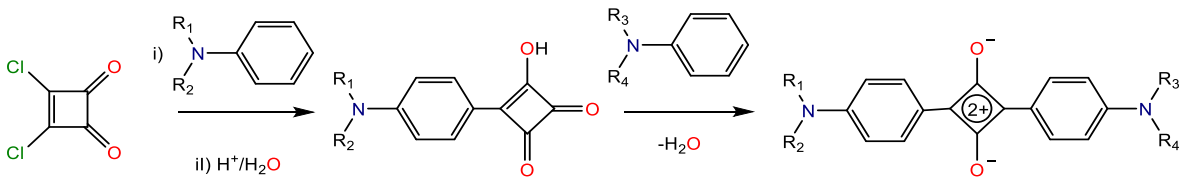
6.3.1 Squaraines

Squaraines are an important class of organic dyes[32] which have been extensively studied in the literature and have been shown to have applications spanning bio-imaging,[33] nonlinear optics,[34–36] photovoltaics,[37–39] photodynamic therapy,[40,41] ion[42–45] and ammonia[46] sensing. These molecules feature a central electron deficient four-membered ring (C_4O_2) and two electron donating groups (*e.g. N,N*-dialkylanilines, benzothiazoles, phenyls, pyrroles *etc.*) in a donor-acceptor-donor (D-A-D) form which is resonance stabilised over the π-conjugated zwitterionic structure (Scheme 6.4).[47] Squaraines often have strong absorptions ($\varepsilon \geq 10^5$ dm^3 mol^{-1} cm^{-3}) in the visible to near IR (NIR) region due to their rigid planar structure *via* and intramolecular charge transfer (CT) from the electron-rich donor to the electron-poor central C_4O_2 unit. [48]



Scheme 6.4 Resonant forms of a π-conjugated zwitterionic squaraine molecule.[47]

Symmetrical squaraines are usually synthesised through condensation reactions between electron-rich aromatic or heterocyclic compounds with squaric acid in a mixed solvent system or propan-2-ol with azeotropic removal of water.[49,50]



***Scheme 6.5 Synthesis of unsymmetrical squaraine dye.*[33]**

Unsymmetrical squaraines, featuring different donors on either side of the central C_4O_2 unit, are also well known and are synthesised by first treating the aniline derivative with squaryl dicholoride to give the stable semi-squaraine intermediate which is subsequently heated with a second aniline derivative to give the unsymmetrical squaraine (Scheme 6.5Scheme).[33] The asymmetry in the molecule has been shown to enhance the photophysical properties, where the absorption band is broader, improving light harvesting efficiency, and to provide anchoring groups to the TiO_2 surface in dye sensitised solar cells (DSSCs).[38,39,51]

There are few examples of squaraines with no heteroatoms substituents on the donor arms which are limited to azulene derivatives (Figure 6.1).[52]

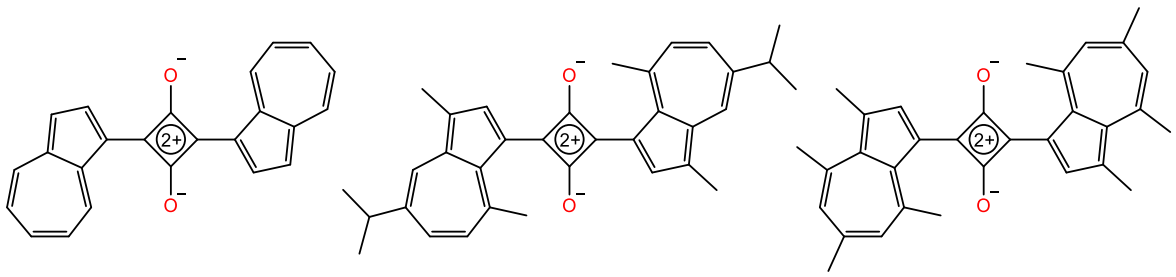


***Figure 6.1 Squaraines with no heteratom containing substituents on the donor substituents.*[52]**

6.3.1.1 Spectroscopic Analysis of Squaraines 29^{Mes} and 29$^{2,6\text{-}Xyl}$

29^{Mes} has been analysed spectroscopically through use of ^{1}H and ^{13}C{^{1}H} NMR, MS, IR and UV/Vis measurements. Despite multiple attempts, it has not been possible to isolate and purify **29$^{2,6\text{-}Xyl}$** in sufficient quantity for analysis by NMR, IR and UV/Vis spectroscopy due to contamination with unidentified paramagnetic species. The accurate mass measurements for both **29^{Mes}** and **29$^{2,6\text{-}Xyl}$** agree well with the crystallographic formulations (Scheme 6.3). The solution IR spectrum of **29^{Mes}** in toluene shows an absorption at 1673 cm^{-1}, which is higher than those reported in the literature (1594-1633 cm^{-1})[37,39,50,53–56] indicating stronger C=O character in **29^{Mes}** *versus* that in other squaraines.

The ^{1}H NMR of **29^{Mes}** features a characteristic triplet and doublet from the *para*- and *meta*-CH's on central aryl ring of the *m*-terphenyl ligand at 7.01 and 6.79 ppm respectively. The singlet at 6.86 ppm is assigned to the C*H* protons on the flanking Mes substituent with the methyl protons at 2.19 and 1.98 ppm which is very similar to the ^{1}H NMR of the lithium dimer [2,6-Mes$_2$C$_6$H$_3$Li]$_2$ (**4**).[57] The ^{13}C{^{1}H} NMR spectrum is largely similar to **4** with peaks in the aromatic reaction (141.1 to 128.9 ppm) from the aryl carbons on *m*-terphenyl the ligand with two peaks at 21.3 and 21.1 ppm from the methyl carbons on the flanking Mes substituent. The most remarkable feature is the resonance at 269.7 ppm from the *C*–O carbon of the C_4O_2 ring with the remaining carbons in the ring (*C*C–O) occurs at 177.3 ppm. This high chemical shift of 269.7 ppm is rather unusual however its assignment is confirmed *via* a heteronuclear multiple bond correlation (HMBC) experiment where the *meta*- and *para*-protons on the central aryl ring of the *m*-terphenyl correlate to the *C*–O signal (Figure 6.2). Other squaraines reported in the literature either do not have the ^{13}C{^{1}H} NMR spectrum reported, with few papers citing the insolubility of the resulting squaraine in common organic solvents,[47,53] or have

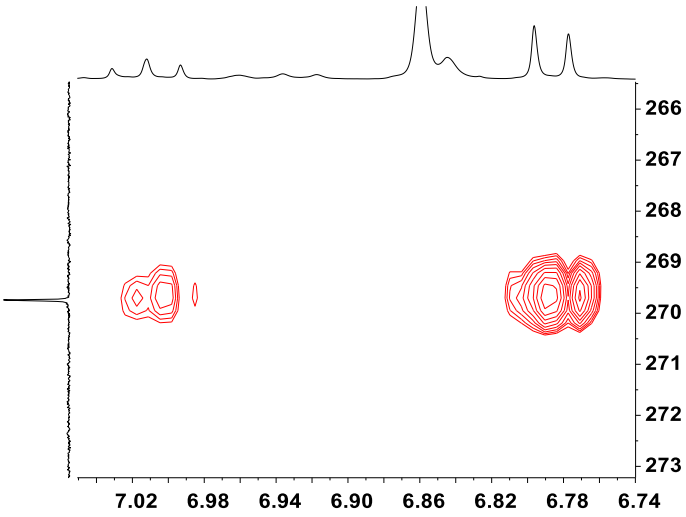


Figure 6.2 HMBC spectra of 29 on C–O region.

unassigned NMR spectra. Of the latter, the highest chemical shifts (assuming the highest is the *C*–O) range from 192.2 to 172.9 ppm with the second highest (*C*C–O) in the range of 163.1-189.4 ppm which our value of 177.3 ppm agrees with.[38,39,41,51,53,58,59] This discrepancy with the literature could be a consequence of the sterically bulky nature of the *m*-terphenyl squaraine and lack of charge delocalisation onto the whole molecule, *i.e.* there could be sufficient negative charge on the carbon of *C*–O resulting in a high chemical shift, similar to the chemical shift of a carbene centre.[60] However unlikely, the possibility of the chemical shift range not being extended to higher ppm window, and therefore chemical shifts were not reported in the literature, cannot be dismissed.

The UV/Vis absorption spectrum of **29^{Mes}** in dichloromethane, (Figure 6.3) features a transition in the NIR region (742 nm) from the intramolecular charge transfer (CT) from the donor aryl to the electron poor C_4O_2 ring. There are also two blue shifted CT transitions at 480 and 515 nm which is possibly due to H-aggregation in solution, well documented for other squaraines in the literature.[61–64] This seems unlikely however due to the highly twisted nature of the central aryl of the *m*-terphenyl and the C_4O_2 ring (see Section 6.3.1.2). The UV/Vis spectrum also features strong absorptions below 300 nm from the π–π* transitions in the aryl rings.

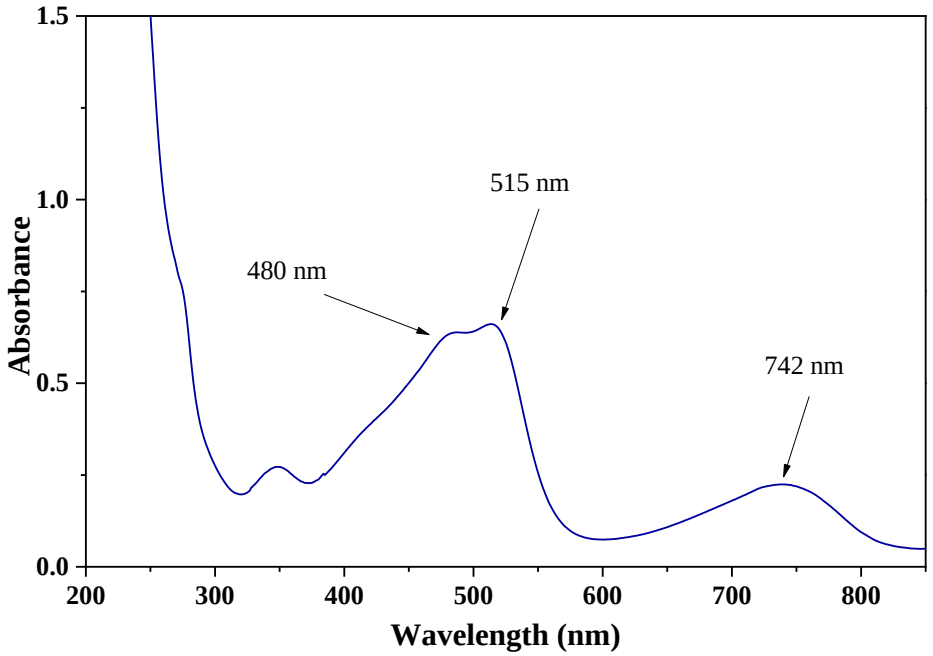


Figure 6.3 UV/Vis absorption spectrum of 29 in dichloromethane.

In order to gain insight into the origin of the features of the UV/Vis spectrum of **29^{Mes}**, preliminary gas-phase time-dependent density functional theory calculations (TD-DFT) were performed by Dr J. McMaster at the University of Nottingham on a geometry optimized model of **29^{Mes}** derived from the X-ray crystal structure. The calculations were performed using the Amsterdam Density Functional (ADF) suite version 2012.01.[65,66] The DFT geometry optimisations employed all-electron Slater type orbital (STO) triple-ζ-plus polarisation basis sets from the TZP database of the ADF suite for the C, O, and H atoms. The local density approximation (LDA) with the correlation potential due to Vosko *et al.*[65] was used in all of the calculations. Gradient corrections were performed using the functionals of Becke[65] and Perdew.[65] TD-DFT calculations were used to estimate the energies of the first 20 UV/Vis transitions of **29^{Mes}**. The calculations suggest that the LUMO (190a) is localized principally on the squaraine component with some delocalization on to the central aryl ring of the *m*-terphenyl unit (Figure 6.4, **A**). The HOMO (189a) possesses lone pair O character, which resides in the plane of the squaraine ring (Figure 6.4, **B**). The TD-DFT calculated UV/Vis spectrum of **29^{Mes}** (Figure

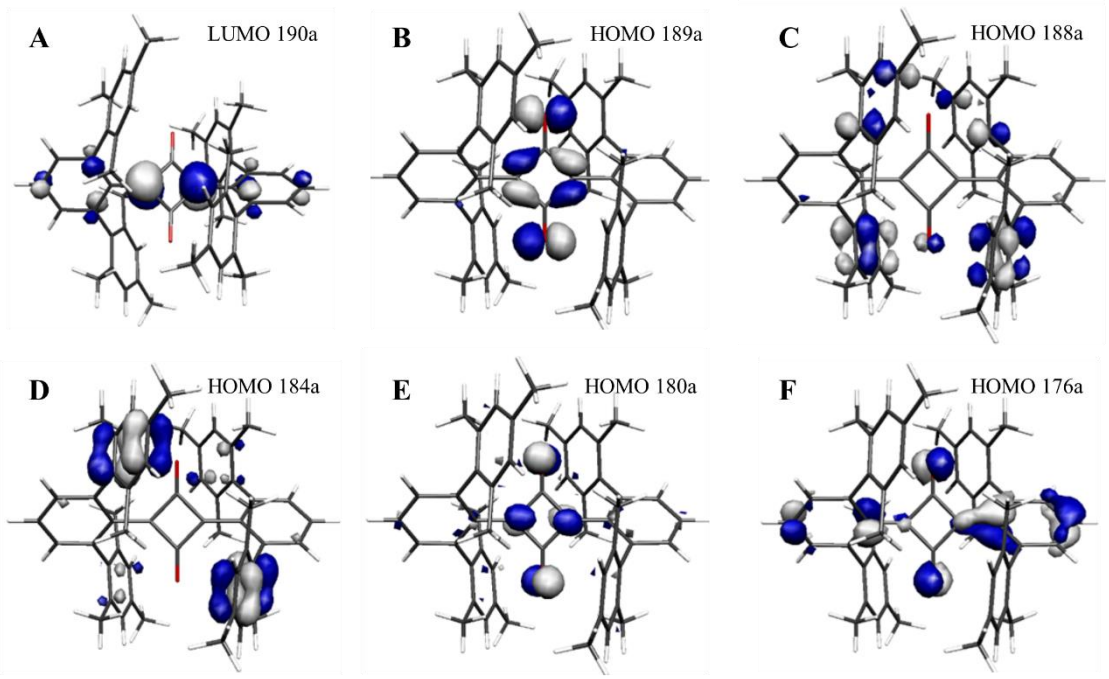


Figure 6.4 Calculated molecular orbitals of 29.

6.5) in the gas phase possesses transitions that are considerably shifted from those observed in the experimental spectrum (Figure 6.3). These shifts may be associated with the gas-phase nature of the TD-DFT calculations. Nevertheless, the relative order of the transitions and their relative intensities suggests that the broad absorption at 742 nm in the experimental spectrum results from transitions from orbitals localized principally on the pendant aryl rings of the *m*-terphenyl unit (188a and 184a, Figure 6.4, **C** and **D**) into the LUMO (190a). A comparison of the calculated and experimental absorption spectra suggest that the more intense transition at 515 nm in the experimental spectrum may be assigned to a π–π* transition that is localized on the squaraine unit which involves the 180a orbital (Figure 6.4, **E**) and the LUMO (190a). The higher energy transition at 480 nm in the experimental spectrum may be assigned to a π–π* transition involving an orbital (176a, Figure 6.4, **F**) possessing O-lone pair character C– π contributions derived from central aryl ring of the *m*-terphenyl unit and the LUMO (190a).

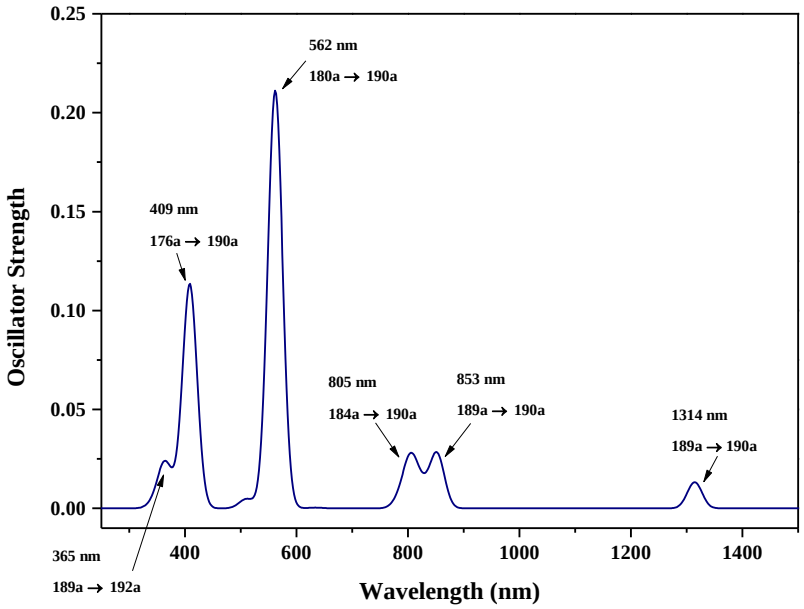


Figure 6.5 Calculated UV/Vis spectrum of 29.

The electrochemical properties of **29^{Mes}** were investigated using cyclic voltammetry in dichloromethane containing [^{n}Bu$_4$N][BF$_4$] (0.4 M) as the supporting electrolyte. Potentials are reported against the Fc^{+}/Fc couple used as an internal standard (where Fc = ferrocene). **29^{Mes}** shows a reduction process at $E_{1/2}$ –0.79 V and an oxidation process at E_p^a 0.48 V (Figure 6.6). The reduction gave peak anodic and cathodic potentials that were independent of scan rate and the separation of peak potentials (potentials ($\Delta E = E_p^a - E_p^c$) was 1.58 V. Moreover, a plot of the peak currents (I_p^a and I_p^c) *vs.* the square root of scan rate was linear in the scan rate range 20 to 300 mVs and the ratio of $-I_p^a/I_p^c$ is in the range of 0.54-0.66. The reduction potential observed for **29^{Mes}** is higher than those seen for other squaraines in the literature (–1.40 to –0.98).[38,63] The oxidation process showed no evidence for a return wave in the range of scan rates employed. Given a lack of shift of peak potential to more positive values on increasing the scan rate, a property of an electrochemically irreversible process, this oxidation is tentatively assigned as an 'EC'

type process, where oxidation of **29**^{Mes} to [**29**^{Mes}]$^{+}$ results in chemical reactivity of the cationic species and hence its removal from the diffusion layer.

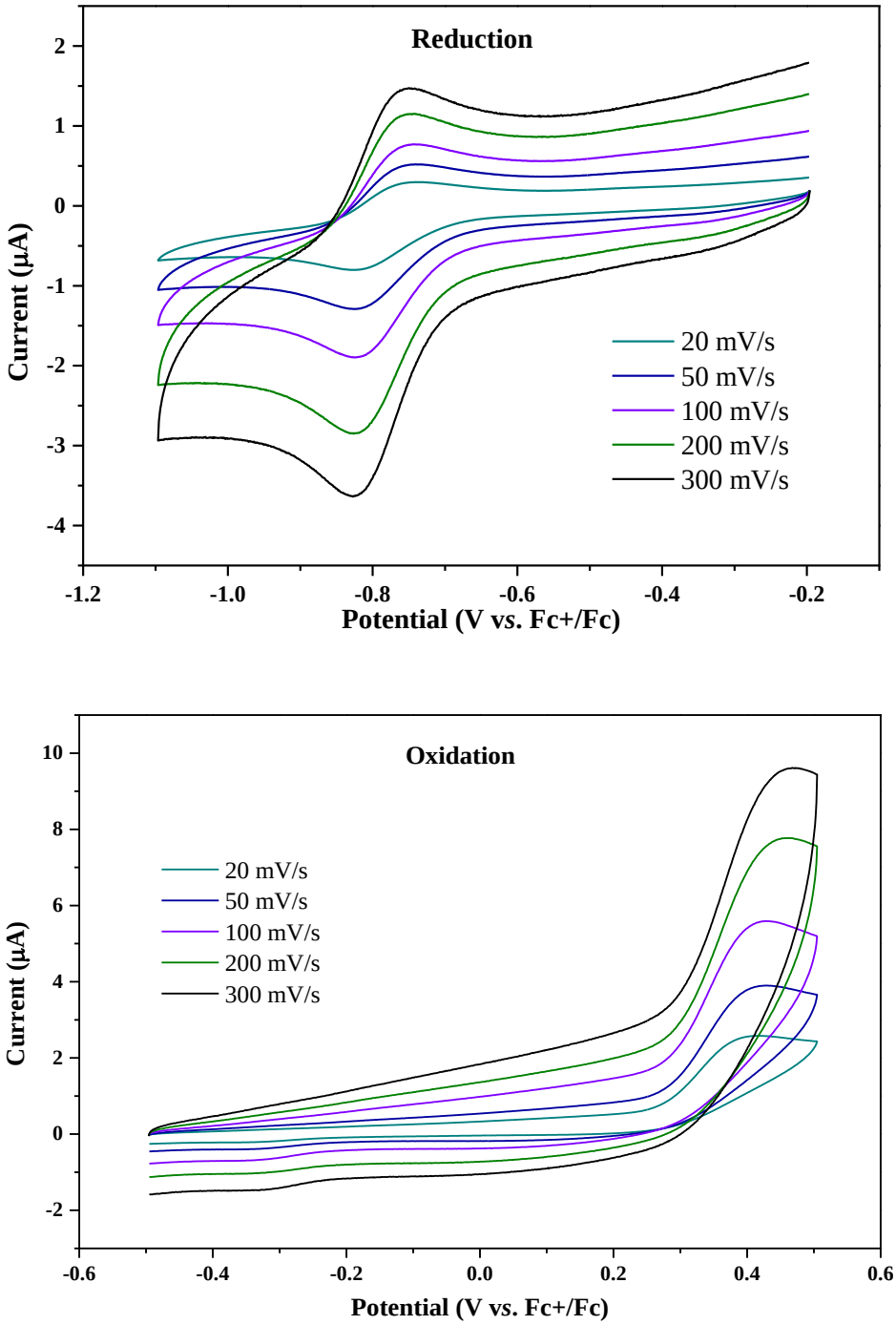


Figure 6.6 Cyclic voltammograms of 29 in dichloromethane containing 0.4 M [^{n}Bu$_4$N][BF$_4$] as the supporting electrolyte, reduction (top) oxidation (bottom).

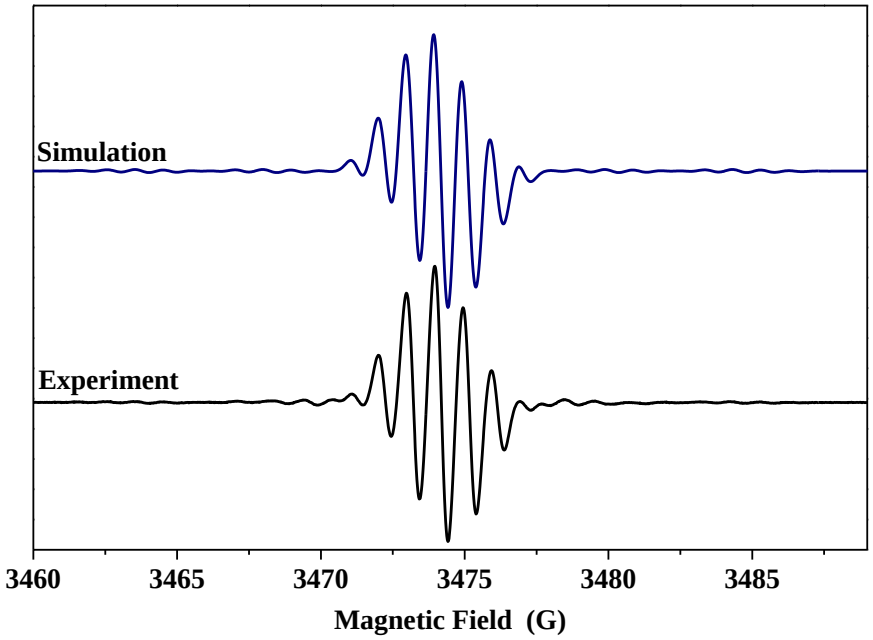
The EPR activity of monoanionic **29^{Mes}** was investigated by chemical reduction of the parent compound with *ca*. 1 equivalent of cobaltocene. The experimental X-band EPR spectrum obtained as a fluid solution at room temperature with its simulated spectra is shown in Figure 6.7, top. On cooling to 77 K no additional spectral features were observed. A reasonable reproduction of the experimental spectral profile was achieved by simulation using one set of two equivalent hydrogens and one set of four equivalent hydrogens (*para*- and *meta*-C*H*s on the central aryl ring of the *m*-terphenyl substituent respectively) and two sets of two equivalent carbons (C_4O_2 ring) (see Table 6.1 for full parameters).

Compound	g_{iso}	$a_{iso}/10^{-4}cm^{-1}$	***Linewidth/G***	***Lineshape***
29^{Mes}	2.0028	0.96 (4H) 0.76 (2H) 19.43 (2C) 11.12 (2C)	0.52	Gaussian
29$^{2,6\text{-Xyl}}$	2.0027	1.11 (4H) 0.85 (2H)	0.23	Lorentzian

Table 6.1 Parameters for the experimental and simulated EPR spectra for squaraines.

It should be noted that monoanionic **29^{Mes}** was detected by EPR spectroscopy in a purified sample of **29^{Mes}**, prior to chemical reduction with Cp_2Co, albeit in very small quantities. Upon addition of Cp_2Co to an already EPR active sample of **29^{Mes}** in dichloromethane, the EPR signal increased significantly, which suggests that during the formation of **29^{Mes}** small quantities of a reducing agent are generated in the reaction mixture. Given this result, the EPR activity of a sample of **29$^{2,6\text{-Xyl}}$** was investigated whereupon it was found that a small amount of the monoanionic species was also present in the sample (Figure 6.7, bottom). The simulation of the experimental spectrum using one set of two equivalent hydrogens and one set of four equivalent hydrogens (*para*- and *meta*-C*H*s on the central aryl ring of the *m*-terphenyl respectively) reproduced the central

features reasonably well, although in this case hyperfine coupling to carbon, observed as undulations in the baseline either side of the central features, were not sufficiently resolved to allow for their incorporation in the simulation parameters. Full parameters are shown in Table 6.1.



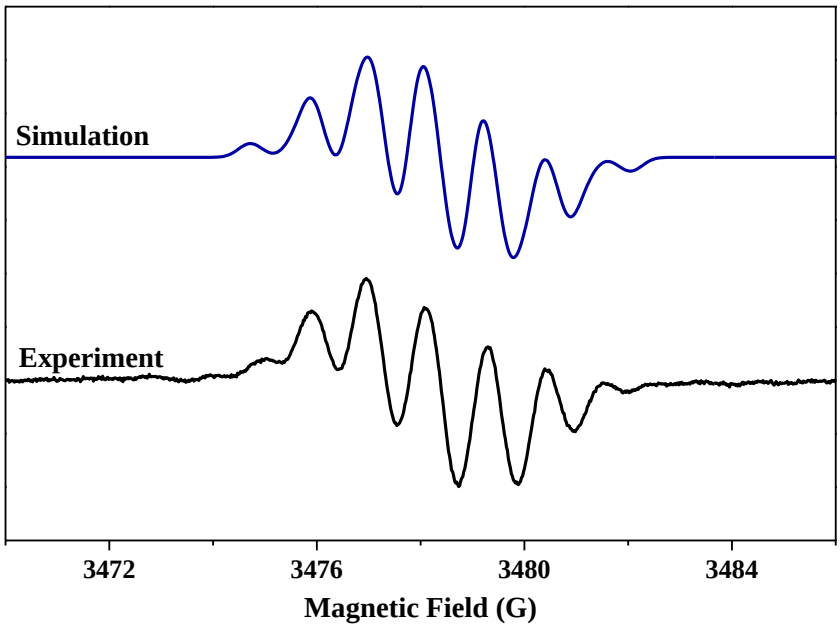


Figure 6.7 EPR spectra of the monoanionic squaraines (29^{Mes}, top; $29^{2,6\text{-}Xyl}$, bottom). Experimental data (black) simulated data (blue).

6.3.1.2 Crystallographic Analysis

The solid state structures of **29^{Mes}** and **29$^{2,6\text{-}Xyl}$** were determined by single crystal X-ray diffraction and are shown in Figure 6.8. The molecular structures of **29^{Mes}** and **29$^{2,6\text{-}Xyl}$** features a central four membered ring with an *m*-terphenyl substituent on either side.

29^{Mes} was found to crystallise in the triclinic space group *P*-1 with one molecule in the asymmetric unit cell with a disordered solvent molecule of crystallisation. **29$^{2,6\text{-}Xyl}$** crystallises in the orthorhombic space group *Ccce* with half a molecule in the asymmetric unit. Relevant bond distances and angels are shown in Table 6.2.

The central C_4O_2 ring is twisted somewhat out of plane with respect to the central aryl on the *m*-terphenyl moiety [**29^{Mes}**: 56.38(15)°, 51.71(11)°; **29$^{2,6\text{-}Xyl}$**: 129.0719(17)°, 50.9281(17)°] presumably a consequence of the steric demands of the bulky Mes and 2,6-Xyl substituents on the flanking aryls. This observation is rather opposed to other crystallographically characterised squaraines in the literature which exhibit a rigid planar core structure where the plane to plane twist angle (with respect to the C_4O_2 ring and the adjacent aryl) ranges between 0.37(6)-3.23(9)°.[38,41,59,63,67] The aforementioned guaiazulenyl-derived squaraine (Figure 6.1, middle) exhibits a larger plane to plane twist angle of 17.41(12)°,[56] but is still significantly lower than observed for **29^{Mes}** and **29$^{2,6\text{-}Xyl}$**.

The C–O bond lengths in **29^{Mes}** and **29$^{2,6\text{-}Xyl}$** (see Table 6.2) are slightly shorter than observed for other squaraines in the literature (1.2269(19)-1.260(5) Å),[38,41,56,59,63,67] which is indicative the C–O bond possessing more C=O bond character, and was also reflected in the higher IR absorbance frequency of the C–O bond as discussed in Section 6.3.1.1.

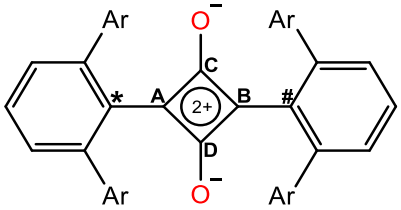
	***29^{Mes}***	***29$^{2,6\text{-}Xyl}$***
	**** = 1***	**** = 1***
	# = 25	***# = 1'***
	A = 49	***A = 13***
	B = 51	***B = 13''***
	C = 50	***C = 14'***
	D =52	***D = 14***
C(*)–C(A)	1.450(4)	1.451(2)
C(#)–C(B)	1.442(3)	-
C(A)–C(C)	1.474(3)	1.4838(18)
C(A)–C(D)	1.472(4)	1.4837(18)
C(B)–C(C)	1.469(3)	1.4837(18)
C(B)–C(D)	1.476(3)	-
C(C)–O(1)	1.215(3)	1.212(2)
C(D)–O(2)	1.218(3)	-
C(A)–C(C)–C(B)	88.98(19)	-
C(A)–C(D)–C(B)	89.17(19)	88.66(15)
C(C)–C(A)–C(D)	90.9(2)	91.34(15)
C(C)–C(B)–C(D)	90.95(19)	-
(C_6H_3)plane···(Ar)plane	75.89(12)	107.3502(13)
	81.50(11)	72.6498(13)
	74.40(8)	-
	79.48(8)	-
(C_6H_3)plane···(C_4O_2)plane	56.38(15)	129.0719(17)
	51.71(11)	50.9281(17)

Table 6.2 Selected bond lengths (Å) and angles (°) for 29^{Mes} and 29$^{2,6\text{-}Xyl}$.Symmetry operation: ' = 1 – x, + y, 3/2 – z; ''= 1 – x, 3/2 – y,+ z.

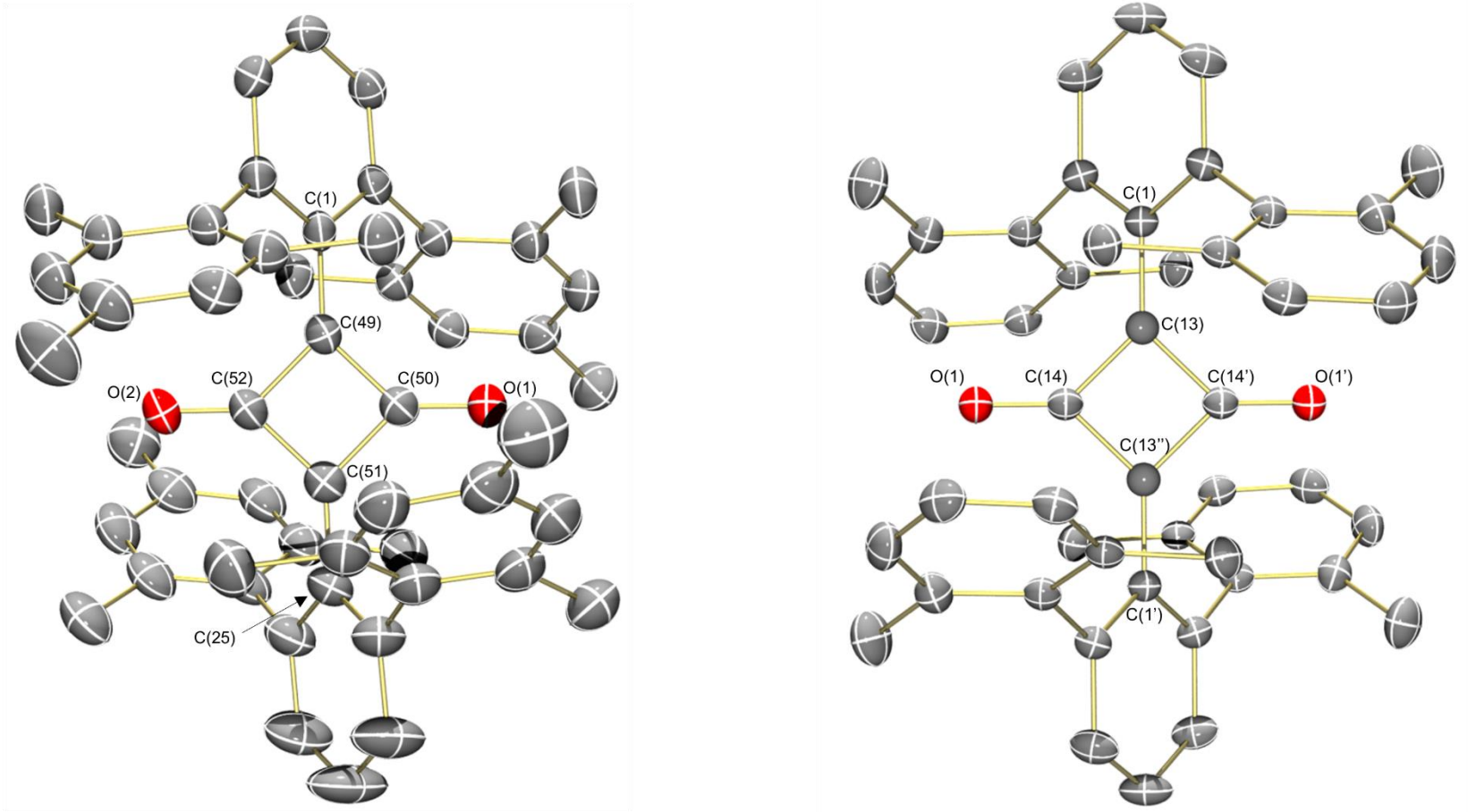


Figure 6.8 Crystal structures of 29^{Mes} (left) and $29^{2,6\text{-}Xyl}$ (right). Thermal ellipsoids are set at the 50% probability level. Hydrogen atoms and solvent of recrystallisation omitted for clarity. Symmetry operation: ' = 1 – x, 3/2 – y,+ z; '' = 1 – x, + y, 3/2 – z.

6.3.2 Diironcarboxylate Complex

Diiron carboxylates featuring *m*-terphenyl ligands are abundant in the literature where the carboxylate-bridged diiron(II) centre are similar to catalytic centres in proteins such as soluble methane monooxygenase (sMMO), the R2 subunit of ribonucleotide reductase (RNR-R2), Δ^9 stearoyl-acyl carrier protein desaturase (Δ^9D), and toluene/*o*-xylene monooxygenase (ToMO) amongst others, which activate O_2 for a variety of uses.[68,69]

These diiron(II) complexes are synthesised by metathesis reactions between a metal salt of a carboxylate ligand, $ArCO_2M$ (Ar = *m*-terphenyl; M = Li, Na, Tl), and an iron(II) source ($Fe(OTf)_2$·MeCN, $FeCl_2$ or $FeBr_2$) to form $[Fe_2(\mu\text{-}O_2CAr)_2(O_2CAr)_2(L)_2]$ where L = N or O bound ligand.[70–73] These complexes generally crystallise in one of two conformations where the carboxylate ligands support the doubly bridged (windmill **I**) or quadruply bridged (paddlewheel **II**) diiron(II) cores as shown in Figure 6.9.[74]

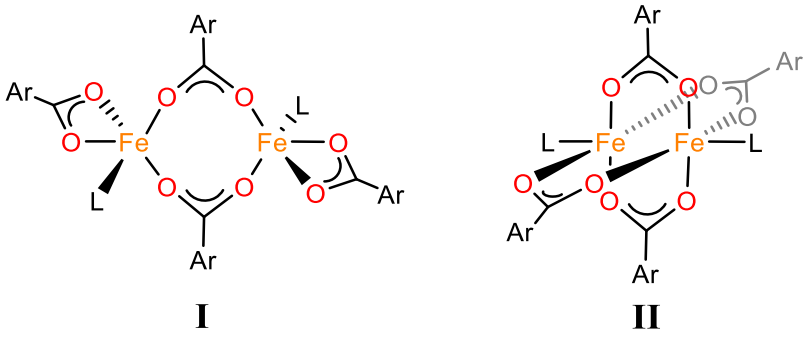


Figure 6.9 Windmill (I) or paddlewheel (II) conformation of $[Fe_2(\mu\text{-}O_2CAr)_2(O_2CAr)_2(L)_2]$.[74]

6.3.2.1 Spectroscopic Analysis of Diiron Carboxylate Complex $30^{2,6\text{-Xyl}}$

$30^{2,6\text{-Xyl}}$ was synthesised through reaction of **14** with CO for 16 h, upon work up and recrystallisaton from a solution in hexane, **$30^{2,6\text{-Xyl}}$** was isolated as a red microcrystalline solid. It is highly unlikely that this reaction proceeded *via* the metathesis reaction of the

aryl lithium carboxylate $ArCO_2Li$ due to the rigorous exclusion of air and moisture throughout all manipulation. Despite numerous attempts, the sample of **30$^{2,6\text{-Xyl}}$** was obtained in such small quantities that analysis by X-ray crystallography could only be performed. Solution IR spectra from *in situ* reaction monitoring (see Section 6.3.3.1) shows a peak at 1751 cm^{-1} which could be **30$^{2,6\text{-Xyl}}$** which is higher than related diiron carboxylate complexes (1614-1570 cm^{-1}).[70–72,74–78] possibly due to the lack of coordinating ligand (L), but closer in value to 1697 cm^{-1} for the complex $Fe_2(\mu\text{-}O_2CAr^{Tol})_2(O_2CAr^{Tol})_2(4\text{-AcPy})$ (where ArTol = 2,6-*p*-$Tol_2C_6H_3$; AcPy = 4-cyanopyridine).[79] The MS **30$^{2,6\text{-Xyl}}$** is not conclusive as the molecular ion was not detected by EI or MALDI, with also the possibility that the sample contained a mixture of species.

6.3.2.2 Crystallographic Analysis of Diiron Carboxylate Complex 30$^{2,6\text{-Xyl}}$

30$^{2,6\text{-Xyl}}$ crystallised in the monoclinic space group *I2/a* with half a molecule in the asymmetric unit with 1.5 hexane molecules per moiety in the unit cell. These disordered hexane molecules could not be sensibly modelled therefore Platon SQUEEZE was used to account for these diffuse molecules. **30$^{2,6\text{-Xyl}}$** is geometrically similar to the 'windmill' conformation (Figure 6.9, **I**) with the absence of two additional N or O bound coordinating ligands. The iron atoms are coordinated to one terminal and two bridging carboxylate ligands ($2,6\text{-}(2,6\text{-Xyl})_2C_6H_3CO_2^-$) where the flanking 2,6-Xyl groups encapsulate the diiron core (Figure 6.10, top). Selected bond angles and lengths of **30$^{2,6\text{-Xyl}}$** are shown in Table 6.3. The coordination of each iron centres (Figure 6.10, bottom) can be described as distorted tetrahedral with a four-coordinate geometry index value (τ_4) of 1.10 (see Chapter II, Equation 2.1).[80] The Fe(1)···Fe(1') distance of 4.74314(11) Å is

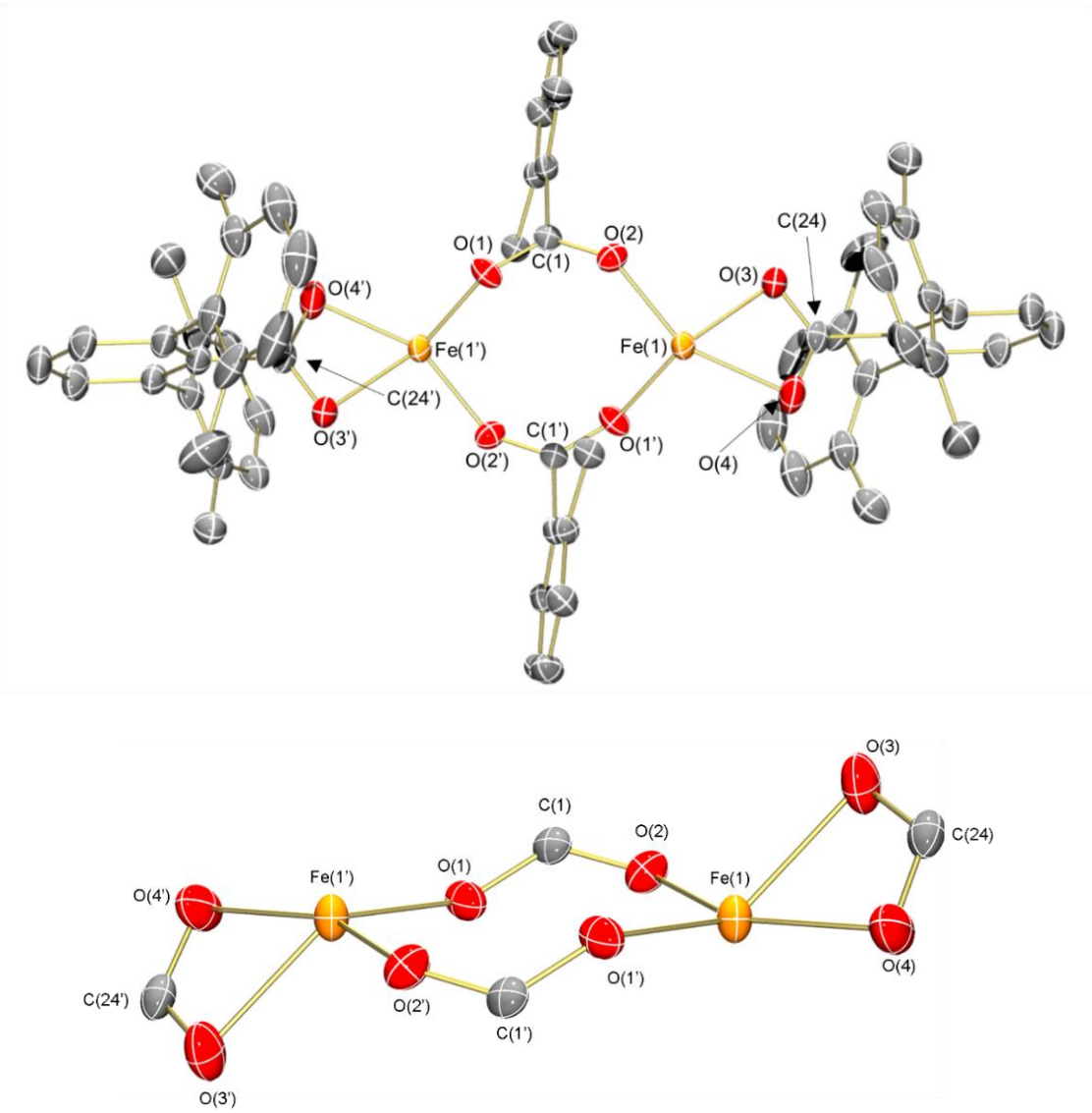


Figure 6.10 Top: crystal structure of 30$^{2,6\text{-Xyl}}$ with hydrogen atoms and flanking 2,6-Xyl moieties on bridging aryls omitted for clarity. Bottom: side on view of diiron core. Thermal ellipsoids are set at the 50% probability level. Symmetry operation: ' = ½ – x, 3/2 – y, ½ – z.

larger than that in related diiron carboxylate complexes in the windmill conformation which range between 3.355(10)-4.6052(9) Å,[69–78,81–83] possibly a consequence of the more sterically demanding 2,6-Xyl substituents.[69] The Fe–O distances of the bridging ligand [1.9612(12)-1.9779(12) Å] are shorter than the analogous distances for the terminal carboxylate [2.0830(14)-2.1509(14) Å] which is similar to those observed in the literature.[70,73,77–79,81]

	$30^{2,6\text{-Xyl}}$
Fe(1)···Fe(1')	4.74314(11)
C(1)–O(1)	1.252(2)
C(1)–O(2)	1.254(2)
C(24)–O(3)	1.250(2)
C(24)–O(4)	1.252(2)
Fe(1)–O(1')	1.9779(12)
Fe(1)–O(2)	1.9612(12)
Fe(1)–O(3)	2.0830(14)
Fe(1)–O(4)	2.1509(14)
Fe(1')–O(1)	1.9778(12)
O(1')–Fe(1)–O(3)	153.19(6)
O(1')–Fe(1)–O(4)	94.33(5)
O(2)–Fe(1)–O(1')	98.47(6)
O(2)–Fe(1)–O(3)	106.15(6)
O(2)–Fe(1)–O(4)	130.62(6)
O(3)–Fe(1)–O(4)	61.53(5)

Table 6.3 Selected bond lengths (Å) and angles (°) for $30^{2,6\text{-Xyl}}$. Symmetry operation: ' = ½ – x, 3/2 – y, ½ – z.

6.3.3 In situ Reaction Monitoring

To gain insight into the reaction mechanism and to identify any possible intermediates, *in situ* reaction monitoring studies were undertaken using IR and EPR spectroscopies. The presence of paramagnetic species in solution hampered attempts to follow the reaction *via* NMR spectroscopy.

6.3.3.1 Reaction Monitoring via Solution IR Spectroscopy

A mixture of either **11** or **14** in toluene was exposed to an atmosphere of CO gas where an immediate colour change was observed. Samples of the reaction mixture (0.4 mL) were removed from the reaction vessel under an atmosphere of CO and dried under vacuum for *ca*. 1 h to remove any volatile iron carbonyl compounds and residual CO. This sample was redissolved in toluene and the solution IR spectrum was recorded. Samples were

taken shortly after addition of CO (35 min to 1 h) to the reaction vessel then every 24 h. IR spectra obtained throughout the reaction are shown in Figure 6.11 (top: **11** with CO; bottom: **14** with CO).

Initially, three new bands appeared shortly after addition of CO to the reaction mixture (Figure 6.11, left, green spectra; **11**: 2097, 2050, 1978 cm^{-1}; **14**: 2099, 2050, 1980 cm^{-1}) where the band at highest wavenumber increased with time and the remaining two decreased with time. The band at 2097/2099cm^{-1} is indicative of a free or η^1-coordinated ketene, which appear around from 2080 to 2250 cm^{-1},[84,85] whereas the bands at 2050 and 1978/1980 cm^{-1} are most probably due to and iron carbonyl or coordination of a ketene *via* C=C bond.[86] After 1 day a shoulder appears at 2030/2031 cm^{-1} which could be an iron carbonyl intermediate. The iron carbonyl CO stretches seen in the IR spectra are similar to the CO absorption bands aforementioned iron acyl complex (Scheme 6.1, left; 2000 and 1944 cm^{-1}) and the metallacyclic iron carbene complex (Scheme 6.1, right; 2051, 1982, 1966 cm^{-1}).[28,31] There is also formation of two new bands at lower wavenumber (Figure 6.11, right; **11**: 1751, 1673 cm^{-1}; **14**: 1751, 1675 cm^{-1}) where the peak at 1751 cm^{-1} could be due to the formation of the diiron carboxylate complex and the peak at 1673/1675 cm^{-1} is most likely the squaraine molecule (measurement from purified $\mathbf{29^{Mes}}$: 1673 cm^{-1}).

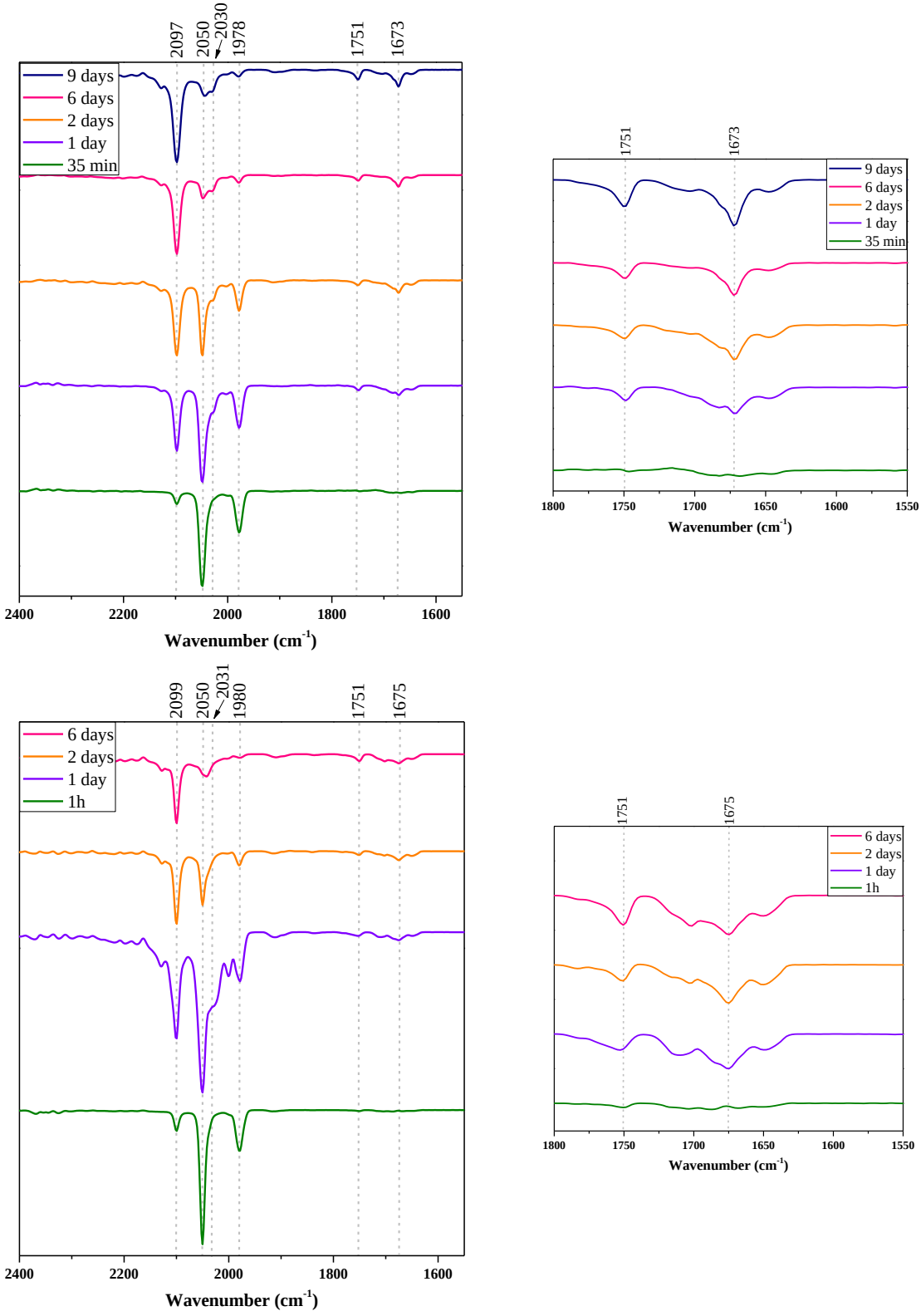


Figure 6.11 Solution IR spectra obtained for the reaction of 11 (top) or 14 (bottom) with CO. Spectra on right show a close-up of the region 1800-1550 cm^{-1}.

6.3.3.2 Reaction Monitoring via EPR Spectroscopy

As mentioned in Section 6.3.1.1, occasionally the isolated squaraines are EPR active without the need to add a reducing agent, Cp_2Co. This result prompted the investigation into possible radical intermediates in the reaction mixture.

The fluid solution X-band EPR spectrum of the iron diaryl, **11** or **14**, at room temperature was silent. Upon addition of CO to this EPR silent solution an immediate colour change was observed and the reaction mixture was monitored by EPR spectroscopy.

The reaction of **11** with CO gave a room temperature fluid solution EPR spectrum featuring a peak at g_{iso} = 2.0981 after 24 hours. At 77 K a rhombic spectrum is obtained for this sample, which maybe suggestive of a metal-based radical, possibly containing CO coordinated to an iron centre (Figure 6.12). No hyperfine coupling was resolved for this feature. The simulated parameters for the 77 K frozen solution spectrum are shown in Table 6.4.

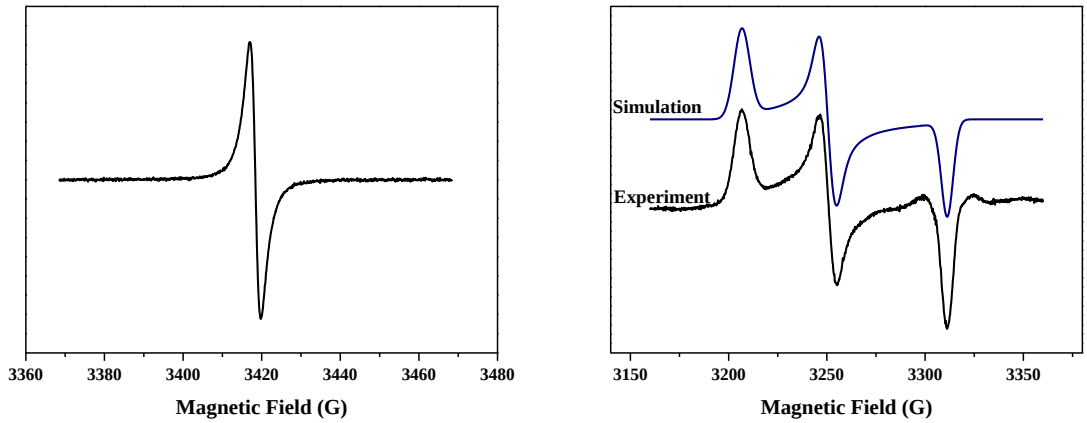


Figure 6.12 EPR spectra obtained from reaction of 11 with CO after 1 day. Left: room temperature; right: 77 K with the simulated spectrum in blue.

	g	***Linewidth/G***	***Lineshape***
g_x	2.069	8	Gaussian
g_y	2.041	7	
g_z	2.003	6	

Table 6.4 Parameters for the experimental and simulated EPR spectra at 77 K.

After 2 days a new peak appears at g_{iso} = 2.0033 (Figure 6.13 right and dotted circle in left). This peak exhibits hyperfine coupling (Figure 6.13 right) very similar to the coupling seen for **29**$^{\mathbf{Mes}}$ (Figure 6.7, top).

When **14** is reacted with CO a similar result is obtained. After *ca*. 24 h the sample is EPR active. A large peak and a smaller peak are observed at g_{iso} = 2.0386 and 2.0049 respectively (Figure 6.14, top). As with **11**, the feature at g_{iso} = 2.0386 shows no hyperfine coupling at room temperature and is rhombic at 77 K suggesting the presence of a metal based radical (Figure 6.14, bottom left). The feature at g_{iso} = 2.0049 shows hyperfine coupling (Figure 6.14, bottom right) the magnitude of which is very similar to that observed for **29**$^{\mathbf{2,6\text{-}Xyl}}$ (Figure 6.7, bottom).

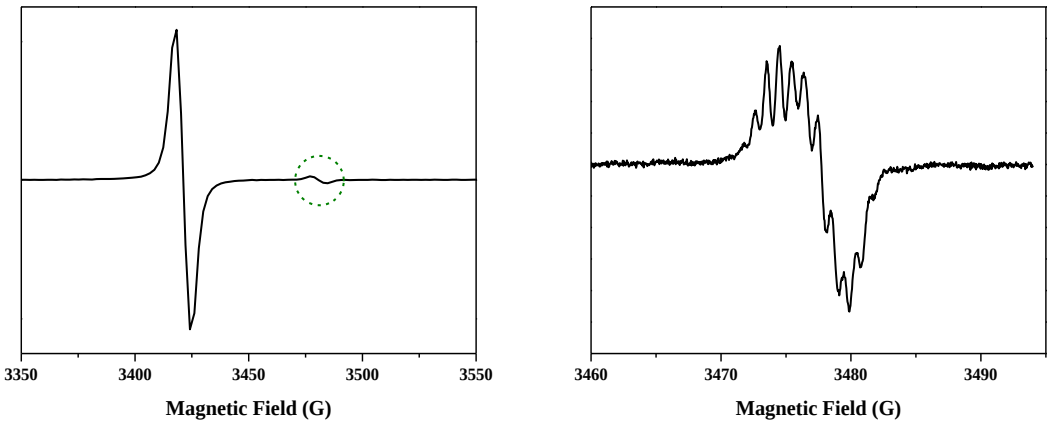


Figure 6.13 EPR spectra obtained from reaction of 11 with CO after 2 days. Wide field sweep (left) and narrow field sweep (right) focussing on the feature at g_{iso} = 2.0033 (dotted circle in left spectrum)

It is important to highlight that other EPR active species could be present in the reaction solution that are not detectable by EPR spectroscopy under the conditions of these experiments and that may require lower temperatures, higher fields or different frequencies for their study.

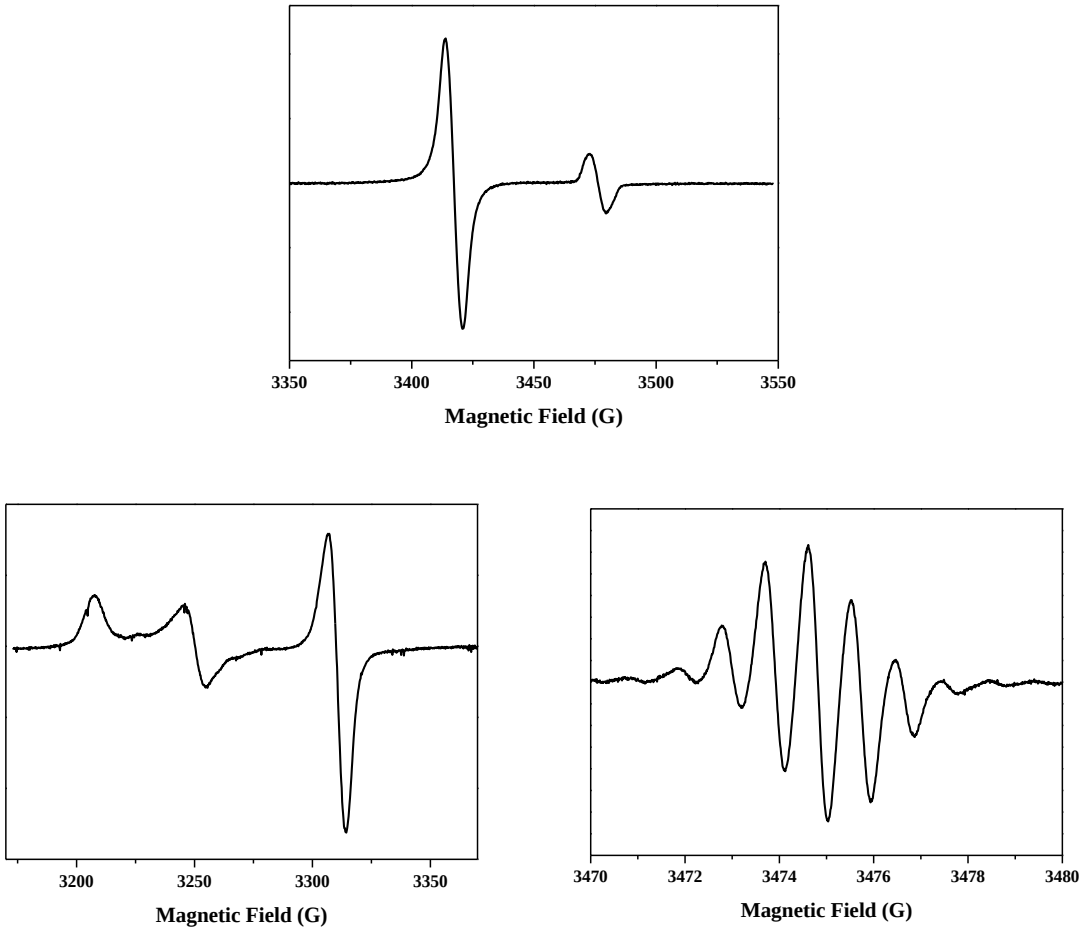
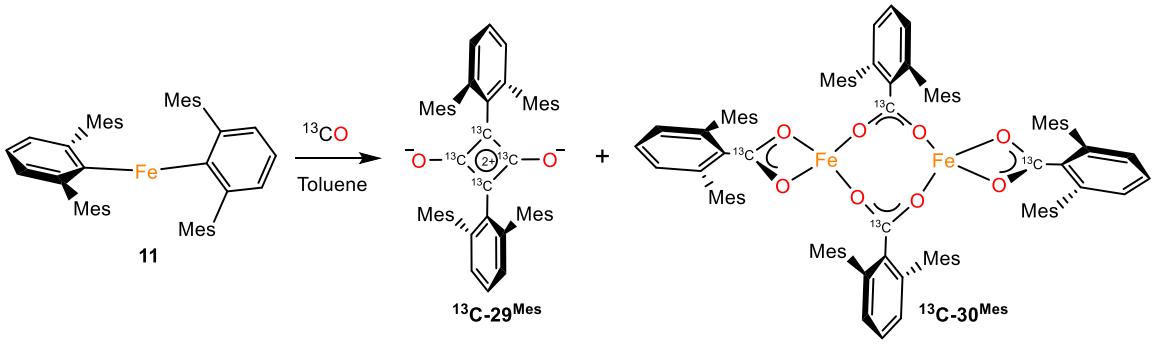


Figure 6.14 EPR Spectra obtained from reaction of 14 with CO after 1 day. Top: wide field sweep spectrum; bottom left: 77 K spectrum; bottom right: narrow field sweep centred on the feature at g_{iso} = 2.0049 (small feature to the right in the wide sweep spectrum).

6.3.4 Carbon-13 Labelling Studies



Scheme 6.6 Reaction of 11 with ^{13}CO.

In order to provide further evidence that CO bond scission has occurred, carbon-13 labelling studies were undertaken using ^{13}CO (99%). As **29^{Mes}** could be reliably isolated and purified, the reaction between **11** and ^{13}CO gas was performed (Scheme 6.6). Addition of ^{13}CO gas to a solution of **11** in toluene resulted in an immediate colour change from a yellow to a red solution. A sample of the reaction solution was removed from the reaction vessel after 1 h and after 6 days for analysis by solution IR spectroscopy, the results of which are discussed in detail in Section 6.3.4.2. After subsequent workup and crystallisation, a small amount of pure 1,3-(2,6-$Mes_2C_6H_3)_2{}^{13}C_4O_2$ (**^{13}C-29^{Mes}**) was isolated as red needles in sufficient quantity for analysis by ^{1}H, ^{13}C{^{1}H} NMR, IR, EPR spectroscopies and mass spectrometry.

6.3.4.1 Spectroscopic Analysis of 1,3-(2,6-$Mes_2C_6H_3)_2{}^{13}C_4O_2$ (^{13}C-29^{Mes})

Accurate mass measurements were found to be in good agreement with the negative ion: [**^{13}C-29^{Mes}**+MeO]$^{-}$ and ^{1}H NMR of **^{13}C-29^{Mes}** is essentially identical to **29^{Mes}** confirming the sample purity. The ^{13}C{^{1}H} NMR is rather striking: after only 8 scans the carbon signals arising from the central $^{13}C_4O_2$ ring appeared at triplets at 269.7 and 177.3 ppm each with a coupling constant of 45 Hz (Figure 6.15, left), upon full

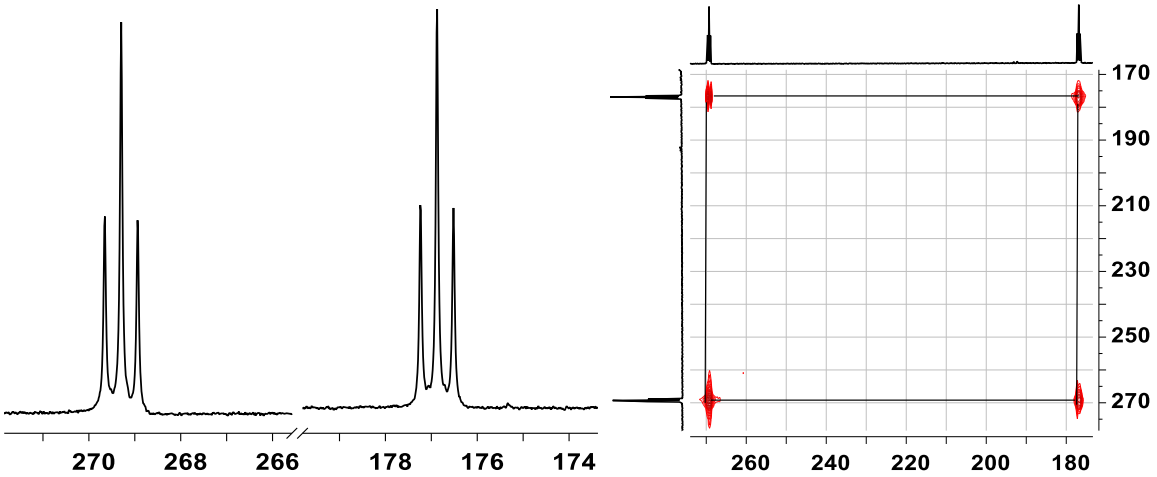


Figure 6.15 $^{13}C\{^1H\}$ (left) and $^{13}C,^{13}C$ COSY (right) NMR spectra of the C_4O_2 ring in ^{13}C-29^{Mes}

acquisition the remaining carbon peaks were observed which did not differ from the $^{13}C\{^1H\}$ NMR of **29^{Mes}**. The one bond coupling constant of 45 Hz between the adjacent for the carbons in the central C_4O_2 ring are similar to other one bond ^{13}C, ^{13}C coupling constants in the literature.[87–89] The ^{13}C, ^{13}C correlation (COSY) experiment clearly showed correlation between these carbons (Figure 6.15, right), which strongly implies that these carbons are derived from ^{13}CO. Two very small doublets at 171.3 and 24.5 ppm with a coupling constant of *ca.* 106 Hz were observed in the $^{13}C\{^1H\}$ NMR which is similar to the chemical shifts of a ketene,[10,84,90–92] (where 171.3 ppm: $^{13}\mathit{C}=^{13}C=O$; 24.5 ppm $^{13}C=^{13}\mathit{C}=O$) further supporting the theory of a ketene intermediate as observed in the solution IR of the reaction mixture (see Section 6.3.3.1).

The solution IR spectrum of **^{13}C-29^{Mes}** in toluene showed an absorption at 1638 cm^{-1} which corresponds to an isotopic shift of 35 cm^{-1} when compared to **29^{Mes}** (1673 cm^{-1}), similar other isotopic CO/^{13}CO shifts in the literature (*ca.* 40 cm^{-1}).[12,19,20,93–95]

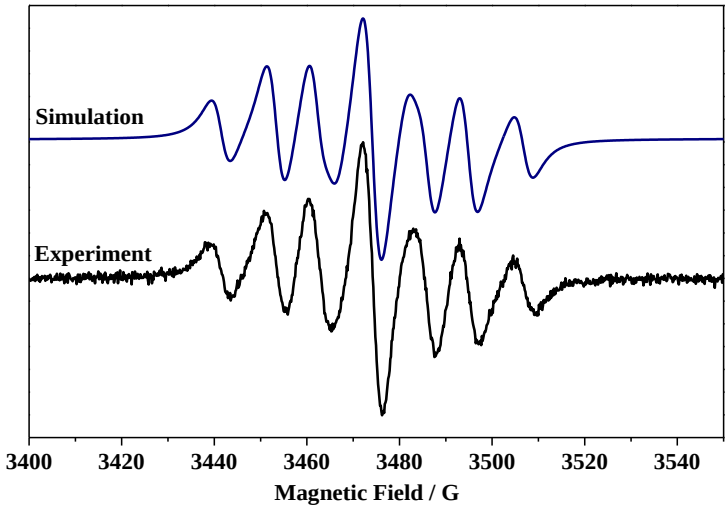


Figure 6.16 EPR spectra of the monoanionic ^{13}C-29^{Mes}. Experimental data (black) simulated data (blue).

^{13}C-29^{Mes} was found to be EPR active upon chemical reduction of **^{13}C-29^{Mes}** with Cp_2Co in dichloromethane. The fluid EPR spectrum recorded at room temperature is shown in Figure 6.16. The feature at g_{iso} = 2.0028 shows hyperfine coupling where the simulation of the experimental spectrum was produced using parameters as shown in Table 6.5, identical to **29^{Mes}**, however accounting for 99% abundance of ^{13}C in the C_4O_2 ring.

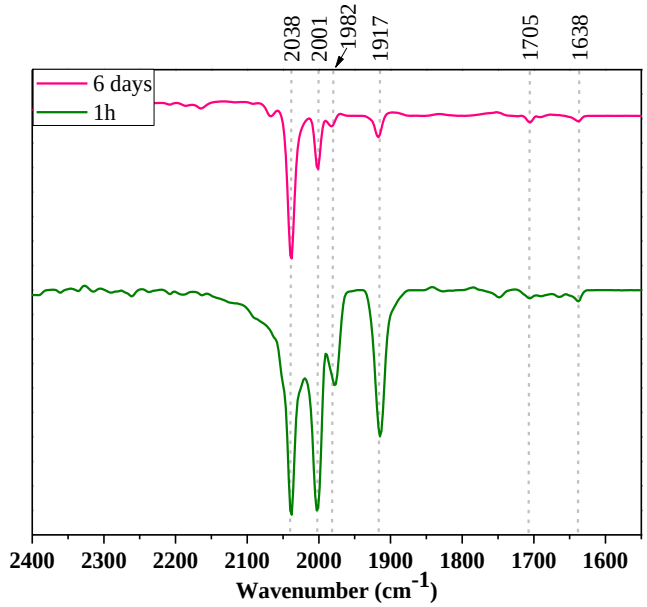
g_{iso}	$a_{iso}/10^{-4}cm^{-1}$	Linewidth/G	Lineshape
2.0028	0.96 (4H) 0.76 (2H) 19.43 (2C) 11.12 (2C)	3.60	Lorentzian

Table 6.5 Parameters for the experimental and simulated EPR spectra of ^{13}C-29^{Mes}

6.3.4.2 In situ Reaction Monitoring via Solution IR Spectroscopy with ^{13}CO

Samples of the reaction solution of **11** with ^{13}CO were taken from the vessel after 1 h and after 6 days, dried under vacuum removing any ^{13}CO and volatile carbonyl compounds, and a solution IR spectrum in toluene was performed. The IR spectra feature bands

between 2038-1638 cm^{-1} all of which are shifted with respect to the analogous reaction between **11** and natural abundance CO (Figure 6.17) which shows that all these intermediates are derived from CO.



CO	*^{13}CO*	*Isotopic Shift*
2097	2038	–59
2050	2001	–49
2030	1982	–48
1978	1917	–61
1751	1705	–46
1673	1638	–35

Figure 6.17 Left: IR spectra obtained from the reaction of 11 with ^{13}CO. Right: summary of IR bands with reaction of 11 with CO and ^{13}CO with the respective isotopic shifts in cm^{-1}.

6.3.5 Calculations

The following calculations were performed on The University of Nottingham's High Performance Computer by Dr David Robinson. Initial calculations were performed with the restricted active space self-consistent field (RASSCF) method (including π-orbitals and non-bonding orbitals) to determine the nature of the singlet state (closed-shell or open-shell). These calculations indicated a closed-shell singlet form of the molecule. Further calculations were then performed with density functional theory (DFT) with the ωB97X-D functional and 6-31G(d) basis set. Optimised geometries, with a Ph group as the flanking aryl, of the neutral (Figure 6.18) and reduced forms were obtained; vibrational frequencies were calculated for each structure (both ^{12}C and ^{13}C, Table 6.6).

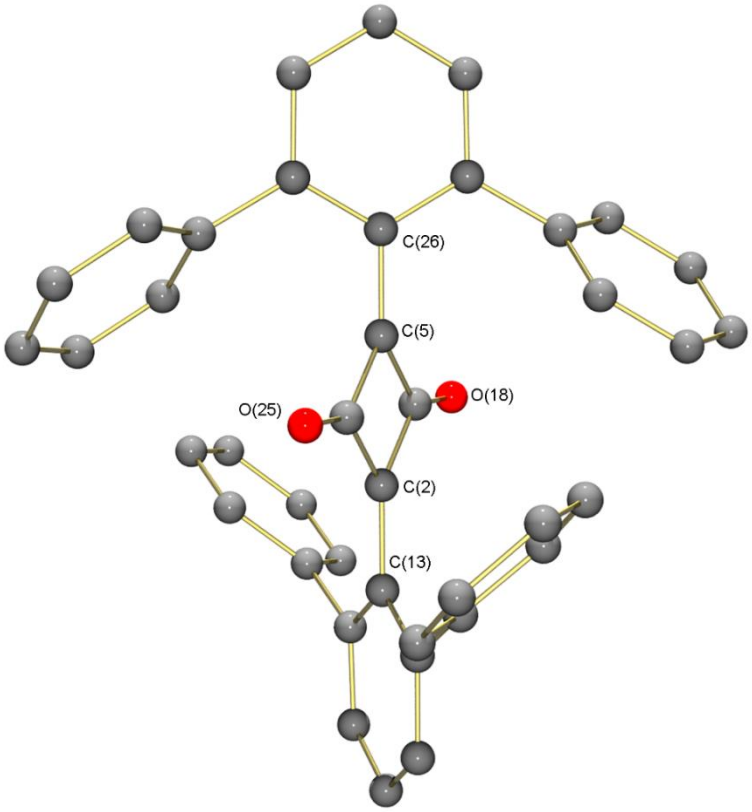


Figure 6.18 Optimised geometry of the neutral form of 1,3-(2,6-$Ph_2C_6H_3)_2C_4O_2$. Hydrogen atoms omitted for clarity.

It has been documented that when calculations assume a harmonic approximation for the potential wells this leads to an overestimation of the IR frequencies, and as such the frequencies have been scaled by 0.95.[27] The calculated bond lengths for the neutral species (C–C = 1.47 Å, C–O = 1.21 Å) are in good agreement with those determined crystallographically [C–C = 1.469(3)-1.474(3) Å, C–O = 1.215(3), 1.218(3) Å]. The calculated structure features a non-planar core with a plane to plane twist angle of the central C_4O_2 ring with respect to the central aryl on the *m*-terphenyl moiety of 132.74° and 47.38°, similar to those observed in **29^{Mes}** and **29$^{2,6\text{-}Xyl}$**.

The calculated C–O stretching frequency for **29^{Mes}** was found to be 1720 cm^{-1} which is slightly higher than the experimentally measured value (1672 cm^{-1}), and similarly the calculated C–O stretching frequency for **^{13}C-29^{Mes}** was 1675 cm^{-1} (higher than the

experimental value of 1638 cm^{-1}), which corresponds to a shift of 45 cm^{-1} lower than the calculated value for **29^{Mes}**. The reduced forms, [**29^{Mes}**]$^{-}$ and [**^{13}C-29^{Mes}**]$^{-}$, (reduced *in situ* with Cp_2Co in DCM), showed a similar discrepancy between the measured and calculated C–O stretching frequencies. The experimental IR spectra for [**29^{Mes}**]$^{-}$ and [**^{13}C-29^{Mes}**]$^{-}$ featured the C–O band at 1574 and 1523 cm^{-1} respectively, corresponding shift 51 cm^{-1} lower on ^{13}C enrichment. The C–O stretching frequencies for calculated for [**29^{Mes}**]$^{-}$ and [**^{13}C-29^{Mes}**]$^{-}$ were found to be 1666 and 1623 cm^{-1} respectively ($\Delta\bar{\nu}$ = 43 cm^{-1}) and were found to be higher than those observed experimentally by 92 and 100 cm^{-1}

Compound	***Experimental $\bar{\nu}$(C–O) (cm^{-1})***	***Calculated $\bar{\nu}$(C–O) (cm^{-1})***	***Exp. – Calc.***
29^{Mes}	1672	1720	-48
[**29^{Mes}**]$^{-}$	1574	1666	-92
^{13}C-29^{Mes}	1638	1675	-37
[**^{13}C-29^{Mes}**]$^{-}$	1523	1623	-100

Table 6.6 Experimental and calculated C–O stretching frequencies for the neutral and reduced squaines from reaction of 11 with CO or ^{13}CO.

6.3.6 Mechanistic Discussion

The mechanism for the formation of squaraines and carboxylate complexes from the reaction of iron diaryl complexes **11** and **14** with CO still remains uncertain at this time. However, without further isolation of intermediates, partial spectroscopic analysis of reaction products and without further support from calculations, the reaction mechanism proposed herein is entirely speculative. Exactly how the CO bond scission occurs is not completely understood, however, from experimental observations though IR, EPR and NMR spectroscopies, there is precedent for the proposal of numerous intermediates.

EPR spectroscopy of the reaction mixture shows the generation of at least two radical species in solution: one inorganic and one organic. The organic radical in both reactions cases strongly resembles the respective monoanionic squaraine species. The other radical is likely to be iron based due to the appearance of a rhombic spectrum when the measurement is performed at 77 K. This species is possibly a result of CO coordination to the iron metal centre.

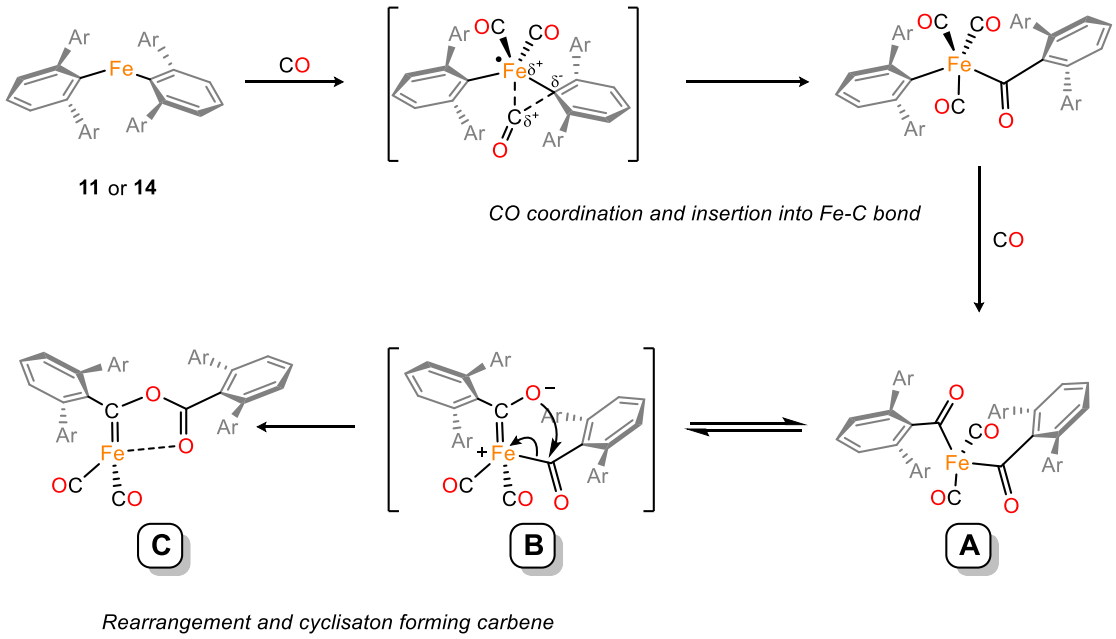
Iron carbonyls are also generated in the reaction evidenced by IR spectra features the presence of bands in the range of 2050-1978 cm^{-1} which are indicative of iron carbonyl CO stretches.[96] This is most likely due to CO insertion into the Fe–C bond as seen previously by Power[28] and Kays.[31]

There is also precedent for a ketene intermediate, which have long been proposed as intermediates in the Fischer-Tropsch process.[97–99] The increasing band at *ca.* 2100 cm^{-1} in the IR spectra during the course of the reaction (Figure 6.11) is similar to a free or coordinated ketene.[27,84] Evidence has also been seen in the $^{13}C\{^{1}H\}$ NMR data from the reaction of **11** with ^{13}CO. The isolated sample of **^{13}C-29^{Mes}** showed two very small

doublets at 171.3 and 24.5 ppm ($R_2{}^{13}C={}^{13}C=O$) which could correspond to a minor amount of a ketene.[84,90,91]

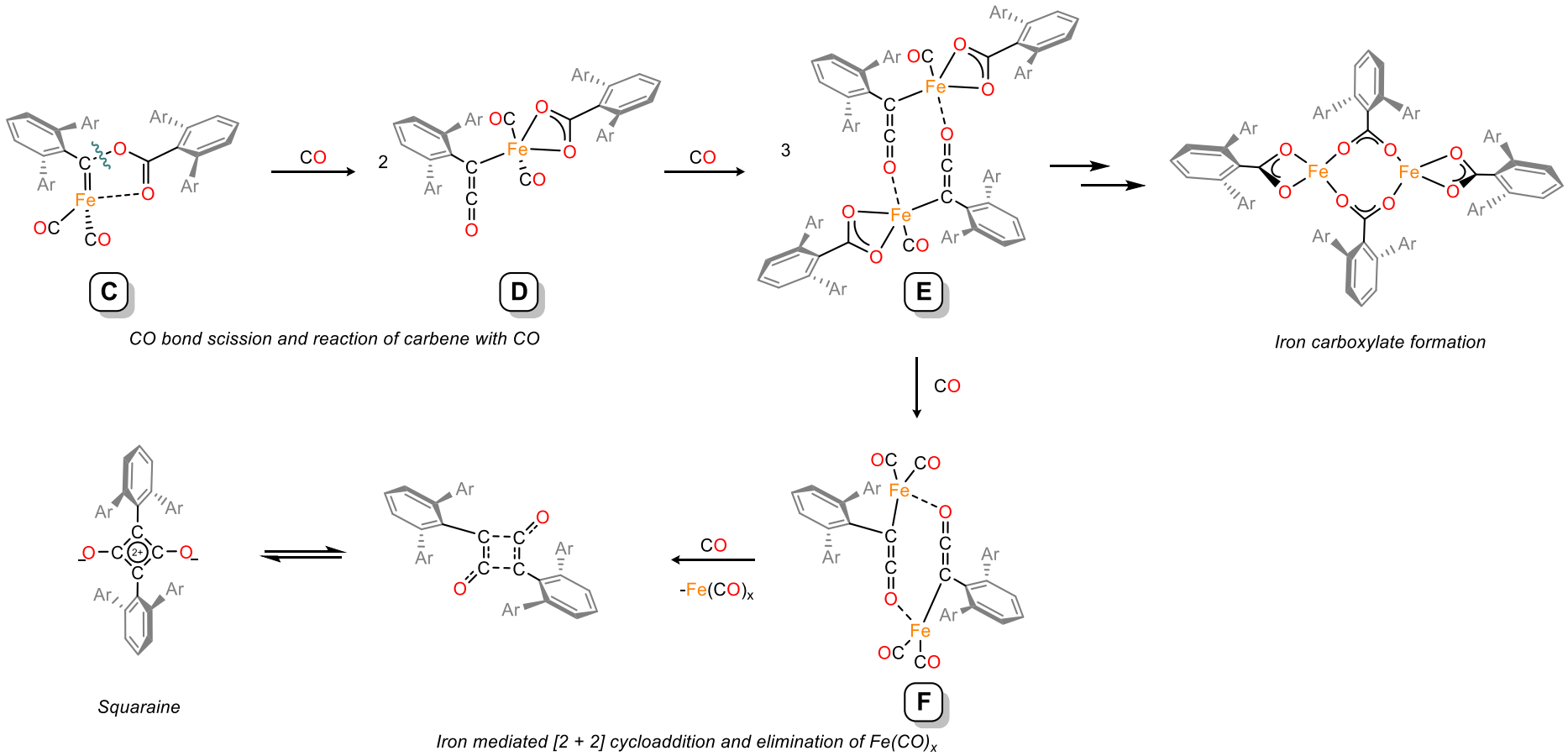
Previous reactivity within the Kays group has shown the formation of a metallacyclic Fe(II) carbene, $(CO)_3Fe[C(2,6\text{-}Naph_2C_6H_3)OC(O)(2,6\text{-}Naph_2C_6H_3)]\cdot OEt_2$, through reaction of an iron *m*-terphenyl diaryl featuring 1-napthyl flanking groups with CO.[31] Furthermore, carbenes have been shown to react with CO to form ketenes, either on their own[100–102] or between a metal-carbene centre (rhodium,[103] iridum,[84,104] samarium[25] or lanthanum[27]). Ketenes have also been shown dimerise in a [2+2] cycloaddition reactions to form 1,3-cyclobutanedione and the β-lactone dimer, where the former is possibly how the squaraine forms.[84]

With this information, it is plausible to assume that CO first coordinates to the iron(II) centre forming an iron radical, which then undergoes 1,1-migratory insertion of two CO molecules into the Fe−C σ-bonds of the *m*-terphenyl ligand to form an acyl intermediate species (Scheme 6.7, **A**) which resembles the closely related Fe(II) bis(η^2-acyl) complex $(\eta^2\text{-}2,6\text{-}Dipp_2C_6H_3CO)_2Fe(CO)_2$.[28] The cyclisation process could then proceed first by rearrangement of the iron acyl species **A**, to the carbene intermediate **B** where a C=Fe double bond and an anionic CO^- is formed. Attack of the carbonyl carbon by the nucleophilic oxygen with coordination of the carbonyl carbon forms the iron carbene **C**, similar to the proposed formation of the iron carbene species $(CO)_3Fe[C(NEt_2)OC(O)NEt_2]$.[105,106] The carbene intermediate **C** reacts with another molecule of CO, to produce a ketene, and undergoes CO bond scission between the carbene carbon and carboxylate oxygen (Scheme 6.8, **C**) to form intermediate **D** which features an iron centre bound to a ketene moiety ($2,6\text{-}Ar_2C_6H_3C=C=O$) and a carboxylate ligand ($[2,6\text{-}Ar_2C_6H_3CO_2]^-$) (Scheme 6.8). Intermediate **D** could then dimerise to form an iron ketene carboxylate complex **E**, reminiscent to those observed from reaction of CO



Scheme 6.7 Proposed mechanism for the formation of the iron carbene intermediate C.

with low valent organolanthanide complexes.[25,27] Intermediate **E** could then form a ketene iron complex **F** which aids the [2 + 2] cycloaddition reaction forming the squaraine. The carboxylate moieties on **E** could go on to dimerise to form the diiron carboxylate complex. Exactly how **E** converts to the carboxylate complex **F** is still very much unknown, and further study and isolation of possible intermediates would allow for a deeper understanding and insight into the mechanism.



Scheme 6.8 Proposed mechanism for the formation of the iron carboxylate complex and squaraine from reaction of iron carbene (C) with CO.

6.4 Conclusions

Two-coordinate iron complexes have been shown to react with carbon monoxide under ambient conditions to form novel squaraines and diironcarboxylate complexes, from a result of CO bond scission, *via* analysis by single crystal X-ray diffraction.

The diiron carboxylate complex crystallised in the windmill conformation where the iron is bound to a terminal and two bridging carboxylate ligands. This is the first diiron carboxylate complex bearing *m*-terphenyl carboxylate ligands with the absence of coordinating N or O ligands.

The crystal structures of the squaraines **29^{Mes}** and **29$^{2,6\text{-}Xyl}$** show a large plane to plane twist angle between the central aryl ring of the *m*-terphenyl moiety as a result of the steric demands of the flanking aryls, by far the highest observed for any other squaraines in the literature. The IR spectra of the squaraines show a higher C–O stretch than those observed in the literature, highlighting the greater double bond character possessed by the C–O bond in **29^{Mes}** and **29$^{2,6\text{-}Xyl}$** compared to other squaraines. This is also reflected in the shorter C–O bond distance in the solid state structures of **29^{Mes}** and **29$^{2,6\text{-}Xyl}$**. The $^{13}C\{^{1}H\}$ NMR for **29^{Mes}** features a very high chemical shift for the *C*–O carbon at 269.7 ppm which is like those observed for a carbene centres. The monoanionic forms of **29^{Mes}** and **29$^{2,6\text{-}Xyl}$** are EPR active where the radical couples to protons on the central aryl of the *m*-terphenyl and the two inequivalent carbon atoms on the central C_4O_2 ring.

To gain insight into the reaction mechanism, *in situ* reaction monitoring was performed using IR and EPR spectroscopies. The IR spectrum showed bands which suggest the presence of ketene and iron carbonyl intermediates, with formation of bands which correspond to the squaraine molecule and the diiron carboxylate complex. EPR spectroscopy revealed the presence of radical species in the reaction medium with the

initial formation of a peak at g_{iso} = 2.0981 and 2.038 (**11** and **14** respectively) which appears as a rhombic signal when the measurement was performed at 77 K. This was accompanied by a new peak at g_{iso} = 2.0033 or 2.0049 which showed hyperfine coupling similar to that observed from the monoanioinic squaraines [**29**$^{\mathbf{Mes}}$]$^-$ and [**29**$^{\mathbf{2,6\text{-}Xyl}}$]$^-$ respectively.

Carbon-13 labelling studies on the reaction of **11** with ^{13}CO were performed to fully elucidate the origin of the carbons from the central C_4O_2. The IR spectra of the reaction mixture showed CO bands which where all shifted to lower wavenumber, which is expected due to the weakening of the C–O bond though isotopic substitution. The isolated **^{13}C-29^{Mes}** was spectroscopically characterised though NMR, EPR spectroscopy and MS. The $^{13}C\{^1H\}$ NMR featured triplets at 269.7 and 177.3 ppm from coupling between the inequivalent carbons on the $^{13}C_4O_2$ ring, which was confirmed *via* NMR correlation experiments. The monoanionic **^{13}C-29^{Mes}** EPR spectrum was accurately simulated using the same hyperfine coupling parameters as for the simulation of **29^{Mes}**, with the difference of 99% abundance of ^{13}C. These spectroscopic observations strongly support the origin of the carbons in the C_4O_2 ring are indeed from carbon monoxide.

From spectroscopic observations of the reaction mixture, a mechanism for the reaction is proposed in Scheme 6.7 and Scheme 6.8 where coordination of carbon monoxide to the iron centre results in CO insertion into the iron–carbon bond forms an iron(II) bis(acyl) complex which undergoes rearrangement into a carbene. The reaction between the carbene and CO forms a ketene which then encounters CO bond scission yielding a ketene carboxylate complex which subsequently dimerises (**E**). Intermediate **E** could then form a ketene iron complex **F** which aids the [2 + 2] cycloaddition reaction forming the squaraine and the carboxylate moieties on **E** could go on to dimerise to form the iron carboxylate complex: exactly how **E** converts to the carboxylate complex is still very

much unknown, and further study and isolation of possible intermediates would allow for a deeper understanding and insight into the mechanism.

The radical pathway is not fully understood however it could be possible that an iron carbonyls reduces the squaraine forming the monoionic species which are EPR active. There could also be other radical intermediates which are not detected *via* the X-band EPR spectrometer.

6.5 Future Work

The most urgent future work is the isolation and full characterisation of **29$^{2,6\text{-Xyl}}$** and the carboxylate complexes (**30**). This would allow for comparison for IR bands as seen in the reaction monitoring studies to enable greater confidence in the assignments and hence the mechanism of formation of these reaction products. The properties of the squaraines **29^{Mes}** and **29$^{2,6\text{-Xyl}}$** could be explored and investigated further with respect to their optical properties and possible applications in solar cells.[63]

Previous reactivity of iron(II) *m*-terphenyl complexes bearing more sterically demanding flanking groups (Dipp and Naph) have shown to give different reaction products with CO. Hence, it would be interesting to investigate the extent of how the ligand environment effects the resulting reaction products, for example, if the steric demands of the ligand were lower, *e.g.* Tmp in **16**, or if the electronics of the ligand were altered with electron donating or withdrawing substituents on the ligand backbone.

It would also be beneficial to perform low temperature reaction studies to enable the isolation of reaction intermediates to gain further understanding of the mechanism. Stoichiometric reactions with the iron diaryl (**11** or **14**) with CO in a 1:1 ratio could also allow for the isolation of intermediates and provide further insight into the mechanism.[20]

From the IR spectra from the reaction mixture, it can be seen after 6 days that the bands corresponding to the squaraines (1673/1675 cm^{-1}) are rather weak as compared to the other higher energy bands: this could be a consequence of the metal carbonyl which absorb more strongly or could be indicative that the squaraines and carboxylates are only presence as a minor component. Therefore, it would be beneficial to try alternate reaction conditions such as other solvents, increasing or decreasing the temperature and whether an increase of CO pressure would effect of the formation of the end products.

It would be interesting to perform the reaction in the presence of a reducing agent, such as potassium, and in the presence of a silane, where these substrates have been shown to aid CO bond scission.[24,26] This would most likely allow for alternate reaction pathways to proceed.

6.6 References

1 P. L. Arnold, Z. R. Turner, R. M. Bellabarba and R. P. Tooze, *Chem. Sci.*, 2011, **2**, 77–79.

2 H. Schulz, *Appl. Catal. A Gen.*, 1999, **186**, 3–12.

3 R. A. Kerr, *Science*, 2005, **310**, 1106–1108.

4 G. Christian, R. Stranger, S. Petrie, B. F. Yates and C. C. Cummins, *Chem. Eur. J.*, 2007, **13**, 4264–4272.

5 Y. Hu, C. C. Lee and M. W. Ribbe, *Science*, 2011, **333**, 753–755.

6 N. M. West, A. J. M. Miller, J. A. Labinger and J. E. Bercaw, *Coord. Chem. Rev.*, 2011, **255**, 881–898.

7 M. D. Anker, M. S. Hill, J. P. Lowe and M. F. Mahon, *Angew. Chem. Int. Ed.*, 2015, **54**, 10009–10011.

8 X. Wang, Z. Zhu, Y. Peng, H. Lei, J. C. Fettinger and P. P. Power, *J. Am. Chem. Soc.*, 2009, **131**, 6912–6913.

9 H. Braunschweig, T. Dellermann, R. D. Dewhurst, W. C. Ewing, K. Hammond, J. O. C. Jimenez-Halla, T. Kramer, I. Krummenacher, J. Mies, A. K. Phukan and A. Vargas, *Nat. Chem.*, 2013, **5**, 1025–1028.

10 M. Majumdar, I. Omlor, C. B. Yildiz, A. Azizoglu, V. Huch and D. Scheschkewitz, *Angew. Chem. Int. Ed.*, 2015, **54**, 8746–8750.

11 A. J. M. Miller, J. A. Labinger and J. E. Bercaw, *J. Am. Chem. Soc.*, 2008, **130**, 11874–11875.

12 X. X. Zhang, G. F. Parks and B. B. Wayland, *J. Am. Chem. Soc.*, 1997, **119**, 7938–7944.

13 V. L. Coffin, W. Brennen and B. B. Wayland, *J. Am. Chem. Soc.*, 1988, **110**, 6063–6069.

14 D. L. M. Suess and J. C. Peters, *J. Am. Chem. Soc.*, 2013, **135**, 12580–12583.

15 G. T. Sazama and T. A. Betley, *Organometallics*, 2011, **30**, 4315–4319.

16 P. A. Belmonte, F. G. N. Cloke and R. R. Schrock, *J. Am. Chem. Soc.*, 1983, **105**, 2643–2650.

17 T. Watanabe, Y. Ishida, T. Matsuo and H. Kawaguchi, *J. Am. Chem. Soc.*, 2009, **131**, 3474–3475.

18 O. T. Summerscales, F. G. N. Cloke, P. B. Hitchcock, J. C. Green and N. Hazari, *Science*, 2006, **311**, 829–831.

19 B. M. Gardner, J. C. Stewart, A. L. Davis, J. McMaster, W. Lewis, A. J. Blake and S. T. Liddle, *Proc. Natl. Acad. Sci.*, 2012, **109**, 9265–9270.

20 A. S. Frey, F. G. N. Cloke, P. B. Hitchcock, I. J. Day, J. C. Green and G. Aitken, *J. Am. Chem. Soc.*, 2008, **130**, 13816–13817.

21 O. T. Summerscales, F. G. N. Cloke, P. B. Hitchcock, J. C. Green and N. Hazari, *J. Am. Chem. Soc.*, 2006, **128**, 9602–9603.

22 T. Shima and Z. Hou, *J. Am. Chem. Soc.*, 2006, **128**, 8124–8125.

23 S. P. Mansell, N. Kaltsoyannis and P. L. Arnold, *J. Am. Chem. Soc.*, 2011, **133**, 9036–9051.

24 J. A. Buss and T. Agapie, *Nature*, 2016, **529**, 72–75.

25 W. J. Evans, J. W. Grate, L. A. Hughes, H. Zhang and J. L. Atwood, *J. Am. Chem. Soc.*, 1985, **107**, 3728–3730.

26 R. E. LaPointe, P. T. Wolczanski and J. F. Mitchell, *J. Am. Chem. Soc.*, 1986, **108**, 6382–6384.

27 W. J. Evans, D. S. Lee, J. W. Ziller and N. Kaltsoyannis, *J. Am. Chem. Soc.*, 2006, **128**, 14176–141874.

28 C. Ni and P. P. Power, *Chem. Commun.*, 2009, 5543–5545.

29 H. Lei, B. D. Ellis, C. Ni, F. Grandjean, G. J. Long, P. P. Power and Missouri, *Inorg. Chem.*, 2008, **47**, 10205–10207.

30 B. M. Gridley, A. J. Blake, A. L. Davis, W. Lewis, G. J. Moxey and D. L. Kays, *Chem. Commun.*, 2012, **48**, 8910–8912.

31 B. M. Gridley, PhD Thesis, The University of Nottingham, 2013.

32 S. Sreejith, P. Carol, P. Chithra and A. Ajayaghosh, *J. Mater. Chem.*, 2008, **18**, 264–274.

33 J. J. Gassensmith, J. M. Baumes and B. D. Smith, *Chem. Commun.*, 2009, 6329–6338.

34 G. J. Ashwell, G. Jefferies, D. G. Hamilton, D. E. Lynch, M. P. S. Roberts, G. S. Bahra and C. R. Brown, *Nature*, 1995, **375**, 385–388.

35 C. W. Dirk, W. C. Herndon, F. C. Henry, S. Martinez, P. Kalamegham, A. Tan, G. Campos, M. Velez, J. Zyss, I. Ledoux and L. Chengg, *J. Am. Chem. Soc.*, 1995, **117**, 2214–2225.

36 B. T. Makowski, B. Valle, K. D. Singer and C. Weder, *J. Mater. Chem.*, 2012, **22**, 2848–2850.

37 Z. Yan, S. Guang, X. Su and H. Xu, *J. Phys. Chem. C*, 2012, **116**, 8894–8900.

38 S. Wang, L. Hall, V. V Diev, R. Haiges, G. Wei, X. Xiao, P. I. Djurovich, S. R. Forrest and M. E. Thompson, *Chem. Mater.*, 2011, **23**, 4789–4798.

39 R. Bisht, M. F. M. K., A. K. Singh and J. Nithyanandhan, *J. Org. Chem.*, 2017, **82**, 1920–1930.

40 P. F. Santos, L. V Reis, P. Almeida, A. S. Oliveira and L. F. V Ferreira, *J. Photochem. Photobiol. A*, 2003, **160**, 159–161.

41 E. Arunkumar, P. K. Sudeep, P. V Kamat, B. C. Noll and B. D. Smith, *New J. Chem.*, 2007, **31**, 677–683.

42 C. Chen, H. Dong, Y. Chen, L. Guo, Z. Wang, J.-J. Sun and N. Fu, *Org. Biomol. Chem.*, 2011, **9**, 8195–8201.

43 U. Oguz and E. U. Akkaya, *Tetrahedron Lett.*, 1998, **39**, 5857–5860.

44 W. Sun, S. Guo, C. Hu, J. Fan and X. Peng, *Chem. Rev.*, 2016, **116**, 7768–7817.

45 J. J. Gassensmith, S. Matthys, J. J. Lee, A. Wojcik, P. V. Kamat and B. D. Smith, *Chem. Eur. J.*, 2010, **16**, 2916–2921.

46 X. Xiao, X. F. Cheng, X. Hou, J. H. He, Q. F. Xu, H. Li, N. J. Li, D. Y. Chen and J. M. Lu, *Small*, 2017, **13**, 1602190.

47 L. Hu, Z. Yan and H. Xu, *RSC Adv.*, 2013, **3**, 7667–7676.

48 K. Y. Law, *Chem. Rev.*, 1993, **93**, 449–486.

49 H. E.- Sprenger and W. Ziegenbein, *Angew. Chem. Int. Ed.*, 1967, **6**, 553–554.

50 K. K. Law and F. C. Bailey, *J. Org. Chem.*, 1992, **57**, 3278–3286.

51 K. M. Shafeekh, S. Das, C. Sissa and A. Painelli, *J. Phys. Chem. B*, 2013, **117**, 8536–8546.

52 W. Ziegenbein and H. E.- Sprenger, *Angew. Chem. Int. Ed.*, 1966, **5**, 893–894.

53 P. M. Kazmaier, G. K. Hamer and R. A. Burt, *Can. J. Chem.*, 1990, **69**, 530–536.

54 D. G. Hamilton, D. E. Lynch and G. Smith, *Aust. J. Chem.*, 1996, **49**, 1339–1343.

55 J. G. Chen, D. Y. Huang and Y. Li, *Dye. Pigment.*, 2000, **46**, 93–99.

56 P. H. Wöbkenberg, J. G. Labram, J.-M. Swiecicki, K. Parkhomenko, D. Sredojevic, J.-P. Gisselbrecht, D. M. de Leeuw, D. D. C. Bradley, J.-P. Djukic and T. D. Anthopoulos, *J. Mater. Chem.*, 2010, **20**, 3673–3680.

57 K. Ruhlandt-Senge, J. J. Ellison, R. J. Wehmschulte, F. Pauer and P. P. Power, *J. Am. Chem. Soc.*, 1993, **115**, 11353–11357.

58 T. Maeda, S. Mineta, H. Fujiwara, H. Nakao, S. Yagi and H. Nakazumi, *J. Mater. Chem. A*, 2013, **1**, 1303–1309.

59 C. G. Collins, J. M. Lee, A. G. Oliver, O. Wiest and B. D. Smith, *J. Org. Chem.*, 2014, **79**, 1120–1130.

60 D. Bourissou, O. Guerret, F. P. Gabbaï and G. Bertrand, *Chem. Rev.*, 2000, **100**, 39–91.

61 K. Saito, *J. Phys. Chem. B*, 2001, **105**, 4235–4238.

62 C. Li, W. Wang, X. Wang, B. Zhang and Y. Cao, *Chem. Lett.*, 2005, **34**, 554–555.

63 G. Chen, H. Sasabe, Y. Sasaki, H. Katagiri, X.- Wang, T. Sano, Z. Hong, Y. Yang and J. Kido, *Chem. Mater.*, 2014, **26**, 1356–1364.

64 J. Wojtyk and A. McKerrow, *Can. J. Chem.*, 1999, **77**, 903–912.

65 G. te Velde, F. M. Bickelhaupt, E. J. Baerends, C. Fonseca Guerra, S. J. A. van Gisbergen, J. G. Snijders and T. Ziegler, *J. Comp. Chem.*, 2001, **22**, 931–967.

66 C. Fonseca Guerra, J. G. Snijders, G. te Velde and E. J. Baerends, *Theor. Chem. Acc.*, 1998, **99**, 391–403.

67 J. R. Cox, P. Muller and T. M. Swager, *J. Am. Chem. Soc.*, 2011, **133**, 12910–12913.

68 L. H. Do and S. J. Lippard, *J. Inorg. Biochem.*, 2011, **105**, 1774–1785.

69 S. Friedle, E. Reisner and S. J. Lippard, *Chem. Soc. Rev.*, 2010, **39**, 2768–2779.

70 E. C. Carson and S. J. Lippard, *J. Inorg. Biochem.*, 2006, **100**, 1109–1117.

71 J. R. Hagadorn, L. Que and W. B. Tolman, *J. Am. Chem. Soc.*, 1998, **120**, 13531–13532.

72 D. Lee and S. J. Lippard, *Inorg. Chem.*, 2002, **41**, 827–837.

73 E. Reisner, T. C. Abikoff and S. J. Lippard, *Inorg. Chem.*, 2007, **46**, 10229–10240.

74 D. Lee and S. J. Lippard, *Inorg. Chem.*, 2002, **41**, 2704–2719.

75 D. Lee and S. J. Lippard, *J. Am. Chem. Soc.*, 1998, **120**, 12153–12154.

76 E. C. Carson and S. J. Lippard, *Inorg. Chem.*, 2006, **45**, 837–848.

77 E. C. Carson and S. J. Lippard, *Inorg. Chem.*, 2006, **45**, 828–836.

78 S. Friedle and S. J. Lippard, *Eur. J. Inorg. Chem.*, 2009, 5506–5515.

79 M. Zhao, D. Song and S. J. Lippard, *Inorg. Chem.*, 2006, **45**, 6323–6330.

80 L. Yang, D. R. Powell and R. P. Houser, *Dalton Trans.*, 2007, 955–964.

81 S. Yoon and S. J. Lippard, *Inorg. Chem.*, 2006, **45**, 5438–5446.

82 J. Kuzelka, J. R. Farrell and S. J. Lippard, *Inorg. Chem.*, 2003, **42**, 8652–8662.

83 E. C. Carson and S. J. Lippard, *J. Am. Chem. Soc.*, 2004, **126**, 3412–3413.

84 T. T. Tidwell, *Ketenes II*, Wiley, New York, 2nd edn., 2006.

85 K. R. Birdwhistell, T. L. Tonker and J. L. Templeton, *J. Am. Chem. Soc.*, 1985, **107**, 4474–4483.

86 S. A. Gonsales, I. Ghiviriga, K. A. Abboud and A. S. Veige, *Dalton Trans.*, 2016, **45**, 15783–15785.

87 V. Wray and P. E. Hanson, *Org. Magn. Reson.*, 1981, **15**, 102–103.

88 R. P. Kirchen and T. S. Sorensen, *J. Am. Chem. Soc.*, 1977, **99**, 6697–6693.

89 F. J. Weigert and J. D. Roberts, *J. Am. Chem. Soc.*, 1987, **109**, 6021–6025.

90 J. Firl and W. Runge, *Angew. Chem. Int. Ed.*, 1973, **12**, 668–669.

91 T. T. Tidwell, *Acc. Chem. Res.*, 1990, **23**, 273–279.

92 P. J. Stang and K. A. Roberts, *J. Am. Chem. Soc.*, 1986, **108**, 7125–7127.

93 Y. Lee and J. C. Peters, *J. Am. Chem. Soc.*, 2011, **133**, 4438–4446.

94 B. B. Wayland, A. E. Sherry and V. L. Coffin, *J. Chem. Soc., Chem. Commun.*, 1989, 662–663.

95 J. L. Kisko, T. Hascall and G. Parkin, *J. Am. Chem. Soc.*, 1998, **120**, 10561–10562.

96 P. Portius, J. Yang, X.-Z. Sun, D. C. Grills, P. Matousek, A. W. Parker, M. Towrie and M. W. George, *J. Am. Chem. Soc.*, 2004, **126**, 10713–10720.

97 H. Kandler, W. Bidell, M. Jänicke, M. Knickmeier, D. Veghini and H. Berke, *Organometallics*, 1998, **17**, 960–971.

98 D. B. Grotjahn, G. A. Bikzhanova and J. L. Hubbard, *Organometallics*, 1999, **18**, 5614–5619.

99 P. Hofmann, L. A. Perez-moya, O. Steigelmann and J. Ride, *Organometallics*, 1992, **11**, 1167–1176.

100 A. D. Allen and T. T. Tidwell, *Eur. J. Org. Chem.*, 2012, 1081–1096.

101 T. Schulz, C. Färber, M. Leibold, C. Bruhn, W. Baumann, D. Selent, T. Porsch, M. Holthausen and U. Siemeling, *Chem. Commun.*, 2013, **49**, 7–10.

102 U. Siemeling, C. Färber, C. Bruhn, M. Leibold, D. Selent, W. Baumann, M. von Hopffgarten, C. Goedecke and G. Frenking, *Chem. Sci.*, 2010, **1**, 697.

103 Z. Tang, S. Mandal, N. D. Paul, M. Lutz, P. Li, J. I. van der Vlugt and B. de Bruin, *Org. Chem. Front.*, 2015, **2**, 1561–1577.

104 D. B. Grotjahn and H. C. Lo, *J. Am. Chem. Soc.*, 1996, **118**, 2097–2098.

105 D. Luart, N. Gall and J. Salau, *Organometallics*, 1998, **17**, 2680–2682.

106 R. Siebenlist, H. Frühauf, K. Vrieze, W. J. J. Smeets and A. L. Spek, *J. Org. Chem.*, 2001, **617**, 483–494.

Chapter VII

Concluding Remarks

The purpose of this thesis sought to expand understanding of low-coordinate transition metal complexes bearing sterically demanding *m*-terphenyl ligands. The synthesis of low-coordinate transition metal complexes, their reactivity towards small molecules and their application as catalysts for organic transformations is reported. There are significant challenges with these systems due to the need for rigorous exclusion of air and moisture. As a result, low-coordinate complexes challenge preconceived ideas of structure and bonding and often exhibit unusual and unique reactivity.

The steric demands of the *m*-terphenyl ligand were easily modified through substitution of the flanking aryl with either a Mes, 2,6-Xyl and Tmp moiety. The *m*-terphenyl ligand bearing an asymmetric Tmp substituent enabled the synthesis of novel two-coordinate Group 12 (**7**-**9**) and three-coordinate open shell (**15**, **16**) complexes. The Group 2 complexes **7**-**9** were found to exhibit conformational isomerism in solution as evidenced by the broad overlapping signals in the ^{1}H and $^{13}C\{^{1}H\}$ NMR spectra with multiple peaks in the $^{113}Cd\{^{1}H\}$ and $^{199}Hg\{^{1}H\}$ NMR spectra for complexes **8** and **9** respectively. The analogous reaction between the aryl lithium salt (**4**) and the transition metal dihalide afforded the three-coordinate complexes **15** and **16** where a molecule of THF is coordinated to the transition metal centre. The solid state structures, as determined *via* X-ray crystallography, showed the flanking Tmp substituents of the *m*-terphenyl in the *syn*-conformation whereas the Group 12 complexes are in the *anti*-conformation.

The reaction of the two-coordinate diaryls **10** and **11** with an excess of acetonitrile yielded the four-coordinate complexes **17** and **18** respectively where the metal centre is bonded to two *m*-terpheyl ligands and two molecules of acetonitrile in a seesaw geometry.

The electronic structure of the open shell complexes **15**-**17** were analysed by Evans' method where the magnetic moments are indicative of a high spin M(II) centre. Further,

more rigorous measurements using SQUID and EPR spectroscopy would provide further understanding of the electronic structure.

The two- and three-coordinate Mn(II) and Fe(II) complexes **10**, **11**, **15**, and **16** were investigated towards the catalytic cyclotrimerisation of isocyanates, a well-known reaction, as the first foray into these systems acting as catalysts. Interestingly, these complexes were only able to catalyse reaction between primary isocyanates, a limit that does not seem to be apparent in literature. Investigations of the lack of catalytic reactivity towards secondary and tertiary aliphatic isocyanates and aromatic isocyanates suggested that the formation of a M-amidate species prevents formation of the catalytically active species, as suggested from the stoichiometric reaction of 3,5-dimethoxyphenyl isocyanate with **11**. The reaction rate decreased as the chain length of the primary alkyl isocyanate increased (ethyl, *n*-propyl, *n*-hexyl) and was found necessary to heat the reaction to 60 °C to achieve high conversions after 14 h. Initial assessments of other two-coordinate *m*-terphenyl complexes (**12** and **14**) were found to have low catalytic activity than the aforementioned complexes and were therefore not assessed further. Kinetic experiments were performed at variable concentrations of precatalyst (**10**) and isocyanate (EtNCO) using the initial rates method, where analysis of the rate order reveals first-order behaviour with respect to both the precatalyst and the isocyanate.

Further investigations of the catalytic activity of these low-coordinate systems were extended to the hydrophosphination of isocyanates where these reactions often suffer from poor functional group tolerance, side product formation, where the active species catalyses the cyclo-oligomerisation of reactive isocyanates, an obstacle overcome with these systems, and the requirement for stoichiometric amounts of additives.

The two- and three-coordinate iron complexes **11** and **16** were found to be efficient precatalysts for the hydrophosphination of isocyanates producing mono (PCA) and/or diinsertion (PDCA) products where the PDCAs are a new family of derivatised functionalised phosphines. This work represents the first example of an iron system to catalyse this reaction and also, the first example of the diinsertion process in the hydrophosphination of isocyanates, demonstrating the fine line between low-coordination number and unique steric pocket around metal centre which enables these systems to act differently to those previously reported.

The product selectivity appeared to be dominated by the sterics of the isocyanate substrate where the more sterically demanding secondary and tertiary alkyl isocyanates afforded the mono-insertion product (PCAs) exclusively whereas the less bulky aryl isocyanates (aryl and primary alkyl isocyanates) produced a mixture. Through small alterations to the reaction conditions, the product selectivity could be easily controlled. The addition of a weak acid selectively produced the PCDA whereas performing the reaction in THF rather than C_6D_6 produced the PCA only. However, a significant drop in the catalytic activity was also observed where these reaction required heating to 60 °C to achieve moderate conversions after 48 h.

Due to the inherent low-coordination number and relatively high oxidation state of the iron precatalysts **11** and **16**, the normal catalytic steps of oxidative addition and reductive elimination did not seem likely as the iron centre would have to undergo and 2 electron change from Fe(II) to Fe(IV). Hence, the mechanism proposed was a Lewis acid type mechanism with a two-stage cycle. Initial coordination of the isocyanate to the Lewis acidic iron centre is activated towards nucleophilic attack by the phosphine. 1,3-Proton shift followed by displacement with a new isocyanate moiety enables the formation of the PCA. If the sterics of the isocyanate is somewhat lower, the reaction can proceed to Cycle

2 where the PCA reacts with the catalytically active species, 1,3-proton shift followed by displacement of an isocyanate allows the formation of PDCA.

The initial coordination chemistry of the phosphines were investigated towards $[Ru(p\text{-cym})Cl_2]_2$ leading to the isolation of coordination products **23** and **24**. The solid state structures show coordination of the PCA and PCDA to the ruthenium centre *via* the phosphorus lone pair. **23** and **24** feature intramolecular hydrogen bond interactions between the NH and Cl moieties. This interaction, in combination of the π···π stacking of the *p*-tolyl and a phosphorus-aryl substituent in **24** results in significant twisting of the PDCA core (Figure 5.8) which highlighting the flexibility of the PDCA ligand.

Low-coordinate manganese(II) *m*-terphenyl complexes **10**, **13**, and **15** were also found to be active in the dehydrocoupling of dimethylamine borane, which have potential uses in chemical hydrogen storage, under mild conditions. The only previous example of a manganese-based catalyst was found to suffer from long reaction times and required UV irradiation to initiate the reaction. It was found that small changes in the ligand architecture drastically alter the reaction mechanism: for precatalysts **10** and **13** it is likely that the reaction proceeds *via* a homogeneous Lewis acid type mechanism where $Me_2NH{\cdot}BH_3$ is first converted to the linear diborazane **26**, which then transforms into the cyclic dimer **25** with evolution of H_2 gas. When precatalyst **15** is used, however, the reaction is catalysed *via* a heterogeneous mechanism where Mn particles are present in the solution, which was corroborated *via* analysis by DLS and TEM measurements. It is possible that the lower steric demands of the Tmp substituent *vs.* that of 2,6-Xyl and Mes could render the metal centre in **15** more susceptible to reduction.

The final experimental Chapter in this thesis sought to investigate the reactivity of iron(II) *m*-terphenyl complexes towards CO. Complexes **11** and **14** lead to the unprecedented

formation of squaraine molecules and diironcarboxylate complexes, from a result of CO bond scission. The diiron carboxylate complex **30**$^{2,6\text{-Xyl}}$ is the first diiron carboxylate complex bearing *m*-terphenyl carboxylate ligands with the absence of coordinating N or O ligands. The crystal structures of the squaraines **29**^{Mes} and **29**$^{2,6\text{-Xyl}}$ show a large plane to plane twist angle between the central aryl ring of the *m*-terphenyl moiety as a result of the steric demands of the flanking aryls, by far the highest observed for any other squaraines in the literature. The monoanionic forms of **29**^{Mes} and **29**$^{2,6\text{-Xyl}}$ are EPR active where the radical couples to protons on the central aryl of the *m*-terphenyl **29**^{Mes} and **29**$^{2,6\text{-Xyl}}$ and the two inequivalent carbon atoms on the central C_4O_2 ring (**29**^{Mes} only).

To gain insight into the reaction mechanism, *in situ* reaction monitoring was performed using IR and EPR spectroscopies. The IR showed bands which suggest the presence of ketene and iron carbonyl intermediates, with formation of bands which correspond to the squaraine molecule and the diiron carboxylate complex. EPR spectroscopy revealed the presence of radical species in the reaction medium with the initial formation of a peak which appears as a rhombic signal when the measurement was performed at 77 K, indicative of an inorganic based radical. This was accompanied by a new peak at g_{iso} = 2.0033 or 2.0049 which showed hyperfine coupling similar to that observed from the monoanionic squaraines [**29**^{Mes}]$^-$ and [**29**$^{2,6\text{-Xyl}}$]$^-$ respectively. Reaction of ^{13}CO and **11** was performed in order to elucidate the reaction mechanism and to understand the origin of the carbons in the central C_4O_2 ring in the squaraine. The IR spectra from the reaction mixture showed all carbonyl bands shifted to a lower wavenumber due to isotopic substitution. **^{13}C-29**^{Mes} was successfully isolated and characterised using NMR, EPR spectroscopy and MS which confirmed that the formation of the central C_4O_2 originated from carbon monoxide.

The mechanism for the formation of squaraines and diiron carboxylate complexes proposed involves the formation of an iron carbene complex which reacts with CO to form a ketene carboxylate complex which subsequently dimerises. This goes on to form a ketene iron complex, where a [2 + 2] cycloaddition reaction forms the squaraine, and the carboxylate moieties could then dimerise and form the diiron carboxylate complex. This mechanism will require further investigation in order to fully determine the reaction pathway, however, ketene intermediates long thought these are intermediates in Fischer-Tropsch process, hence, this reaction further supports this theory.

Chapter VIII

General Experimental

8.1 General Experimental Techniques

8.1.1 Manipulation of Air-sensitive Compounds

Due to the highly air- and moisture-sensitive nature of the compounds synthesised, all manipulation of solids and liquids were carried out under strict anhydrous and anaerobic conditions through the use of standard Schlenk line and glove box techniques unless stated otherwise.

8.2 Physical Measurements

8.2.1 NMR Spectroscopy

Air-sensitive samples were prepared under an inert atmosphere using standard glovebox techniques and sealed in Young's tap modified borosilicate glass NMR tube. NMR spectroscopy were performed on either a Bruker DPX300, DPX400, AV400, AV(III)400, AV(III)400HD, AV(III)500, AV(III)600 or AV(III)800 spectrometers. Chemical shifts are quoted in ppm relative to neat TMS (^{1}H, ^{13}C{^{1}H}), LiCl/D_2O solution (^{7}Li{^{1}H}), $CdMe_2$ (^{113}Cd{^{1}H}), $HgMe_2$ (^{199}Hg{^{1}H}), $BF_3{\cdot}OEt_2$ (^{11}B{^{1}H}), H_3PO_4 (^{31}P{^{1}H}) and $MeNO_2$ (^{15}N) (in the case of ^{113}Cd{^{1}H}, ^{199}Hg{^{1}H} and ^{11}B{^{1}H}NMR, 0.1 M $Cd(ClO_4)_2/D_2O$, 1.0 M $Hg(ClO_4)_2/D_2O$ and 0.04M $NaBPh_4$/MeCN-d_3 were used as internal standards respectively). Residual solvent signals were used as internal references for ^{1}H and ^{13}C{^{1}H} NMR measurements, and ^{1}H, ^{13}C and ^{15}N assignments were confirmed with the use of ^{1}H, ^{1}H, ^{1}H, ^{13}C, ^{1}H, ^{15}N and ^{1}H, ^{31}P correlation experiments where necessary.

8.2.2 IR Absorption Spectroscopy

Air-sensitive samples for IR absorption spectroscopy were prepared under an inert atmosphere as a solution in dry degassed solvents in a cell with KBr windows. Spectra were recorded on a Bruker Alpha FTIR instrument. None air sensitive samples were recorded on a Bruker Alpha FTIR instrument with a 'Platinum' ATR attachment.

8.2.3 Mass Spectrometry

Air-sensitive compounds for mass spectrometry were prepared in an inert atmosphere and sealed in glass capillary tubes. EI-MS measurements were carried out either by Dr Mick Cooper at the University of Nottingham, using a Bruker Apex IV FTICR-MS (Bruker Daltonics, Billerica, MA, USA) with heptacosafluorotributylamine (FC43) as mass calibrant, or else at the EPSRC National Mass Spectrometry Facility (Swansea University, UK) using a perfluorotributyl high resolution MS reference, on a Finnigan MAT 95 XP (Thermo Fisher Scientific, Bremen, Germany) double focussing mass spectrometer. GC-EIMS measurements were carried out at the University of Nottingham by Dr Mick Cooper using a JEOL AccuTOF GCX mass spectrometer equipped with an Agilent 7890B gas chromatograph. Again, mass calibration was performed using perfluorotributylamine calibrant. ESI-MS measurements were performed on highly dilute (*ca.* 10ng μL^{-1}) sample solutions in methanol, using an automated LC-MS system based on a Bruker micrOTOF mass spectrometer (Bruker Daltonik, Bremen, Germany), at the University of Nottingham, with sodium formate as mass calibrant.

8.2.4 Elemental Microanalysis

Air-sensitive elemental analysis samples were prepared in a glove box and sealed in glass ampoules under and argon atmosphere using Schlenk techniques. Elemental microanalyses were carried out using a Carlo Erba CE1108 Elemental Analyser by Mr Stephen Boyer at the Microanalysis Service, London Metropolitan University.

8.2.5 UV/visible Absorption Spectroscopy

UV/visible absorption samples were prepared as solutions of known concentrations under an inert atmosphere. Spectra were obtained in a Young's tap modified 10 mm quartz cell using a Perkin Elmer Lambda 5 or Lamda 750 spectrophotometer over a wavelength range of 200-900 nm with 1 nm data spacing.

8.2.6 Evans Method

Magnetic moments were calculated using Evans method at 298 K in benzene-d_6 using Equation 8.1. Diamagnetic corrections were calculated according to Pascal's constants.[1–3]

$$X = \frac{3\Delta f}{2\pi f m} + X_0 + \frac{X_0(d_0 - d_s)}{m}$$

Equation 8.1 X = mass susceptibility, Δf = frequency separation between signals (Hz), m = mass of substance (in 1 ml solution), X_0 = mass susceptibility of solvent, d_0 = density of solvent and ds = density of solution.

8.2.7 X-ray Crystallography

Under a flow of nitrogen, crystals suitable for analysis by X-ray diffraction were quickly removed from the crystallisation vessel and covered in YR-1800 perfluoropolyether oil. Crystals were mounted on a MiTeGen MicroMount™ and cooled rapidly in a cold stream of nitrogen using an Oxford Cryostreams open flow cryostat.[4] Single crystal X-ray diffraction data were collected on an Agilent SuperNova diffractometer (mirror-monochromated Cu-Kα radiation source; λ = 1.54184 Å; ω scans), equipped with either an Atlas, AtlasS2 or TitanS2 detector. Cell parameters were refined from the observed positions of all strong reflections in each data set and absorption corrections were applied using an Gaussian numerical method with beam profile correction (CrysAlisPro).[5] The structures were solved either by direct or iterative methods and all non-hydrogen atoms refined by full-matrix least-squares on all unique F^2 values with anisotropic displacement parameters with the exception of some partially occupied disordered atoms, detailed in the enclosed .cif files, which could not be refined anisotropically and were therefore refined isotopically. Hydrogen atoms were refined with constrained geometries and riding thermal parameters with the exception of amide hydrogen atoms whose positions were refined freely. Where necessary, Platon SQUEEZE[6] was used to account for the scattering from highly disordered solvent molecules that could not be sensibly modelled. Programs used include CrysAlisPro[5] (control and integration of Supernova), SHELXL[7] (structure refinement), SHELXT[8] (structure solution), SHELXS[9] (structure solution), Superflip[10] (structure solution), Platon[6] (SQUEEZE) and OLEX2[11] (molecular graphics). CIF files were checked using checkCIF[12] and by Dr William Lewis at the University of Nottingham Crystal Structure Service.

8.2.8 Electron Paramagnetic Resonance Spectroscopy

Continuous wave X band EPR spectra were carried in a Young's tap modified Wilmad quartz EPR tube and recorded using a Bruker EMX spectrometer by Dr E. Stephen Davies at the University of Nottingham. Frozen solution spectra were collected using a Wilmad quartz EPR dewar with liquid N_2. The simulations of CW EPR spectra were performed using the Bruker WINEPR SimFonia package.

8.2.9 Cyclic Voltammetry

Cyclic voltammetry (CV) measurements were carried out by Dr E. Stephen Davies at the University of Nottingham using an Autolab PGSTAT320N potentiostat and performed using a three-electrode system in a single compartment cell containing a glassy carbon working electrode, a Pt wire secondary electrode and a saturated calomel reference electrode, chemically isolated from the test solution *via* a bridge tube containing electrolyte solution and fitted with a porous vycor frit. The concentration of solutions were 1 mM for test compound and 0.4 M for the supporting electrolyte $[^{n}Bu_4N][BF_4]$ in dichloromethane under an argon atmosphere. Redox potentials are referenced to the ferrocenium-ferrocene (Fc^{+}/Fc) couple by an internal calibration.

8.2.10 Dynamic Light Scattering

Dynamic light scattering (DLS) measurements were carried out by Dr Graham Rance at the Nanoscale and Microscale Research Centre, The University of Nottingham. Samples were prepared as a suspension in dry degassed benzene in a sealed quartz cuvette under

an inert atmosphere and intensity particle size distributions acquired using a Malvern Zetasizer Nano-ZS at 25 °C.

8.2.11 Transmission Electron Microscopy

Transmission electron microscopy (TEM) measurements were performed by Dr Michael Fey and Mr. Rhys Lodge at the Nanoscale and Microscale Research Centre, The University of Nottingham using a JEOL 2100F transmission electron microscope (field emission electron gun source, information limit 0.19 nm). TEM samples were prepared by casting several drops of the reaction mixture onto copper-mesh holey-carbon films and dried under an inert atmosphere or in air.

8.2.12 Scanning Transmission Electron Microscopy

Scanning transmission electron microscopy (STEM) images were acquired using the JEOL digital STEM system by Dr Michael Fey and Mr. Rhys Lodge at the Nanoscale and Microscale Research Centre, The University of Nottingham. STEM samples were prepared by casting several drops of the reaction mixture onto copper-mesh holey-carbon films and dried under an inert atmosphere or in air.

8.2.13 Energy Dispersive X-ray Spectroscopy

Energy dispersive X-ray (EDX) spectra were recorded using an Oxford Instruments 30mm^2 Si(Li) detector or an Oxford Instruments x-Max 80 SDD running on an INCA microanalysis system by Dr Michael Fey and Mr. Rhys Lodge at the Nanoscale and Microscale Research Centre, The University of Nottingham. EDX samples were prepared

by casting several drops of the reaction mixture onto copper-mesh holey-carbon films and dried under an inert atmosphere or in air.

8.3 Preparation of Solvents and Reagents

Solvents were dried *via* heating at reflux over molten potassium (toluene and benzene), sodium/benzophenone (THF), calcium hydride (acetonitrile, dichloromethane and 1,2-dimethoxyethane) or sodium-potassium alloy (diethyl ether) for a minimum of three days before distillation and storage. *Iso*-Hexane and *n*-pentane were dried by passage over a drying column with 4 Å molecular sieves. All solvents were stored in ampoules either over a potassium mirror (toluene, benzene *iso*-hexane and *n*-pentane) or activated 4 Å molecular sieves (THF, acetonitrile, dichloromethane and 1,2-dimethoxyethane) and were thoroughly degassed *in vacuo* prior to use. Deuterated solvents were dried by heating in sealed ampoules at 80 °C over molten potassium (benzene-d_6 and toluene-d_8) or calcium hydride (THF-d_8, chloroform-*d*, dichloromethane-d_2 and acetonitrile-d_3) for a minimum of 5 days. After distillation, the solvents were degassed with three freeze–pump–thaw cycles prior to use.

The transition metal halide adducts $FeCl_2(THF)_{1.5}$ and $CoBr_2(DME)$ (where DME = 1,2-dimethoxyethane) were prepared by minor modifications to literature procedures.[13,14] All of the isocyanates were commercially available and were transferred directly into the glovebox after which 4 Å molecular sieves were added with the exception of 3,5-dimethoxyphenyl isocyanate which was dried *in vacuo* for 16 h. Diphenylphosphine (Sigma-Aldrich) was supplied in a Sure/Seal™ bottle and was transferred directly into the glove box. Ammonia borane ($NH_3{\cdot}BH_3$) and dimethylamine borane ($Me_2NH{\cdot}BH_3$) were transferred directly into the glove box and stored at –30 °C. Mercury was cleaned by

washing with conc. HCl (3 × 10 mL), water (3 × 10 mL) and acetone (3 × 10 mL) and dried overnight *in vacuo*. ^{13}CO (^{13}C, 99%) was supplied by CK Isotopes and used as received.

8.4 References

1 D. F. Evans, *J. Chem. Soc.*, 1959, 2003–2005.

2 G. A. Bain and J. F. Berry, *J. Chem. Educ.*, 2008, **85**, 532–536.

3 R. H. Peters, *Proc. Chem. Soc.*, 1958, 93–124.

4 J. Cosier and A. M. Glazer, *J. Appl. Cryst*, 1986, **19**, 105–107.

5 CrysAlisPRO Oxford Diffraction/Agilent Technologies UK Ltd Yarnton England.

6 A. L. Spek, *Acta Crystallogr. Sect. D Biol. Crystallogr.*, 2009, **65**, 148–155.

7 G. M. Sheldrick, *Acta Crystallogr. Sect. C Struct. Chem.*, 2015, **71**, 3–8.

8 G. M. Sheldrick, *Acta Crystallogr. Sect. A Found. Crystallogr.*, 2015, **71**, 3–8.

9 G. M. Sheldrick, *Acta Crystallogr. Sect. A Found. Crystallogr.*, 2008, **64**, 112–122.

10 L. Palatinus and G. Chapuis, *J. Appl. Crystallogr.*, 2007, **40**, 786–790.

11 O. V Dolomanov, L. J. Bourhis, R. J. Gildea, J. A. K. Howard and H. Puschmann, *J. Appl. Cryst*, 2009, **42**, 339–341.

12 http://checkcif.iucr.org/

13 H. Y. Liu, B. Scharbert and R. H. Holm, *J. Am. Chem. Soc.*, 1991, **113**, 9529–9539.

14 G. W. A. Fowles, D. A. Rice and R. A. Walton, *J. Inorg. Nucl. Chem.*, 1969, **31**, 3119–3131.

Appendices

Crystallographic Data

	7	***9***	***15***
Formula	$C_{48}H_{50}Zn$	$C_{48}H_{50}Hg$	$C_{52}H_{58}OMn$
M_w	692.25	827.47	753.92
T (K)	120(2)	120(2)	120(2)
Crystal System	Tetragonal	Orthorhombic	Orthorhombic
Space Group	$P4_32_12$	$Pca2_1$	*Ccce*
a (Å)	12.50531(16)	12.0175(3)	18.67834(16)
b (Å)	12.50531(16)	19.1672(3)	21.44845(18)
c (Å)	48.7716(13)	16.7438(3)	21.13621(17)
α (°)	90	90	90
β (°)	90	90	90
γ (°)	90	90	90
V (Å^3)	7627.0(3)	3856.79(13)	8467.62(12)
Z	8	4	8
D_{calc} (g cm^{-3})	1.206	1.425	1.183
μ (mm^{-1})	1.116	7.379	2.798
F_{000}	2944.0	1672.0	3224.0
Crystal Size (mm^3)	0.1109 × 0.0815 × 0.0543	0.4243 × 0.1772 × 0.0492	0.2361 × 0.1696 × 0.0756
λ (Å)	1.54184	1.54184	1.54184
2θ range for data collection (°)	7.25 to 148.77	8.684 to 148.902	7.542 to 148.53
Reflections. collected	35023	9894	16280
Independent reflections	7690	4924	4254
R_{int}	7690	0.0227	0.0184
GooF on F^2	1.014	1.063	1.053
R_1, wR_2 [$I > 2\sigma(I)$]	0.0352, 0.0835	0.0276, 0.0717	0.0301, 0.0814
R_1, wR_2 (all data)	0.0402, 0.0855	0.0302, 0.0740	0.0331, 0.0839
Largest diff. peak/hole (eÅ^{-3})	0.37/-0.33	1.20/-1.04	0.23/-0.30
Code	ZNHRSA	GADLKH	MNHRSC

	16	***17***	***18***
Formula	$C_{52}H_{58}FeO$	$C_{58}H_{65}MnN$	$C_{58}H_{65}FeN_5$
M_w	754.83	887.09	888.00
T (K)	120(2)	120(2)	120(2)
Crystal System	Orthorhombic	Monoclinic	Monoclinic
Space Group	*Pnna*	*C*2/*c*	*C*2/*c*
a (Å)	18.6528(2)	10.96523(12)	10.90871(15)
b (Å)	43.7692(5)	22.8713(3)	22.9285(5)
c (Å)	10.50646(11)	20.5974(2)	20.5205(5)
α (°)	90	90	90
β (°)	90	93.2876(11)	92.7247(15)
γ (°)	90	90	90
V (Å^3)	8577.65(17)	5157.11(11)	5126.79(18)
Z	8	4	4
D_{calc} (g cm^{-3})	1.169	1.143	1.15
μ (mm^{-1})	3.079	2.383	2.662
F_{000}	3232.0	1892.0	1896
Crystal Size (mm^3)	0.2723 × 0.1438 × 0.0917	0.1675 × 0.1312 × 0.0946	0.4272 × 0.283 × 0.1551
λ (Å)	1.54184	1.54184	1.54184
2θ range for data collection (°)	8.08 to 148.422	7.73 to 148.842	7.712 to 148.718
Reflections. collected	50578	16575	10829
Independent reflections	8631	5157	5089
R_{int}	0.0316	0.0203	0.0191
GooF on F^2	1.078	1.093	1.104
R_1, wR_2 [$I > 2\sigma(I)$]	0.0456, 0.1038	0.0381, 0.1027	0.0379, 0.1037
R_1, wR_2 (all data)	0.1038, 0.1067	0.0406, 0.1049	0.0392, 0.1049
Largest diff. peak/hole (eÅ^{-3})	0.44/-0.54	0.25/-0.26	0.31/-0.29
Code	FEHRSI	MNHRSB	FEHRSA

	20	***21a***	***21c***
Formula	$C_{36}H_{42}NO_3$	$C_{19}H_{16}NOP$	$C_{21}H_{20}NO_3P$
M_w	536.7	305.3	365.35
T (K)	120(2)	120(2)	120(2)
Crystal System	Monoclinic	Orthorhombic	Orthorhombic
Space Group	*C*2/*c*	*Pbca*	*Iba*2
a (Å)	31.251(2)	10.3671(4)	37.803(3)
b (Å)	12.6345(10)	9.7004(3)	10.3736(7)
c (Å)	16.0331(12)	30.7223(11)	9.4895(7)
α (°)	90	90	90
β (°)	99.824(7)	90	90
γ (°)	90	90	90
V (Å^3)	6237.8(8)	3089.59(18)	3721.3(5)
Z	8	8	8
D_{calc} (g cm^{-3})	1.143	1.313	1.304
μ (mm^{-1})	0.558	1.573	1.476
F_{000}	2312	1280	1536
Crystal Size (mm^3)	0.157 × 0.073 × 0.041	0.612 × 0.217 × 0.143	0.2603 × 0.0832 × 0.0633
λ (Å)	1.54184	1.54184	1.54184
2θ range for data collection (°)	7.564 to 149.91	10.294 to 148.912	8.84 to 149.442
Reflections. collected	20065	7371	4993
Independent reflections	6245	3060	2553
R_{int}	0.0557	0.0244	0.044
GooF on F^2	1.039	1.058	1.084
R_1, wR_2 [$I > 2\sigma(I)$]	0.0587, 0.1380	0.0348, 0.0878	0.0661, 0.1694
R_1, wR_2 (all data)	0.1059, 0.1692	0.0399, 0.0916	0.0716, 0.1754
Largest diff. peak/hole (eÅ^{-3})	0.33/-0.28	0.39/-0.23	0.78/-0.46
Code	MNHRSI	FEHRTL	FEHRTQ

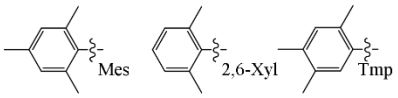
	21d	***21f***	***21g***
Formula	$C_{19}H_{15}NOPB$	C19H22NOP	$C_{16}H_{18}NOP$
M_w	384.2	311.34	271.28
T (K)	120(2)	120(2)	120(2)
Crystal System	Monoclinic	orthorhombic	Orthorhombic
Space Group	$P2_1/c$	*Iba2*	*Pbca*
a (Å)	16.4956(7)	34.1888(3)	11.1668(2)
b (Å)	10.3340(5)	10.64763(8)	9.5381(2)
c (Å)	9.7346(4)	9.49011(9)	28.3885(5)
α (°)	90	90	90
β (°)	94.043(4)	90	90
γ (°)	90	90	90
V (Å^3)	1655.28(13)	3454.68(5)	3023.67(10)
Z	4	8	8
D_{calc} (g cm^{-3})	1.542	1.197	1.192
μ (mm^{-1})	4.319	1.408	1.536
F_{000}	776	1328	1152
Crystal Size (mm^3)	0.323 × 0.145 × 0.102	0.849 × 0.311 × 0.182	0.321 × 0.088 × 0.048
λ (Å)	1.54184	1.54184	1.54184
2θ range for data collection (°)	10.108 to 148.846	8.698 to 147.574	10.078 to 147.404
Reflections. collected	6619	37101	15166
Independent reflections	6619	3273	3017
R_{int}	-	0.0426	0.0397
GooF on F^2	1.013	1.066	1.026
R_1, wR_2 [$I > 2\sigma(I)$]	0.0729, 0.1972	0.0360, 0.0949	0.0350, 0.0922
R_1, wR_2 (all data)	0.0837, 0.2079	0.0360, 0.0949	0.0401, 0.0963
Largest diff. peak/hole (eÅ^{-3})	2.40/-0.76	0.18/-0.28	0.49/-0.25
Code	OAMGLE	FEHRTV	FEHRTW

	21h	***22a***	***22b***
Formula	$C_{17}H_{20}NOP$	$C_{26}H_{21}N_2O_2P$	$C_{28}H_{25}N_2O_2P$
M_w	285.31	424.42	452.47
T (K)	120(2)	120(2)	120(2)
Crystal System	Triclinic	Orthorhombic	Monoclinic
Space Group	*P-1*	$P2_12_12_1$	$C2/c$
a (Å)	10.1317(3)	5.9842(2)	26.103(3)
b (Å)	10.5022(4)	10.9578(5)	5.7961(5)
c (Å)	14.6490(6)	31.8272(12)	32.100(4)
α (°)	87.932(3)	90	90
β (°)	89.517(3)	90	104.115(11)
γ (°)	89.127(3)	90	90
V (Å^3)	1557.48(9)	2087.01(15)	4710.0(9)
Z	4	4	8
D_{calc} (g cm^{-3})	1.217	1.351	1.276
μ (mm^{-1})	1.515	1.377	1.251
F_{000}	608	888	1904
Crystal Size (mm^3)	0.981 × 0.164 × 0.081	0.606 × 0.081 × 0.071	0.456 × 0.072 × 0.049
λ (Å)	1.54184	1.54184	1.54184
2θ range for data collection (°)	8.426 to 147.656	5.554 to 147.524	6.984 to 151.008
Reflections. collected	11349	5909	27055
Independent reflections	6080	3561	4797
R_{int}	0.0347	0.0515	0.0917
GooF on F^2	1.046	1.067	1.066
R_1, wR_2 [$I > 2\sigma(I)$]	0.0343, 0.0876	0.0597, 0.1546	0.0779, 0.2126
R_1, wR_2 (all data)	0.0386, 0.0917	0.0660, 0.1587	0.0942, 0.2316
Largest diff. peak/hole (eÅ^{-3})	0.42/-0.29	0.40/-0.62	0.76/-0.54
Code	FEHRTS	OAMGLD	FEHRTK

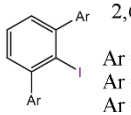
	23	***24***	***29^{Mes}***
Formula	$C_{32}H_{38}Cl_2NOPRu$	$C_{45}H_{47}N_2O_2PCl_2Ru$	$C_{55}H_{57}O_2$
M_w	655.57	850.78	750
T (K)	120(2)	120(2)	120(2)
Crystal System	triclinic	Monoclinic	Triclinic
Space Group	*P*-1	$P2_1/c$	*P-1*
a (Å)	10.6269(9)	13.7569(4)	11.0869(8)
b (Å)	12.5033(13)	11.3299(3)	11.7248(6)
c (Å)	12.5086(9)	25.8146(10)	17.6257(11)
α (°)	88.346(7)	90	79.831(5)
β (°)	89.950(6)	96.096(3)	79.293(6)
γ (°)	66.060(9)	90	83.642(5)
V (Å^3)	1518.3(2)	4000.8(2)	2208.7(3)
Z	2	4	2
D_{calc} (g cm^{-3})	1.434	1.412	1.128
μ (mm^{-1})	6.486	5.008	0.506
F_{000}	676	1760	806
Crystal Size (mm^3)	0.225 × 0.141 × 0.075	0.244 × 0.172 × 0.106	0.1641 × 0.0438 × 0.0328
λ (Å)	1.54184	1.54184	1.54184
2θ range for data collection (°)	7.07 to 147.608	6.462 to 147.096	7.686 to 147.408
Reflections. collected	10786	18329	18751
Independent reflections	5905	7855	8637
R_{int}	0.0274	0.0422	0.0692
GooF on F^2	1.034	1.152	1
R_1, wR_2 [$I > 2\sigma(I)$]	0.0248, 0.0623	0.0516, 0.1180	0.0649, 0.1438
R_1, wR_2 (all data)	0.0263, 0.0633	0.0606, 0.1219	0.1148, 0.1781
Largest diff. peak/hole (eÅ^{-3})	0.41/-0.67	1.01/-0.62	0.22/-0.27
Code	RUHRSB	RUHRSC	FEHRSM

	***29*$^{2,6\text{-Xyl}}$**	***30*$^{2,6\text{-Xyl}}$**
Formula	$C_{48}H_{42}O_2$	$C_{101}H_{105}Fe_2O_8$
M_w	325.41	1558.54
T (K)	120(2)	120(2)
Crystal System	Orthorhombic	Monoclinic
Space Group	*Ccce*	*I*2/*a*
a (Å)	11.7258(5)	22.1583(5)
b (Å)	19.0058(8)	11.7559(3)
c (Å)	16.1304(7)	32.9915(8)
α (°)	90	90
β (°)	90	91.687(2)
γ (°)	90	90
V (Å^3)	3594.8(3)	8590.3(4)
Z	4	4
D_{calc} (g cm^{-3})	1.203	1.205
μ (mm^{-1})	0.551	3.147
F_{000}	1384	3308
Crystal Size (mm^3)	0.122 × 0.104 × 0.052	0.4467 × 0.2437 × 0.1245
λ (Å)	1.54184	1.54184
2θ range for data collection (°)	9.306 to 147.156	7.984 to 148.418
Reflections. collected	4697	19141
Independent reflections	1770	8551
R_{int}	0.0317	0.031
GooF on F^2	1.032	1.035
R_1, wR_2 [$I > 2\sigma(I)$]	0.0410, 0.1033	0.0442, 0.1206
R_1, wR_2 (all data)	0.0527, 0.1114	0.0495, 0.1256
Largest diff. peak/hole (eÅ^{-3})	0.28/-0.18	0.46/-0.48
Code	FEHRTO	FEHRSH

List of Compounds

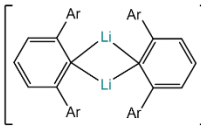


Chapter II



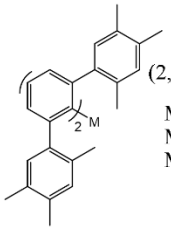
2,6-$Ar_2C_6H_3I$

Ar = Mes	**1**
Ar = 2,6-Xyl	**2**
Ar = Tmp	**3**



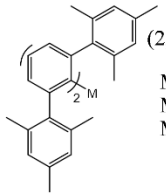
$[2,6\text{-}Ar_2C_6H_3Li]_2$

Ar = Mes	**4**
Ar = 2,6-Xyl	**5**
Ar = Tmp	**6**



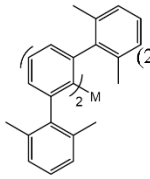
$(2,6\text{-}Tmp_2C_6H_3)_2M$

M = Zn	**7**
M = Cd	**8**
M = Hg	**9**



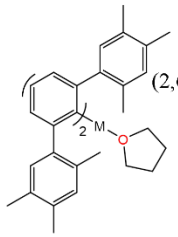
$(2,6\text{-}Mes_2C_6H_3)_2M$

M = Mn	**10**
M = Fe	**11**
M = Co	**12**



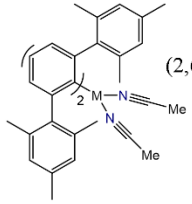
$(2,6\text{-}(2,6\text{-}Xyl)_2C_6H_3)_2M$

M = Mn	**13**
M = Fe	**14**



$(2,6\text{-}Tmp_2C_6H_3)_2M(THF)$

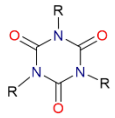
M = Mn	**15**
M = Fe	**16**



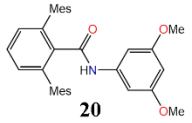
$(2,6\text{-}Mes_2C_6H_3)_2M(MeCN)_2$

M = Mn	**17**
M = Fe	**18**

Chapter III

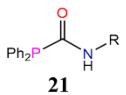


R = Et	**19a**
R = ^{n}Pr	**19b**
R = ^{n}Hx	**19c**
R = Bn	**19d**

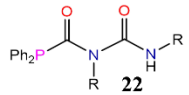


20

Chapter IV

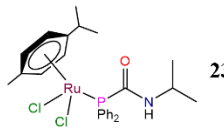


21

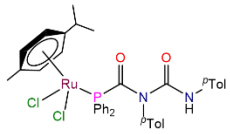


22

R = Ph	**(a)**
R = ^{p}Tol	**(b)**
R = 3,5-$(OMe)_2C_6H_3$	**(c)**
R = 4-BrC_6H_4	**(d)**
R = ^{n}Hx	**(e)**
R = Cy	**(f)**
R = ^{i}Pr	**(g)**
R = ^{t}Bu	**(h)**
R = Ph, Cy	**(i)**

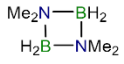


23

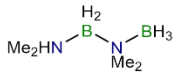


24

Chapter V



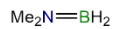
25



26

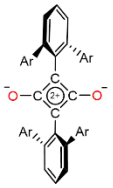


27

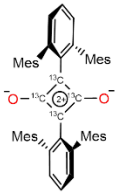


28

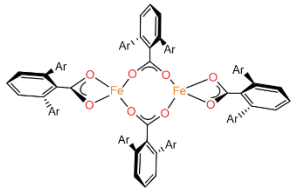
Chapter VI



Ar = Mes	29^{Mes}
Ar = 2,6-Xyl	$29^{2,6\text{-}Xyl}$



^{13}C-29^{Mes}



Ar = Mes	30^{Mes}
Ar = 2,6-Xyl	$30^{2,6\text{-}Xyl}$